8-2010

Design and testing of orifice valves for use in freight railcars hydraulic suspension system

Awni K. Alshakhshir
University of Texas-Pan American

DESIGN AND TESTING OF ORIFICE VALVES FOR USE IN FRIEGHT RAILCARS HYDRAULIC SUSPENSION SYSTEM

A Thesis

by

AWNI K. ALSHAKHSHIR

Submitted to the Graduate School of the
University of Texas-Pan American
In partial fulfillment of the requirements for the degree of

MASTER OF SCIENCE

August 2010

Major Subject: Mechanical Engineering

DESIGN AND TESTING OF ORIFICE VALVES FOR USE IN FRIEGHT RAILCARS HYDRAULIC SUSPENSION SYSTEM

A Thesis
by
AWNI K. ALSHAKHSHIR

COMMITTEE MEMBERS

Dr. Constantine Tarawneh
Co-Chair of Committee

Dr. Stephen Crown
Co-Chair of Committee

Dr. Javier Kypuros
Committee Member

Dr. Arturo Fuentes
Committee Member

August 2010

ABSTRACT

Alshakhshir, Awni K., Design and Testing of Orifice Valves for Use in Freight Railcars Hydraulic Suspension System. Master of Science (MS), August, 2010, 287 pp., 52 tables, 169 figures, 101 titles, 4 appendices.

The work presented in this thesis describes the specific steps undertaken to design and test two spool type control valves that will be part of Amsted Rail's innovative vertical hydraulic damper system. The design challenge lies in the requirement that these spool valves must maintain a linear relation between pressure drop, flow rate, and position, during the extension and retraction cycles of the hydraulic damper. To this end, a series of laboratory experiments were conducted on spools having different land geometries in order to acquire the optimum apertures that will produce the desired performance based on simulation data provided by Amsted Rail. The effect of the working fluid temperature on the performance of the two designed spool valves was also investigated. Experimental testing was successful in identifying two spool valves that meet the provided design criteria within 2% for AW46 hydraulic oil working fluid at a temperature of 25°C (77°F).

DEDICATION

My deepest gratitude goes to my family for their unflagging love and support throughout my life; this thesis is simply impossible without them. I am indebted to my father, Khalid, for his care and love. As a typical father in a Jordanian family, he worked industriously to support the family and spared no effort to provide the best possible environment for me to grow up and attend school. He has never complained in spite of all the hardships in his life. I cannot ask for more from my mother, Rawheyah, as she is simply perfect. I have no words that can fully describe her everlasting love for me. I remember many sleepless nights with her accompanying me when I was sick. I remember her constant support when I encountered difficulties and I remember, most of all, her delicious dishes. Mother, I love you. I feel proud of both my sisters, Kholod and Reham, for their talents. They had been a role model for me to follow unconsciously when I was a teenager and have always been my best counselors.

Last but not least, I thank God Almighty for my life through all tests in the past three years. You have made my life more bountiful. May your name be exalted, honored, and glorified.

ACKNOWLEDGEMENTS

I especially want to thank my advisor, Dr. Constantine Tarawneh, for his constant guidance and relentless support throughout my tenure at The University of Texas Pan-American. He sets an example of a world-class researcher for his rigor and passion for research.

I was also delighted to interact with Dr. Stephen Crown by having him as my co-advisor. I appreciate all the assistance he provided me regarding the use of the Labview program software. In addition, he was always accessible and willing to help me with any questions I had which made my research progress a lot smoother.

Dr. Javier Kypuros and Dr. Arturo Fuentes deserve special thanks for accepting to serve in my thesis committee.

All my lab colleagues at the Bearing Research Laboratory have inspired me in my research and life through our interactions during the long hours in the lab. Thanks.

Special acknowledgment is given to Amsted Rail Inc. for financially supporting the work conducted in this project.

TABLE OF CONTENTS

Page

LIST OF TABLES

Page

LIST OF FIGURES

Page

NOMENCLATURE

$A_{clearance}$	opening area component due to the clearance between the spool body and the valve seat [in^2]
A_{spool}	opening area component of the spool aperture [in^2]
A_t	total opening area for half of the spool [in^2]
c	speed of sound [m/s]
D_{body}	spool body diameter [in]
D_h	hydraulic diameter [in]
E_v	bulk modulus [N/m^2]
F_{dry}	dry friction force [N]
$F_{hydraulic}$	viscous damping force [N]
f	output frequency of the turbine flow meter [Hz]
h	valve gap [in]
I	output current [mA]
K	K-factor of the turbine flow meter [pulse/GAL]
K_e	exit loss coefficient
K_f	friction loss coefficient
K_i	entrance loss coefficient
k	orifice flow coefficient

M	Mach number
P	pressure between surfaces [Pa]
P_c	calculated gage pressure [psi]
$P_{clearance}$	wetted perimeter component due to the clearance between spool body and valve seat [in]
P_{spool}	wetted perimeter component of the spool aperture [in]
P_t	total wetted perimeter for half of the spool [in]
Q	volumetric flow rate [GPM]
R	resistor [KΩ]
Re	Reynolds number
R_p	potentiometer resistance [KΩ/turn]
r_e	radius at valve gap exit [m]
r_i	radius at valve gap inlet [m]
S	contact surface area [m^2]
s	spool stop number [quarter turn]
T	total number of turns the trailing wheel rotated [turns]
T_{flow}	temperature of the flow [^oC]
$T_{thermostat}$	temperature settings of the hydraulic power unit's thermostat [^oC]
U	average flow velocity [m/s]
u_i	flow velocity at valve inlet [m/s]
V	voltage drop [V]
V_{in}	input voltage from the DC-supply [V]
V_{out}	output voltage from 23 KΩ resistor [V]

x	spool displacement [in]
$z^{\bullet}$	relative velocity of motion [m/s]

Greek

β	damping coefficient of the hydraulic damper [N.s/m]
Δp	pressure drop across the valve [Pa]
μ	absolute viscosity [cP]
μ_s	friction coefficient
υ	kinematic viscosity [cSt]
ρ	flow density [kg/m^3]

CHAPTER I

INTRODUCTION AND BACKGROUND

In the fall of 2008, Amtrak approached Amsted Rail to assist them in resolving an issue related to the suspension system used in Amtrak's freight railcars. Mr. Paul Wike[1] of Amsted Rail suggested the use of a hydraulic damper system as a possible solution to Amtrak's suspension problem. To that end, he took the initiative in designing a preliminary hydraulic damper system that utilizes two spool valves to provide a linear control for the vertical suspension system of Amtrak's railcars.

In the same semester, Dr. Brent Wilson[2] and Mr. Paul Wike of Amsted Rail shared information about this project with the UTPA research team and requested their assistance in testing the preliminary design of the hydraulic damper and suggesting improvements and modifications to the initial design.

The proposed hydraulic damper will be mounted on the side frame of Amtrak's truck shown in Figure 1, in series with the spring set located at the compression member in order to damp the truck's vertical oscillations due to track irregularities. The exact location of the proposed vertical suspension damper with two units per each side frame of Amtrak's truck is shown in Figure 2.

---

[1] Mr. Paul Wike is a Principal Engineer in Amsted Rail.
[2] Dr. Brent Wilson is the Director of Research and Development in Amsted Rail.

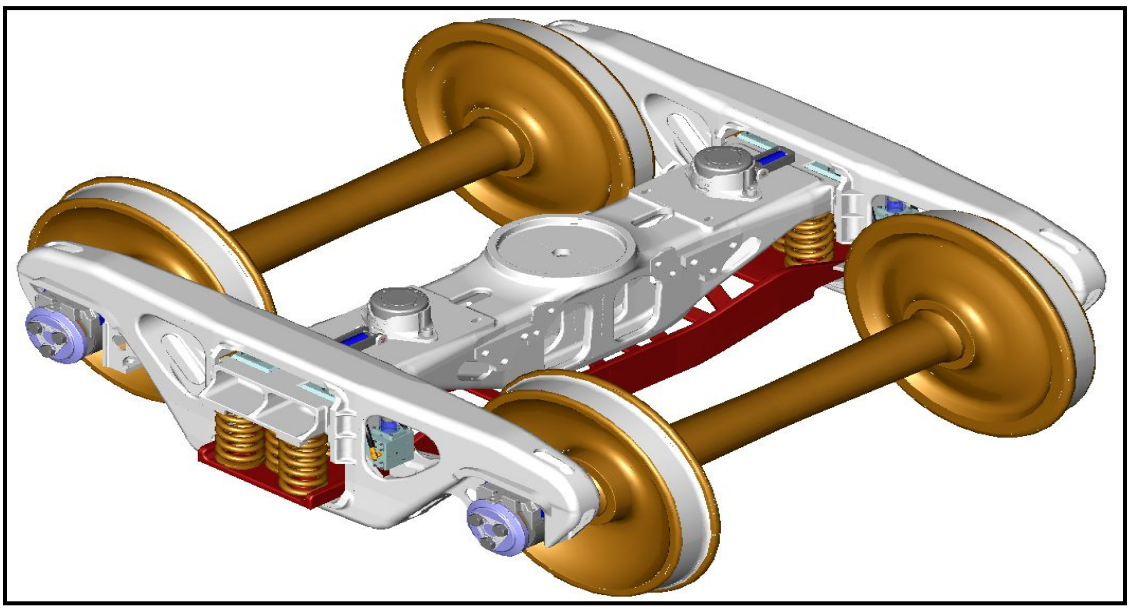

Figure 1: CAD model of Amtrak's modified truck (Courtesy of Amsted Rail)

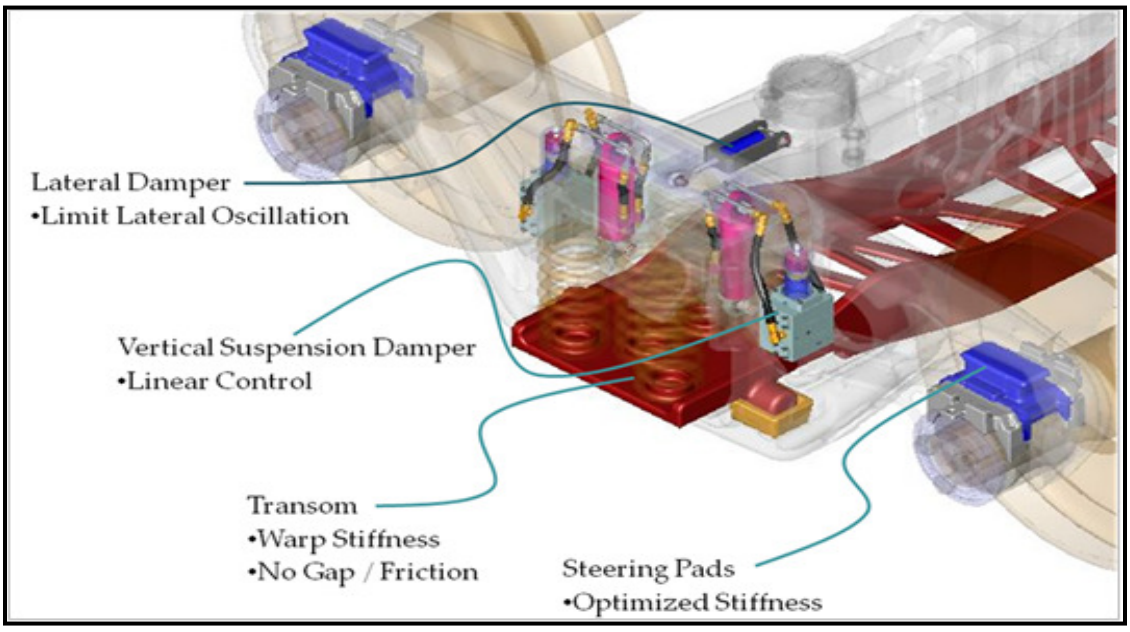

Figure 2: CAD model of Amtrak's modified truck shows the location of the vertical suspension damper (Courtesy of Amsted Rail).

The proposed hydraulic damper consists of a cylinder/piston assembly, valve block and connecting hoses. Figure 3 shows all the hydraulic damper components.

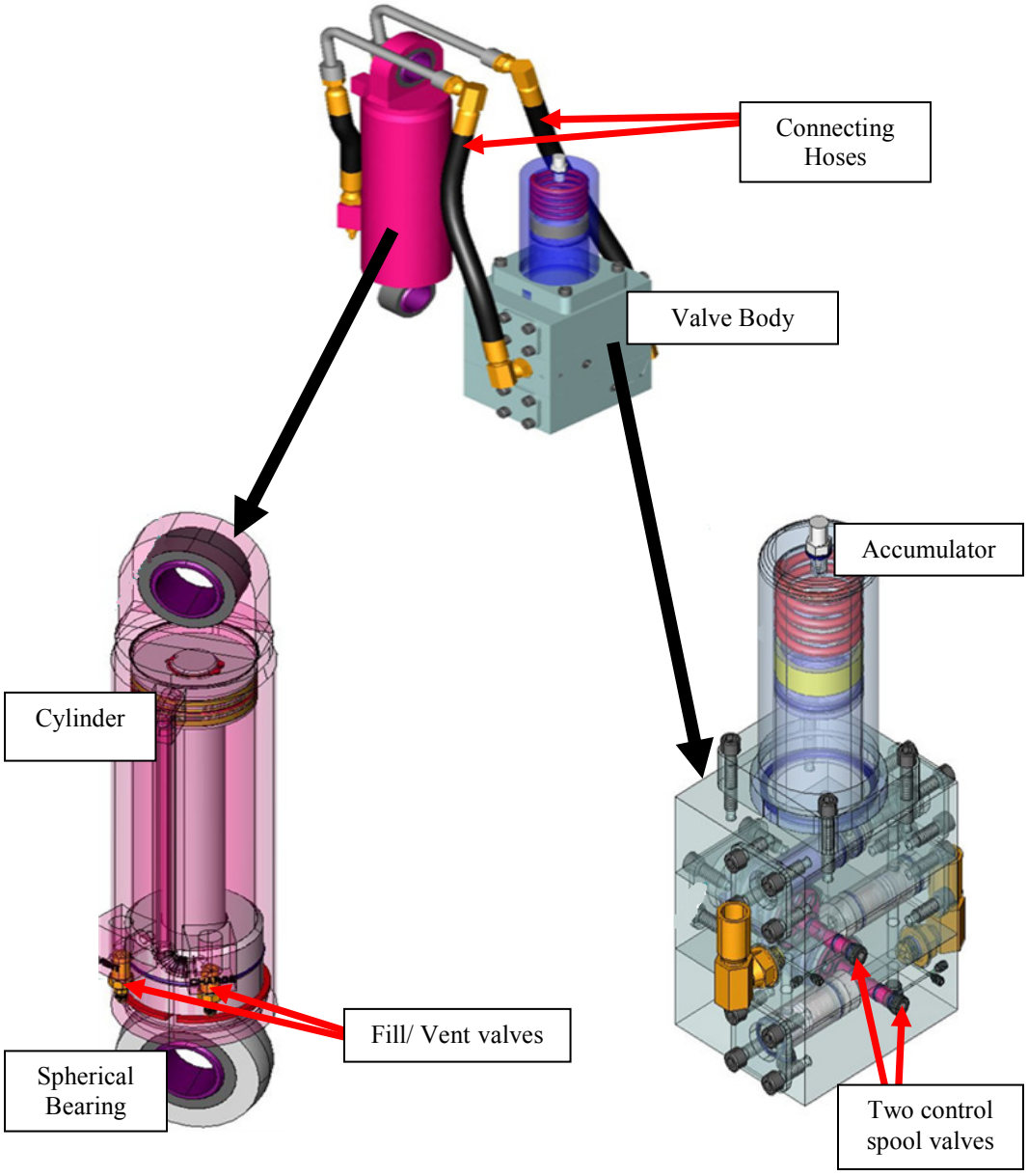

Figure 3: CAD model of the proposed hydraulic damper components (Courtesy of Amsted Rail).

As shown in Figure 3, the cylinder has a 2.00 in. bore with 4.75 in. stroke and its maximum operating pressure is 3000 psi. A 2.0 in. diameter piston is packaged inside of the cylinder with a spherical bearing end type. The side frame of Amtrak's truck will be modified at the compression member (where the springs set are attached) with a hanger box weldment to anchor the upper part of the cylinders as shown in Figure 4.

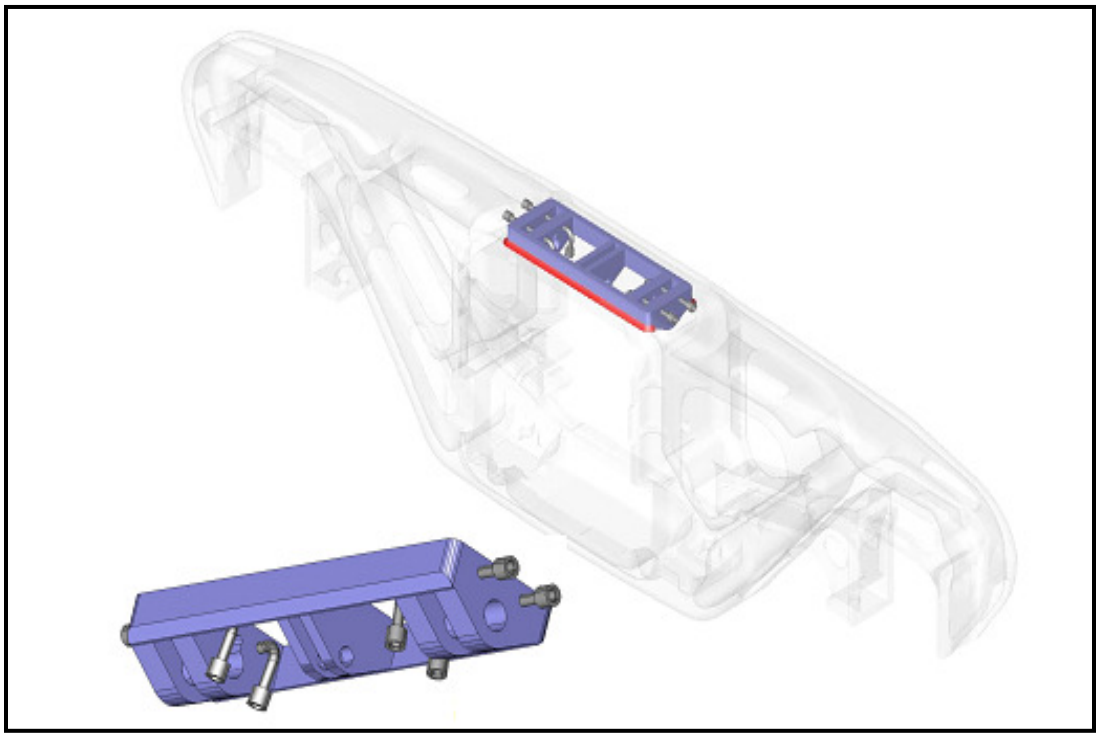

Figure 4: CAD model of the side frame cylinder anchor.

(Courtesy of Amsted Rail)

The truck bolster will also be modified at the shoe pockets with a box weldment to anchor the other end of the cylinders as shown in Figure 5.

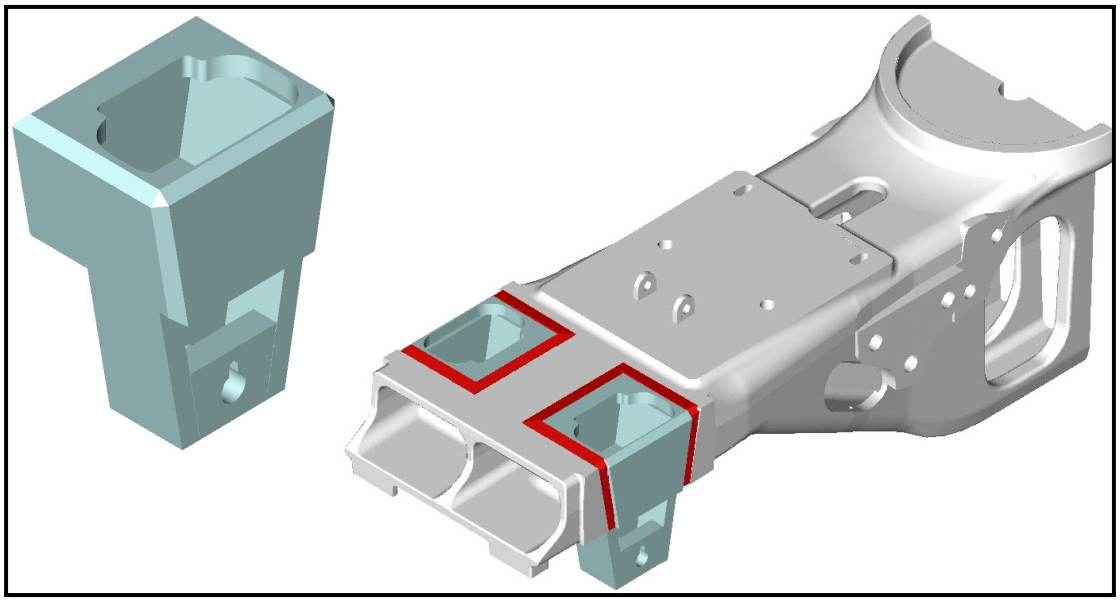

Figure 5: CAD model of the bolster cylinder anchor.

The valve body has two flow controls and an accumulator, see Figure 3. The valve will be packaged inside the side frame and will be visible through the triangular brake aperture (see Figure 1). The accumulator has a 6.60 cubic in. capacity with an operating pressure in the range of 209 to 304 psi, and is made of clear polycarbonate to provide a visual means to check the fluid level and pressure holding capability of the cylinder.

The objective of the proposed hydraulic damper is to mitigate vertical accelerations over 1 g and/or reduce the wheel load to less than 15 percent over extreme vertical track perturbations. A parametric study was undertaken by Amsted Rail to fulfill these design conditions. The damping system was simulated using Universal Mechanism software (see Figure 6) under empty, half-loaded and fully-loaded car configurations at a range of speeds up to 90 mph through a section of actual track in North Carolina. This track profile was chosen because it

crosses over an intersection. As the truck moves along the path, the springs of the suspension are exposed to continuous compression and extension, Lambeau Leap effect. The simulation provides the worst case scenario for the suspension of the truck and its damping system. The track profile consists of 1.25 in. vertical pitches on 33 ft centers that extend for six consecutive pitches.

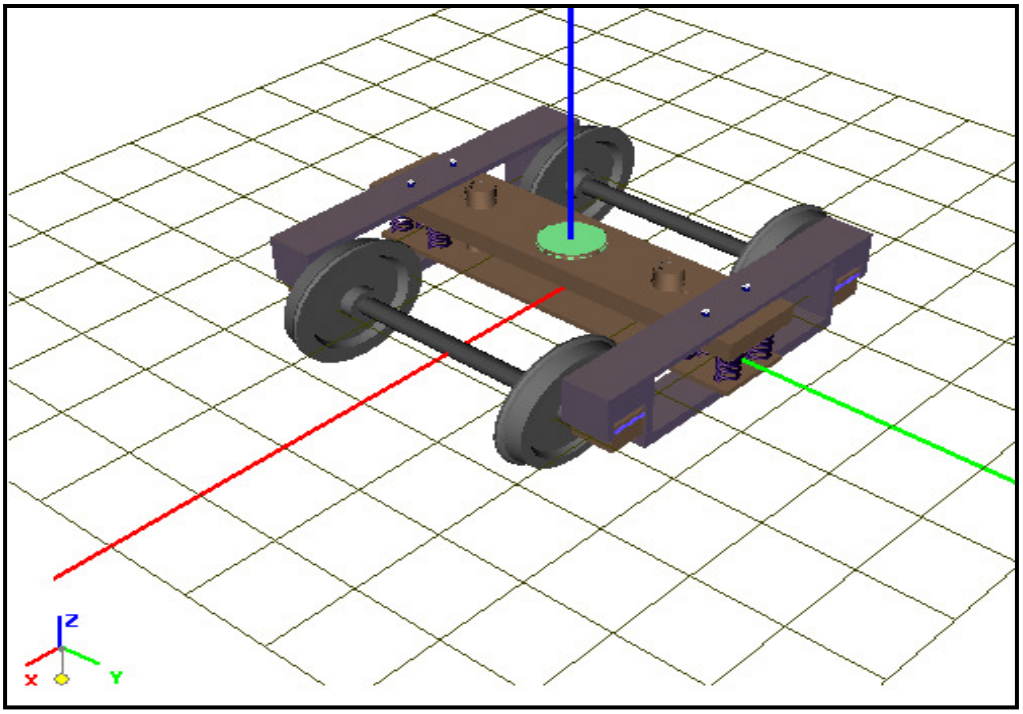

Figure 6 : Model of the bogie of Amtrak freight railcars created using Universal Mechanism Software. (Courtesy of Amsted Rail)

The damper bounded envelope performance for 70, 80, and 90 mph is illustrated in Figure 7.

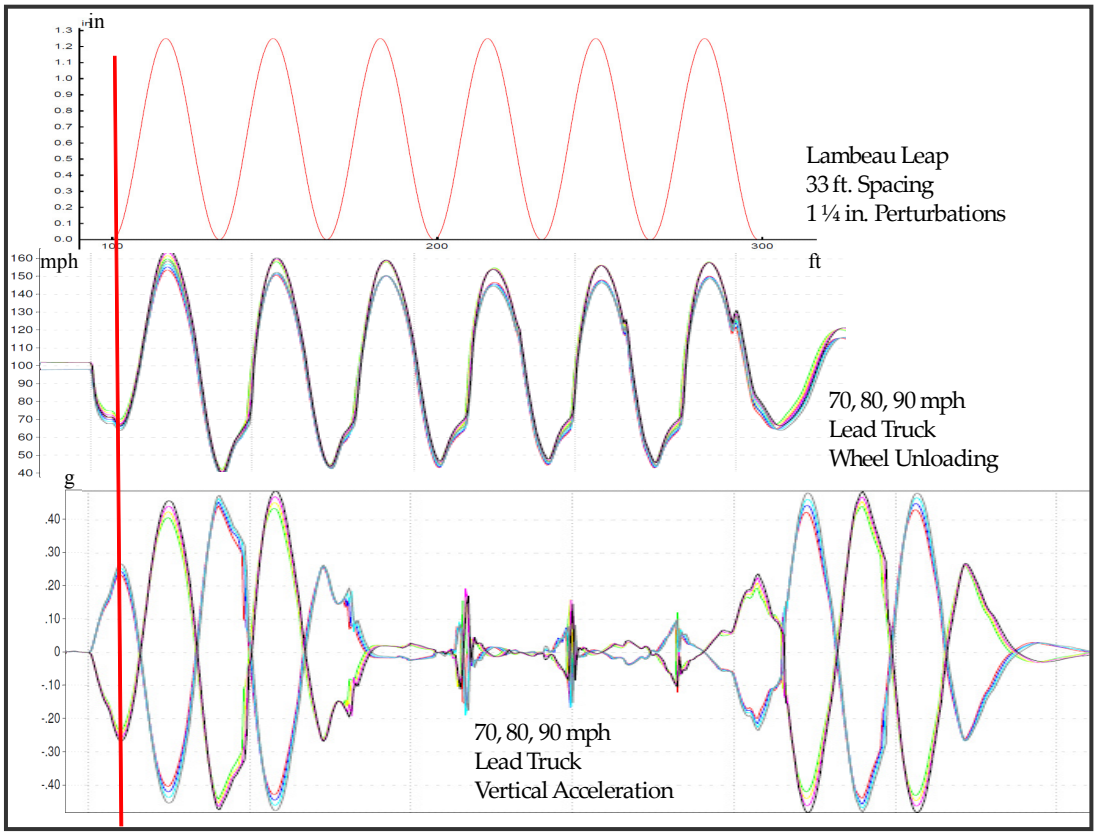

Figure 7: Damper envelope performance. (Courtesy of Amsted Rail)

Based on the simulation results, Amsted Rail Engineering has found that the truck maintains 40 percent of the wheel load with 0.5 g's vertical accelerations at 90 mph. In addition, the required damping for loading (retraction action) and unloading (extension action) of the suspension springs was found to be different as will be shown later in this Chapter.

In order to achieve the required damping characteristics, a pair of linear control valves was necessary. The valves are pressure operated flow controls which are positioned to normally closed on the blind side of the cylinder and normally open on the rod side. Figure 8 and 9 show

how the proposed hydraulic damper responds as the springs of suspension are under compression (retraction action) and as they are under rebound (extension action), respectively.

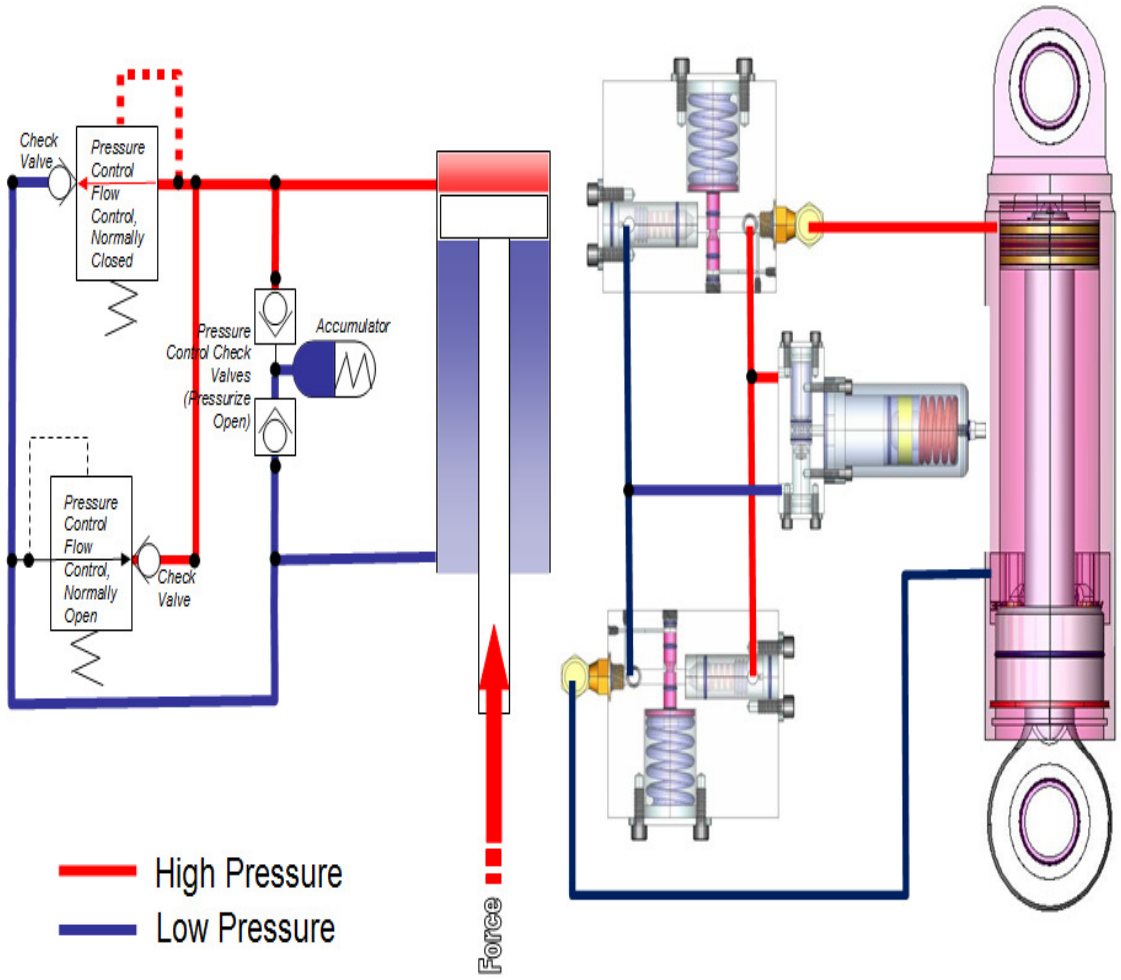

Figure 8: Schematic of the proposed hydraulic damper shows its response as the springs of the suspension are being compressed. (Courtesy of Amsted Rail)

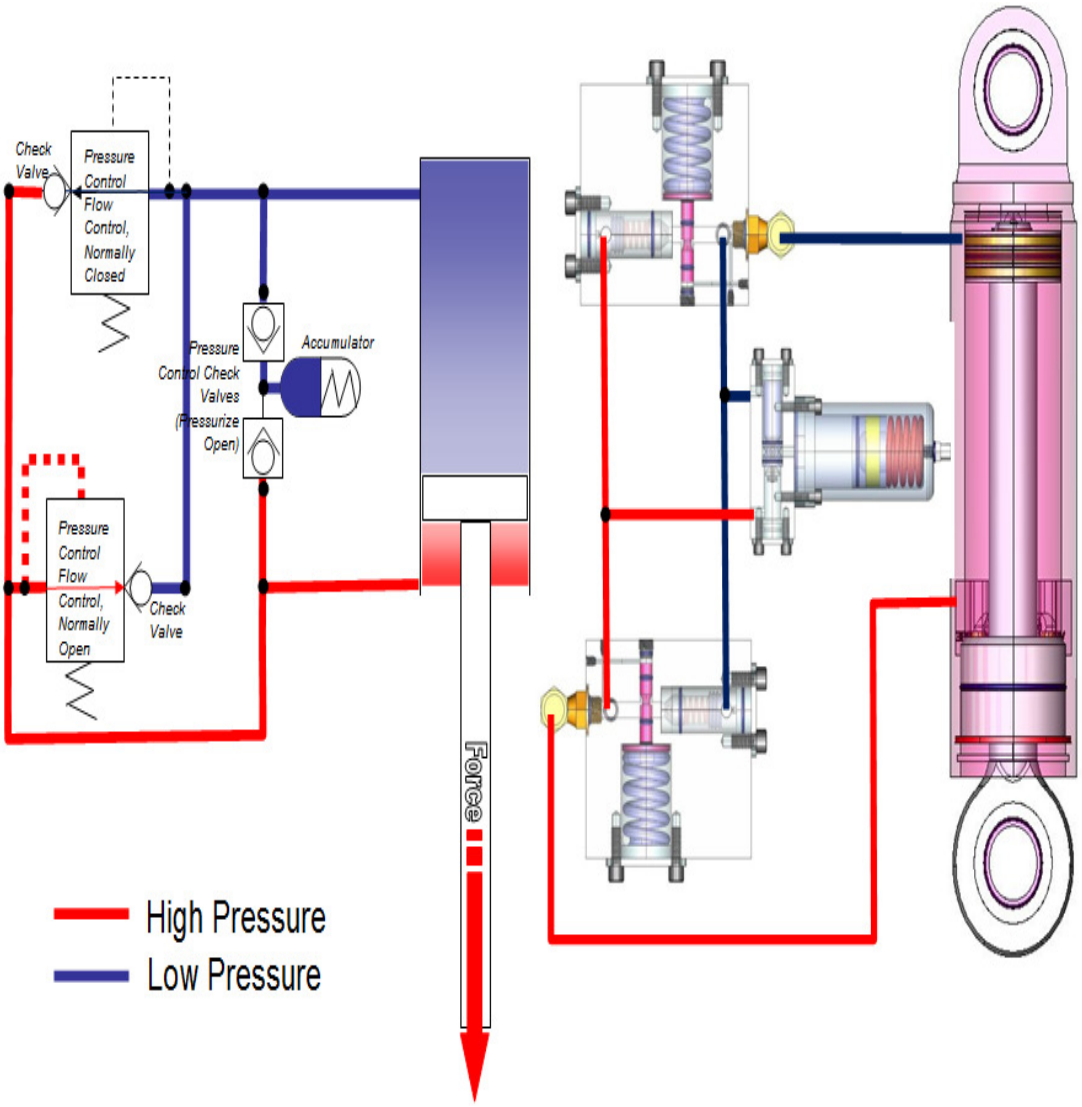

Figure 9: Schematic of the proposed hydraulic damper shows its response as the springs of the suspension are being extended (Courtesy of Amsted Rail)

Based on the movement of the suspension, the flow will be directed to one spool at a time using check valves in order to meter it according to the damper performance requirements established by Amsted Engineering as shown in Figure 10.

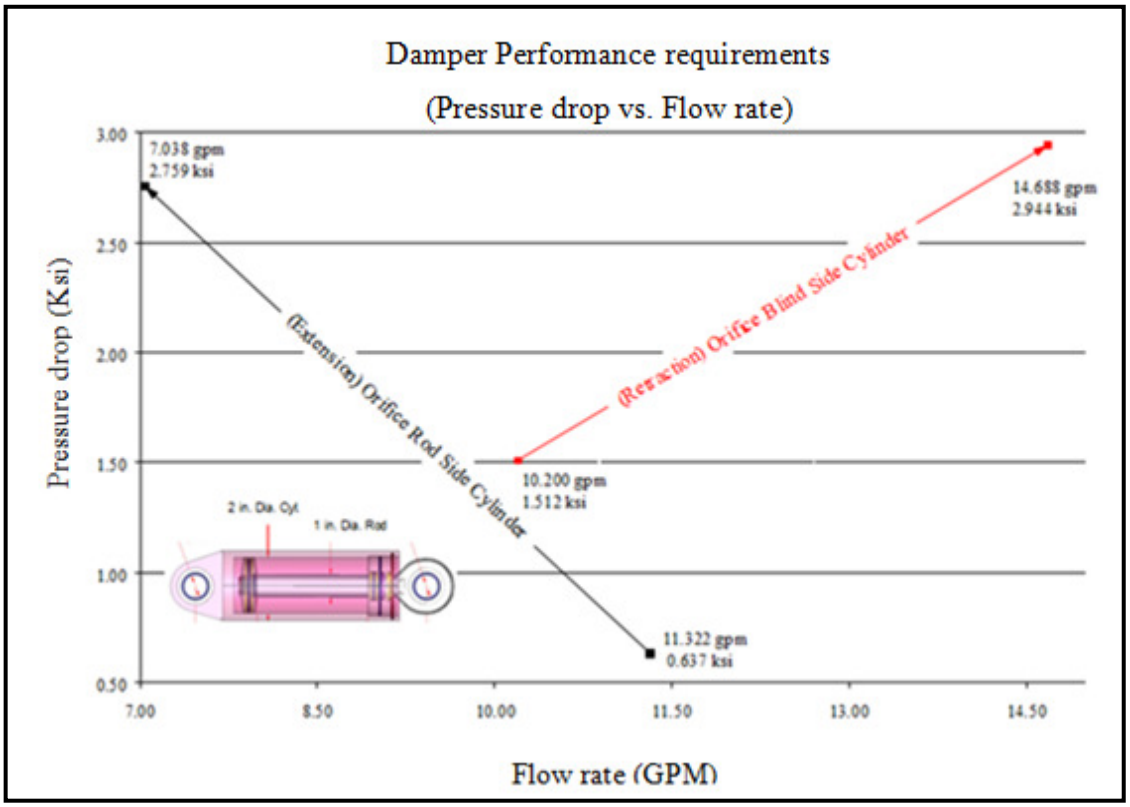

Figure 10: Damper Performance requirements for both retraction and extension actions of the suspension. (Courtesy of Amsted Rail)

The two required control valves each have a different role to play. One valve, the extension side performance spool, will create a pressure drop that decreases as the flow past the spool land increases. Whereas the second valve, the retraction side performance spool, will generate a pressure drop that increases as the flow past the spool land increases.

As requested by Amsted Rail, the two control valves will be pressure / spring controlled spools (see Figure 11). Thus, importance was placed on ensuring that a linear relationship was maintained between flow rate and spool land position for both of the proposed spools.

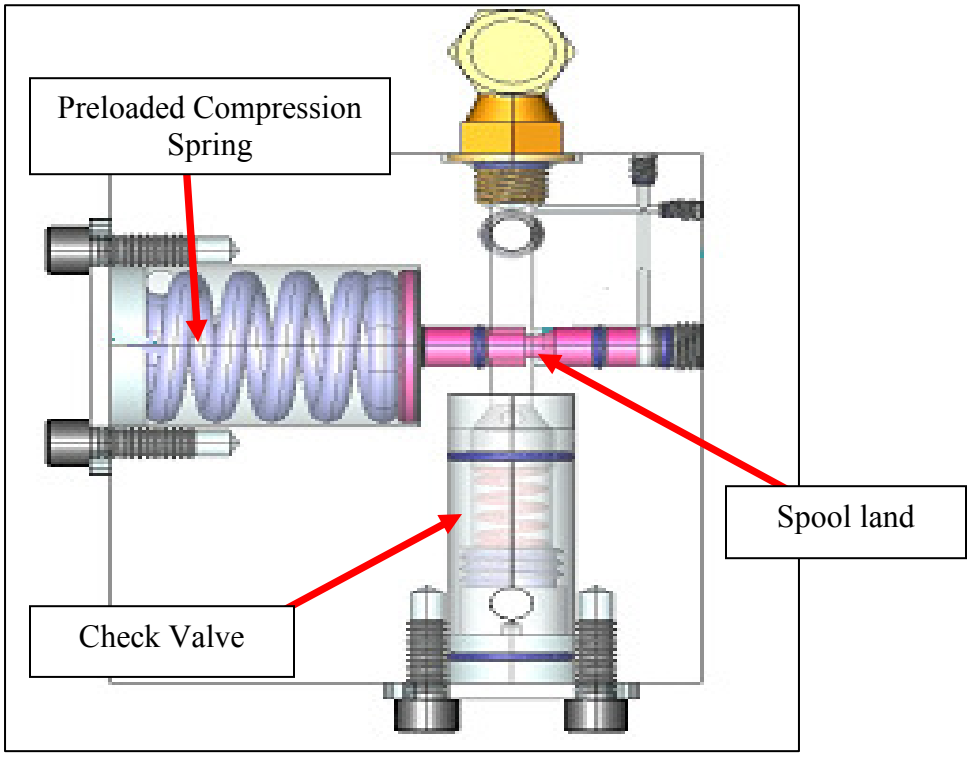

Figure 11: Schematic of the control valve manifold.

(Courtesy of Amsted Rail)

In an effort to develop the required control valves, the work presented in this thesis focused on testing and quantifying the flow characteristics of different spool lands to find the optimum apertures that produce the desired linear flow performance for both retraction and extension actions of Amtrak truck's suspension. Note that each of the spools that were tested provided some insight into the appropriate profiles for the two desired spools that produce linear control on the incoming flow. In Chapter II, a thorough literature review of general suspension concepts

(passive, active suspensions and control valves) and previous research efforts conducted in the area of spool type control valves are provided. Chapter III contains a detailed description of the experimental work carried out in order to acquire the optimum performance for the two spool valves. Chapter IV contains a thorough discussion of the results obtained in Chapter III. It shows the methodology that was followed to obtain the initial proposed profiles for the control valves of both sides based on the damper performance requirments. Chapter V presents an investigation on the effect of the hydraulic oil temperature on the turbine flow meter readings and spool performance. It also describes the testing results of the initial proposed spools at different temperatures. Chapter VI contains the revised simulation data of pressure drop and flow rate provided by Amsted Rail along with the testing results of different spools. This Chapter provides the proposed two spool valve designs that were selected. Finally, Chapter VII provides a summary of the main conclusions of this study and the future work.

CHAPTER II

LITERATURE REVIEW

Suspension in general is the term given to the system of springs, dampers (shock absorbers) and linkages (constraints, bump stops, etc...) that connect a vehicle (car body**)** to its wheels.

Railway vehicle suspensions are made up of a number of different components which can range from mechanically simple coil springs and friction dampers to sophisticated arrangements of air springs, leveling valves and reservoirs or fully active or semi-active components [1].

The suspension system has either one stage or two stages. If the bogie has a rigid frame (see Figure 12) then usually the suspension consists of two stages; primary suspension (axle box suspension) that connects the wheel sets to the bogie frame and secondary suspension (central suspension) between the bogie frame and car body. In general, freight vehicles which have sometimes only a single-layer suspension (*i.e.* primary suspension) have less sophisticated suspensions than passenger vehicles which have generally both a primary and secondary suspensions[1, 2].

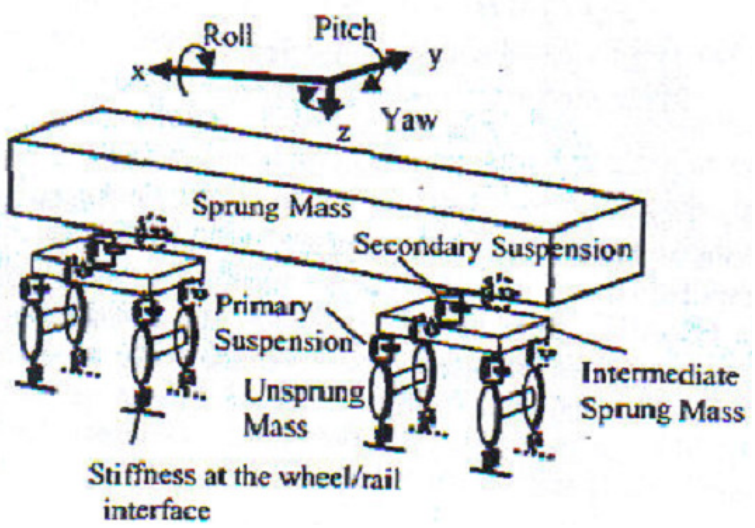

Figure 12: Ride model for a two stage suspension railway vehicle [3].

For a railway vehicle, the suspension unit ought to be able to reduce chassis acceleration within the constraint of a set working space, support the weight of the vehicle statically and dynamically, transmit the traction and braking forces from the wheels whilst isolating passengers and freight from irregularities in track geometry and aerodynamic forces [2]. Accordingly, the suspension influences vehicle ride comfort and stability, and should be designed to guide the vehicle so that it follows the track, prevent and minimize undue damage to track or vehicle components from dynamic forces and to maintain suitable space between the track and car body. It follows that there are a number of quite basic conflicts in these requirements and all suspension design is an intermediate state between conflicting alternatives. Some of these conflicts are well understood, for example the conflict between the requirements of stability and curving (*i.e.* the need for a stiff suspension for high speed stability versus a flexible suspension for finding a way through small radius curves).

From the degree of control point of view, a vehicle suspension system can be categorized as passive and active systems [4].

Passive Suspension Systems

Passive suspension systems include conventional springs, dampers and contain no mechanism for feedback control such as sensors, actuators and electronic controllers; therefore, the force elements in a passive suspension are not adjustable and can not be controlled [4]. In addition, the absence of a power supply can be regarded as the factor that distinguishes passive suspensions among the other types of suspension systems. Spring rate and damping of passive suspensions are chosen according to comfort, road holding and handling specifications.

Due to the fact that further improvements in, for example, ride comfort are restricted for passive suspension systems and in order to achieve acceptable behavior over the whole range of working frequencies, the railway vehicle dynamics has changed from being an essentially mechanical engineering discipline to one that is increasingly starting to include sensors, electronics and computer processing and the implementation of active technology becomes more common. On the other hand, passive suspensions are still very competitive with actively controlled suspensions and still dominant in the marketplace; since they are simple, reliable and inexpensive.

The typical passive suspension system can be considered as a spring in parallel with a damper placed at each corner of the vehicle.

Generally, springs are used to [2];

- Equalize the vertical loads between wheels; since unloading of any wheel is dangerous because it causes a reduction /loss of guidance forces.
- Stabilize the motion of vehicles on the track.
- Reduce the dynamic forces and accelerations due to track irregularities.

The principal types of elastic elements (springs) are;

1. Leaf spring. (Figure 13-a)
2. Plate spring or washer. (Figure 13-b)
3. Ring spring. (Figure 13-c)
4. Coil spring. (Figure 13-d)
5. Torsion spring. (Figure 13-e)
6. Air spring. (Figure 13-f)
7. Rubber-metal spring. (Figure 14)

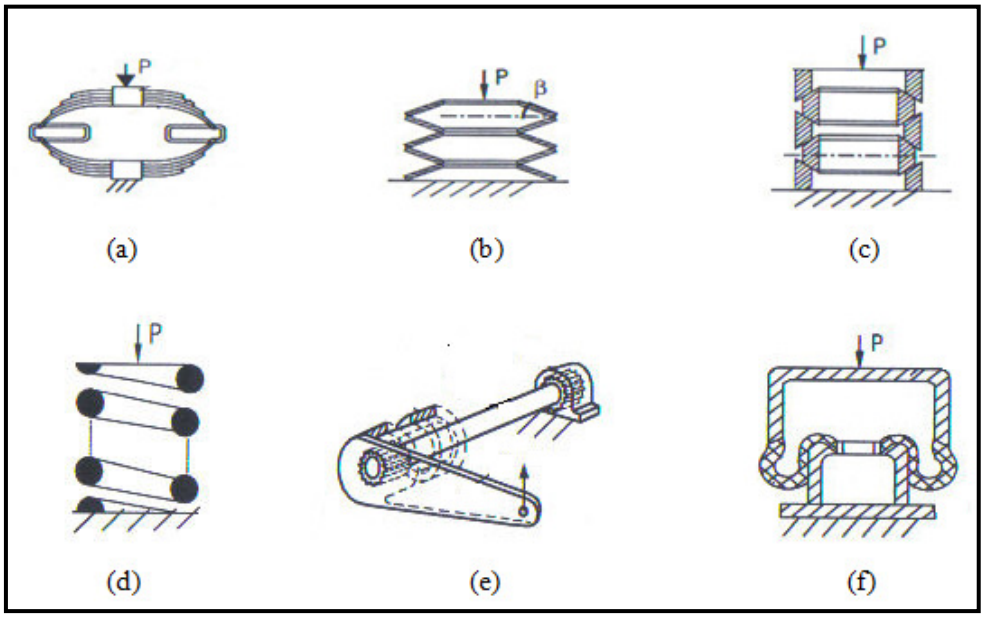

Figure 13: Principal types of elastic elements (springs). [2]

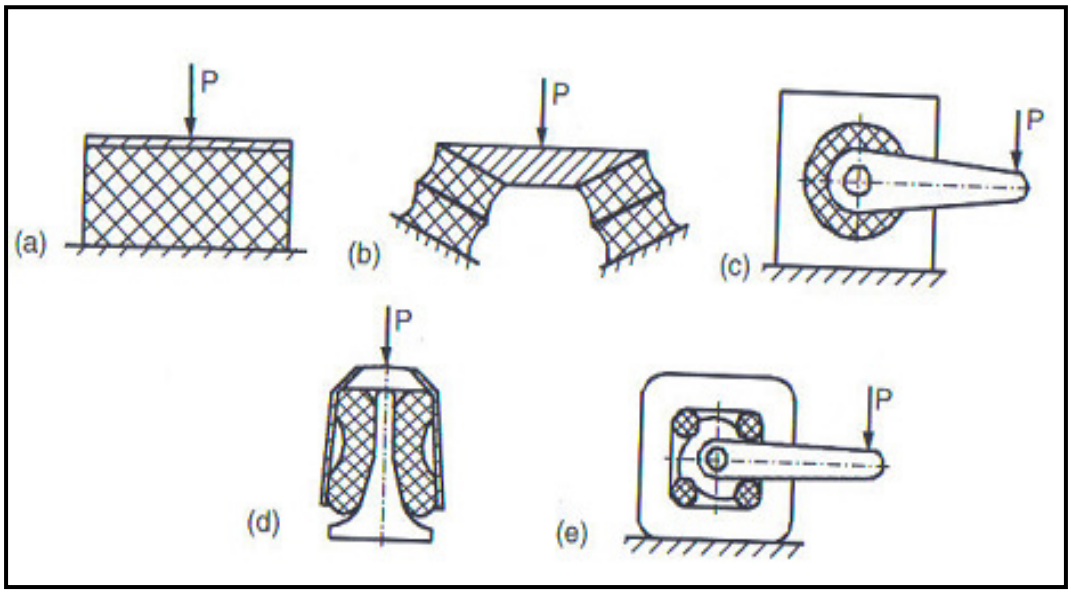

Figure 14: Rubber-metal springs a) Compression (b Compression and shear (c Torsion (d bell type (e Cam type. [2]

Damping is usually provided in railway vehicle suspension by the use of viscous or friction damping devices that controls oscillations in the primary or secondary suspension of the vehicle by energy dissipation.

In friction dampers the energy of oscillations is transformed into heat energy by dry friction. The friction force results from the relative slip between two rigid bodies in contact and this force can be constant or dependent on the mass of the car body, but always acts to resist the relative motion. Also, this friction force is proportional to friction coefficient μ_s, pressure between surfaces *P*, and contact surface area *S*. This dependence can be represented by the following formula:

$$F_{dry} = -\mu_s SP \frac{z^{\bullet}}{|z^{\bullet}|} \tag{1}$$

Where $z^{\bullet}$ is the relative velocity of motion and the minus sign denotes that the friction force is always in the opposite direction to the velocity.

Depending on their construction, friction dampers may be classified as one of four types; Integrated with the elastic element, integrated into the spring suspension, telescopic and lever as shown in Figure 15. Friction dampers are mainly used in freight vehicle suspensions due to their low cost and simplicity.

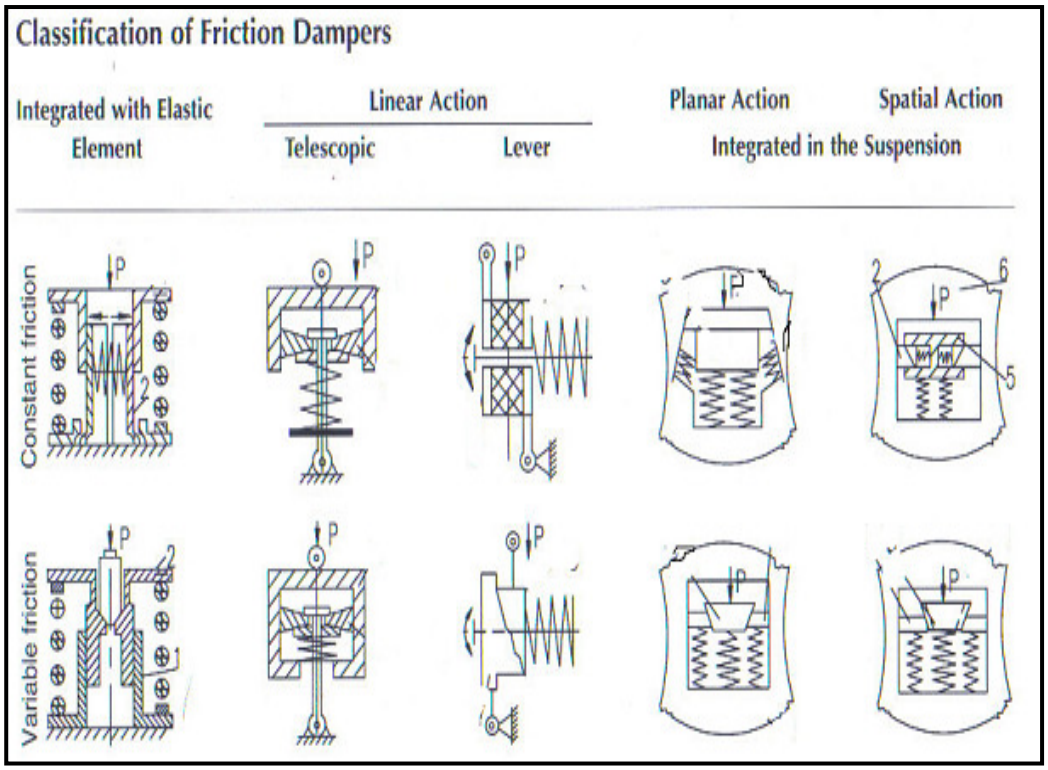

Figure 15: Classification of friction dampers. [2]

On the other hand, viscous damping develops between two parts separated with a layer of viscous liquid (lubricant) or in devices known as hydraulic dampers, where the viscous liquid flows through an orifice and dissipates the energy. The damping force in the viscous case is proportional to the velocity and is represented by the following:

$$F_{hydraulic} = -\beta\left(z^{\bullet}\right)^{n} \tag{2}$$

Where β is the damping coefficient for the hydraulic damper; n is the power; $z^{\bullet}$ the velocity of relative motion. If the liquid flow is laminar, then n = 1 and damping is described as linear viscous damping. For n = 2, damping is called turbulent or quadratic.

The energy dissipated in a hydraulic damper is proportional to its relative velocity, therefore to the amplitude and frequency of vibration. Thus the hydraulic damper is self-tuning to dynamic excitations along with providing reliable and predictable damping of vehicle oscillations.

Railway vehicles normally use the telescopic hydraulic dampers as shown in Figure 16. The hydraulic damper operates by forcing the working fluid through an orifice from one chamber into the other as the vehicle oscillates on the suspension. This produces viscous damping and the kinetic energy of oscillations is transformed into heat.

Telescopic hydraulic dampers (see Figure 16) consist of the body (1) with the sealing device, the working cylinder (2) with valves (4) and the shaft (3) with a piston (5) that also has valves (6). When the piston moves relative to the cylinder, the working fluid flows through the valves from the chamber over the piston to the chamber under it and back.

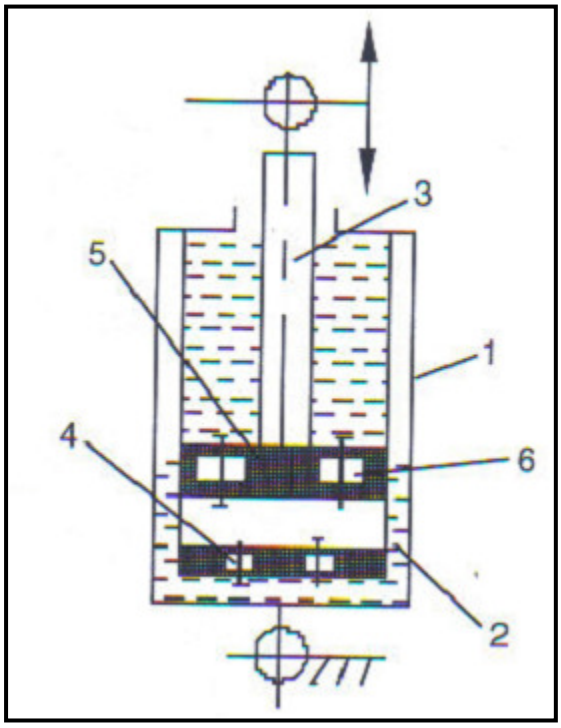

Figure 16: Telescopic type hydraulic damper. [2]

The reliability of hydraulic dampers mostly depends on the sealing between the shaft and the body. Occasionally malfunction of this unit causes excessive pressure in the chamber over the piston resulting in leakage of the working fluid. The capability of hydraulic damper to dissipate energy is characterized by its force versus velocity characteristic, which is the dependence between the resistance force developed in the hydraulic damper, and the piston displacement velocity.

The damper characteristic may be either symmetrical, when the resistance forces are the same for extension and compression, or asymmetric. Dampers with symmetric characteristics are typically used in secondary suspensions. In primary suspensions, asymmetric dampers are often used as the motion of the wheel over a convex irregularity causes larger forces than negotiating a

concave one. As a result, dampers may be designed with an asymmetric characteristic providing a smaller force in compression than in extension. However, large damping forces in extension can significantly decrease the vertical wheel load, thus increasing the risk of derailment. Therefore the railway dampers are less asymmetric than automobile ones.

There are four important parameters which should be carefully considered in designing automobile vehicle suspension system which generally apply to railway vehicles [5]:

1. Ride Comfort is directly related to the acceleration sensed by passengers when traveling on a rough road.
2. Body motions which are known as bounce, pitch and roll of the sprung mass are created primarily by cornering and braking maneuvers. Body motions may be present even on perfectly smooth roads.
3. Road handling is associated with the contact forces of the tires and the road surface. These contact forces create the necessary friction which prevents the tires from sliding on the road surface.
4. Suspension travel refers to the relative displacement between the sprung and the unsprung masses. All suspension systems trade-off the suspension travel for an improved ride comfort.

No suspension system could minimize all the four of the abovementioned parameters simultaneously due to many technical challenges that associated with the application of the methodologies which lead to the optimum selection of the suspension damping and stiffness parameters of the vehicle.

Generally speaking, passive suspension system design used fixed-points theory in the past [6-8]. This design method is based on the existence of 3 fixed-points in frequency response curves of the system. By choosing the optimal positions of these 3 points, designers are able to design the optimal parameters. But this method could not be applied for complex systems that have more than 2-degrees of freedom and moreover the results of design usually depend on the designer's experiences.

Recently, a great deal of research has been carried out into the optimization of vehicle suspensions. A classified bibliography, including nearly 600 papers was presented by Elbeheiry et al. [9]. Comprehensive surveys can also be found in the papers by Hedrick and Wormely [10], Sharp and Crolla [11] and Hrovet [12].In addition, there are numerous optimization methods that have been proposed to replace the classical method. Some researchers have utilized the LQG (linear Quadratic Gaussian) optimal control theory for the design of passive mechanical systems [13-17]. L. Zuo, et al. in [9] and D.Iba, et al. in [8] utilized the H2 and $H\infty$ norm optimization to design passive mechanical suspension [13,14], MDOF tuned mass damper [8,15,16] and in vibration control of nuclear components [17] . Li and Pin [18] employed evolutionary algorithms to optimize a passive quarter-car suspension. Optimization of a quarter-car suspension was formulated as an H2 optimal control problem by Corriga et al. [19] and a simplex direct search was employed to find the optimum values of two parameters .Camino et al. [20] applied a linear-matrix –inequality (LMI) based min/max algorithm for static output feedback to the design of passive H2 optimal quarter-car suspensions. Elbeheiry et al. [21] obtained suboptimal designs of both passive and active suspensions based on full-car models. Li and Zhang [22] obtained the suboptimal parameters of LQG passive suspensions based on a half-car model. Elmadany [23] developed a procedure based on covariance analysis and direct search method to optimize the

passive suspension of a three-axle half-Vehicle model. Castillo et al. [24] used sequential linear programming to minimize the weighted acceleration of the passenger subject to a constraint on the suspension stroke. Non-Linear characteristics of dampers have been taken into account by Demic [25] using the modified Hooke and Jeeves method and by Spentzas [26] using Box's method. Other attempts that have been made to apply and modify linear and non linear programming methods and effectively optimize riding quality and safety of vehicles are the Nelder-Mead method (Demic [27]) and sequential linear approximations (Pintado and Benitez [28]).

In general, the design optimization of a mechanical system is multidisciplinary [29] and the task is to find effective trade-off solutions for complicated and conflicting design criteria [30] and so the optimization of suspension parameters can be performed by means of multiobjective programming. The adoption of MOP has been proposed to solve many vehicle system engineering problems. Basically, optimization procedures based on MOP allow the best trade-off among user-defined performance indices to be found. Given the model, the designer is often charged with the hard task of finding "one optimal solution" by changing a number of parameters. When many performance indices have to be taken into account at the same time, and many parameters may be changed, often the optimization problem cannot be handled easily; i.e. a solution cannot be found a straight forward way. The concept of optimal solution to be considered may be synthesized by stating that, if more than one criterion (*i.e.* performance index) has to be satisfied by changing one or more parameters, the possible optimal solutions constitute a set known as Pareto-optimal solutions which are optimal in the sense that they minimize all the objective functions simultaneously. This implies that the designer has to choose a preferred solution among those solutions belonging to the set. As the solutions of the set are directly

related to performance indices, the task of the designer is to reason about performance indices instead of reasoning about parameters. The methods and related computer programs that allow such a way of operation are presented and reviewed in [31-35]. Successful applications of the method in the field of ground vehicle design are reported in [31, 36 and 37].

In rail vehicle suspension design, the task is to search for a compromised design while considering lateral stability, curving performance, and ride quality. Figure 17 gives an example of the relation between ride comfort and vehicle stability for the design of passive suspension.

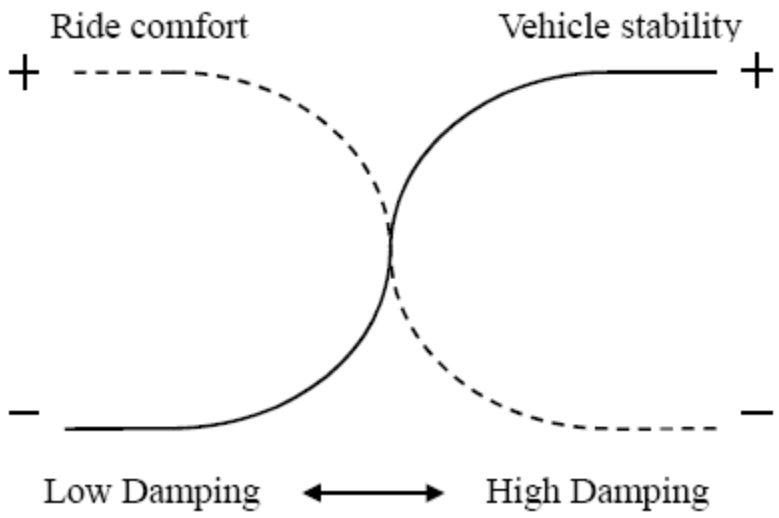

Figure 17: Relationship between ride comfort and vehicle stability.

In the past decades, only a limited number of papers have been focused on the optimal design of railway vehicle suspensions [38]. Recently researchers have paid more attention to the investigation of problems of this kind [39-41]. Mastinu [42] derived new analytical formulae defining the settings of some relevant railway vehicle suspension parameters and an optimization method based on multi objective programming with the aim of achieving the desired trade-off among conflicting performances such as standard deviation of the body acceleration versus standard deviation of the secondary suspension stroke.

YUPING HE and John McPHEE [43] used a hybrid multidisciplinary optimization method which is a combination of the individual discipline feasible (IDF) method and the All-in-one (A-i-O) method to optimize a complex rail vehicle model with respect to lateral stability, curving performance, and vertical ride quality. The hybrid MDO method combines the lateral stability model with 17 DOF, the nonlinear dynamic curving performance model with 21 DOF and the vertical ride quality model with 36 DOF. After that genetic algorithms were used to optimize the coupled systems simultaneously.

Niahn-Chung and other coworkers [44] proposed a systematic and effective optimization process for the design of vertical passive suspension of light rail vehicles (LRVs) using new constrained multiobjective evolution algorithms. A multibody dynamic model of the three-car train set was presented and the suspension spring and damping parameters were optimally designed. A new design of the passive suspension was aided by the use of evolution algorithms to attain the best compromise between ride quality and suspension deflections due to irregular gradient tracks.

Hung chi and other coworkers [45] utilized feedback control theory in designing passive suspension systems of railway vehicles with a proposed model of 6 degrees of freedom. The

advantage of applying control theory is that the number of degree-of-freedom can be increased until the model approaches to real-life situations, and the design results do not depend on the designer's experience as with classical method.

Active Suspension Systems

In the beginning railway systems were a strictly mechanical concept. Over the years, however, it has tended to become more electronically based. Railway vehicles of today are very much dependent on electronics and computer processing. The concept of active technology in rail vehicles has been analyzed theoretically and experimentally since the 1970s, but has not yet made its convincing breakthrough in operational use (except for the tilting train technology, which will be mentioned briefly later in the context), as has been experienced in, for example, aircraft and automotive industry. The likely reason for the unsuccessful of implementing and maintaining active technology in rail vehicles is that it is expensive. Compared to a passive solution, the active suspension system must prove to be at least as reliable and safe, in order to be considered as an option. However, if a concept can be found that manages good performance and acceptable costs simultaneously, there is significant potential for future implementation.

Active suspension is a generic term which defines the use of actuators, sensors, and electronic controllers to enhance and/or replace the springs and dampers that are the key constituents of a conventional, purely mechanical, "passive" suspension. The elastic and the damping characteristics of passive system are controlled closed-loop (controlling a certain signal with the signal itself) using control algorithms which considered as the brain of the active suspension [2, 46]. The control forces generated at each wheel of an active suspension can be based on the entire sensor signals employed in the system, whereas the forces generated at a

given wheel of a passive suspension can depend only on the relative displacement and velocity at that wheel.

The subject of active suspensions has been under study for railway vehicles for many decades, with major surveys having been presented in 1975[47], 1983 [48], 1997 [49] and 2007 [50]. More recent papers have reviewed the subject of mechatronics for railway vehicles (which includes active suspensions) [51] and also considered innovative possibilities from a Japanese perspective [52].

Active technology in rail vehicles can be utilized in order to achieve the following goals which are either impossible or impracticable with passive suspensions;

a) Improve and maintain passenger ride comfort although vehicle speed is increased or/and track conditions are worse,
b) Reduce wheel and rail wear by means of improved curve negotiation,
c) Maintain vehicle stability at higher speed.

Anneli Orvnas in [53] described the basic ideas behind the different active suspension concepts and stated that main goals with active technology in rail vehicles can be divided into two categories; improving running stability and wheel set guidance (mainly controlled through the primary suspension), and improving passenger ride comfort (controlled through various modifications of secondary suspension). The Tilting concept belongs to the active control of the roll mode of the secondary suspension (see Figure 18) and is used to reduce the centrifugal force, or acceleration, felt by the passengers in curves, although the vehicle speed is increased.

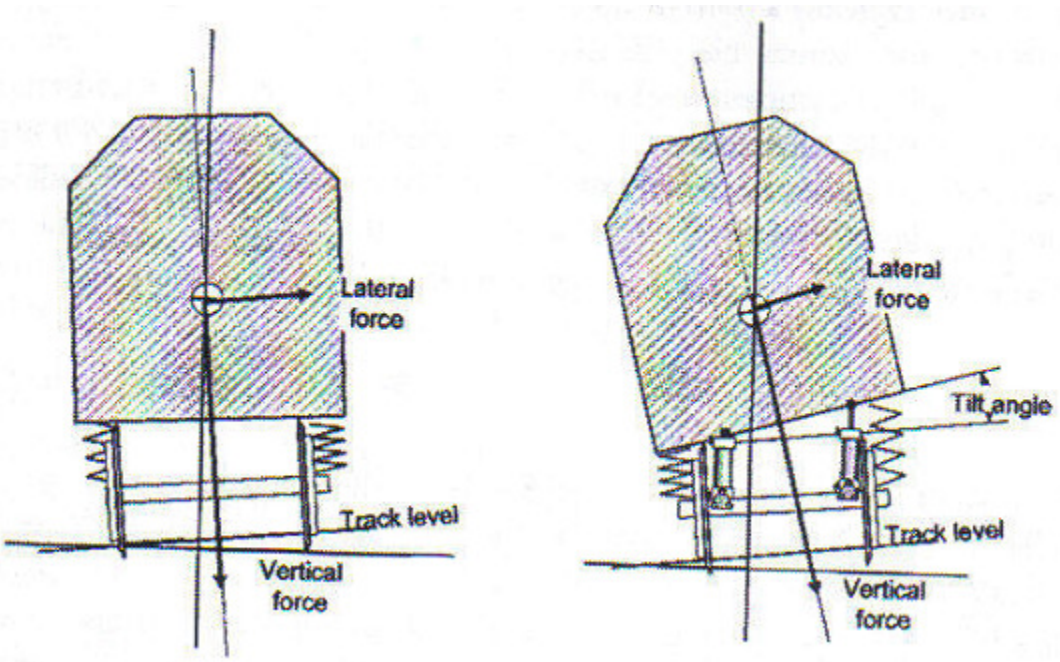

Figure 18: The lateral force is decreased due to tilting of car body. [53]

From the degree of control point of view, there are two main categories of active suspension – fully active and semi-active – basically governed by the required amount of external power, as described by Jalili [54].

Semi-active suspensions provide controlled real-time dissipation of energy and this is achieved through a mechanical device called controllable damper, although the concept is not restricted to dampers, which is used in parallel with a passive spring [5]. Semi-active control can be grouped in two general categories [4]; the first is continuously variable semi-active control which requires electro-mechanical active controllable damper valve to change its orifice area to any desired size. The second is on/off semi-active control which requires a simpler valve which can switch between a large orifice area (off-state damping) and a small orifice area (on-state

damping). Other Examples of semi-active control devices are controllable friction devices and dampers with controllable fluids (e.g., electro rheological and magneto rheological fluids) [46].

Fully active suspensions use fully controllable actuators (electro-mechanical, electro-magnetic, hydraulic, servo-pneumatic, rheological) with their own power supply, such that the desired control action can be achieved as required to implement the particular control law based on the information that it gets from sensors located at different points of the vehicle to measure the motions of the body, suspension system and/or the unsprung mass (*i.e.* mass of suspension, wheels or components not supported by suspension). For example, the control law can use acceleration signals measured by sensors in order to calculate the required force to the actuator. The accelerations, in turn, depend on the generated actuator force. Hence, the control loop is closed. The actuator may be in parallel with a passive spring and damper or it replaces conventional passive dampers in the secondary suspension (between car body and bogie) [53].

Fully active suspension can broadly be subdivided into low bandwidth or high bandwidth. In low bandwidth systems there will be passive elements which determine the fundamental dynamic response, and the function of the active element is associated with some low frequency activity such as centering. This restriction enables some reduction in force and /or velocity requirement for the actuators. By contrast, high bandwidth active systems have a much enhanced capability, and the overall dynamic response will primarily be determined by the active control strategy, which will probably act throughout the frequency range which is relevant to the particular suspension function being controlled [49]. The principle of an active suspension system is shown in Figure 19.

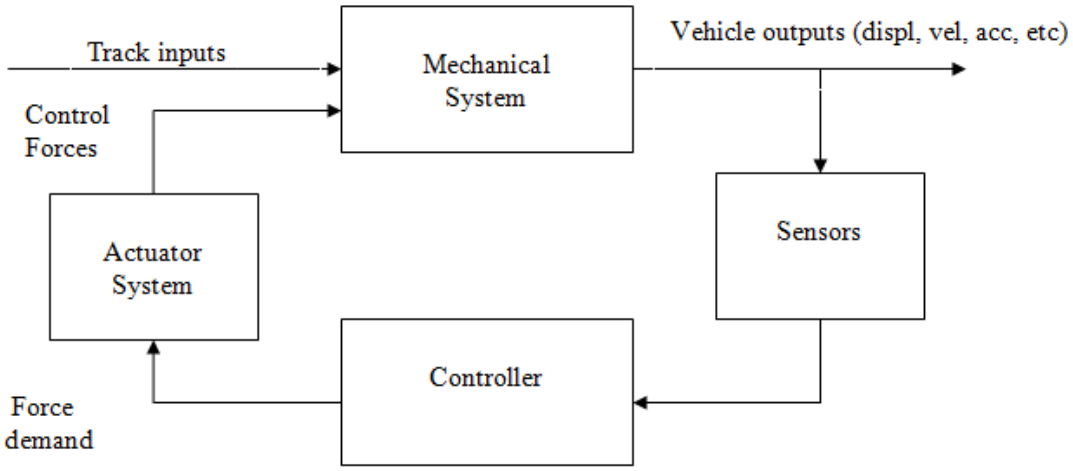

Figure 19: The concept of an active suspension system. [49]

An option which is a trade-off between the semi-active and fully active concepts known variously as semi-passive, adjustable passive or adaptive passive, in which the characteristics are varied on the basis of a variable which is not influenced by the dynamic system being controlled, for example, varying the rate of damping as a function of vehicle speed [49,55].

Semi-active damping systems are still in development to go beyond its current performance of and replace air suspensions (mainly used as passive secondary dampers in passenger railway vehicles [56]) which can operate with a softer spring rate than steel suspensions; therefore, improve the ride comfort.

Semi-active control devices offer reliability comparable to that of passive devices, yet maintaining the versatility and adaptability of fully active systems, without requiring large power sources [46].

The benefit of the semi-active compared with full-active is one of simplicity, because a separate power supply for the actuator is not needed.

The disadvantage of a semi-active damper is that the force remains dependent upon the speed of damper movement, therefore, it cannot produce large forces when the vehicle's speed is low and it cannot develop a positive force when the speed reverses since semi-active suspension can only dissipate energy, not inject it and, therefore, it does not have the potential to destabilize the controlled system [2].The concepts of semi- and fully–active suspensions are schematically shown in Figure 20.

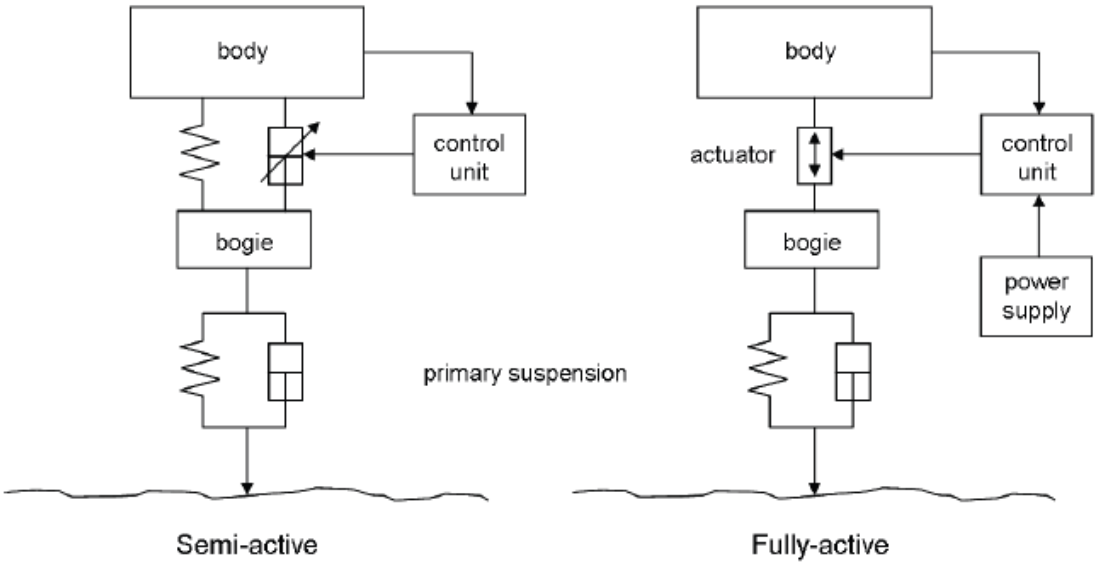

Figure 20: Concepts of semi -active and fully-active suspension control. [49]

To give a clear understanding of the importance of semi-active suspension compared with the fully active one, the author reported the following study which has been described by Norinao in [57]. JR West in Japan was in need of improved ride comfort when aiming at

commercial operation speed of 300km/h. After optimizing the passive suspension parameters a need of further comfort improvement still remained. Both fully-active and semi-active secondary suspension systems were implemented on a Shinkansen train series 500 to perform experimental investigations. The fully-active suspension was applied to the end cars, however, only operating on the rear car in the direction of travel. The actuators were placed in parallel with existing passive dampers; the latter were kept in case of actuator failure. The semi-active dampers were implemented on three first-class cars and two pantograph equipped cars, replacing the existing passive dampers. The results showed that both suspension systems offered satisfactory ride quality improvements .However, due to mass production cost of the active system it was considered that the requirements were sufficiently fulfilled with the semi-active suspension system, Therefore, the fully active suspension was replaced by semi active suspension before the train was taken into service operation.

Figure 21 shows the workspace for the three types of suspension. As shown in Figure 21(a), the workspace of a passive suspension is in the first and third quadrants, since both spring and damper forces oppose the direction of displacement and velocity. The force elements in a passive suspension are not adjustable and cannot be controlled. The shaded area indicates the workspace, while the line indicates typical force element characteristics.

In Figure 21(b), the semi-active suspension workspace is the same as the passive suspension, the force element (spring and/or damper) characteristics of a semi-active suspension can be altered rapidly (faster than the sprung mass natural frequency). The energy required to

switch between characteristics is still lower than fully-active suspension. Other than the switching signal, no energy is added to the system from an external source.

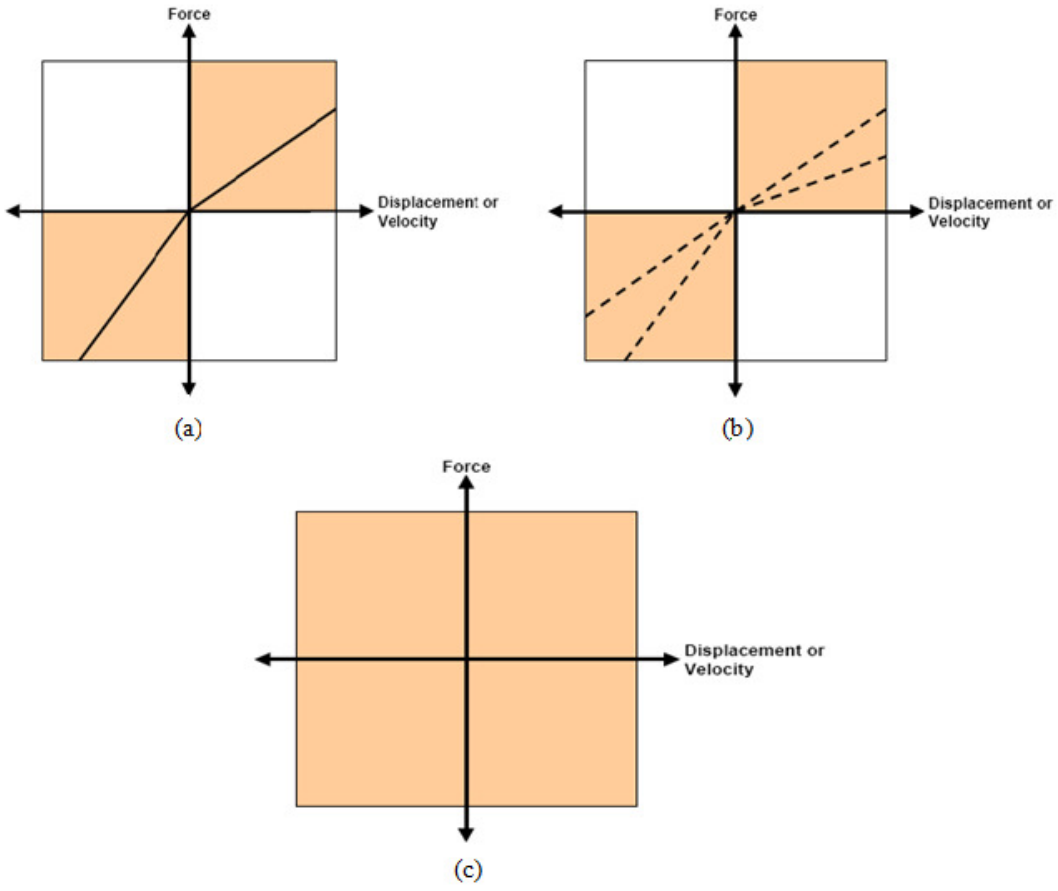

Figure 21: Force -Velocity diagrams for; (a) Passive suspension b) Semi-active suspension (c) Fully-active suspension.

(Courtesy of University of Pretoria; Electronic Theses and Dissertations)[58]

In Figure 21(c), the workspace of a fully active suspension is in all four quadrants, because a positive force can be exerted for negative velocities or displacements and vice versa and so offers high performance control and gives the best response in a wide frequency bandwidth. The bandwidth of an active suspension is similar to that of a semi-active suspension, but the energy consumption is considerably higher .An external power source is required for this type of suspension.

Actively controlled suspensions for railway vehicles widely use the active secondary suspensions and the most common control strategies (with their optimization techniques) of this type of active technology is described by Anneli Orvnas in [53] . These control algorithms are PID control, Sky-hook, $H\infty$ control and LQ/LQG control.

Hydraulic Valves

Valves are an important part of any Hydraulic line design. They are used to regulate the flow and pressure, protect the pipe and pumps from over pressurization, help to prevent transients, prevent reverse flow through pumps, remove air, and perform various other functions. If not properly selected and operated, however, they can also cause problems. Closing a control too fast, using the wrong type of check valve, or filling a line too rapidly can result in severe hydraulic transients.

J. PAUL TULLIS in [59] assorted the valves and their uses in four main categories; Control valves, pressure regulating valves, no return flow valves, and air control valves. Figure 22 lists the typical uses for the aforementioned categories.

Valve Type	Function
Control valves	
Energy dissipation flow and cavitation control	Control flow or dissipate excess energy while limiting cavitation to an acceptable level
Isolation and sectionalizing	Isolate a pump or control valve or isolate a section of a long pipe for repairs.
Free discharge	For release of water from reservoirs and bypass at turbines for transient control
Bypass	For recirculation at a pump start-up, filling a pipeline, an equalizing pressure across large valves or gates prior to opening
Pressure regulating valves	
Pressure-relief	Protects pipe from excessive pressures
Surge-anticipating	Similar to a pressure-relief valve but activated by a signal indicating that a transient has been generated
Pressure-reducing or -sustaining	For maintaining a constant upstream or downstream pressure; usually hydraulically activated by a pressure-sensing pilot system
Nonreturn valves	
Check valves	Prevent reverse flow
Air control	
Air relief–vacuum breaking	To remove or admit air to a pipe during a transient or during filling or draining

Figure 22: Typical uses for valves [59].

These categories are not exclusive because the same valve type may be used with different controls to perform any of the four functions. This same overlapping between categories applies to the valve uses shown in Figure 22.

Since control valves are the main subject of this thesis, the author will consider them exclusively in the literature.

Process plants consist of hundreds, or even thousands, of control loops all networked together to produce a product to be offered for sale. Each of these control loops is designed to keep some important process variable such as pressure, flow, level, temperature, etc. within a required operating range to ensure the quality of the end product. Each of these loops receives and internally creates disturbances that detrimentally affect the process variable, and interaction from other loops in the network provides disturbances that influence the process variable. To

reduce the affect of these load disturbances, sensors and transmitters collect information about the process variable and its relationship to some desired set point. A controller then processes this information and decides based on its built in algorithm what must be done to get the process variable back to where it should be after a load disturbance occurs. When all the measuring, comparing, and calculating are done, some type of final control element must implement the strategy selected by the controller. The most common final control element in the process control industries is the control valve.

Control valves are devices with movable, variable and controlled internal elements that manipulate a flowing fluid, such as gas, steam, water, or chemical compounds to compensate for load disturbance and to keep the regulated process variable as close as possible to the desired set point.

There are numerous valves that can be classified as control valves, the common types are gate valves, butterfly valves, globe valves, cavitation control valves, sleeve control valves, Howell-Bunger valves, Hollow-Jet valves, needle and tube valves, cone, ball and plug valves. Figure 23 contains simplified sketches of typical control valves.

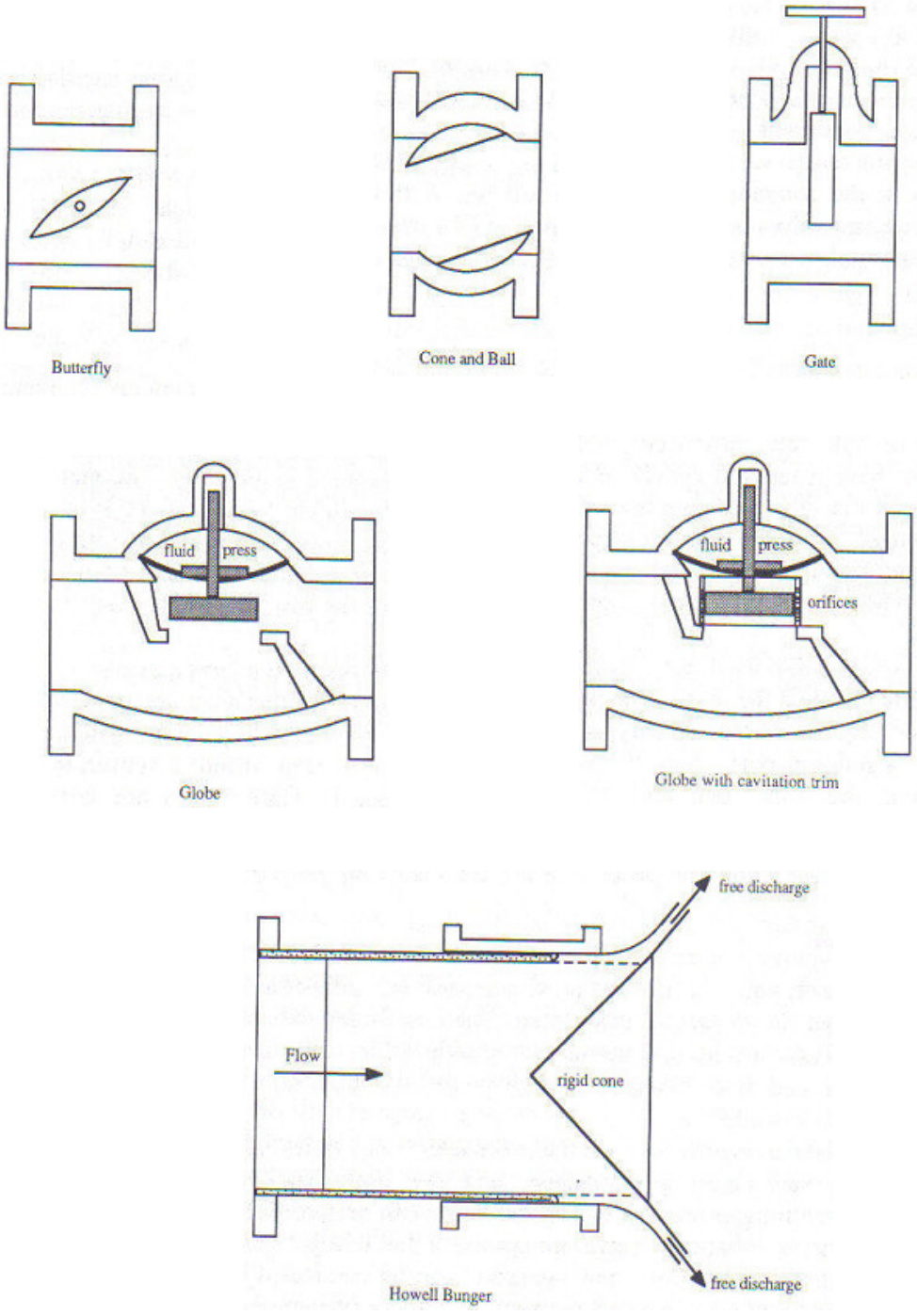

Figure 23: Typical control valves [59].

Many people who talk about control valves or valves are really referring to a control valve assembly. The control valve assembly typically consists of valve body, the internal trim parts, an actuator to provide the motive power to operate the valve, and variety of additional valve accessories, which can include positioners, transducers, supply pressure regulators, manual operators, snubbers, or limit switches. Whether it is called a valve, control valve or a control valve assembly is not as important as recognizing that the control valve is a critical part of the control loop.

For more information about control valve definitions, valve and actuator types, digital valve controllers, analog positioners and other control valve accessories refer to [60].

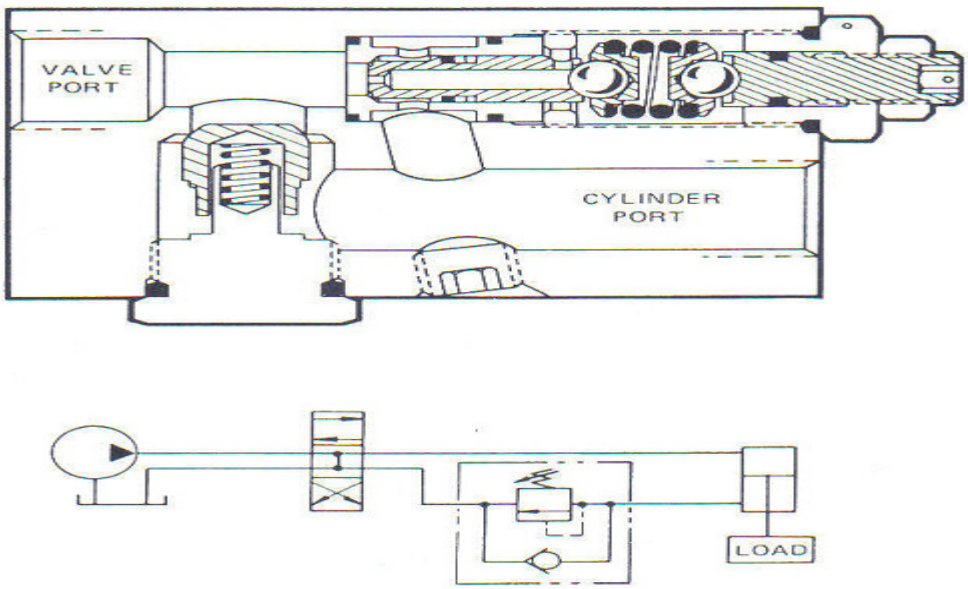

Figure 24: Counterbalance valve can lock and position heavy loads in the up position and prevent drifting. [61]

The two main purposes of control valves are pressure control and flow control valves. Pressure control valves may control either upstream or downstream pressure. For example, a counterbalance valve (see Figure 24) maintains back pressure in a system to prevent a load from drifting or falling. On the other hands, a flow control valve meters the flow. A simple example is a flow divider directs the flow from a single source into two or more branches (as the Howell Bunger valve shown in Figure 23).

Valve in high flux hydraulic transmission systems causes a lot of pressure loss. Conventionally, the pressure loss of hydraulic valves is calculated theoretically or by empirical formula. A general summary of the existing methods for determining the pressure drop across valves has been given by Kleinig in [62, 63] who carried out experiments to determine the pressure drops across high pressure homogenizer valve; uses for such valves range from the homogenizing of milk fat globules in the diary industry to breakage of cell walls in many biological processes, at very small gaps of 8 to 25μm.

In general the pressure loss across the whole valve consists of three parts, an entrance loss, an exit loss and a frictional loss:

$$\frac{2\Delta P}{\rho u_i^2} = k_i + k_f + k_e \tag{3}$$

where ΔP is the total pressure drop across the valve in Pa, ρ is the density in kg/m^3, u_i is the velocity at valve gap inlet in m/s, K_i is the entrance loss coefficient, K_f is the friction loss coefficient and K_e is the exit loss coefficient.

Phipps [64] gave the entrance loss coefficient K_i of 0.5 for sharp entrance and 0.2 for round entrance. Nakayama [65] derived an equation for K_f based on laminar flow, which is given by

$$k_f = \frac{12}{M\,\mathrm{Re}} \ln\left(\frac{r_e}{r_i}\right) \tag{4}$$

where *Re* is Reynolds number, r_e is the radius at valve gap exit in m, r_i is the radius at valve gap inlet in m, and M is evaluated using

$$M = \frac{h}{2r_i} \tag{5}$$

where *h* is the valve gap in m.

Kawaguchi [66] used a 1/7 turbulent velocity profile and derived equation for K_f as given by

$$k_f = \frac{0.076}{M(\mathrm{Re}/2)^{1/4}}\left[1-(\frac{r_i}{r_e})^{3/4}\right] \tag{6}$$

Phipps [64] developed an empirical relationship for K_f for Reynolds number in the range of 1,000-5,000. The relationship was given by

$$k_f = \frac{0.076}{M(\mathrm{Re}/2)^{3/5}}\left[1-(\frac{r_i}{r_e})^{2/5}\right] \tag{7}$$

The exit loss coefficients can be determined from the following equation

$$k_e = \mathrm{C}\left(\frac{r_i}{r_e}\right) \tag{8}$$

where the coefficient *C* was assumed to have the value of 1.0 by Phipps [64]. Nakayama [65] derived the value of 54/35. Kawaguchi [66] used a value of 64/63. Mathew and Xia Dong Chen [67] modeled the valve that used in the experimental investigation by Kleinig et al [62] using a commercial Computational Fluid Dynamics (CFD) code. The two dimensional model results in a remarkable agreement for the pressure drop values that are attained experimentally by Kleinig.

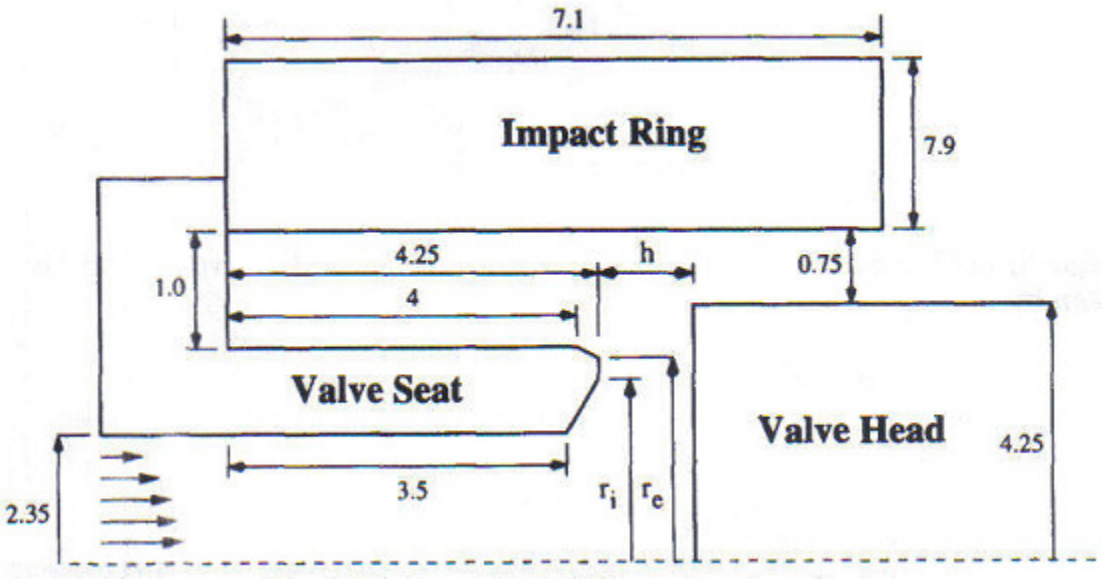

Figure 25: Valve geometry that was used for the experimental investigation by Kleinig et al. [62]. (Dimensions in cm)

Other scientists and engineers that analyzed the flow behavior inside a valve using CFD method and provided the relation between flow, geometry and pressure loses were Amirante et al [68, 69], Beeson et al [70], Chern et al [71], Vu et al [72].

Valve-related problems like the stiction, erosion, vibration, cavitation, etc. were also modeled for effective performance of the valve using CFD methods by Choudhury et al [73, 74], FLUENT user's guide [75], Forder et al [76], Kalsi et al [77] and Newton et al [78].

Other analyses specifically provided the flow patterns for different ports and opening gaps in the valves, which eventually determined the design and operation of the hardware such as Oza et al [79], Parslow et al [80] and Slockers et al [81].

The turbulence modeling around the valve opening for both steady and unsteady flow were carried out in both compressible and incompressible ranges, as a part of determination of flow and viscous forces on valves by Ahuja et al [82], Davis et al [83], Forsyth et al [84], Mazur et al [85] and Oza et al[86].

Others used different methodologies to study the flow field inside valves since it plays an essential role in energy dissipation and systemic efficiency such as Cao Bingang [87] who studied the flow field in a poppet valve numerically using the Boundary Element method, Kuzumi Ito [88] calculated the pressure distribution in a poppet valve based on streamline coordinates.

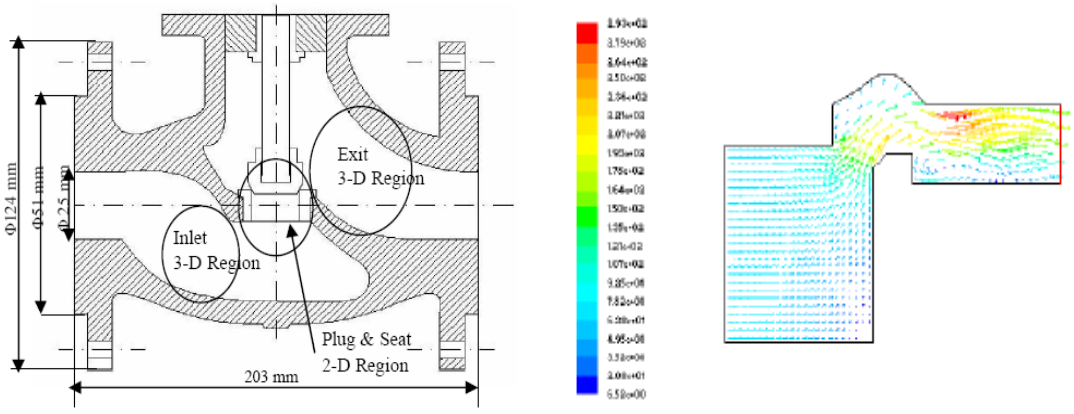

Figure 26: Schematic shows different regions of a globe valve and its modeling using CFD code "Fluent "to find the turbulent velocity profile at specific opening [86].

Spool Type Control Valves

Spool valves are widely used in fluid power transmission and control systems. They are applied as main stage directional control valves, pressure control valves, and servo-valves. The flow structure inside a spool valve has significant on the performance of the valve, thus influencing the property of the whole power systems. Therefore, the investigation of the flow structure inside the valve along with the analysis of energy loss and the steady state flow force acting on the spool by numerical calculations and/or experimental methods has become more and more important in recent years.

Many scholars and researchers have been attracted to the aforementioned research aspects of spool valves and some great achievements have been reached. BORGHI, et al [89], dealt with the application of a simplified numerical analysis of the flow field inside the compensation port based on computational fluid dynamics (CFD). Their objective of study was to evaluate the proposed analysis procedure and to verify the effects related to the presence of steady state flow forces affecting the spool equilibrium. YUAN, et al [90,91], used fundamental momentum and CFD analysis to consider the effect of fluid viscosity on the steady flow force for both positive and negative damping lengths, their research focused on alleviating the need for large solenoids in single stage spool by advantageously using fluid flow forces. BAO, et al [92], used CFD method to investigate the flow behavior inside a spool valve, in addition, the relation between flux, port geometry and pressure loss was analyzed. WANG, et al [93], RUAN, et al [94], both used particle image velocimetry (PIV) method to acquire data in spool chambers. VAUGHAN, et al [95], used the finite difference method to investigate the spool valve field and flow force compensation.

Amirante, et al. [69], investigated the analysis of the flow forces acting on the spool of an open center ON-OFF hydraulic directional control valve experimentally and used CFD to explain the experimental results. Borgahi [96] reported the estimation of the hydraulic locking force in hydraulic conical spools when it is subjected to an unbalanced pressure distribution using a sensitivity analysis of the geometric and functional parameters (dimensions and pressure). GAO Dianrong, et al. [97] used the finite element method (FEM) and particle image velocimetry (PIV) technique to get the flow field along the inlet passage, the chamber, the metering port and the outlet passage of spool valve at three different valve openings.

In the literature, the author has not found papers dealing with the problem of designing a pressure operated spool type valves that maintain a linear relation between pressure drop, flow rate, and position, in order to passively control the damping force over a wide range during different stroke cycles of a hydraulic damper for freight railway vehicles.

Only two papers were found to be close from the general idea aspect adopted in this thesis, which is using a variable valve for controlling the damping force over a wide range in both the extension and the compression stroke of a damper. J. Emura, et al [98], used a step motor of 9 to 140 steps to regulate the orifice in a piston valve for a continuous variable damper for cars. During the extension stroke, the damping force is changed over a wide range, while the damping force becomes limited during the compression stroke. Se Kyung Oh, et al. [99] developed a continuous variable damper for semi-active suspension systems of passenger cars in which the damping force is controlled by regulating disc pressure in pilot valves by the change of spool opening according to the solenoid input current.

CHAPTER III

EXPERIMENTAL SETUP AND PROCEDURE

In this study, a total of five hydrodynamic experiments were initially conducted at the University of Texas-Pan American on the three two-sided spools that were provided by Amsted Rail in order to generate pressure drop versus flow rate plots for all the spool land profiles. This initial phase of testing was called “The Static testing of the control valves”. In the performed experiments, the applied pressure and flow rate were varied to test all the provided spool land profiles at the same range of 500 to 3100 psi for pressure and 0 to 18 GPM for flow rate. The test rig consists of a hydraulic power unit which is capable of giving a pressure supply of up to 3400 psi with maximum flow rate of 18 GPM, sensing instruments for pressure and flow rate and the orifice block assembly (a block which contains a square orifice opening for the static testing phase of the provided spool type control valves). The output data from the calibrated pressure transducers and flow meter were recorded using a lab view program.

A test iteration was conducted on each spool land of the three two-sided spools, with initial land length of 0.1875 in. Pressure drop and flow rate data were recorded for each 0.007813 in. of spool land travel in order to accurately analyze the response.

The movement of the spool inside the valve body in the static phase was controlled using two wheels located on the threaded ends of the tested spool. A calibrated potentiometer was used to make sure that the data were recorded at the desired positions for each spool.

The five aforementioned tests are summarized in Table 1 along with the applied pressure values, the tested land length of each spool profile and the total duration of each test.

It is important to mention that there was no temperature sensing device utilized to measure the flow temperature for the previously mentioned tests. The thermostat of the heat exchanger (see Appendix B) mounted on the hydraulic power unit was used to control the temperature of the hydraulic oil that enters the test valve. The thermostat setting was at its low end temperature which is 40°C during all the previous tests. Since the room where the tester was mounted has a temperature of 17-20°C, it was assumed that the operating temperature of the hydraulic oil during all the previous tests was in the range of 17- 40°C. In addition, it was assumed that the energy associated with a rise in the temperature of the hydraulic oil, as it passes through the test valve, will be dissipated by the heat exchanger, keeping the temperature as it was set originally on the thermostat.

Each test in Table 1 consists of six sub-experiments and each sub-experiment has different applied pressure settings; thus, six different spool land performance lines for pressure drop vs. flow rate were obtained from each test. There was a break of 30 minutes between each sub-experiment of each test. During that time, the applied pressure was taken off to let the hydraulic oil cool for a while and to save the text file, generated by the labview program that

contains the pressure, flow rate and spool position data recorded during each sub- experiment of each test.

Table 1: A brief description of the five laboratory tests conducted to study the performance of different spool land profiles for the proposed orifice valve.

Test #	**Spool Name**	**Experimental Description**
1	Spool #1 (0.3750 in. land length)	Total of six sub-experiments. Applied pressure values were {500, 1000, 1500, 2000, 2500, 3100} psi. Tested length of the spool land was 0.1875 in. (5.30-hour test)
2	Spool #2/slope side (0.1875 in. land length)	Total of six sub-experiments. Applied pressure values were {500, 1000, 1500, 2000, 2500, 3100} psi. Tested length of the spool land was 0.1875 in. (5.30-hour test)
3	Spool #2/ Curved side (0.1875 in. land length)	Total of six sub-experiments. Applied pressure values were {500, 1000, 1500, 2000, 2500, 3100} psi. Tested length of the spool land was 0.1875 in. (5.30-hour test)
4	Spool #3/ J-side (0.1875 in. land length)	Total of six sub-experiments. Applied pressure values were {500, 1000, 1500, 2000, 2500, 3100} psi. Tested length of the spool land was 0.1875 in. (5.30-hour test)
5	Spool #3/ Slope side (0.1875 in. land length)	Total of six sub-experiments. Applied pressure values were {500, 1000, 1500, 2000, 2500, 3100} psi. Tested length of the spool land was 0.1875 in. (5.30-hour test)

The following three sections of this chapter give a detailed and thorough description of the experimental setup, calibration of the used sensing instruments (pressure transducers, flow meter and potentiometer) and the experimental procedure.

Experimental Setup

A picture of the setup used to perform the static testing phase is shown in Figure 27. A Foster hydraulic power unit uses variable displacement (maximum displacement of 18 GPM), pressure compensated by a piston pump -driven by a 40 H.P., 1725 RPM Baldor Electric Motor- to give maximum compensating working pressure of up to 3400 psi. The power unit is equipped with a fan cooled heat exchanger that has a thermostat control to fix the temperature of the working fluid being returned to the 40 Gallon hydraulic reservoir attached to the power unit. One main relief valve and another two cross over reliefs on each working port, 1 and 2, are installed with settings of 3400 psi and 3500 psi respectively to protect the circuit from possible pressure spikes. The relief valve pressure settings are always set at a higher value than the pump's compensating setting to prevent the working fluid from being dumped over the relief valves causing excessive heat build-up. Another feature of the power unit that it is equipped with is a directional control valve (closed center "E" Spool type). This valve will be used in the second phase of testing in which the actual whole control valve block will be under testing for both retraction and compression action of the proposed suspension due to the track irregularities . In this case, the hydraulic power unit will be plumbed to the double acting cylinder which is a main part of the proposed vertical suspension damper.

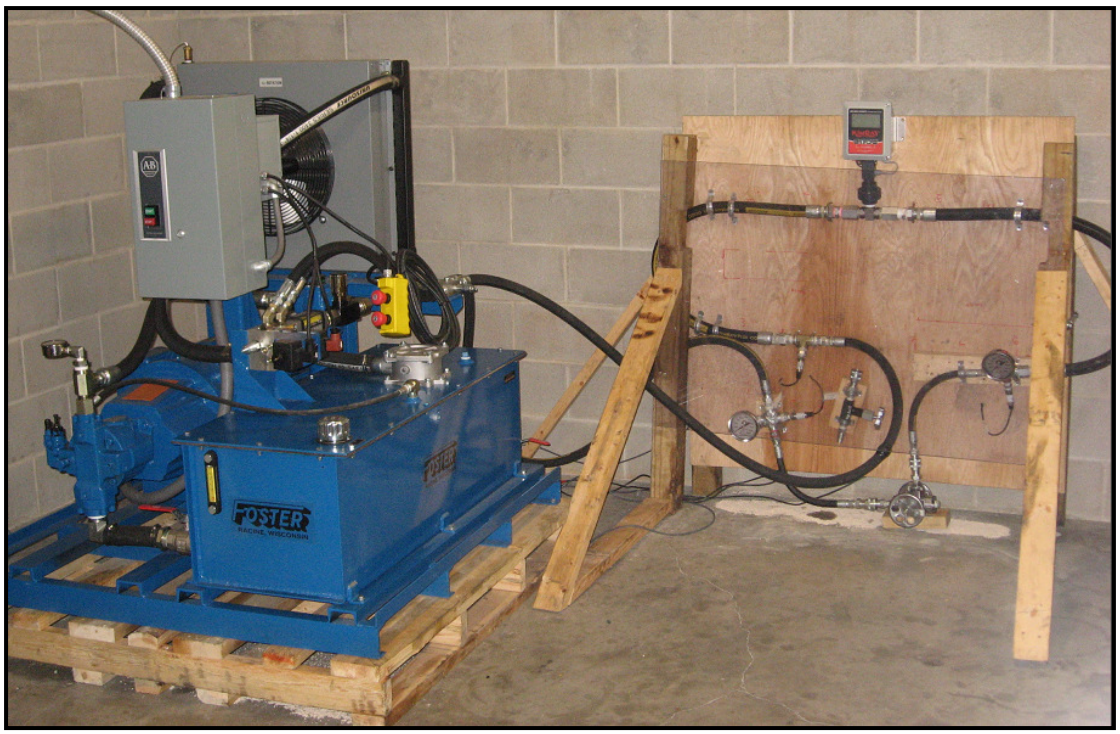

Figure 27: A picture of initial experimental setup used to conduct the static testing phase of the proposed spool valves.

The working ports of the hydraulic power unit were plumbed using Aeroquip hoses of 4000 psi maximum operating pressure to one KIMRAY digital flow monitor/meter assembly, two 5000 psi Omega pressure transducers, two 5000 psi Omega pressure gauge dials and one orifice block assembly. Table 2 gives a summary of all the test rig components with their description.

All pressure and flow rate sensing instruments and part of the hoses were mounted on an (4×4 ×1/12) ft wooden plate which was built using six (2×4) in. and four (4×4) in. wood supports. A polycarbonate cover was mounted on the front side of the wooden plate to protect

the operator from harm due any possible leakage in the system while conducting experiments. Polycarbonate type material was chosen because it is transparent and shock resistant.

Table 2: Static test bench component's name, description and quantity.

Item	Description	Quantity
Hydraulic power unit	Foster Manufacturing Electric Hydraulic Power Unit, Model 400-1P-18-E (see Appendix B)	1
Pressure Transducer	5,000 psi, Omega, Model # PX309-5KGI (4-20 mA Pressure Sensor)	2
Pressure Gauge Dial	0-5,000 psi, Omega, Model # PGS-35B-5000	2
Digital Flow Monitor & Flow meter	B2800 KIMRAY Flow Monitor with 8 digit numeric liquid crystal display comes with stainless steel 1100 KIMRAY Turbine flow meter model that have a maximum pressure rating of 5,000 psi	1
Potentiometer with zigzag grip	10 turns, 50 KΩ, Mouser Spectrol Precision potentiometer, P/N:594-53411-503	1
DC Power supply	MASTECH HY3005D-3 Triple Output Variable DC Power Supply with Voltage range of 0 - 30 V and current range of 0-5 A with Digital Backlit LCD Display Meters	1
USB Data Acquisition device	8 Inputs, 12-bit, 10 kS/s, Multifunction I/O National Instrument USB-6008 (takes Analog voltage signal of +/- 10 V max)	1
Conversion Board	A rectangular board on which there are many connections/resistors being soldering to it to supply the flow monitor & Pressure transducers with electric power from the Dc power supply and in the same time to convert their output current signals into voltage signals for the NI USB-6008 DAQ use	1
Orifice block Assembly	A block that has 0.375 in. square opening for testing different spool land profiles under distinct pressure and flow rate conditions	1

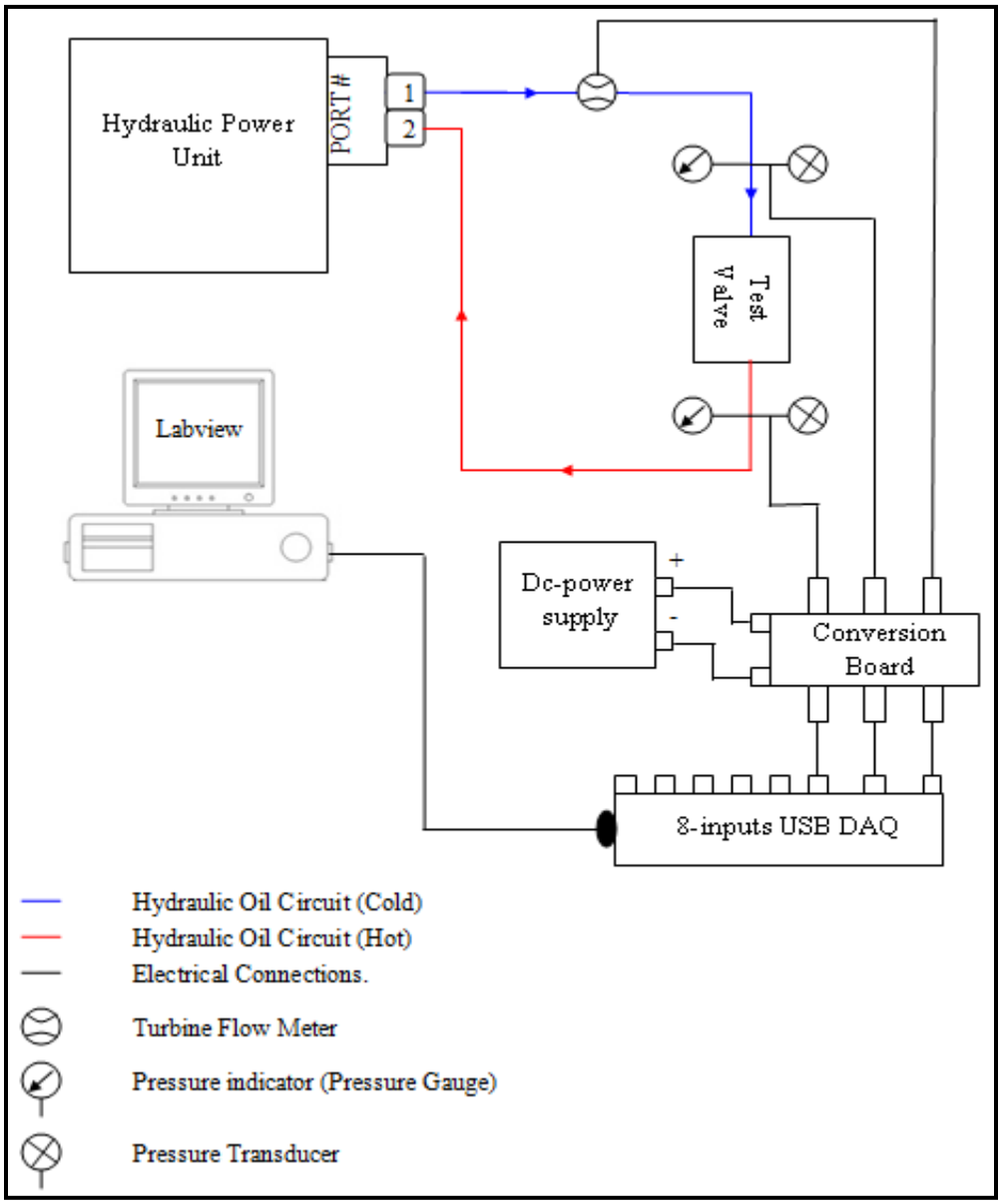

Figure 28: Schematic diagram of the initial experimental setup.

Aeroquip hose's inside diameter were selected based on the sizes of the inlet and outlet of the working ports of the hydraulic power unit, flow meter and the orifice block assembly which are 3/4 in. , 1 in. and 1/2 in. respectively. In addition, hose lengths were chosen based on space limitation and the corresponding tabulated minimum bend radius values. Table 3 lists all the used Aeroquip hoses and summarizes their properties.

Table 3: A Summary table of Aeroquip's hoses.

Hose P/N	Hose I.D. [inch]	Hose O.D. [inch]	Max. Operating Pressure [psi]	Min. Bend Radius [inch]	Used Length [ft]	Weight Of Hose [Ib/ft]
GH493-8	0.50	0.92	4000	7.00	2	0.59
GH493-12	0.75	1.20	4000	9.50	14	0.92
GH493-16	1.00	1.48	4000	12.00	8	1.22

Construction
Synthetic rubber tube, 4-spiral wire reinforcement, black synthetic rubber cover

Operating Temperature Range
-40^{o}C to +121^{o}C [-40^{o}F to +250^{o}F]

Pressure Drop Values (for 10 ft of the Hose without fittings)
Based on Fluid with specific gravity of 0.85, Kinematic viscosity of 20 C.S. at (38^{o}C)

Hose P/N	Pressure drop at minimum tabulated flow rate [psi]	Pressure drop at maximum tabulated flow rate [psi]
GH493-8	2.20 psi (at 3 GPM)	40.00 psi (at 18 GPM)
GH493-12	0.72 psi (at 5 GPM)	6.30 psi (at 18 GPM)
GH493-16	0.55 psi (at 10 GPM)	1.50 psi (at 18 GPM)

LUBRIGUARD AW46 hydraulic oil (approximately 15 weight oil with anti-wear and anti- foam additives) was used to fill the 40-Gallon hydraulic reservoir of the hydraulic power unit shown in Figure 27 . A GRAINGER hand pump was used to supply the reservoir with the oil from a barrel.

Due to oil availability and time constraints, AW46 oil was chosen since it has close specifications to the ones recommended by both Foster Manufacturing (hydraulic power unit manufacturer) and Amsted Rail, regarding the viscosity and the specific gravity values. Table 4 lists the typical properties of the AW46 grade hydraulic oil as provided from Warren Oil Company.

Table 4: A specification table of AW46 grade hydraulic oil

(Courtesy of Warren Oil, Inc.)

Specification	**Description**
Density (at 16°C **)**	872.34 kg/m^3
Kinematic viscosity (at 40°C**)**	46.5 cSt
Kinematic viscosity (at 100°C**)**	6.8 cSt
Specific gravity (H2O=1.0**)**	0.89
Viscosity Index	100
Flash point	220^{o}C
SAE Viscosity Grade	20W

The test valve shown in Figure 28 consists of three main parts; a steel manifold block, a spool valve and two hand wheels.

The manifold is a (3.88×2.12×2.87) in. steel block (see Figure 29) has a 0.5 in. hole that acts as a valve seat. Perpendicular to the valve seat is a 0.375 in. square orifice that will be the test window upon which characterization evaluation for different spool lands will be made.

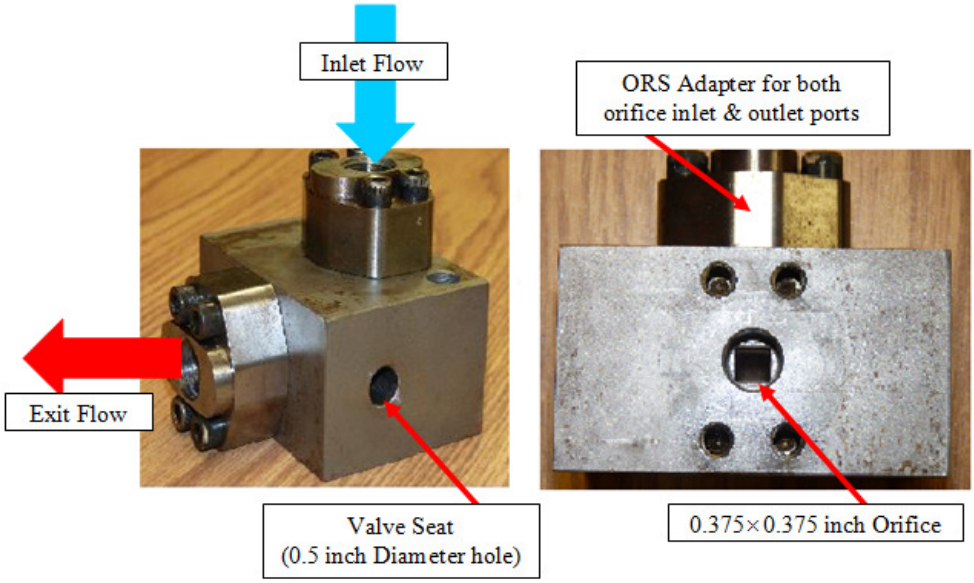

Figure 29: A picture of the steel manifold block that was used to test different spool valves for this study.

The spool valve will act as a metering valve. It will open or close the orifice window inside the manifold block upon its position. The movement of the spool inside the manifold block is controlled by two hand wheels; the trailing wheel will be released to make adjustment and the lead wheel will be tightened to move the spool land to the next position.

All the tested spools in this study are made of C1018 cold roll steel; in addition, all the spools have the same features except the spool land shape (detailed dimensions for all the tested spools in this study can be found in Appendix C). The initial three spools that were tested are spool #1 (has a straight cut land), spool #2 (has two land profiles) and spool #3 (has two land profiles), as shown in Figure 30. All three spools, that were initially tested, were provided by Amsted Rail.

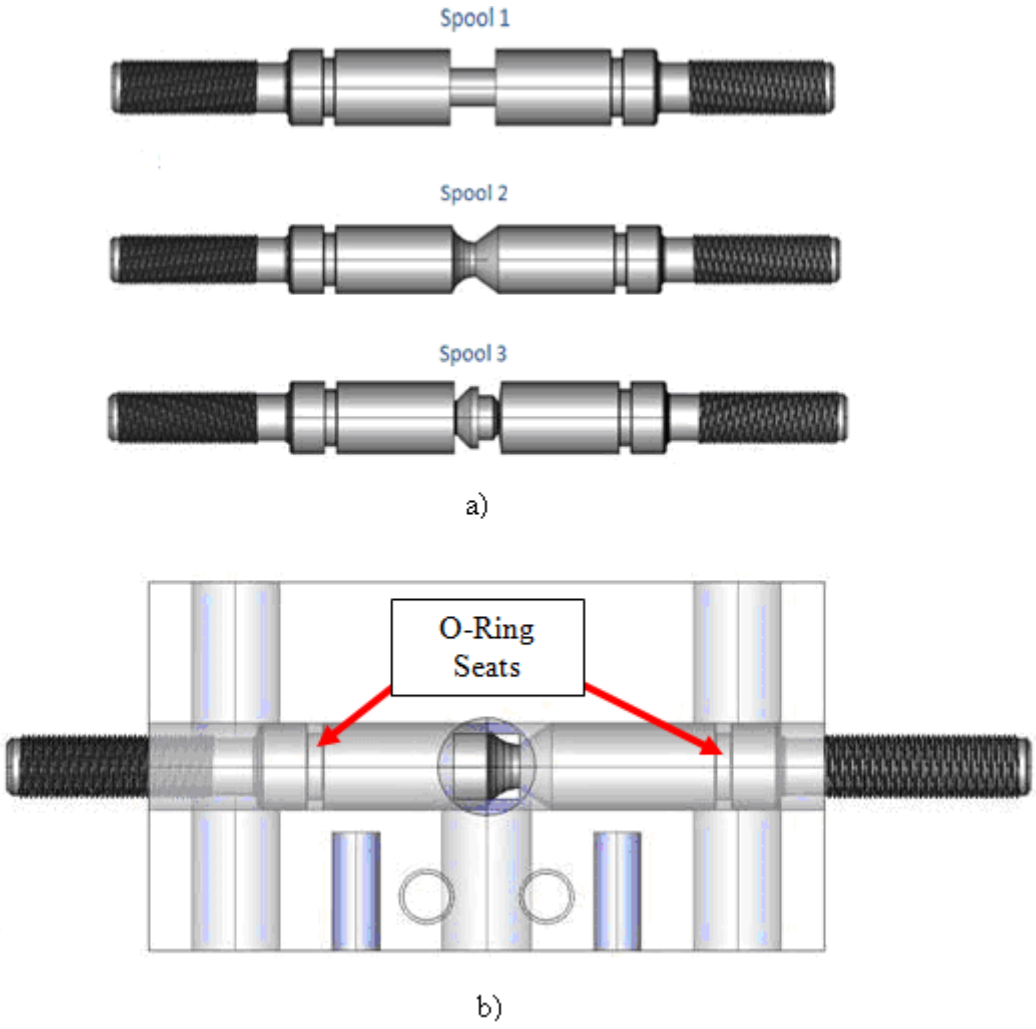

Figure 30: CAD model of the orifice valve used for this study. a) The initially tested spools b) spool valve #2- manifold block assembly (front view).

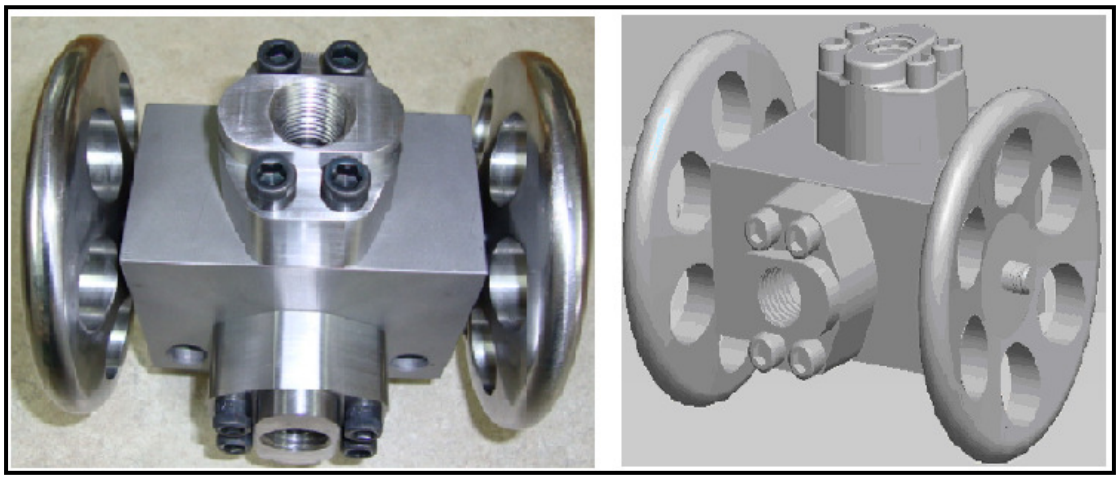

a)

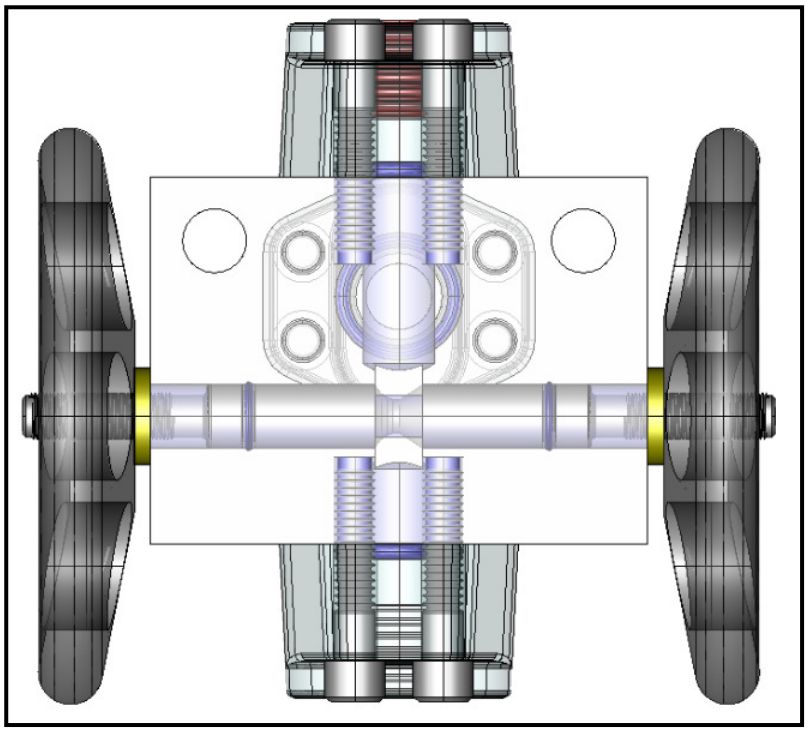

b)

Figure 31: The variable orifice valve used for this study. a) The physical & CAD model of the orifice valve assembly b) the orifice valve assembly (bottom view).

Calibration of the Sensing Instruments

In this section, the calibration methodology will be explained in details for the pressure measuring and indication devices (*i.e.* pressure transducers & pressure gauges), flow rate measuring device (*i.e.* turbine flow meter) and displacement recording device (*i.e.* the potentiometer).

Calibration of the Pressure Transducers & Gauges

A pressure transducer is a transducer that converts pressure into an analog electrical signal. Although there are various types of pressure transducers, one of the most common is the strain-gage base transducer. The conversion of pressure into an electrical signal is achieved by the physical deformation of strain gages which are bonded into the diaphragm of the pressure transducer and wired into a Wheatstone bridge configuration. Pressure applied to the pressure transducer produces a deflection of the diaphragm which introduces strain to the gages. The strain will produce an electrical resistance change proportional to the pressure. Pressure transducers are generally available with three types of electrical output; millivolt, volt and 4-20 mA (known also as pressure transmitters).

Two Omega 4-20 mA pressure transducers (PX 309-5KGI Model, see Figure 32) were used to measure the pressure before and after the test valve. This type of pressure transducers were selected since a 4-20 mA signal is least affected by electrical noise and resistance in the signal wires compared to other types of pressure transducers. Table 5 lists the general specifications of both pressure transducers that were used during the static testing phase of the orifice valve.

Figure 32: A picture of the PX 309-5KGI pressure transducer model.

Table 5: A general specification table of the PX 309-5KGI pressure transducer

Specification	Description
Pressure Range	(0 - 5000) psi /gage pressure
Output Signal	4-20 mA
Supply Voltage	9 - 30 VDC
Operating Temperature Range	-20°C to 120°C
Response Time	< 1 ms
Thermal Effects	± 1% of the Full scale
Accuracy	± 0.25% (includes linearity, hysteresis and repeatability)

Both of the pressure transducers were calibrated originally from the manufacturer. A calibration check was done at University of Texas-Pan American engineering laboratory using Omega dead-weight tester apparatus, see Figure 33.

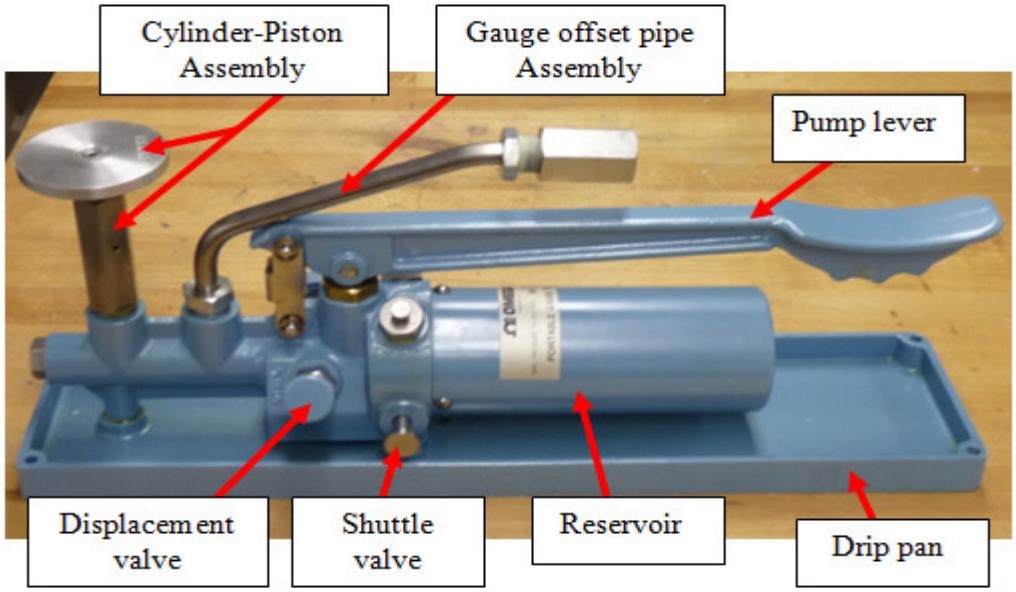

Figure 33: A picture of Omega dead -weight tester apparatus (DWT 1305D) used for calibration check of the pressure transducers.

The deadweight tester consists of a two stage hydraulic pump containing a manifold which is pressurized during operation. Integral to the pump is a shuttle valve that allows the operator to regulate the speed of pressure increase. One connection to the manifold includes a cylinder and a free-floating precision machined piston with a plate for holding calibrated weights. A second connection to the manifold accommodates a gauge or other pressure measuring device to be calibrated or checked. Incorporated into the manifold is a hand operated displacement valve that allows small adjustments in fluid volume to be made without further operation of the pump handle or release valve. The tester is dual range having two interchangeable piston and cylinder assemblies. One is a low pressure piston having an effective

area five times larger than that of the high pressure piston. The low pressure piston is used for making measurements below 2,000 psi (14,000 kPa). The high pressure piston, with an area 1/5 that of the low pressure piston, is used to measure pressure through 10,000 psi (70,000 kPa). The weight masses are pre-measured and identified with the pressure values they produce when operated with the interchangeable piston and cylinder assemblies. Pressure calibration points produced by the deadweight tester are accurate to within ± 0.1% of the reading certified traceable to the National Institute of Standards and Technology (NIST). The tester provides consistent, repeatable accuracy, maintaining its pressure for an appreciable length of time regardless of temperature changes, slight leaks in the pressure system, or changes in volume of the pressurized system due to movement of a Bourdon tube or other device. The set up that was used to check the calibration for the two pressure transducers being utilized in the initial phase of testing of the spools (static testing phase) is shown Figure 34. See Figure 35 for more details regarding the calibration setup.

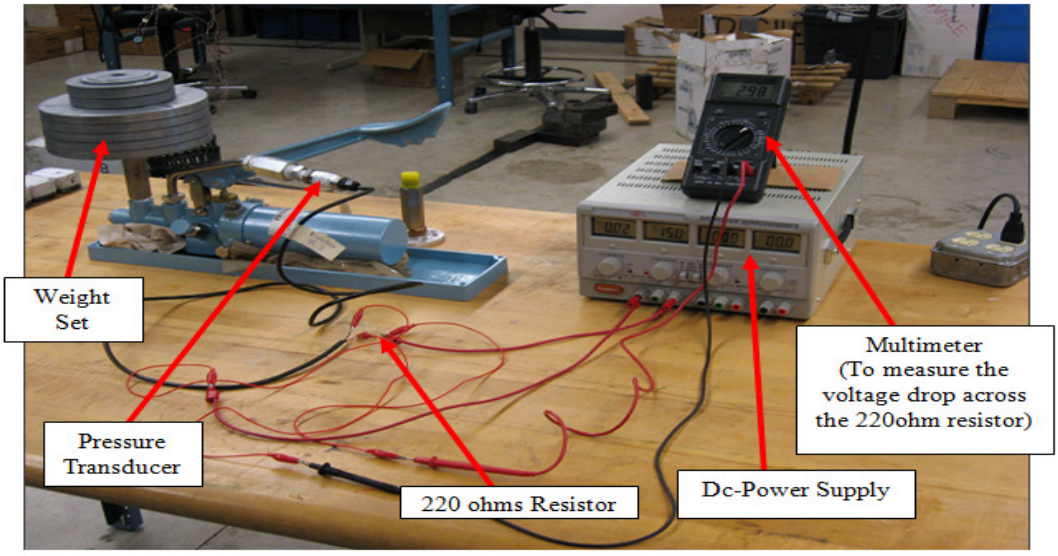

Figure 34: The calibration check setup for pressure transducers.

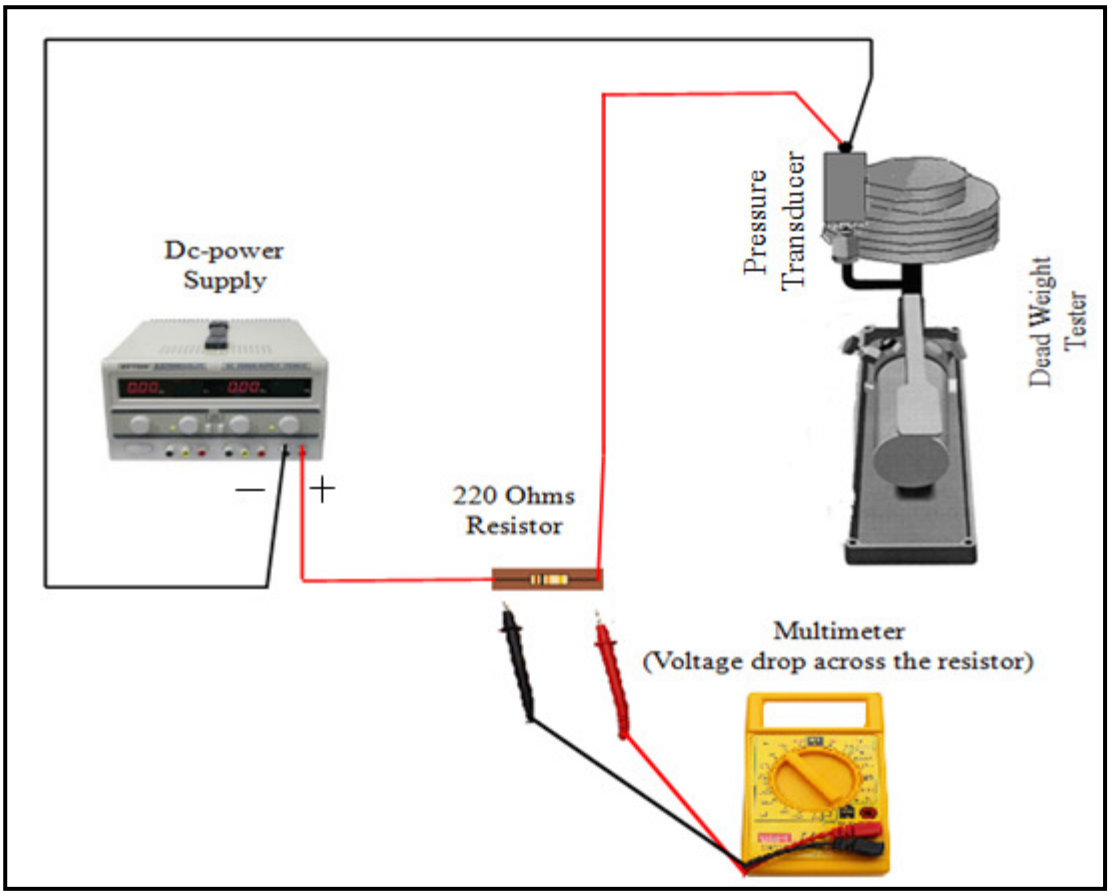

Figure 35: A schematic of the calibration check setup for the pressure transducers.

Before making the calibration test, a bleed procedure provided by Omega was followed to assure that there was no entrapped air inside the pump assembly which could cause the pump to achieve only partial pressure. In addition, a bubble type level had been placed on top of the piston plate before it was revolved slowly to assure the levelness of the dead weight tester, thus it would function properly.

During normal operation, selected weights were added to the plate and piston assembly to equal the desired pressure value. Further, the weights were spun by hand while taking readings; to assure that the piston was floated by the pump's fluid only and not combined with other possible floating forces such as cylinder wall friction.

The calibration check was conducted three times for each pressure transducer; further, the results were identical between all the trials and for both pressure transducers. Table 6 lists the actual applied pressures in increments of 250 psi to a maximum of 3000 psi (controlled by the added weights to the appropriate piston and cylinder assembly), the calculated values based on the tested pressure transducer and the average percentage error between the previously mentioned values.

Table 6: A comparison between the actual applied pressure and the measured one.

Actual pressure [psi]	**Voltage across the 220 Ω resistor [V]**	**Calculated pressure [psi]**	**% Error**
250	1.06	247.6818	0.927273
500	1.24	503.3636	0.672727
750	1.41	744.8409	0.687879
1000	1.59	1000.523	0.052273
1250	1.77	1256.205	0.496364
1500	1.94	1497.682	0.154545
1750	2.08	1696.545	3.054545
2000	2.29	1994.841	0.257955
2250	2.47	2250.523	0.023232
2500	2.65	2506.205	0.248182
2750	2.82	2747.682	0.084298
3000	3.00	3003.364	0.112121

According to the data sheet of the pressure transducer supplied by Omega, zero gage pressure corresponds to 4 mA output current and 5000 psi gage pressure corresponds to 20 mA output current; thus, the calculated gage pressure for a known output current from the pressure transducer is given by

$$I = \frac{V}{220} \times 1000 \tag{9}$$

$$P_C = \frac{[5000 - 0]}{[20 - 4]} \times (I - 4) \tag{10}$$

where I is the output current from the pressure transducer in milliampere, V is the voltage drop across the 220 Ω resistor in volts and P_C is the calculated gage pressure from the pressure transducer in psi. Eq. (10) was formulated based on the linear relation between the input (applied pressure) and the output (electrical current) of the pressure transducer.

The average of the total average percentage error between the actual applied pressure values and the calculated ones was found to be 0.564%. Figure 36 shows the actual applied pressure against the calculated one.

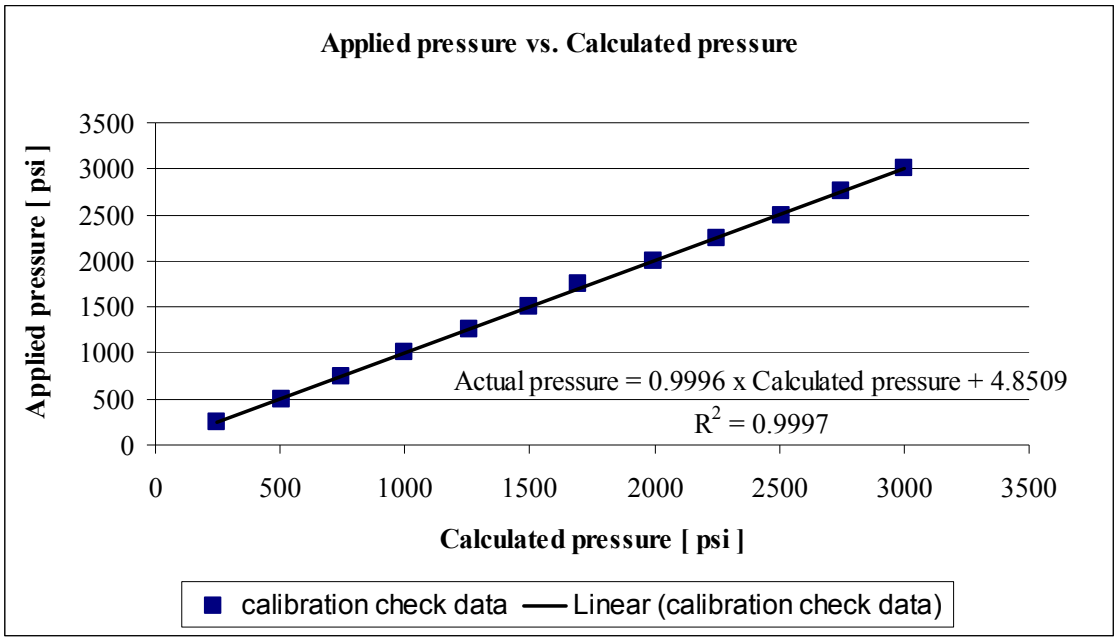

Figure 36: A plot of the actual applied pressure values vs. the calculated ones.

The same procedure was followed to check the calibration of the two pressure gauges that were mounted in parallel with the two pressure transducers. The calibration check setup for the pressure gauges is shown below in Figure 37.

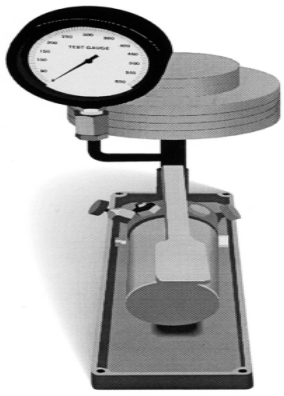

Figure 37: A schematic shows the calibration check setup for the pressure gauges.

It was found that both of the pressure gauges were reading below the actual pressure by 50 psi consistently. The objective of the pressure gauges was to assure that the recorded pressure data by both pressure transducers were correct during valve testing.

Calibration of Kimray Model Turbine Flow Meter

The model 1100 turbine flow meter is designed to withstand the rigorous demands of the most remote flow measurement applications. It can maintains measurement accuracy and mechanical integrity in the corrosive and abrasive fluids commonly found in oil field projects pipelines, in-site mining operations, offshore facilities and plant locations. As recommended by the manufacturer, the flow meter should be installed with a minimum of 10 diameters upstream pipe length and 5 diameters downstream pipe length for optimum performance, thus the Kimray turbine flow meter in the actual setup (see Figure 38) was installed with 1ft upstream and 1 ft downstream hose length since the hoses that are connected to it from both sides are 1 in. in diameter.

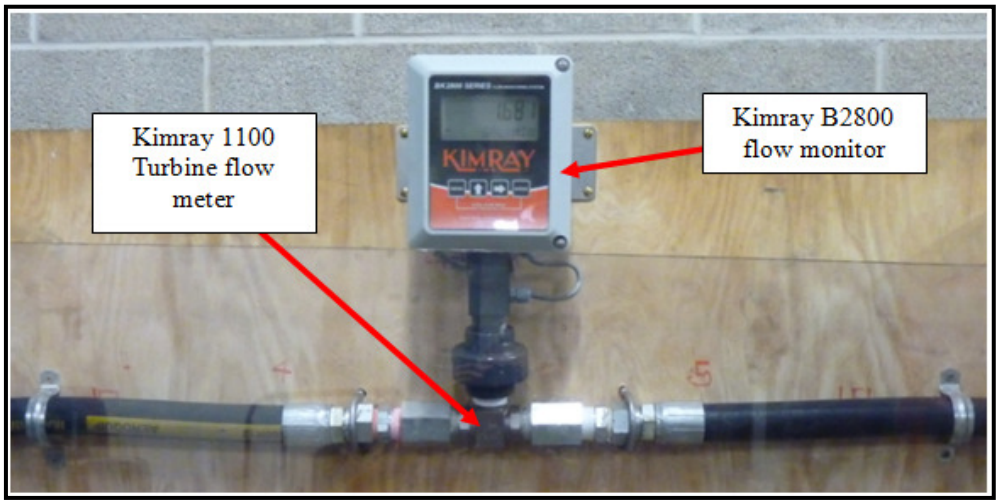

Figure 38: A picture of the Kimray turbine flow meter/monitor with the associated hose connections.

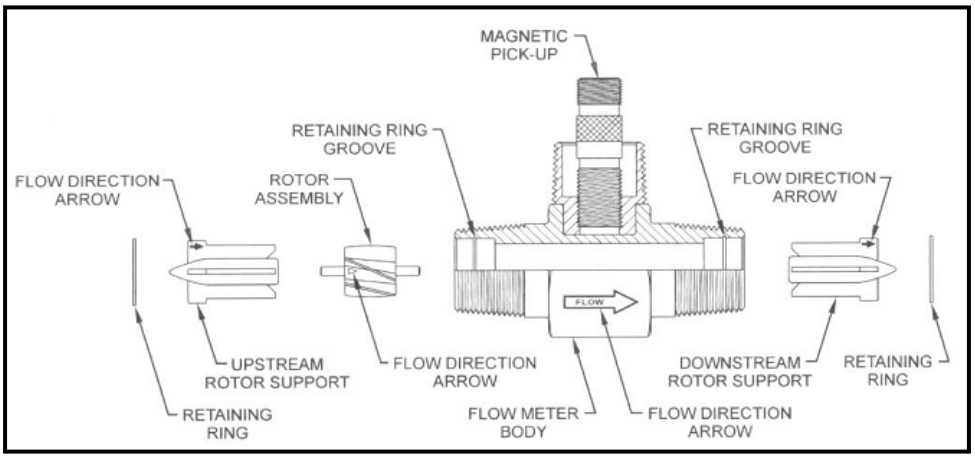

Figure 39: Kimray 1100 turbine flow meter component directory.

The turbine flow meter operates by the fluid entering the meter and passing through the inlet flow straightener which reduces its turbulent flow pattern and improves the fluid's velocity profile. Fluid then passes through the turbine blades causing it to rotate at a speed proportional to the fluid velocity. As each blade passes through magnetic field, created at the base of the pickup transducer, AC voltage, pulse, is generated in the pickup coil (see Figure 40). These impulses produce an output frequency proportional to the volumetric flow through meter.

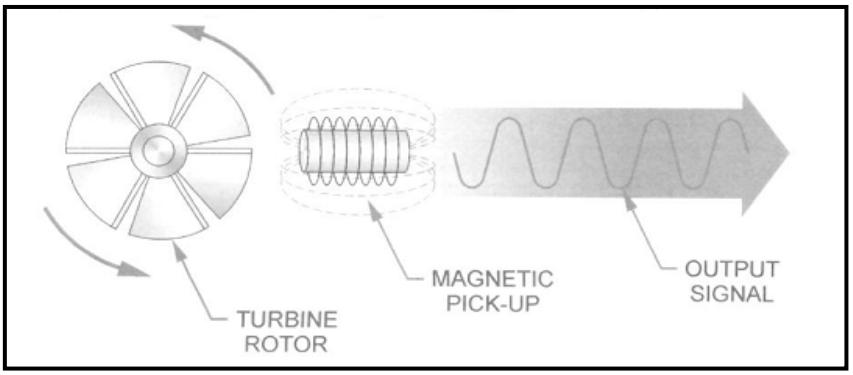

Figure 40: A schematic illustration of electric signal generated by rotor movement of Kimray turbine flow meter.

Prior to installation, the flow meter was checked internally for foreign material and to ensure the turbine rotor spins freely. As recommended by the manufacturer, the hosing size for the turbine meter was made the same as the meter threaded port size which is 1 in. in diameter to make sure that the accuracy of the turbine flow meter will not be affected. Table 7 lists the specifications of the Kimray model 1100 turbine flow meter.

Table 7: A general specification table for Kimray model 1100 turbine flow meter.

Specification	Description
Material of Construction	Kimray Model 1100 turbine meter is constructed of stainless steel and tungsten carbide
Flow Meter Size	7/8 in.
Pressure Rating	5,000.00 psi
Operating Temperature	-101°C to +177°C
Max Flow rate	30.00 GPM
Accuracy	+/- 1.00% of reading
Repeatability	+/- 0.10%
Calibration	Calibrated by the Manufacturer using Water (NIST Traceable Calibration)

Kimray B2800 flow monitor (see Figure 38) takes the AC voltage output that the flow meter produces while operation for calculating flow rate and total. These calculations are based on the set K-factor inside the processor of the flow monitor. The K-factor (with regards to flow) is the number of pulses that must be accumulated to equal a particular volume of fluid. The

frequency aspect of K-factors is the same K-factor number, with a time frame added, can be converted into a flow rate. An example might be a K-factor of 1000 (pulses per gallon). If you accumulated 1000 counts (one gallon) in one minute then your flow rate would be 1 GPM. The output frequency, in Hz, is found simply by dividing the number of counts (1000) by the number of seconds (60) to get the output frequency which here equal to 16.6666 Hz.

If you were looking at the pulse output on a frequency counter an output frequency of 16.666 Hz would be equal to 1 GPM. If the frequency counter registered 33.333 Hz (2 x 16.666Hz) then the flow rate would be 2 GPM.

The K-factor value stored in Kimray B2800 flow monitor was set originally at 2513.3 pulses per gallon by the manufacturer based on water calibration. Since AW46 type hydraulic oil was used, a recalibration of the flow meter was needed.

For the recalibration procedure of the turbine flow meter, HEDLAND variable orifice flow meter, built inside the hydraulic power unit, was used as the master meter; see Figure 41 & Table 8 for its specifications.

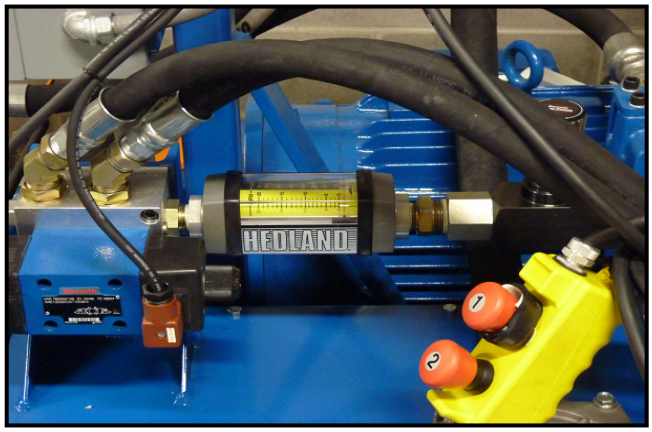

Figure 41: HEDLAND variable orifice flow meter.

The setup shown in Figure 28 was used to recalibrate the Kimray turbine flow meter. A PARKER gate valve (see Figure 42) was used instead of the actual test valve since the actual valve had not been received at the time from Amsted Rail.

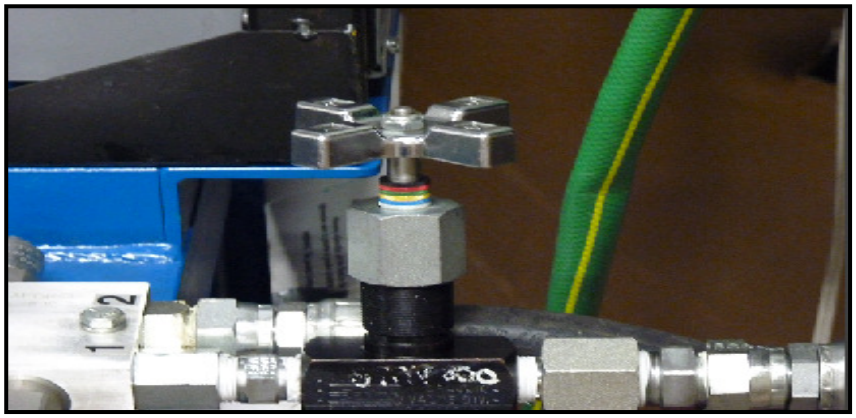

Figure 42: A picture of PARKER gate valve.

Table 8: A general specification table of HEDLAND variable orifice flow meter.

Specification	Description
Pressure Rating	3,500.00 psi
Operating Temperature Range	-29 to 116°C
Maximum Flow rate	18 GPM
Accuracy	+/- 2.00 % full scale
Repeatability	+/- 1.00%
Viscosity Stability	Good viscosity stability
Calibration	Calibrated for 0.876 S.G

During the recalibration process, the gate valve was fully opened and the flow rate was controlled using the HEDLAND flow meter. The thermostat setting of the hydraulic power unit's heat exchanger was kept at the low end which is 40°C. The applied pressure setting of the pump was kept at 1500 psi to assure that maximum flow rate,18 GPM, is reached, thus, the entire flow rate range supplied by the hydraulic power unit is covered by the recalibration process. Flow rate data were recorded from the Kimray turbine flow meter for each 2 GPM increment on the HEDLAND flow meter scale (see Table 9).

Table 9: A comparison between flow rate data recorded from both HEDLAND and KIMRAY flow meters.

HEDLAND Flow Meter Readings	**KIMRAY Turbine Flow meter Readings (B2800)**		
Flow rate [GPM]	**Flow rate [GPM] Trial #1**	**Flow rate [GPM] Trial # 2**	**Flow rate [GPM] Trial#3**
2	2.148	2.146	2.144
4	4.296	4.292	4.288
6	6.444	6.438	6.432
8	8.592	8.584	8.576
10	10.74	10.73	10.72
12	12.888	12.876	12.864
14	15.036	15.022	15.008
16	17.184	17.168	17.152
18	19.332	19.314	19.296

Based on Table 9, the relative percentage error for Trial #1, Trial#2 and Trial#3 was 7.4%, 7.3% and 7.2% respectively. In addition, the average percentage error for the three trials - which was found to be 7.3% - was applied to the initial K-factor (the one set by the manufacturer based on water calibration) to get a new established factor. According to KIMRAY, if the B2800 gives flow rate readings higher than the master flow meter ones, the K-factor will need to be increased by the relative percentage error between both flow meter readings and vice versa. Thus, the initial K-factor (2513.3 pulse/gal) was increased by 7.3% to give the current K-factor value (2696.933 pulse/gal). Based on the new K-factor, flow rate data were recorded again from Kimray turbine flow meter for each 2 GPM increment on the HEDLAND flow meter scale, see the table below.

Table 10: A comparison between Flow rate data recorded from both HEDLAND and KIMRAY flow meters based on the new K-factor.

HEDLAND Flow Meter Readings	**KIMRAY Turbine Flow meter Readings (B2800)**		
Flow rate [GPM]	**Flow rate [GPM] Trial #1**	**Flow rate [GPM] Trial # 2**	**Flow rate [GPM] Trial#3**
2	1.9952	1.9968	1.9976
4	3.9904	3.9936	3.9952
6	5.9856	5.9904	5.9928
8	7.9808	7.9872	7.9904
10	9.976	9.984	9.988
12	11.9712	11.9808	11.9856
14	13.9664	13.9776	13.9832
16	15.9616	15.9744	15.9808
18	17.9568	17.9712	17.9784

Based on Table 10, the relative percentage error for Trial #1, Trial#2 and Trial#3 was 0.12%, 0.16% and 0.24% respectively. The average percentage error for the three trials was found to be 0.17%; as a result, the average percentage error was decreased by 98% using the new K-factor (2696.933 pulse/gal).

The KIMRAY B2800 Model Flow monitor has a 4-20 mA programmable analog output by which the flow rate readings from the flow meter can be interfaced with a labview program. The wiring diagram of B2800 is shown in Figure 43.

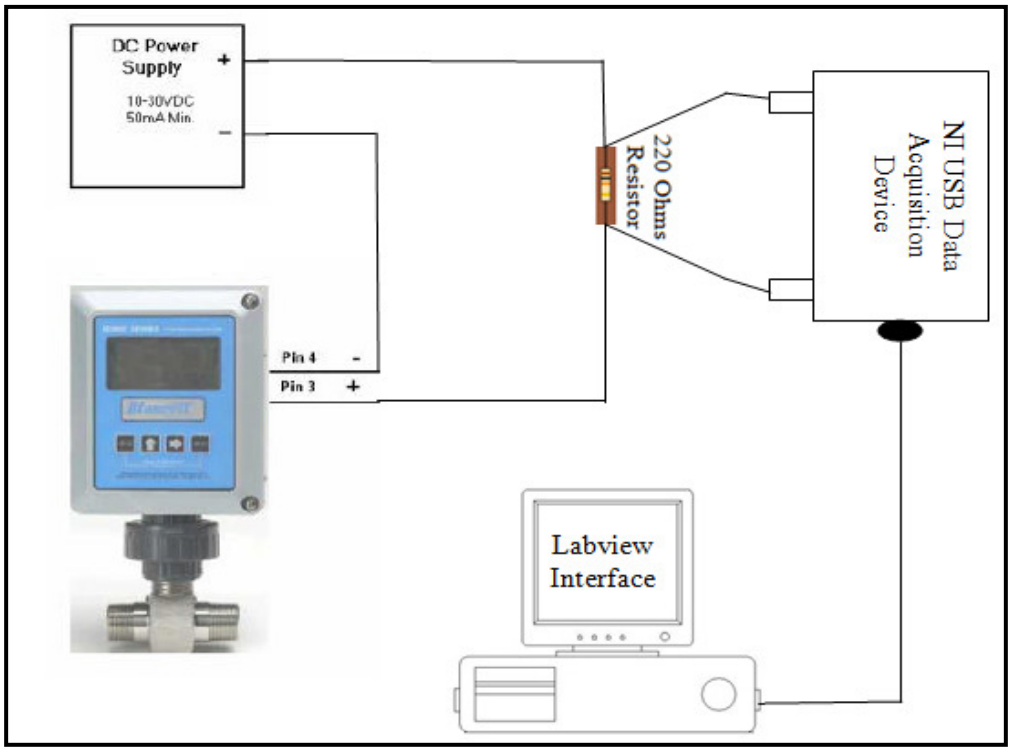

Figure 43: Wiring diagram of B2800 to NI USB data acquisition device.

Using the programming menu of B2800, the 4 mA output current was chosen for zero flow rate reading and the 20 mA output current for the 20 GPM. The equation used to convert from the B2800 output current to flow rate in the labview interface is given by

$$Q = \frac{[20-0]}{[20-4]} \times (I-4) \tag{11}$$

where Q is the flow rate in GPM and I is the output current in milliampere given in Eq. (9).

Calibration of the Potentiometer for Displacement Measurements

During the test, the spool being tested will move inside a 0.5 in. hole which is built inside the steel manifold block provided by Amsted Rail. In the same block, there is another square groove (0.375×0.375) in. that intersects perpendicularly with the previous mentioned hole. The intersection area will be the test window upon which characterization evaluation for different spool lands will be made.

The movement of the spool inside the manifold block is controlled by two hand wheels; the trailing wheel will be released to make adjustment and the lead wheel will be tightened to move the spool land to the next position.

The displacement that the spool moves when rotating both the trailing and the lead wheel one revolution was found to be 0.03125 inch. This value was recorded using a Teclock dial caliper (see Figure 44) that was connected in series with one of the tested spool's leg. The displacement measuring was done on the measurement table located in the technician's machine shop at the engineering building of the University of Texas Pan-American. This measured

displacement was identical with the standardized pitch of 3/8 in. - 32 UNEF thread type; the same thread type for all the tested spool's legs and for both hand wheels.

.

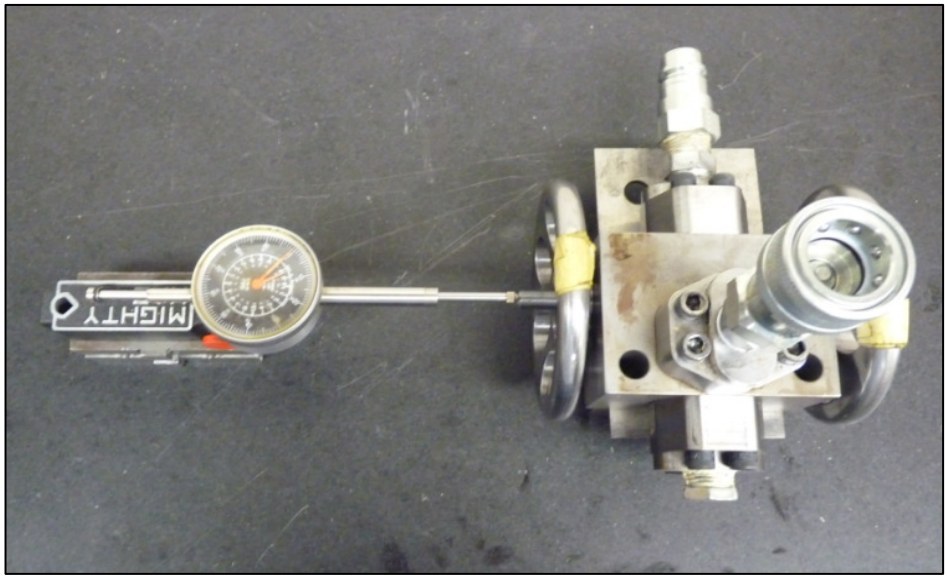

Figure 44: A picture of the Teclock dial caliper that mounted in series with one of the tested spool's leg in order to measure the spool displacement per one revolution of both hand wheels.

In order to save time and effort while recording spool displacement and for more accurate displacement data, a 10 turns Mouser potentiometer was used to keep count of the number of turns for the trailing wheel, thus, the spool displacement was being tracked during the test.

As shown in Figure 45, a rubber coupling was used to connect the rotor of potentiometer with the tested spool leg, while the stator of the potentiometer was connected to the zigzag handle (it was made with zigzag shape to account for the spool axial movement while testing) from one end. The other end of the zigzag handle was connected to the trailing wheel. A small

size hex key was embedded in the middle of the rubber coupling in order to indicate any rolling movement of the spool during testing due to any possible jam between the spool leg threads and the hand wheel.

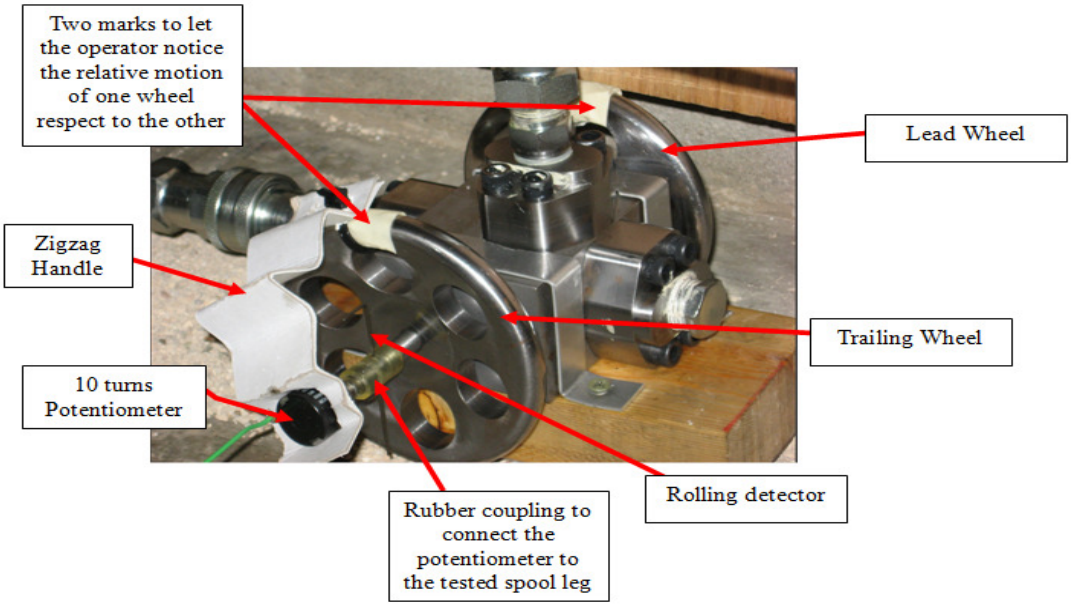

Figure 45: A picture of the potentiometer setup that was used to keep tracking of the tested spool displacement.

The wiring diagram, shown in Figure 46, explains how the connections were made between the Mouser potentiometer and the NI-USB data acquisition system. Both of the 23 and 43 KΩ resistors were chosen to give analog output voltage within the range of the NI-USB data acquisition system (*i.e.* within $\pm$ 10 V). In addition, better resolution for the voltage output was obtained resulting in better sensitivity for the number of turns the trailing wheel rotated.

Using Kirchhoff's voltage law for the wiring diagram shown in Figure 46, a relationship was established between the voltage drop across the 23 KΩ resistor and the total number of turns the trailing wheel rotated as given below

$$T = \frac{\left(\left[\left(\frac{V_{in}}{V_{out}}\right) \times R1\right] - R1 - R2\right)}{R_p} \tag{12}$$

where T is the total number of turns the trailing wheel rotated, V_{in} the input voltage from the DC power supply in volts, V_{out} the voltage output from the 23 KΩ in volts, $R1$ is the 23 KΩ resistor, $R2$ is the 43 KΩ resistor and R_P is the potentiometer resistance in KΩ per turn.

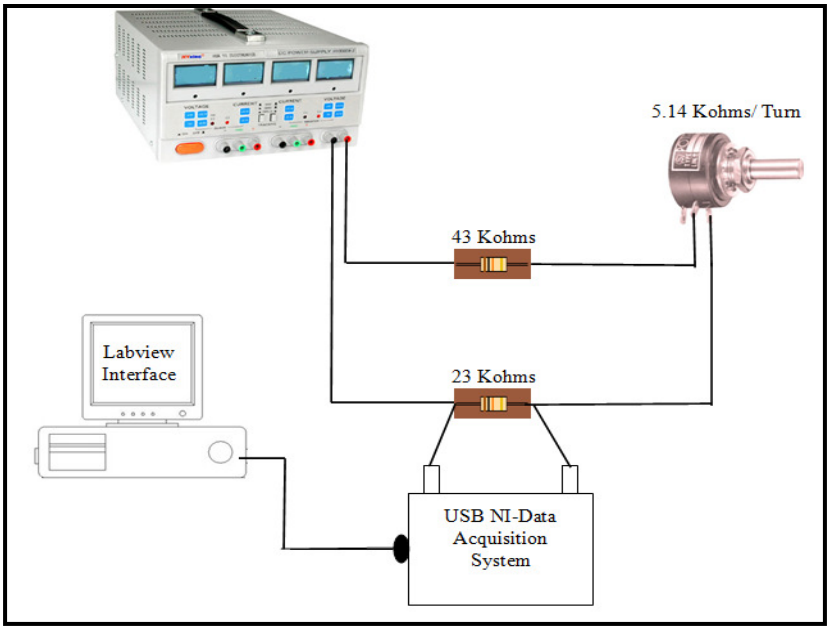

Figure 46: Wiring diagram of the Mouser potentiometer to the NI USB data acquisition device.

In order to keep the number of turns in Eq. (12) a function of the voltage drop across the 23 KΩ resistor only (V_{out}), the input voltage from the DC power supply was kept at 14 V during the calibration of the potentiometer and through all the testing done in this study. As a result, Eq. (12) can be reformulated as below

$$T = \frac{C1}{V_{out}} + C2 \tag{13}$$

where $C1$ and $C2$ are constants that were obtained from the calibration data.

The calibration of the potentiometer was done by counting the number of turns that the trailing wheel rotated (T values) and recording the corresponding voltage drop across the 23 KΩ resistor (V_{out} values), see Table 11.

Table 11: A summary of the calibration data for Mouser potentiometer at 14 V supply voltage.

T **[Number of Turns]**	$\mathbf{V_{out}}$ **[V]**	$\mathbf{1/V_{out}}$ **[V^{-1}]**
0	4.34	0.230415
1	4.04	0.247525
2	3.78	0.264550
3	3.54	0.282486
4	3.34	0.299401
5	3.16	0.316456
6	3.00	0.333333
7	2.85	0.350877
8	2.72	0.367647
9	2.59	0.386100
10	2.48	0.403226

The calibration data in Table 11 were fitted using a linear type fit, thus, the value of both *C1* and C2 was found from the equation of the linear fit function as shown below.

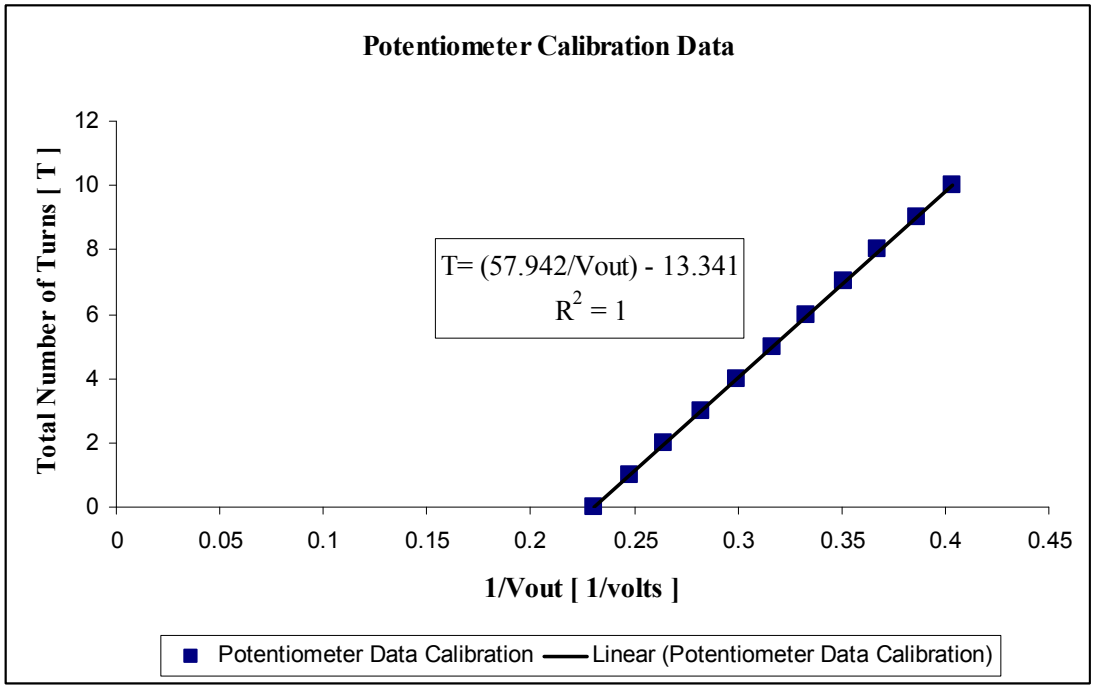

Figure 47: A plot of the trailing wheel total turns vs. voltage drop across the 23 KΩ resistor.

Experimental Procedure

For consistency, the same experimental procedure was implemented for all the tests conducted for this study. After greasing both o-ring seals to avoid tearing the ORS due to spool movement inside the block, the spool to be tested was inserted inside the manifold block and moved to the starting position with a fully closed orifice window (see Figure 48). Furthermore, the orifice valve assembly was connected to the tester shown in Figure 28 using quick connections and the potentiometer was attached to the spool's leg from the trailing wheel side.

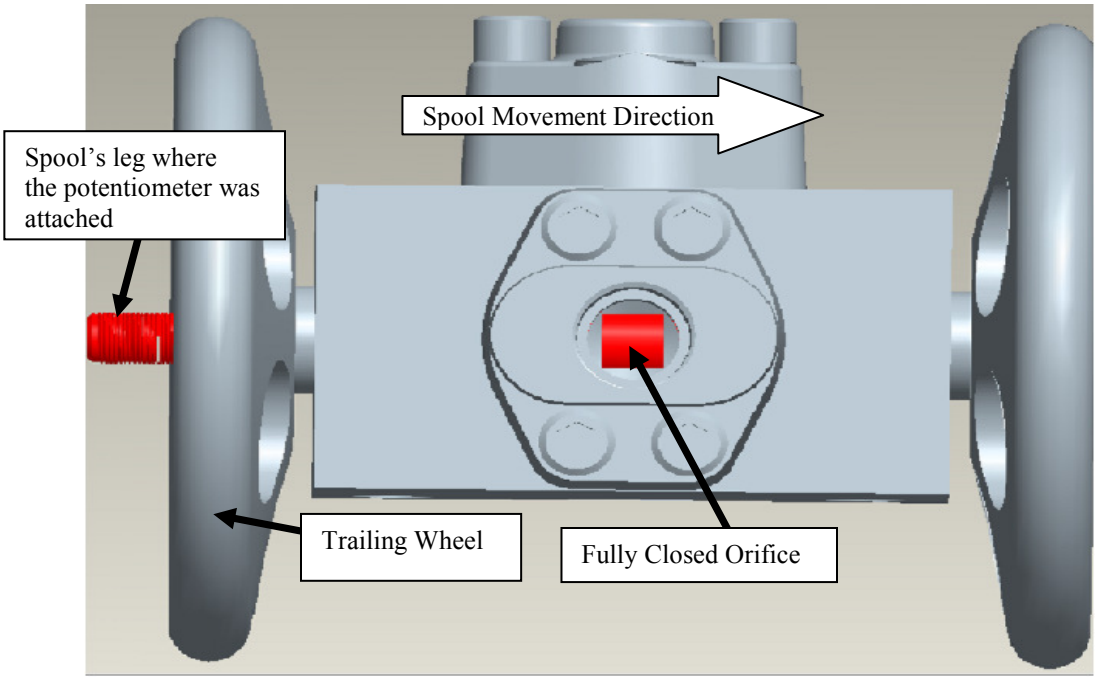

Figure 48: CAD model of the orifice valve assembly (rear view) shows the location of the spool inside the manifold block at the beginning of each sub-experiment of each test.

The power supply was turned on, and its output voltage was adjusted to 14 V. Before starting the hydraulic power unit, its breaker was set manually to ON position, and the HEDLAND flow meter was fully opened so that the flow rate was totally controlled by the test valve. The labview software (programmed to record selected analog voltage signals from the NI USB DAQ and convert it to gage pressure, flow rate and displacement data using Eqs. 9 to 13) was initiated to monitor the real-time data displayed on the computer screen and ensure that all the pressure transducers, turbine flow meter, and the potentiometer were reading well. The NI USB DAQ was set to acquire a maximum of 500 finite analog voltage data for each channel

(total of 4 channels were used), at a sampling rate of 2000 Hz (*i.e.*, 2000 Samples/sec per channel). The developed program produced a text file that contains 9 columns of data with the first column contain the time stamp in ms. The second through the fifth column contain the selected analog voltage signal acquired by the NI USB DAQ in V and the sixth through the ninth one contain the flow rate in GPM, orifice valve upstream pressure in psi, orifice valve downstream pressure in psi and spool displacement in turns respectively.

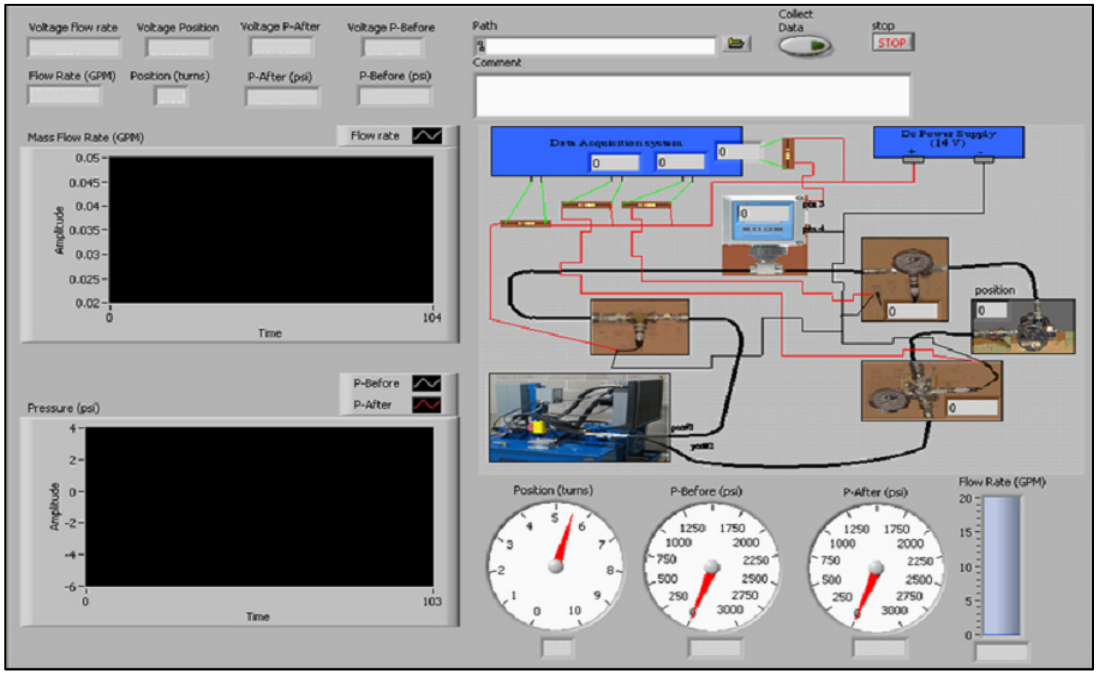

Figure 49: Labview interface that was programmed to show the real-time data from all the calibrated sensing instruments and store the data recorded at all the spool stops on a text file.

The data file name along with its path and comments regarding the spool type and the test conditions were set in the programmed labview interface at the beginning of each sub-experiment of each trial.

Both of the activating switches on the hand held pendant (see Appendix B) were pulled out so that no flow was introduced outside the hydraulic power unit from either port #1 or 2. The applied pressure settings of the pump were adjusted using a setting screw for pressure control to 200 psi, the lowest pressure settings of the pump. Switch #2 was depressed to introduce the flow outside the hydraulic power unit through port #1 to the external hydraulic circuit and returning back to the power unit through port#2. This value of the applied pressure was chosen at the beginning of each sub-experiment of each test to prevent any possible hydraulic shock to the pressure transducers and the turbine flow meter. After introducing the flow in the external hydraulic circuit with the lowest pressure setting of the pump, the applied pressure was adjusted gradually again to a value that assigned for each sub-experiment of each test (500, 1000 …3100 psi). The trailing wheel was released one quarter turn followed by tightening the lead wheel one quarter turn to move the spool to the first stop where data for the pressure along with flow rate were recorded. This movement set of both trailing and lead wheel of one quarter turn at a time was repeated along the whole tested land length which was 0.1875 in. Twenty-four spool stops of data containing gage pressure and flow rate were recorded. Figure 50 through Figure 54 show different spools locations at the beginning and at the end of each sub experiment of each aforementioned test.

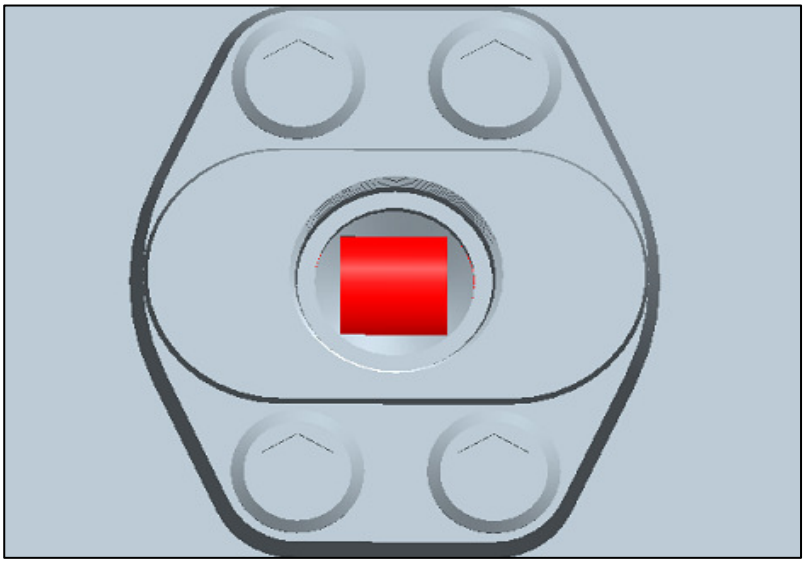

(a

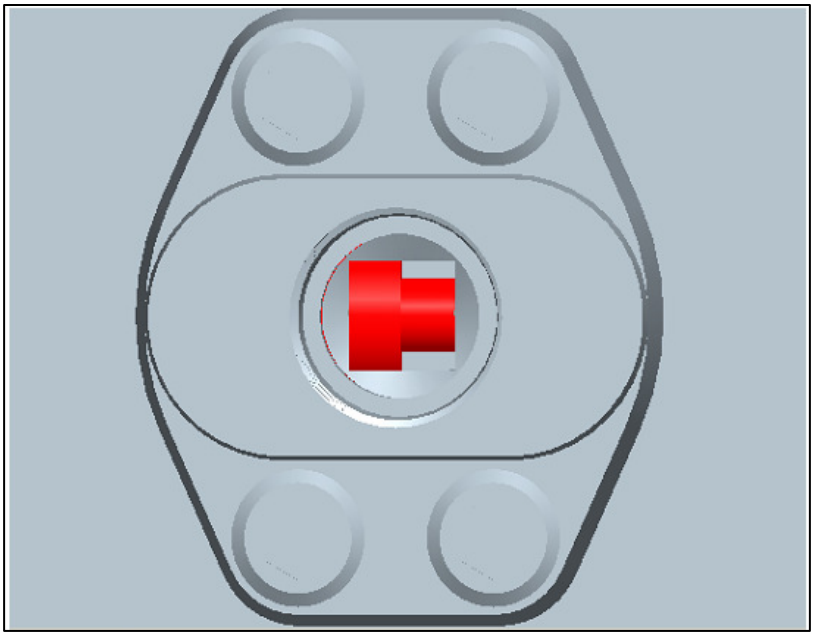

(b

Figure 50: CAD model of the orifice valve assembly (Front view). a) Spool #1 location at the beginning of each sub-experiment of test #1 b) Spool #1 location at the end (after 24 stops) of each sub-experiment of test#1.

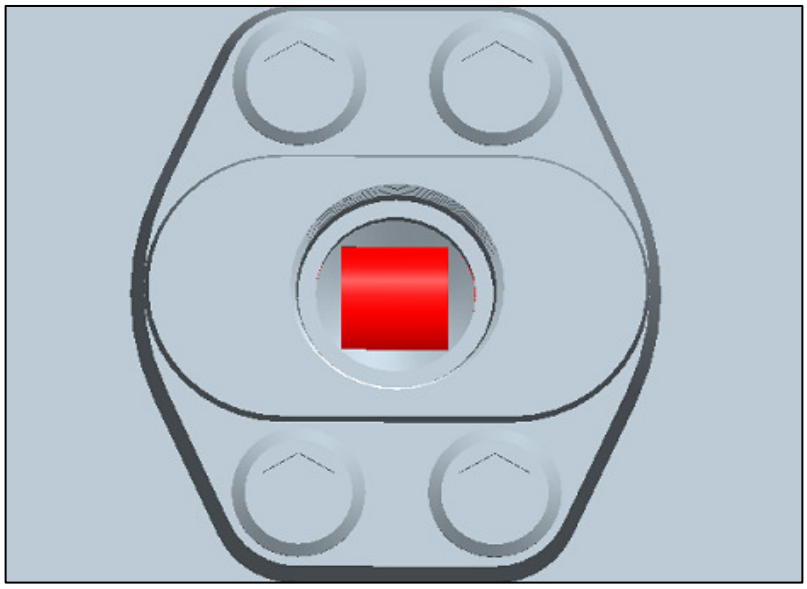

(a

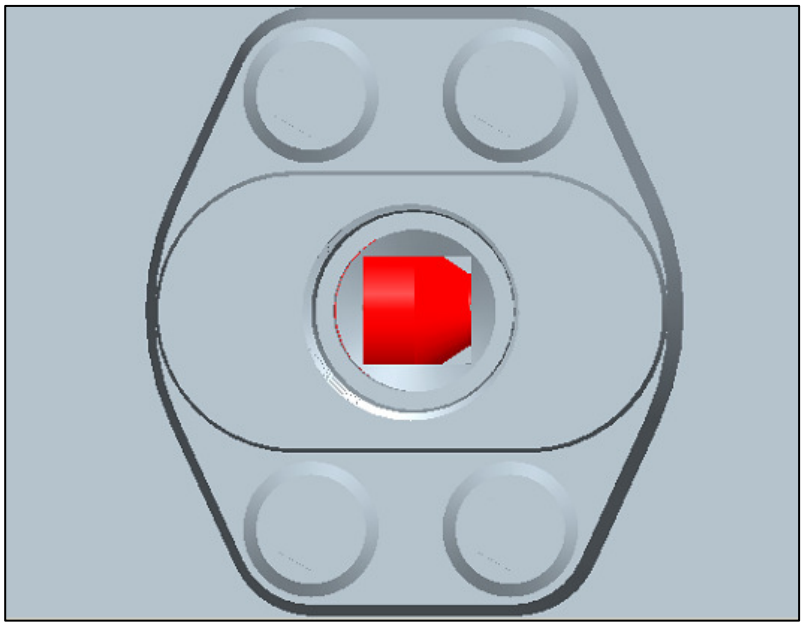

(b

Figure 51: CAD model of the orifice valve assembly (Front view). a) Spool #2 /slope side location at the beginning of each sub-experiment of test #2 b) Spool #2 /slope side location at the end (after 24 stops) of each sub-experiment of test#2.

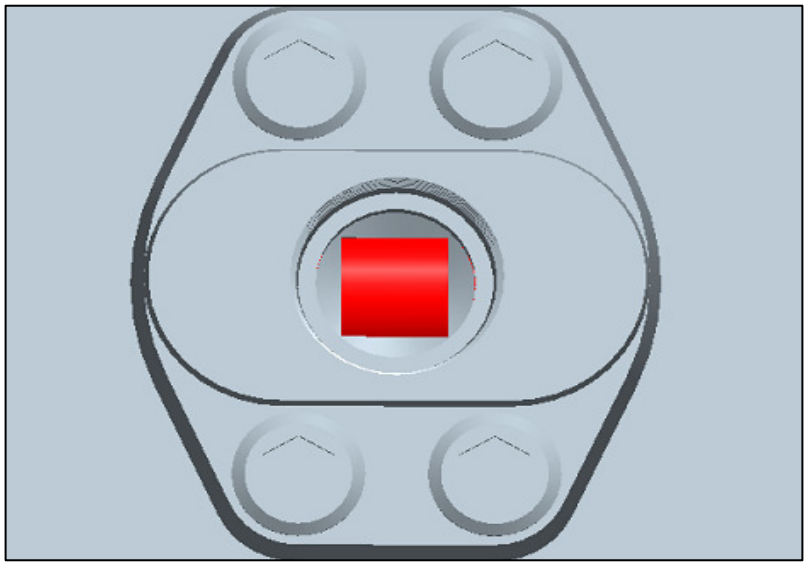

(a

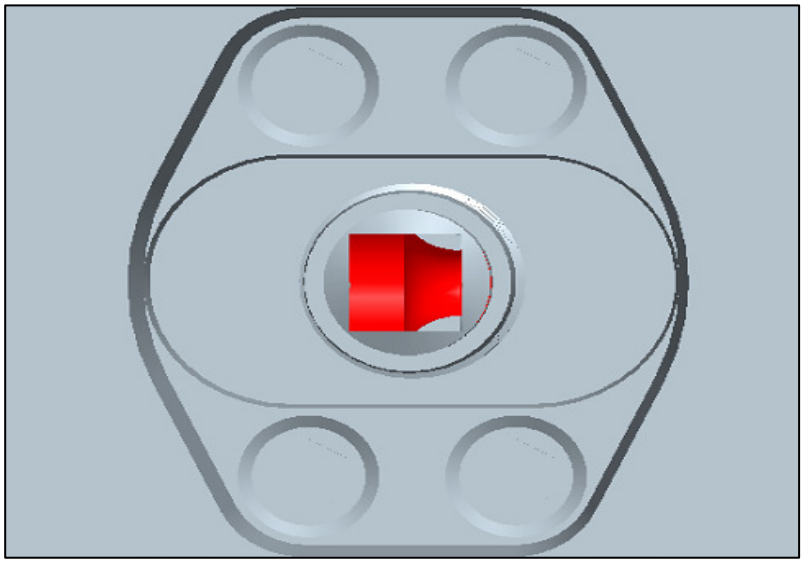

(b

Figure 52: CAD model of the orifice valve assembly (Front view). a) Spool #2 /curve side location at the beginning of each sub-experiment of test #3 b) Spool #2 /curve side locations at the end (after 24 stops) of each sub-experiment of test#3.

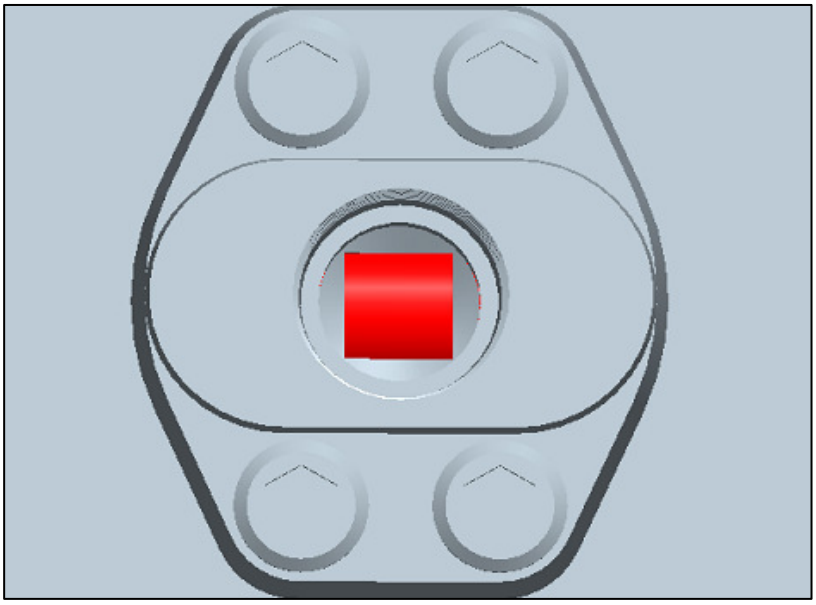

(a

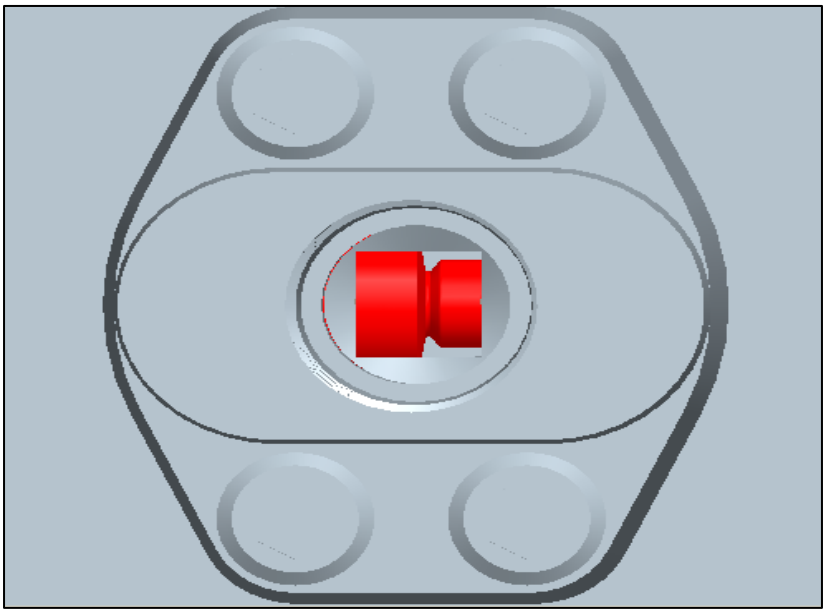

(b

Figure 53: CAD model of the orifice valve assembly (Front view). a) Spool #3 /J-side location at the beginning of each sub-experiment of test #4 b) Spool #3 / J- side location at the end (after 24 stops) of each sub-experiment of test#4.

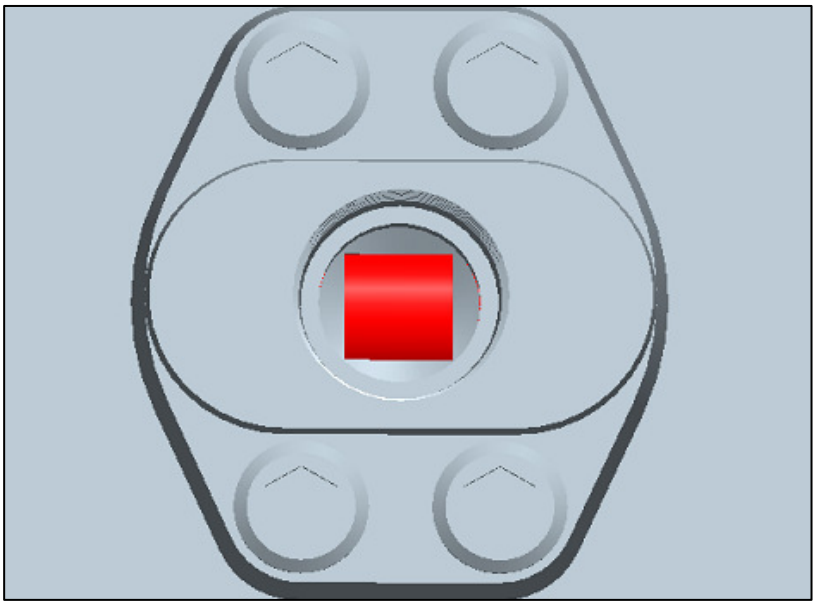

(a

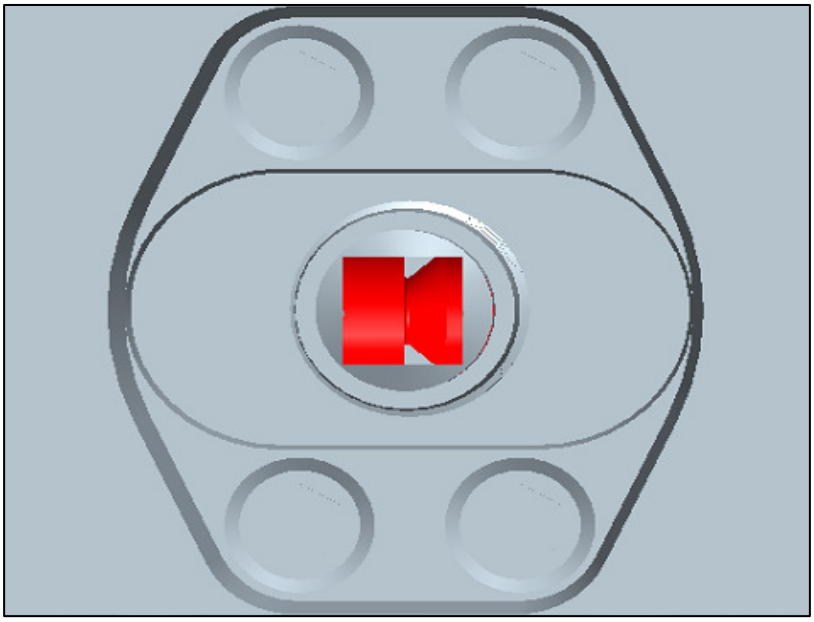

(b

Figure 54: CAD model of the orifice valve assembly (Front view). a) Spool #3 /slope side location at the beginning of each sub-experiment of test #5 b) Spool #3 /slope side location at the end (after 24 stops) of each sub-experiment of test#5.

CHAPTER IV

INTIAL EXPERIMENTAL RESULTS AND DISCUSSION

In this chapter, a discussion of the results acquired from the experimental testing that was initially performed on the three two-sided spools is provided. In order to fully characterize the flow across each aperture, calculations of the opening areas, hydraulic diameters, mean velocities and Reynolds numbers associated with each spool land that was tested were generated. Correlations based on the results of this phase of testing were used to determine an appropriate profile that would give the desired linear performance for both retraction and extension. Table 12 shows the end points for the desired performance of each side of the hydraulic damper.

Table 12: The end points (pressure drop and flow rate values) of the desired linear performance for both retraction and extension sides. (Provided by Amsted Rail)

Spool Type Control Valve Desired Performance			
Retraction side performance		**Extension side performance**	
Flow rate [GPM]	Pressure drop [psi]	Flow rate [GPM]	Pressure drop [psi]
Starting Value		**Starting Value**	
10.2	1512	7.033	2759
Ending Value		**Ending Value**	
14.688	2944	11.322	637

Experimental Results for Spool #1

After the experimental testing for spool #1 was completed, the text file associated with each sub-experiment (six sub-experiments in total with different pressure applied) was imported in Microsoft Excel to generate columns of flow rate, pressure drop and valve position values. The total number of spool stops was 24 for each sub-experiment, with each stop corresponding to one quarter turn of both the trailing and the lead wheel of the test valve. The results of test 1 are shown in Figure 55, 56 and 57.

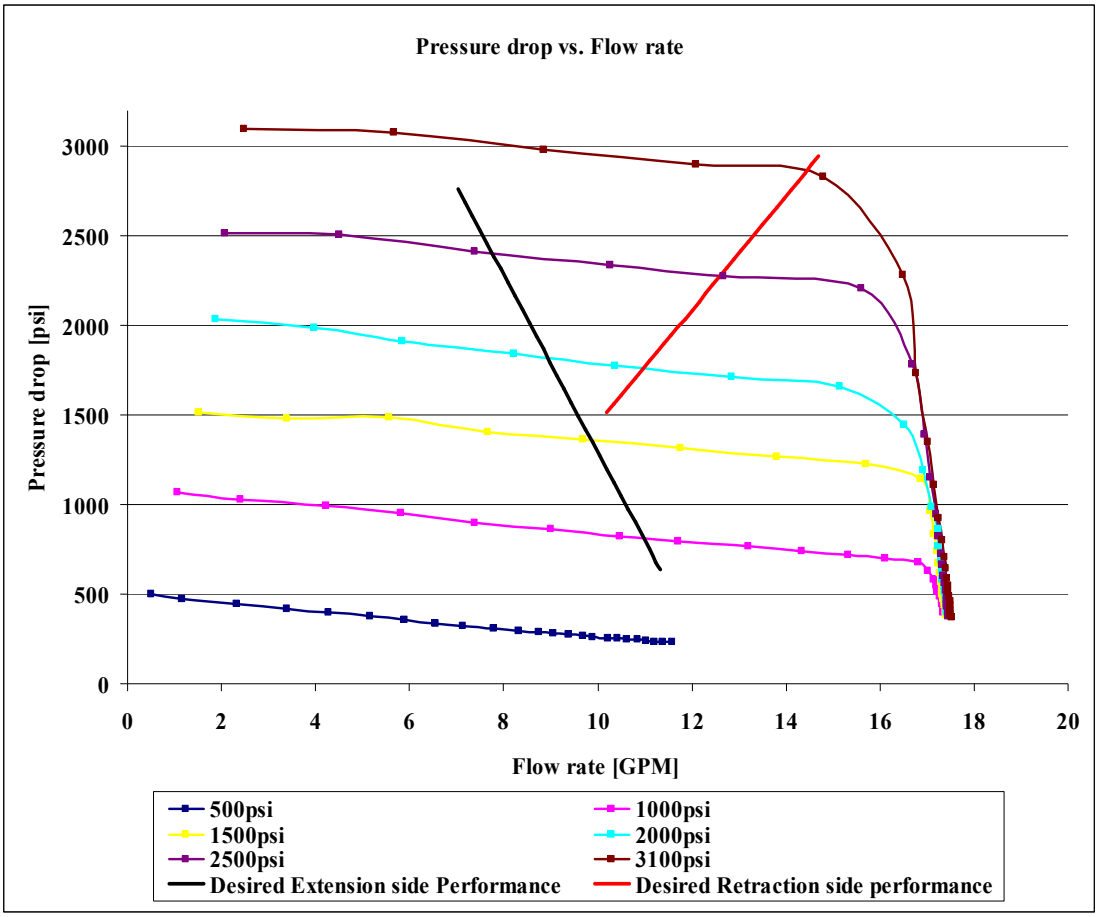

Figure 55: A plot of the pressure drop versus flow rate for the six sub-experiments of test 1. (The results were overlaid with the desired linear performance of the hydraulic damper for comparison).

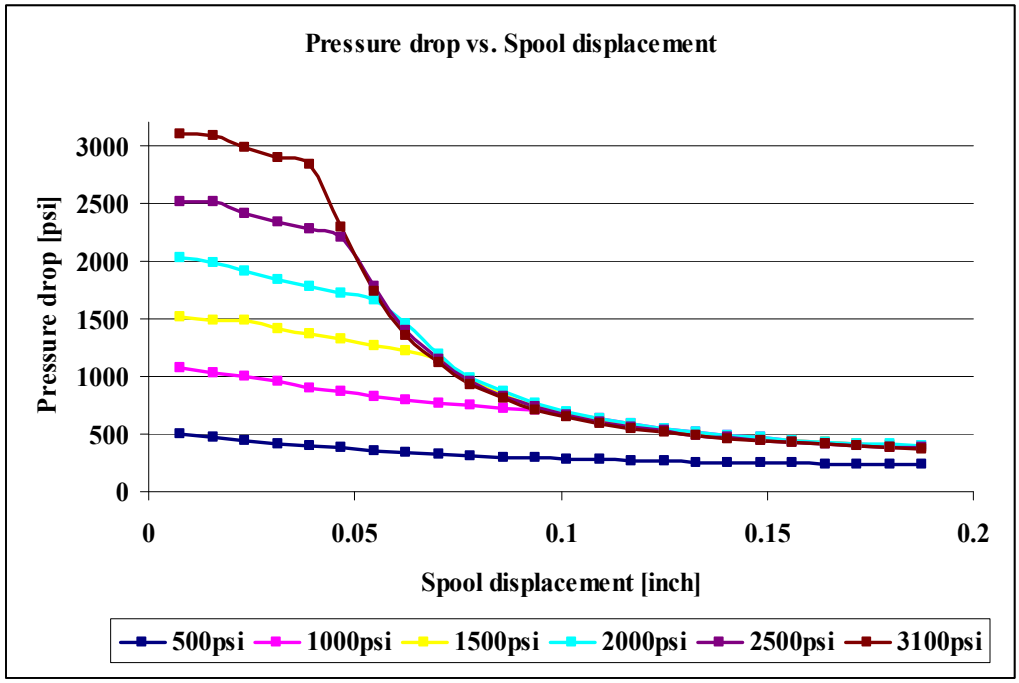

Figure 56: A plot of the pressure drop versus spool displacement for the six sub-experiments of test 1.

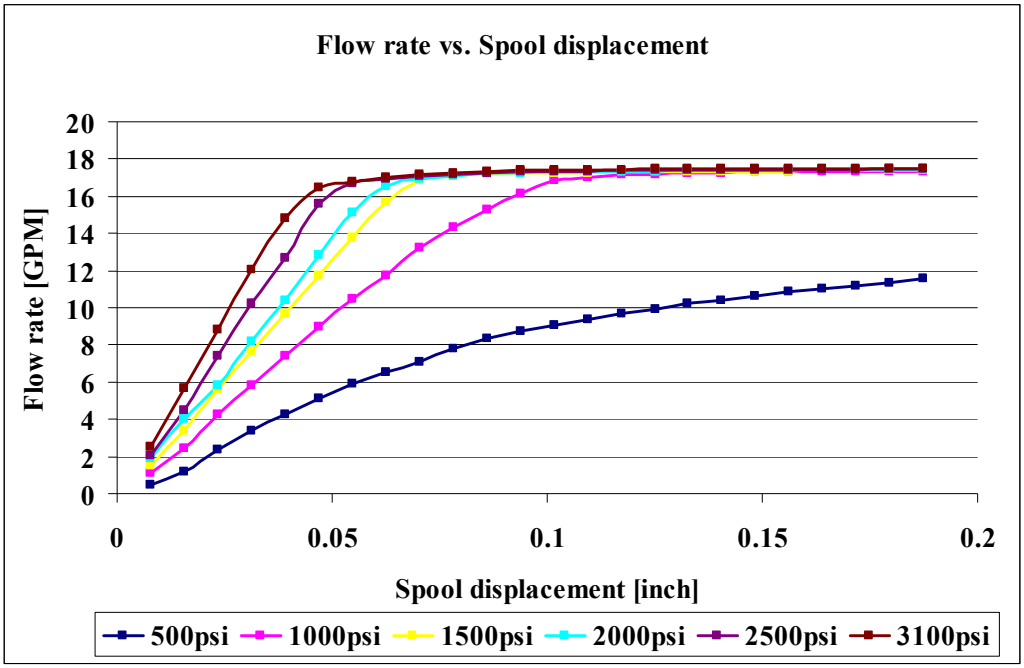

Figure 57: A plot of the flow rate versus spool displacement for the six sub-experiments of test 1.

It is important to mention that the applied pressure in each sub-experiment of test 1 was not constant throughout making the sub-experiment due to the influence of the test valve opening. In addition, the applied pressure performance lines for the six sub-experiments of test 1 were found to have the same trend as the pressure drop performance lines and with small differences between both values.

The total average percentage difference between the applied pressure and the pressure drop values for the six sub-experiments of test 1 was found to be 14%. The pressure drop performance lines start to decline as the flow rate approaches its maximum value of 18 GPM, as shown in Figure 55, since the hydraulic power unit can not sustain the applied pressure settings.

Furthermore, the pressure drop performance line with higher starting applied pressure starts to decrease at earlier spool stops as the spool displaces from the fully closed position as shown in Figure 56.

In Figure 57, the flow rate is almost linear with the spool's position for all the six sub-experiments as was predicted for spool #1 since it has a straight cut; and so spool #1 opening area is linearly proportional to its position .

In order to characterize the flow at each spool stop of test 1, constant spool stop's performance lines of pressure drop and flow rates were generated in Figure 58.

As shown in Figure 58, the pressure drop increases as the flow rate increases at the same spool stop. In addition, the slope of the performance line decreases as the spool opening increases. In other words, a larger opening area needs more flow rate in order to cause the same pressure drop as a smaller opening area.

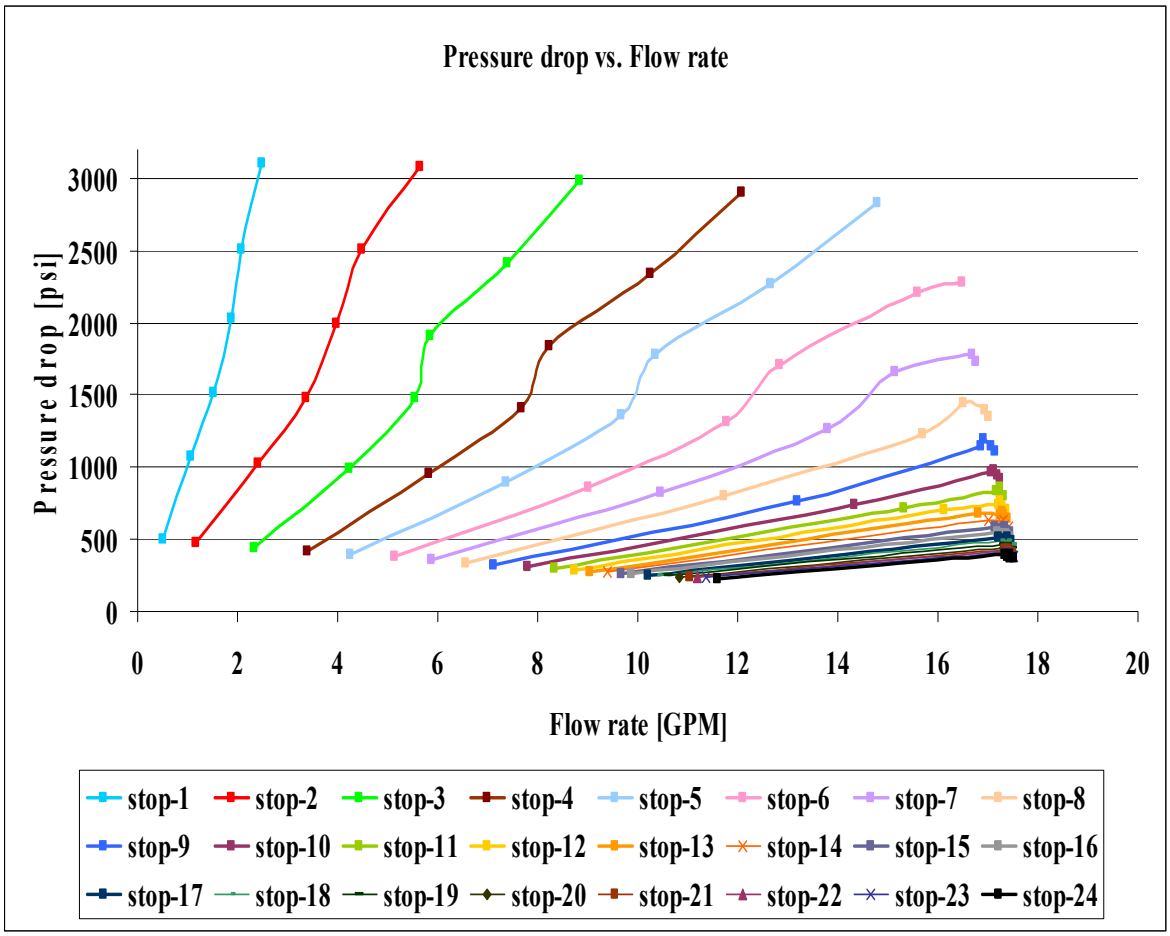

Figure 58: A plot of pressure drop vs. flow rate at each spool stop of test 1.

In this study, it was assumed that the entire pressure drop was caused by the spool land only. Furthermore, pressure losses due to the 0.375 in. square orifice passage along with its entrance and exit losses were assumed to be negligible because it was designed to give minimal losses (see Appendix D). Thus, all average velocity and Reynolds number calculations were based on the spool land region. It was assumed that the viscous flow is incompressible fully developed. Thus, the following formulas were utilized to calculate the mean velocity and Reynolds number values at each spool stop of each sub-experiment for all the tests in this study [100]:

$$U = \left[0.0978 \frac{\text{meter} \times \text{inch}^2 \times \text{minute}}{\text{second} \times \text{US\_GALLON}} \right] \times \frac{Q}{(2A_t)} \tag{14}$$

$$\text{Re} = \left[25400 \frac{\text{second} \times \text{centi\_stoke}}{\text{meter} \times \text{inch}} \right] \times \frac{UD_h}{\upsilon} \tag{15}$$

and

$$D_h = \frac{4A_t}{P_t} \tag{16}$$

where U is the average flow velocity in m/s, Q is the total volumetric flow rate in GPM, A_t is the total opening area for half of the spool in inch.^{2}, Re is the Reynolds number, D_h is the hydraulic diameter in inch, υ is the kinematic viscosity in cSt and P_t is the total wetted perimeter for half of the spool in inch.

The following formulas were used to calculate the total opening area (A_t) and the total wetted perimeter (P_t), see Figure 59:

$$A_t = A_{spool} + A_{clearance} \tag{17}$$

$$P_t = P_{spool} + P_{clearance} \tag{18}$$

and

$$A_{clearance} = (0.375 - x) \times [(0.5 - D_{body})/2] \tag{19}$$

$$P_{clearance} = [2 \times (0.375 - x)] \tag{20}$$

where A_{spool} is the opening area component of the spool aperture in inch^2, $A_{clearence}$ is the opening area component due to the clearance between the spool body and the valve seat in inch^2, P_{spool} is the wetted perimeter component of the spool aperture in inch, $P_{clearenace}$ is the wetted perimeter component due to clearance between the spool body and the valve seat in inch, x is the spool displacement in inch and D_{body} is the spool body diameter in inch.

The spool body diameter of spool #1, 2 and 3 was measured using a micrometer and it was found that all of the three spools have the same body diameter of 0.494 in. (*i.e.* D_{body} is 0.494 in.).

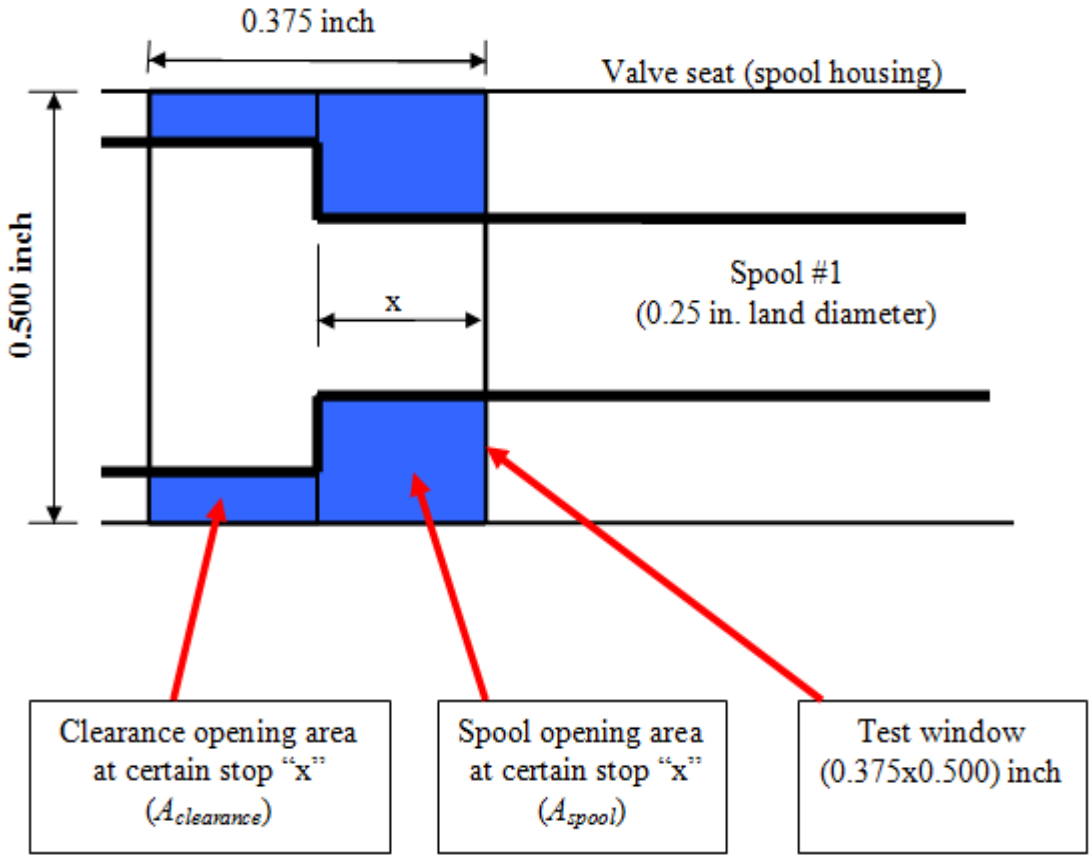

Figure 59: A schematic of spool #1 while making test 1 that shows the total opening area at a certain spool stop (x).

The clearance opening area ($A_{clearence}$) along with the clearance wetted perimeter ($P_{clearenace}$) were the same for all the aforementioned tests and are listed in Table 13.

Table 13: The opening area ($A_{clearance}$) along with the wetted perimeter ($P_{clearance}$) values at each spool stop for spool #1, 2 and 3.

Spool- stop Number	**Spool displacement (x) [inch]**	**Clearance area ($A_{clearance}$) [inch^2]**	**Clearance Wetted perimeter ($P_{clearance}$) [inch]**
1	0.007813	0.001102	0.734375
2	0.015625	0.001078	0.718750
3	0.023438	0.001055	0.703125
4	0.03125	0.001031	0.687500
5	0.039063	0.001008	0.671875
6	0.046875	0.000984	0.656250
7	0.054688	0.000961	0.640625
8	0.062500	0.000938	0.625000
9	0.070313	0.000914	0.609375
10	0.078125	0.000891	0.593750
11	0.085938	0.000867	0.578125
12	0.09375	0.000844	0.562500
13	0.101563	0.000820	0.546875
14	0.109375	0.000797	0.531250
15	0.117188	0.000773	0.515625
16	0.125000	0.000750	0.500000
17	0.132813	0.000727	0.484375
18	0.140625	0.000703	0.468750
19	0.148438	0.000680	0.453125
20	0.15625	0.000656	0.437500
21	0.164063	0.000633	0.421875
22	0.171875	0.000609	0.406250
23	0.179688	0.000586	0.390625
24	0.187500	0.000563	0.375000

The opening area (A_{spool}) along with the wetted perimeter (P_{spool}) values at each spool stop of spool #1 are listed in Table 14.

Table 14: The opening area (A_{spool}) along with the wetted perimeter (P_{spool}) values at each spool stop of spool #1.

Spool- stop Number	**Spool displacement (x) [inch]**	**Opening area (A_{spool}) [inch^2]**	**Wetted perimeter (P_{spool}) [inch]**
1	0.007813	0.000977	0.140626
2	0.015625	0.001953	0.156252
3	0.023438	0.002930	0.171878
4	0.03125	0.003907	0.187504
5	0.039063	0.004883	0.203130
6	0.046875	0.005859	0.218756
7	0.054688	0.006836	0.234382
8	0.062500	0.007813	0.250008
9	0.070313	0.008790	0.265634
10	0.078125	0.009766	0.281260
11	0.085938	0.010743	0.296886
12	0.09375	0.011720	0.312512
13	0.101563	0.012696	0.328138
14	0.109375	0.013673	0.343764
15	0.117188	0.014649	0.359390
16	0.125000	0.015626	0.375016
17	0.132813	0.016603	0.390642
18	0.140625	0.017579	0.406268
19	0.148438	0.018556	0.421894
20	0.15625	0.019533	0.437520
21	0.164063	0.020509	0.453146
22	0.171875	0.021486	0.468772
23	0.179688	0.022462	0.484398
24	0.187500	0.023438	0.500024

The opening area (A_{spool}) along with the wetted perimeter (P_{spool}) values at each spool stop of spool #1 were calculated from the CAD model of spool #1, as shown in Figure 60.

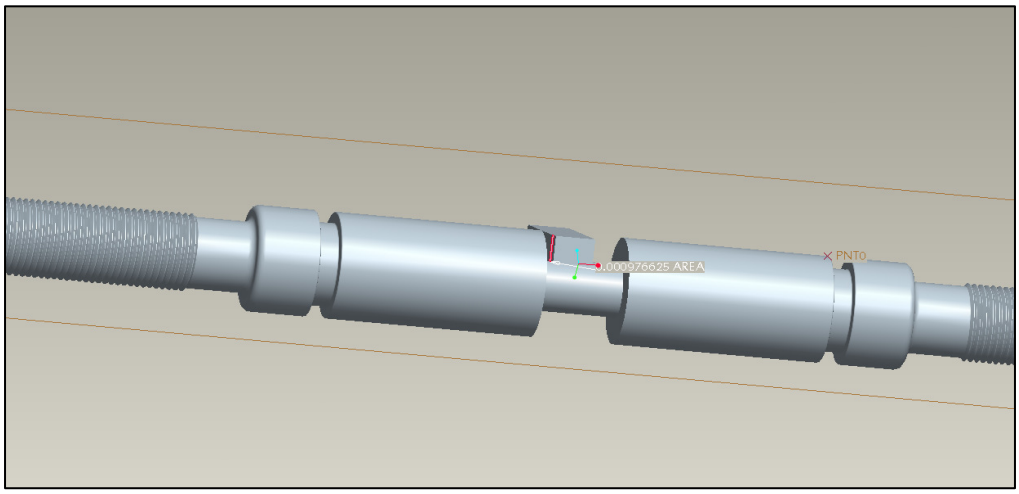

(a)

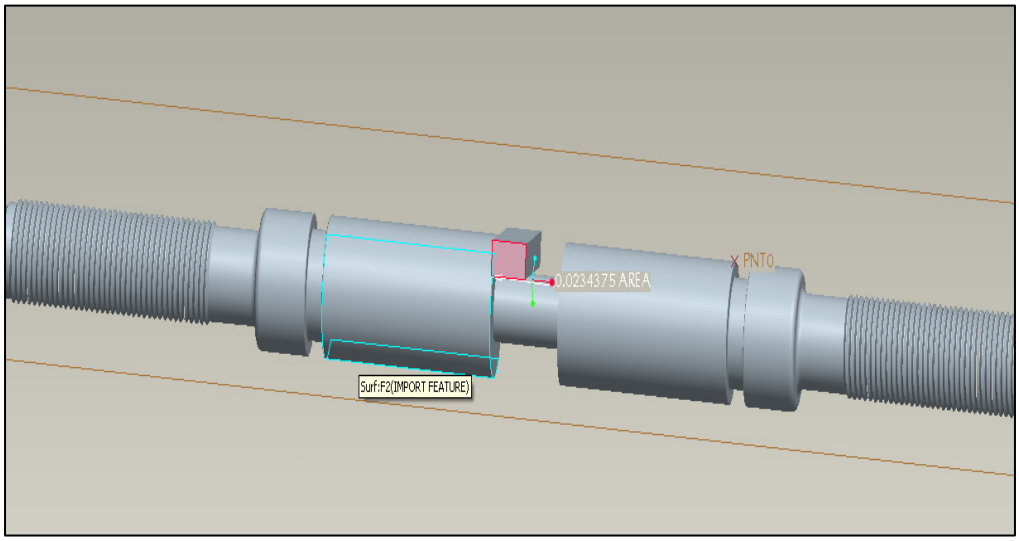

(b)

Figure 60: CAD model of spool #1 that was used to calculate the opening area (A_{spool}) and the wetted perimeter (P_{spool}) at each spool stop. a) area calculation at the first spool stop b) area calculation at the twenty fourth spool stop.

According to the testing procedure shown in Figure 61, the flow was not completely internal, in other words, the flow was not completely bounded by solid surfaces when it passed the spool land region. Thus, it was assumed that the flow passes the spool land region was a flow inside a hydraulic channel for which the wetted perimeter (P_{spool}) will not be the whole circumference of the aforementioned opening areas in Figure 60.

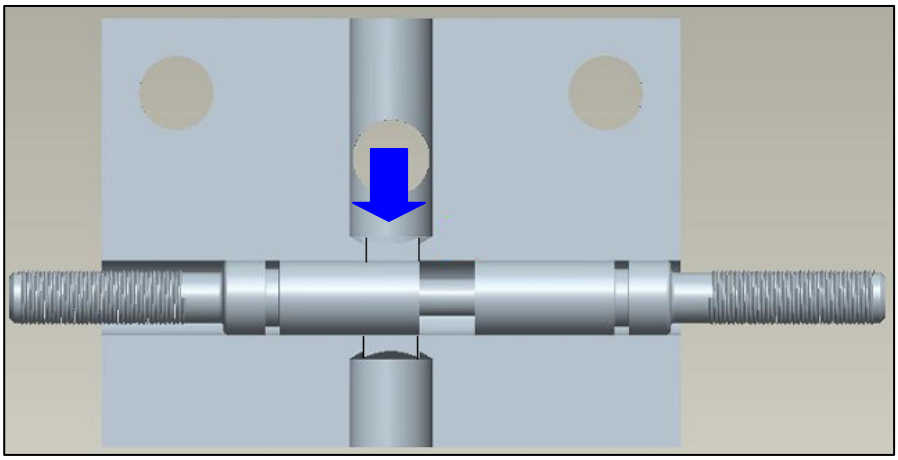

(a)

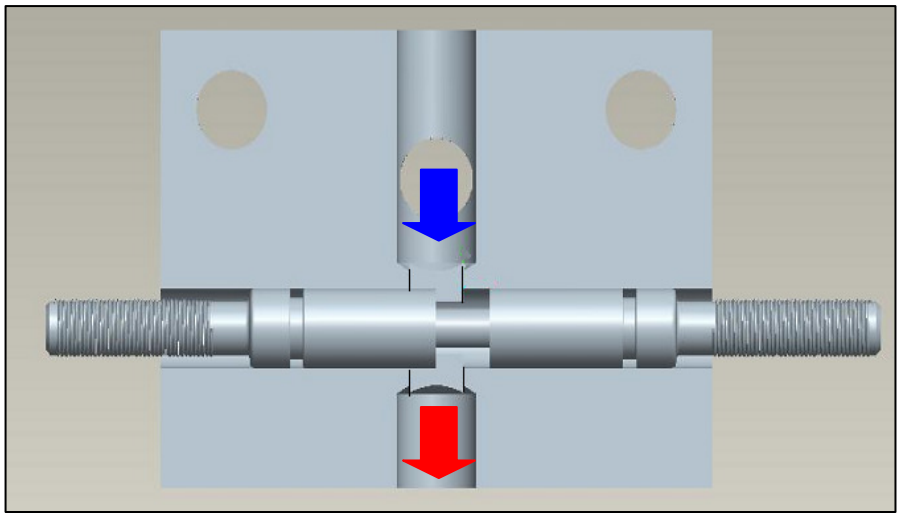

(b)

Figure 61: CAD model of the test valve (Bottom view) shows the location of spool #1 inside the manifold at a) fully closed position b) at 24 spool stop position.

The results of the calculations for mean velocities and Reynolds numbers of test 1 are shown below:

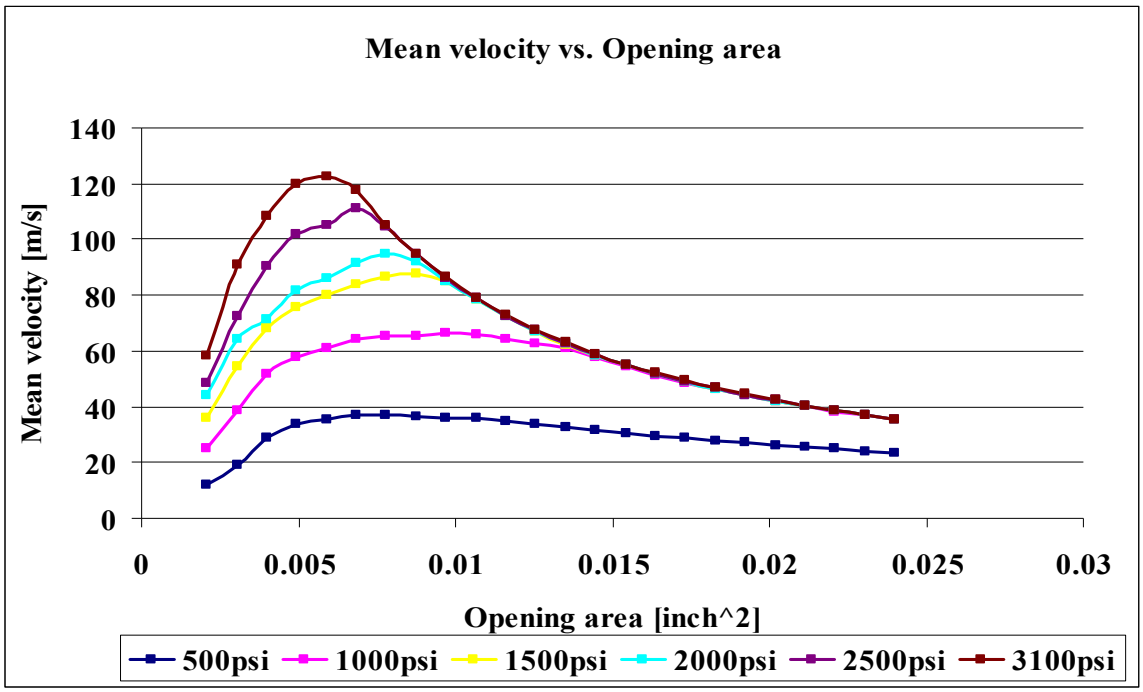

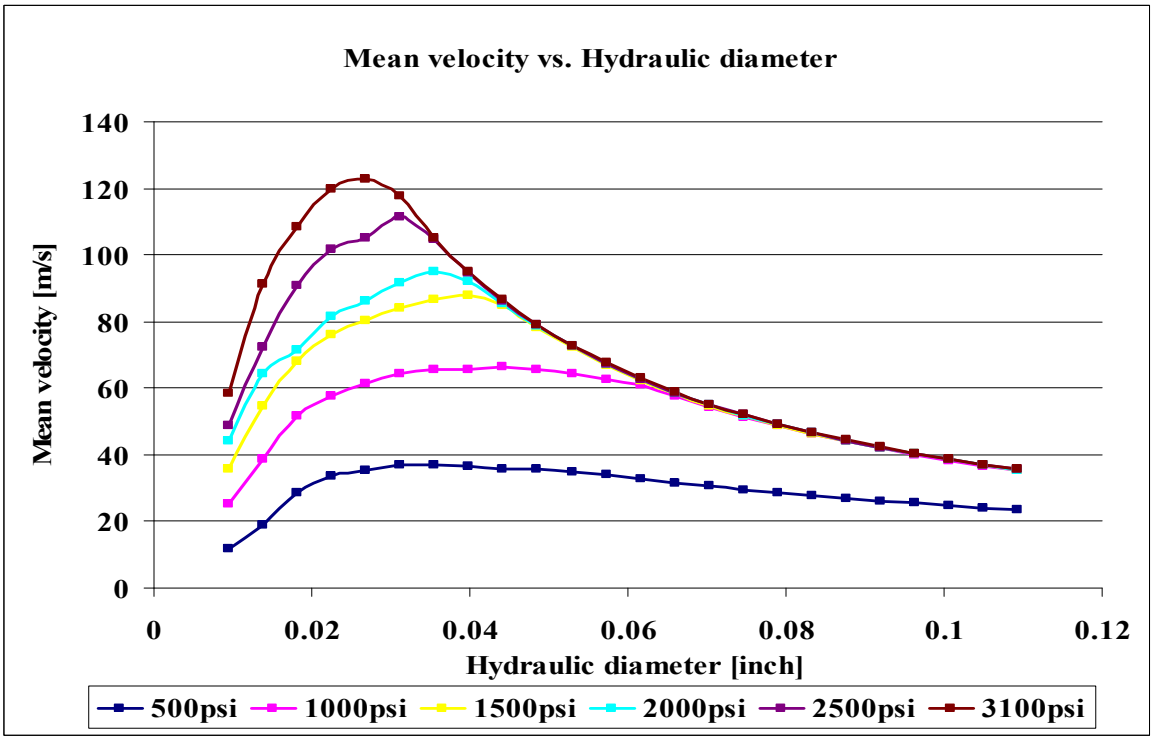

Figure 62: Plots of the flow mean velocity at different spool stops versus the opening area and the hydraulic diameter respectively. (test 1)

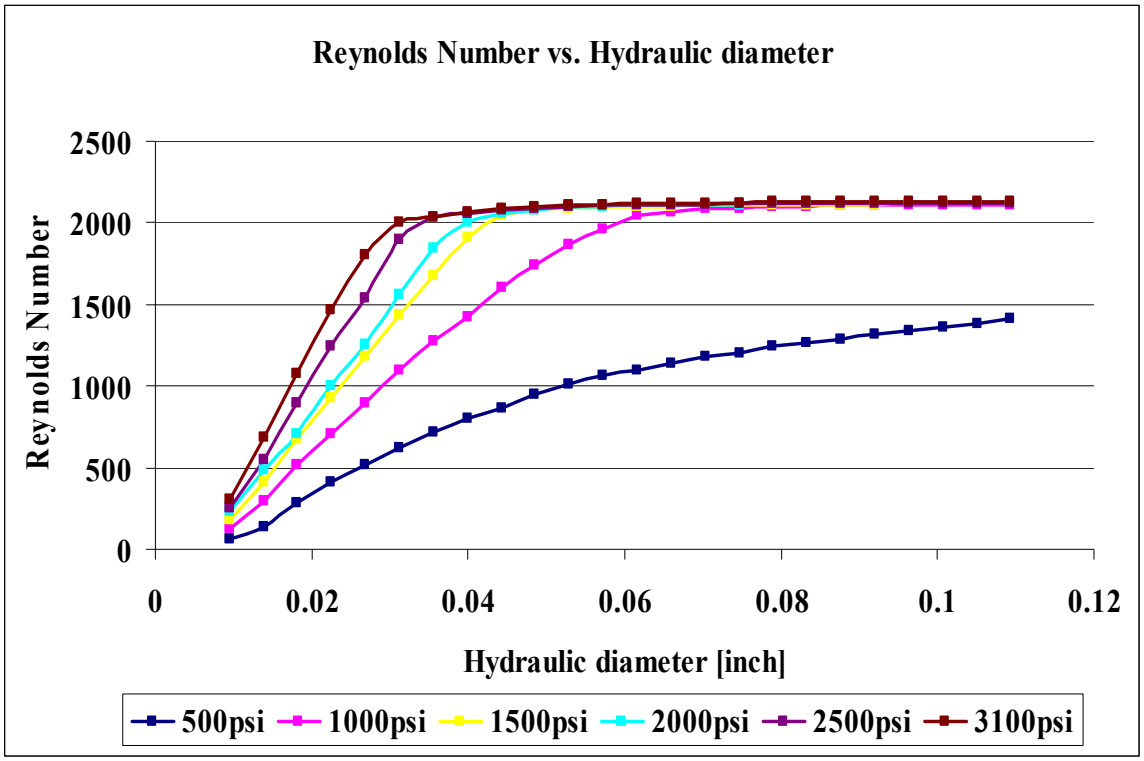

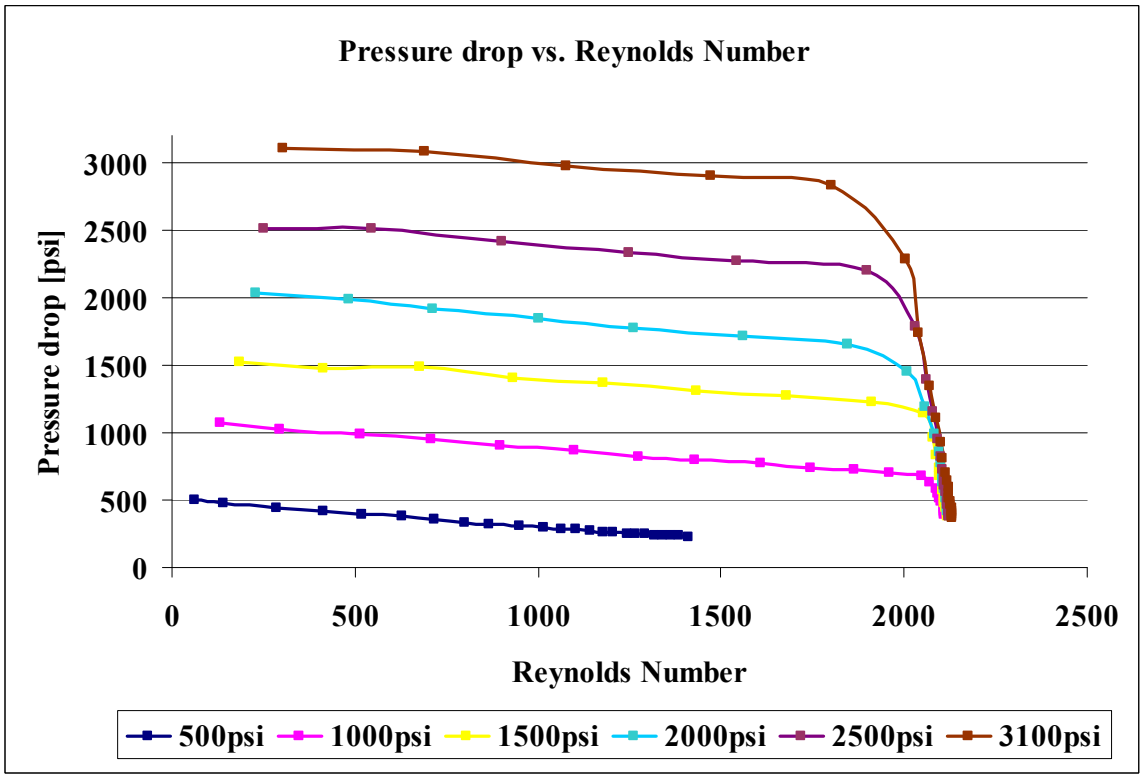

Figure 63: Plots of the flow Reynolds number at different spool stops versus the hydraulic diameter and the pressure drop respectively. (test 1)

As shown in Figure 62, the mean velocity of the flow starts to decrease at earlier spool stop as the applied pressure increases, since the flow rate is reaching its limit of 18 GPM faster. And so, there is no significant increase in the flow rate corresponding to significant increase to both opening area and hydraulic diameter. In addition, Reynolds number reaches a finite value at earlier spool stop as the applied pressure increases due to decrease in the mean velocity accompanied with increase in the hydraulic diameter at the same spool stop, as shown in Figure 63.

To justify the incompressibility assumption of the AW46 hydraulic oil under the aforementioned applied pressure values, the speed of sound for this media was calculated first using the following formula [100]:

$$c = \sqrt{\frac{E_v}{\rho}} \tag{21}$$

where c is the speed of sound in m/s, E_v is the bulk modulus in N/m^2 and ρ is the density in kg/m^3.

No data were found regarding the bulk modulus of AW46 hydraulic oil from its manufacturer. Since AW46 oil is 15 weight oil with additives, the bulk modulus of 15 weight oil was used instead. Thus, if the compressibility condition applies to the 15 weight oil, it will apply for the AW46 oil (since it has additives and thus more incompressible).

The speed of sound calculation for test 1 through test 5 was based on a flow temperature of 40°C. Thus, density and bulk modulus data of 15 weight oil were obtained by interpolating data of both 10 and 30 weight oils that were found in the database of Matlab Simulink (SimHydraulics library), see Table 15.

Table 15: Density & bulk modulus properties of different weight hydraulic oils at 40°C.

Oil Type	**Density (kg/m^3)**	**Bulk Modulus (N/m^2)**
Oil-10W	837.40	1.675210×10^9
Oil-15W (By interpolation**)**	840.55	1.684295×10^9
Oil-30W	850.00	1.711550×10^9

According to Table 15, the speed of sound was found to be 1415.556 m/s in a 15 weight oil medium at 40°C. Thus, the next step was to calculate the Mach number at each spool stop using the following formula [100]:

$$M = \frac{U}{c} \tag{22}$$

where M is Mach number, U is the average velocity at each spool stop in m/s, c is the speed of sound in m/s. According to [100], if M <0.3 then the flow is incompressible.

As shown in Figure 64, the Mach numbers are less than 0.3 for all the spool stops of test 1. As a result, the flow is incompressible for this test.

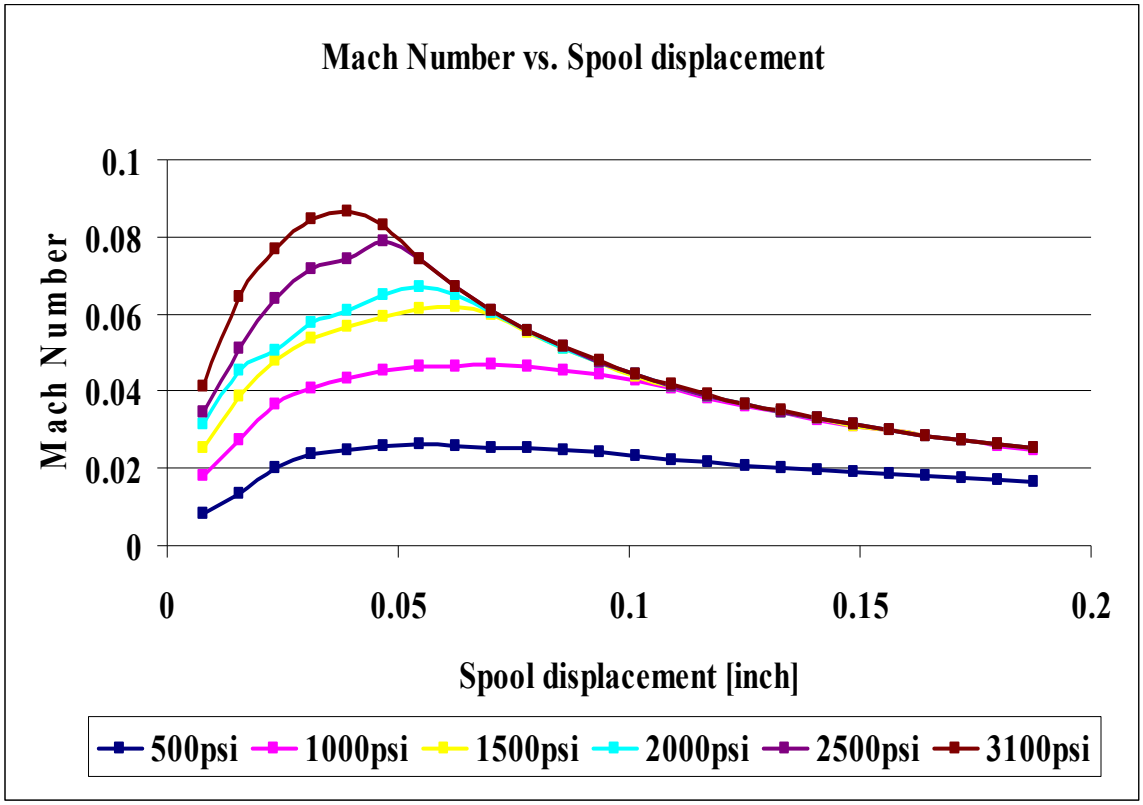

Figure 64: Plot of Mach number versus spool displacement of test 1.

Experimental Results for Spool #2/Slope Side

After the experimental testing for spool #2/slope side was completed, the text file associated with each sub-experiment (six sub-experiments in total with different pressure applied) was imported in Microsoft Excel to generate columns of flow rate, pressure drop and valve position values. The total number of spool stops was 24 for each sub-experiment, with each stop corresponding to one quarter of both the trailing and the lead wheel of the test valve. The results of test 2 are shown in Figure 65, 66 and 67.

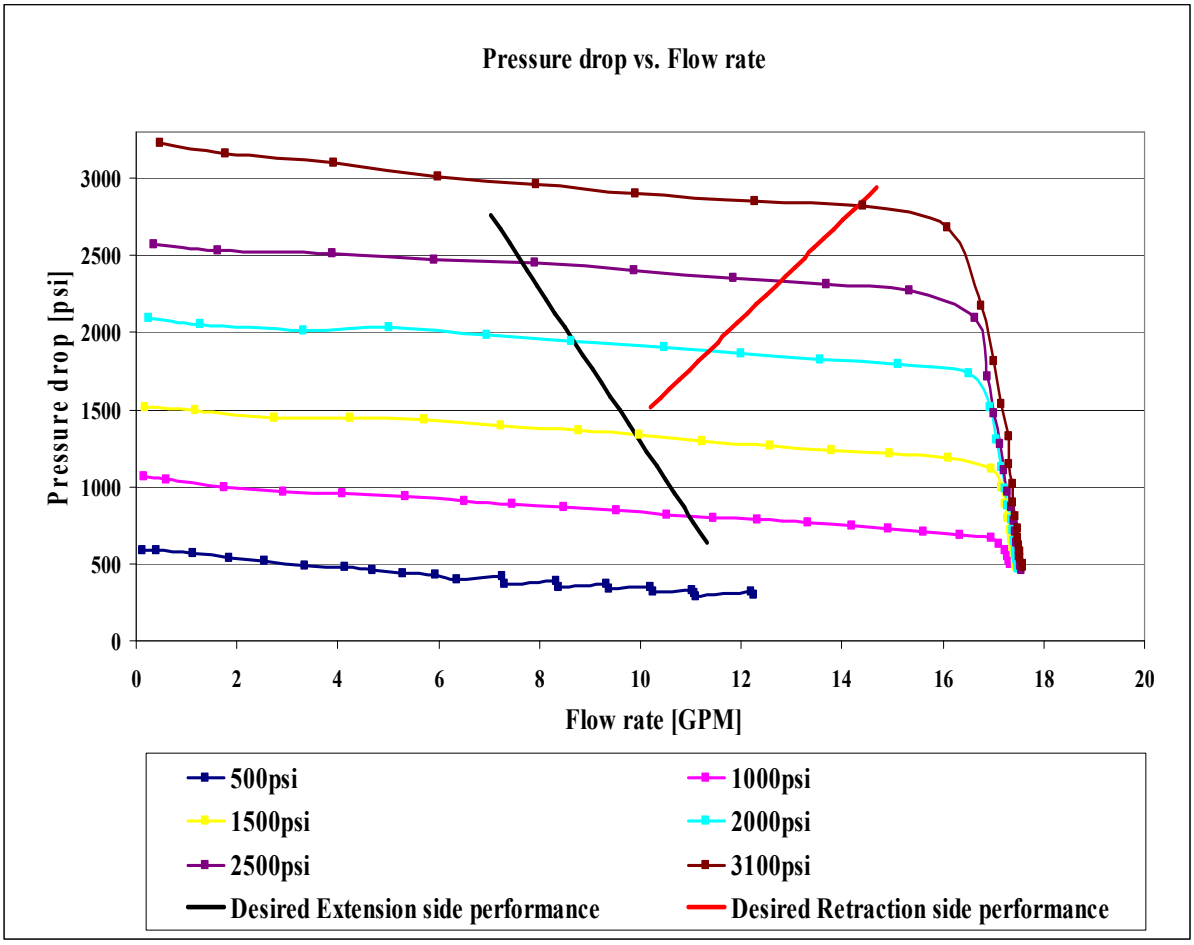

Figure 65: A plot of the pressure drop versus flow rate for the six sub-experiments of test 2. (The results were overlaid with the desired linear performance of the hydraulic damper for comparison).

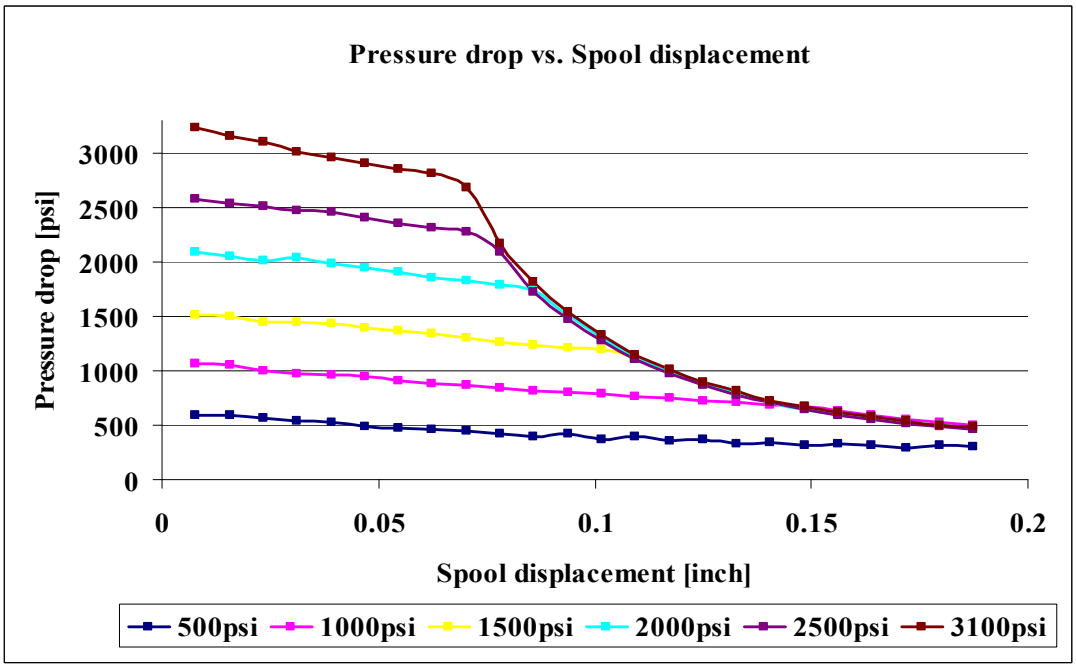

Figure 66: A plot of the pressure drop versus spool displacement for the six sub-experiments of test 2.

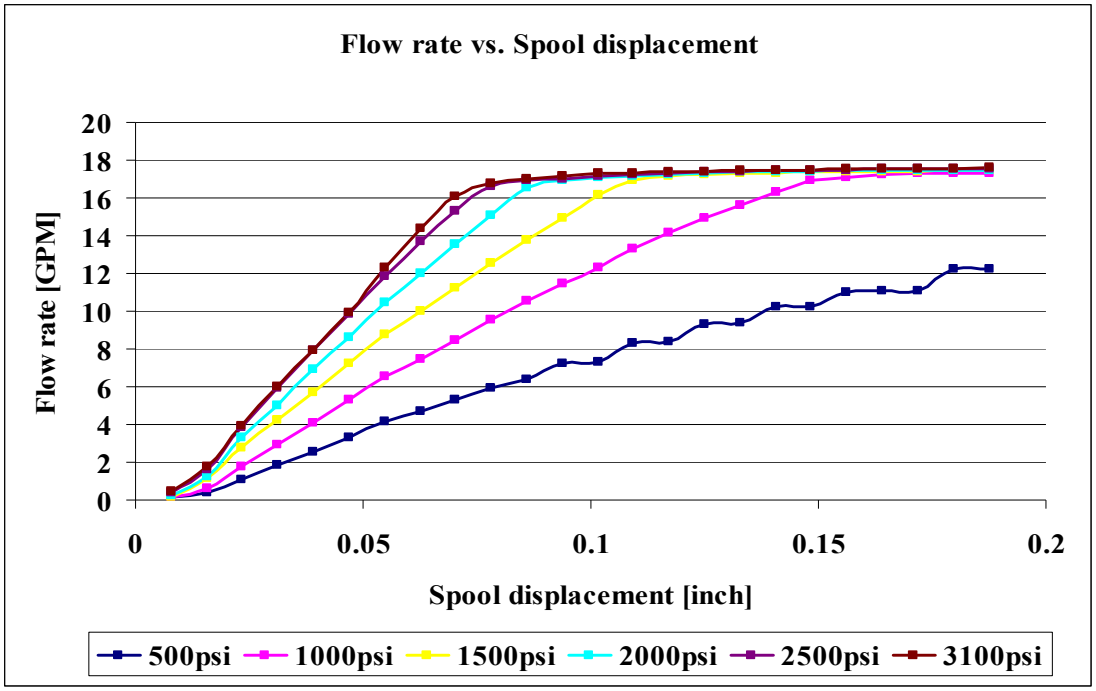

Figure 67: A plot of the flow rate versus spool displacement for the six sub-experiments of test 2.

It is important to mention that the applied pressure in each sub-experiment of test 2 was not constant throughout making the sub-experiment due to the influence of the test valve opening. In addition, the applied pressure performance lines for the six sub-experiments of test 2 were found to have the same trend as the pressure drop performance lines and with small differences between both values.

The total average percentage difference between the applied pressure and the pressure drop values for the six sub-experiments of test 2 was found to be 9%. The pressure drop performance lines start to decline as the flow rate approaches its maximum value of 18 GPM as shown Figure 65, since the hydraulic power unit can not sustain the applied pressure settings.

Furthermore, the pressure drop performance line with higher starting applied pressure will start to decrease at earlier spool stops as the spool displaces from the fully closed position as shown in Figure 66.

In Figure 67, the flow rate is almost linear with the spool's position for all the six sub-experiments as was not predicted for spool #2/slope side since it does not have a straight cut as in spool #1. The cause behind this behavior is that the clearance area, which is a straight cut opening area, influences the flow at earlier spool stops.

In order to characterize the flow at each spool stop of test 2, constant spool stop's performance lines of pressure drop and flow rates were generated in Figure 68.

As shown in Figure 68, the pressure drop increases as the flow rate increases at the same spool stop. In addition, the slope of the performance line decreases as the spool opening increases. In other words a larger opening area needs more flow rate in order to cause the same pressure drop as a smaller opening area.

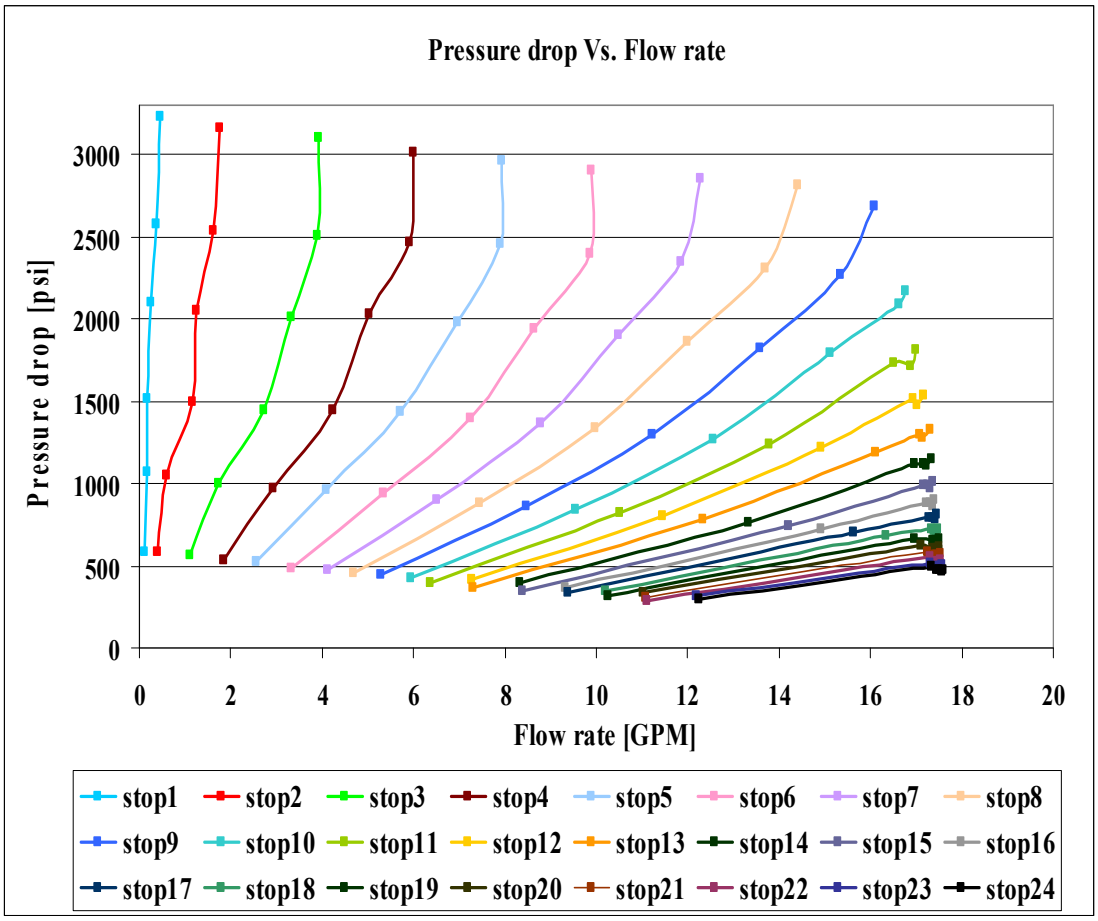

Figure 68: A plot of pressure drop vs. flow rate at each spool stop of test 2.

The opening area (A_{spool}) along with the wetted perimeter (P_{spool}) values at each spool stop of spool #2/slope side are listed in Table 16.

Table 16: The opening area (A_{spool}) along with the wetted perimeter (P_{spool}) values at each spool stop of spool #2/slope side.

Spool- stop Number	**Spool displacement (x) [inch]**	**Opening area (A_{spool}) [inch^2]**	**Wetted perimeter (P_{spool}) [inch]**
1	0.007813	0.000021	0.017203
2	0.015625	0.000081	0.034406
3	0.023438	0.000183	0.051609
4	0.031250	0.000326	0.068812
5	0.039063	0.000509	0.086016
6	0.046875	0.000733	0.103218
7	0.054688	0.000997	0.120421
8	0.062500	0.001302	0.137625
9	0.070313	0.001648	0.154828
10	0.078125	0.002035	0.172030
11	0.085938	0.002462	0.189234
12	0.093750	0.002930	0.206437
13	0.101563	0.003439	0.223640
14	0.109375	0.003988	0.240843
15	0.117188	0.004578	0.258046
16	0.125000	0.005209	0.275250
17	0.132813	0.005880	0.292452
18	0.140625	0.006593	0.309655
19	0.148438	0.007346	0.326859
20	0.156250	0.008139	0.344061
21	0.164063	0.008973	0.361264
22	0.171875	0.009848	0.378468
23	0.179688	0.010764	0.395671
24	0.187500	0.011719	0.412839

The opening area (A_{spool}) along with the wetted perimeter (P_{spool}) values at each spool stop of spool #2/slope side were calculated from the CAD model of spool #2, as shown in Figure 69.

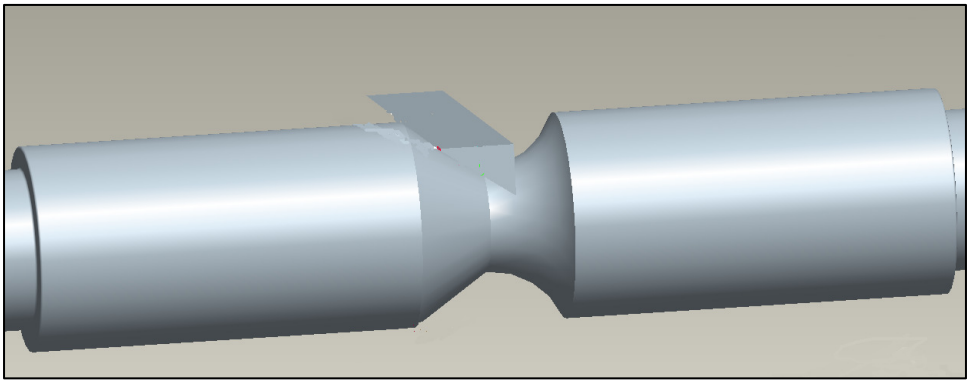

(a)

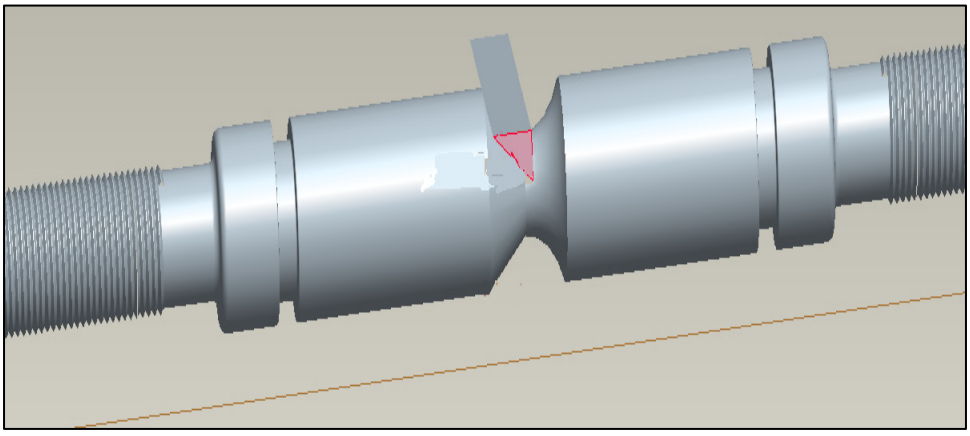

(b)

Figure 69: CAD model of spool #2/slope side that was used to calculate the opening area (A_{spool}) and the wetted perimeter (P_{spool}) at each spool stop. a) area calculation at the first spool stop b) area calculation at the twenty fourth spool stop.

According to the testing procedure shown in Figure 70, the flow was not completely internal, in other words, the flow was not completely bounded by solid surfaces when it passed the spool land region. Thus, it was assumed that the flow passes the spool land region was a flow inside a hydraulic channel for which the wetted perimeter (P) will not be the whole circumference of the aforementioned opening areas in Figure 69.

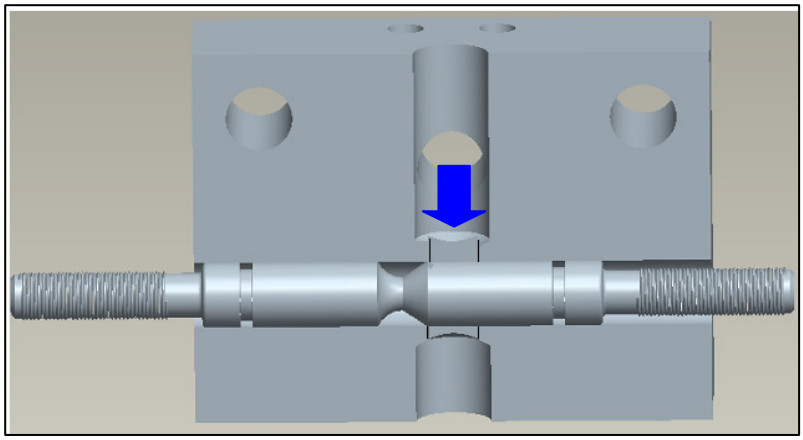

(a)

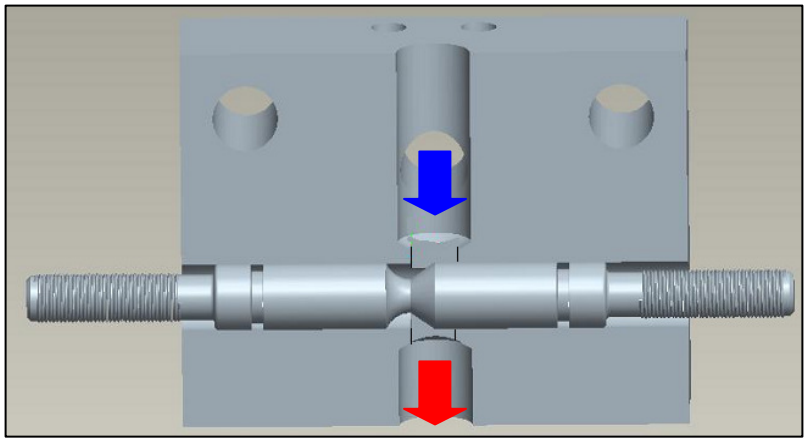

(b)

Figure 70: CAD model of the test valve (Bottom view) shows the location of spool #2/slope side inside the manifold at a) fully closed position b) at 24 spool stop position.

The results of the calculations for mean velocities, Reynolds numbers, and Mach numbers of test 2 are shown below:

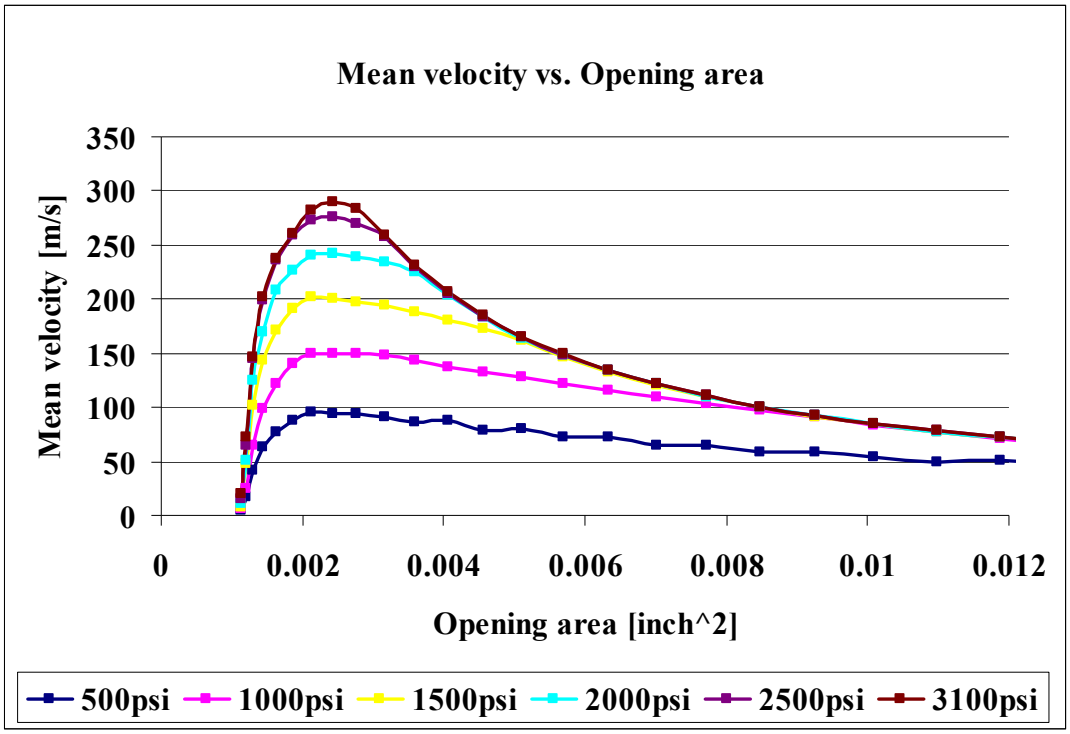

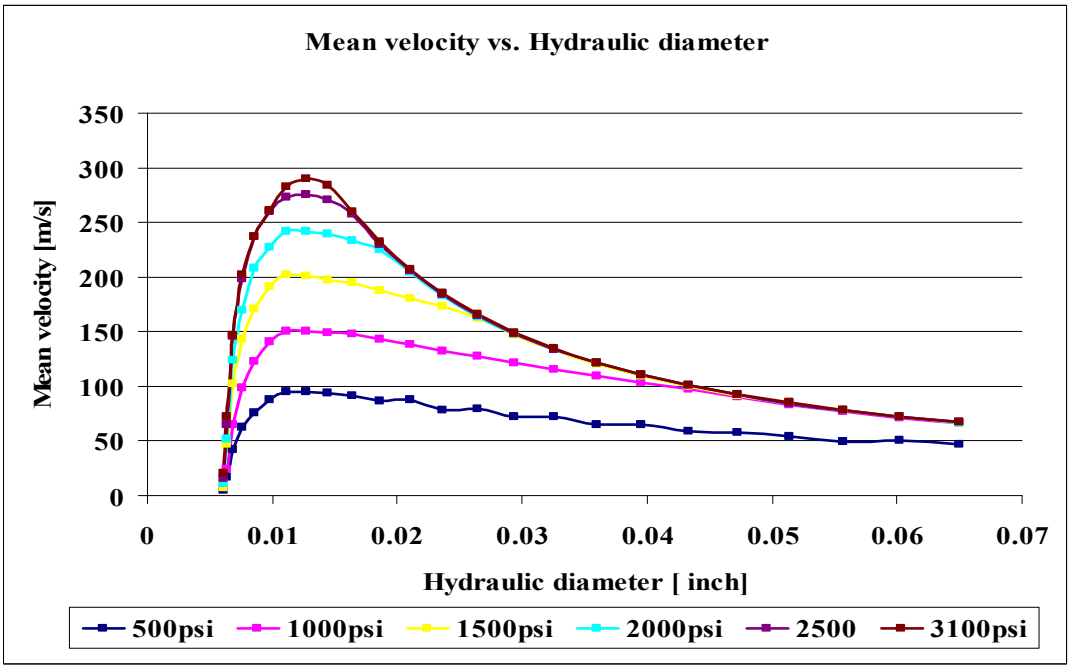

Figure 71: Plots of the flow mean velocity at different spool stops versus the opening area and the hydraulic diameter respectively. (test 2)

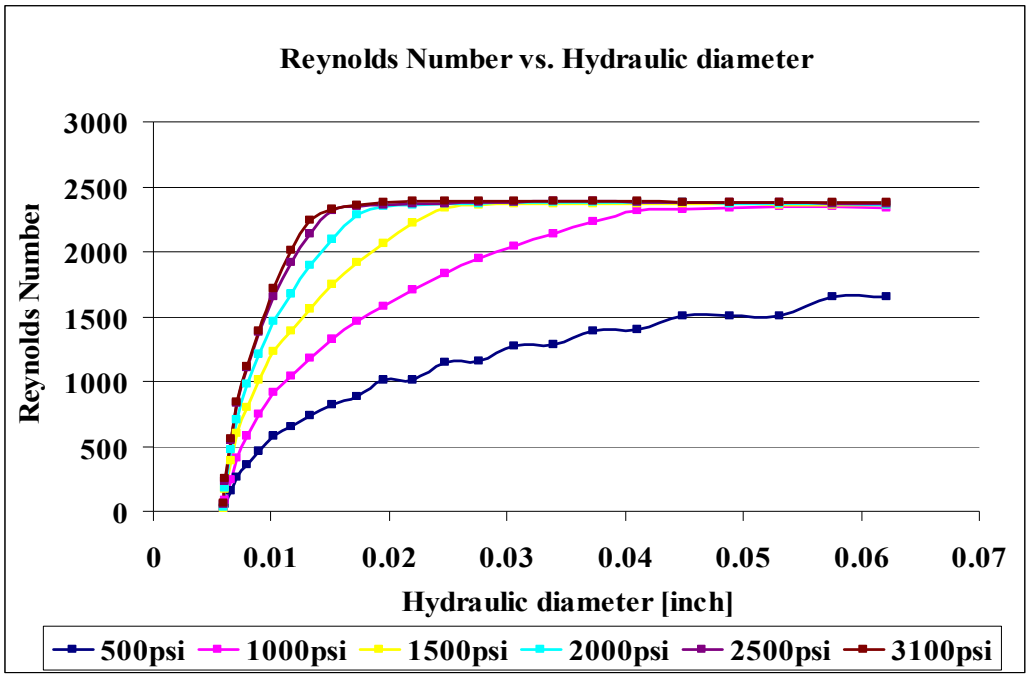

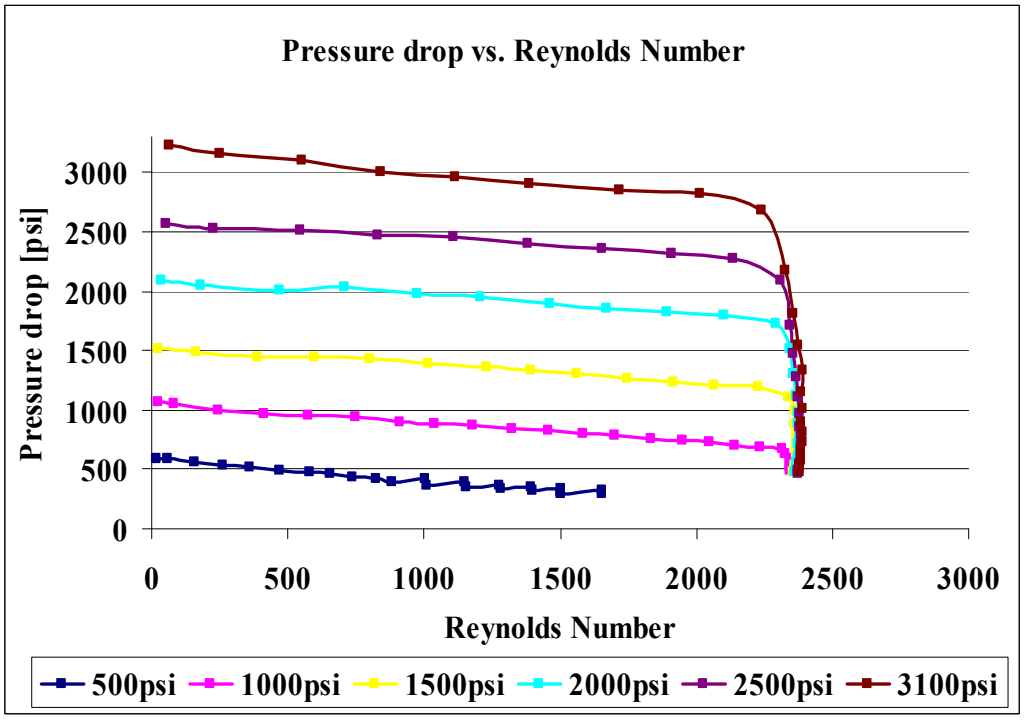

Figure 72: Plots of the flow Reynolds number at different spool stops versus the hydraulic diameter and the pressure drop respectively. (test 2)

As shown in Figure 71, the mean velocity of the flow starts to decrease at earlier spool stop as the applied pressure increases, since the flow rate is reaching its limit of 18 GPM faster. And so, there is no significant increase in the flow rate corresponding to significant increase to both opening area and hydraulic. In addition, Reynolds number reaches a finite value at earlier spool stop as the applied pressure increases due to decrease in the mean velocity accompanied with increase in the hydraulic diameter at the same spool stop, as shown in Figure 72.

As shown in Figure 73, the Mach numbers are less than 0.3 for all the spool stops of test 2. As a result, the flow is incompressible for this test.

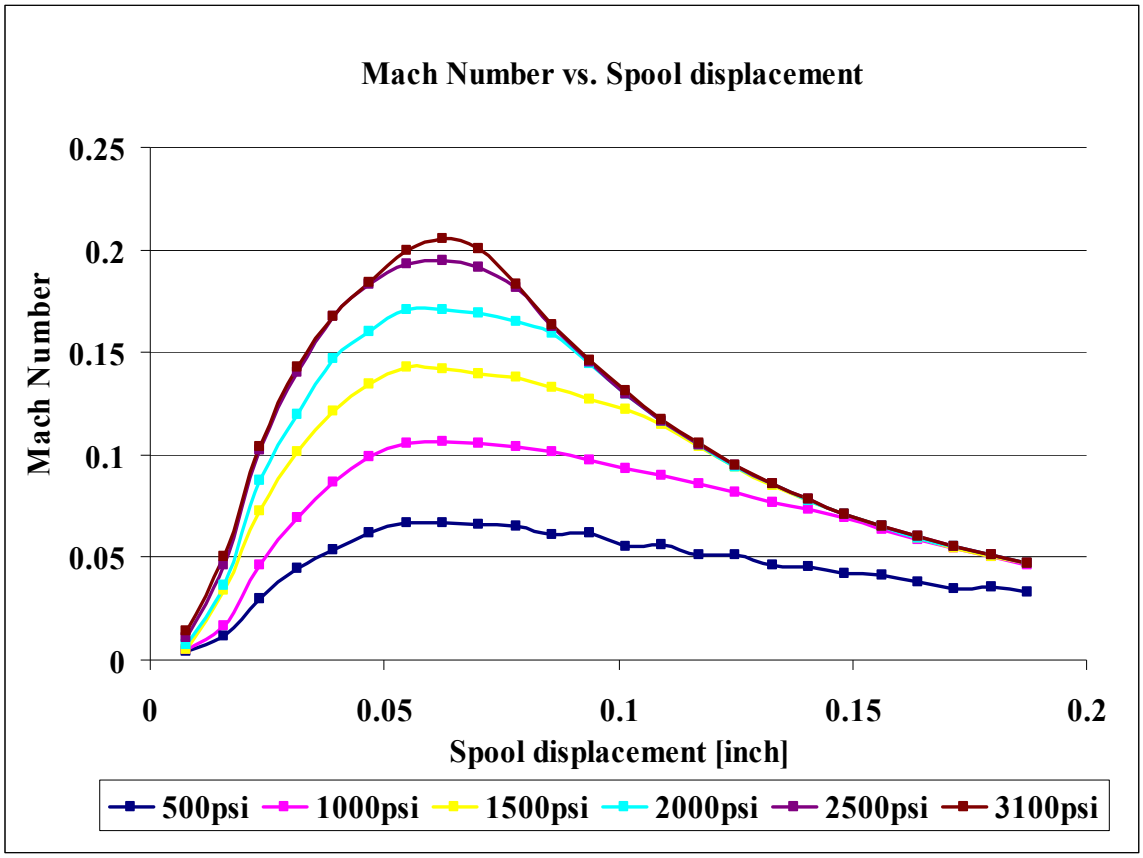

Figure 73: Plot of Mach number versus spool displacement of test 2.

Experimental Results for Spool #2/Curved Side

After the experimental testing for spool #2/curved side was completed, the text file associated with each sub-experiment (six sub-experiments in total with different pressure applied) was imported in Microsoft Excel to generate columns of flow rate, pressure drop and valve position values. The total number of spool stops was 24 for each sub-experiment, with each stop corresponding to one quarter turn of both the trailing and the lead wheel of the test valve. The results of test 3 are shown in Figure 74, 75 and 76.

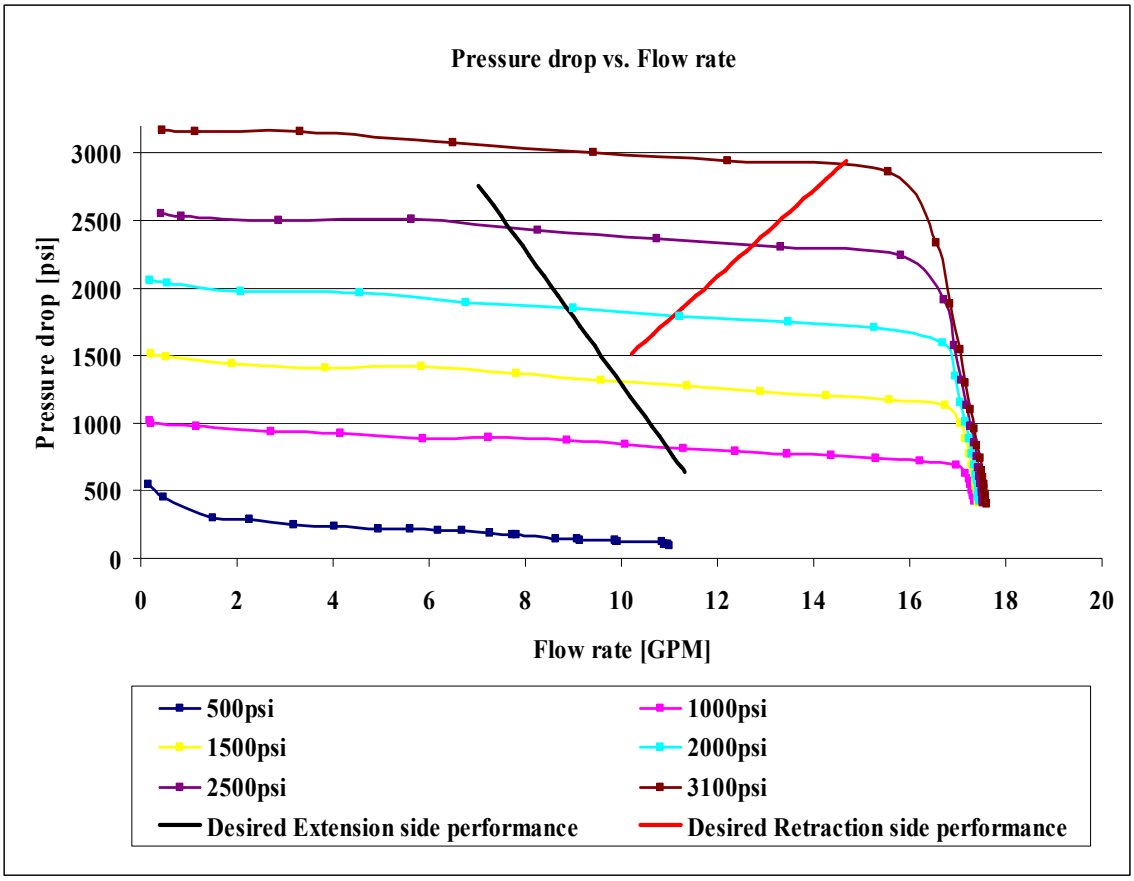

Figure 74: A plot of the pressure drop versus flow rate for the six sub-experiments of test 3. (The results were overlaid with the desired linear performance of the hydraulic damper for comparison).

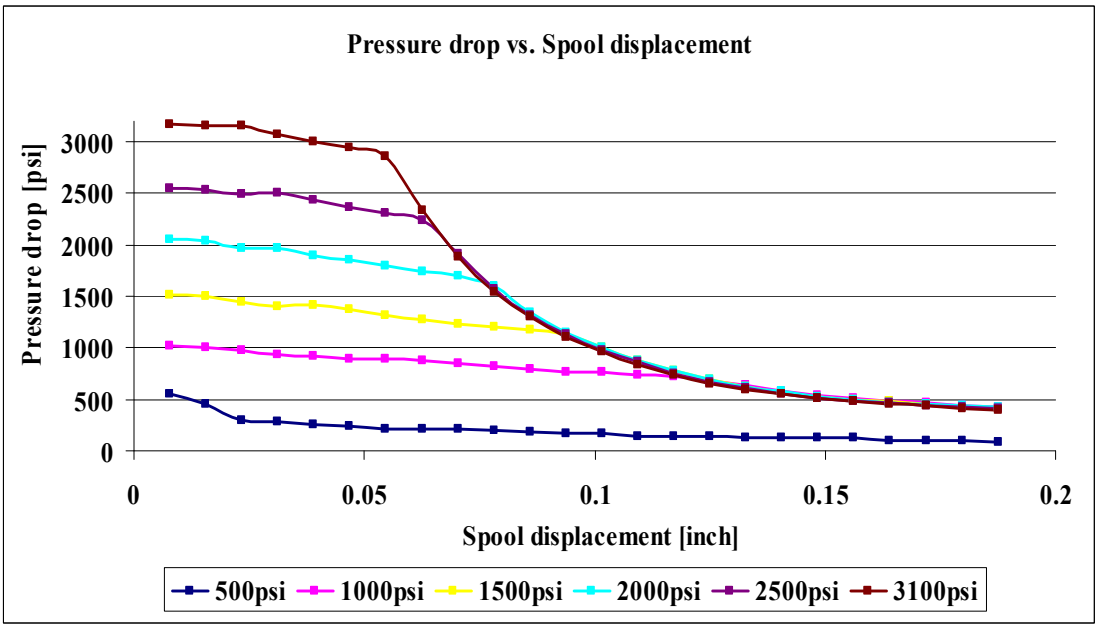

Figure 75: A plot of the pressure drop versus spool displacement for the six sub-experiments of test 3.

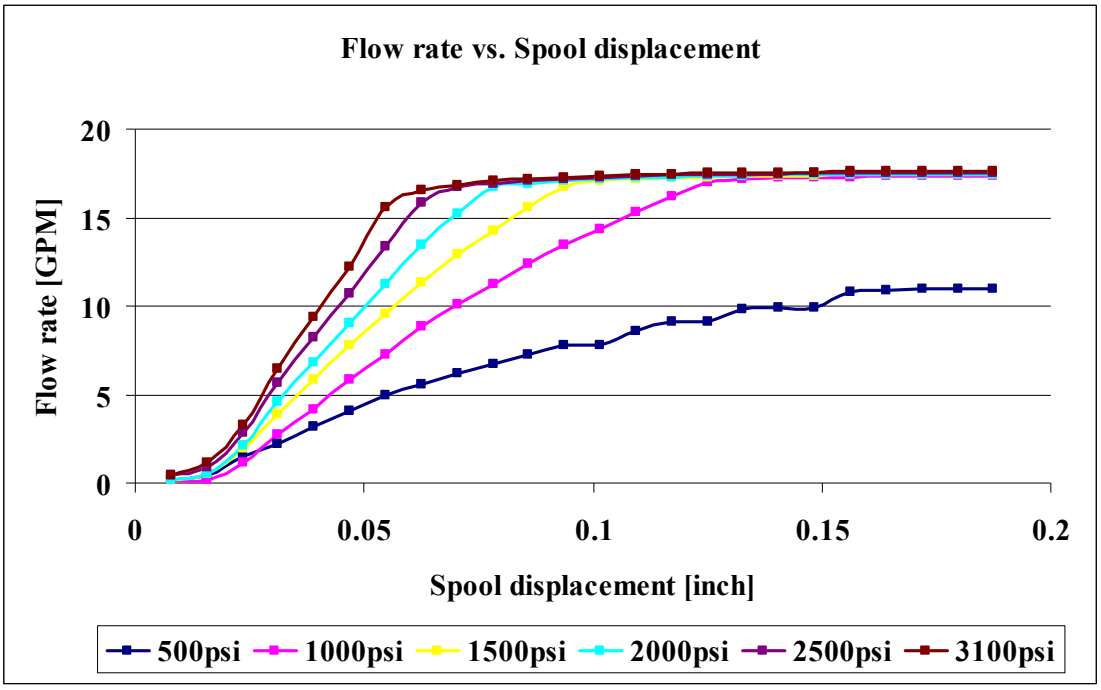

Figure 76: A plot of the flow rate versus spool displacement for the six sub-experiments of test 3.

It is important to mention that the applied pressure in each sub-experiment of test 3 was not constant throughout making the sub-experiment due to the influence of the test valve opening. In addition, the applied pressure performance lines for the six sub-experiments of test 3 were found to have the same trend as the pressure drop performance lines and with small differences between both values.

The total average percentage difference between the applied pressure and the pressure drop values for the six sub-experiments of test 3 was found to be 12.78%. The pressure drop performance lines start to decline as the flow rate approaches its maximum value of 18 GPM as shown Figure 74, since the hydraulic power unit can not sustain the applied pressure settings.

Furthermore, the pressure drop performance line with higher starting applied pressure will start to decrease at earlier spool stops as the spool displaces from the fully closed position as shown in Figure 75.

In Figure 76, the flow rate is almost linear with the spool's position for all the six sub-experiments as was not predicted for spool #2/curved side since it does not have a straight cut as in spool #1. The cause behind this behavior is that the clearance area, which is a straight cut opening area, influences the flow at earlier spool stops.

In order to characterize the flow at each spool stop of test 3, constant spool stop's performance lines of pressure drop and flow rates were generated in Figure 77.

As shown in Figure 77, the pressure drop increases as the flow rate increases at the same spool stop. In addition, the slope of the performance line decreases as the spool opening increases. In other words, a larger opening area needs more flow rate in order to cause the same pressure drop as a smaller opening area.

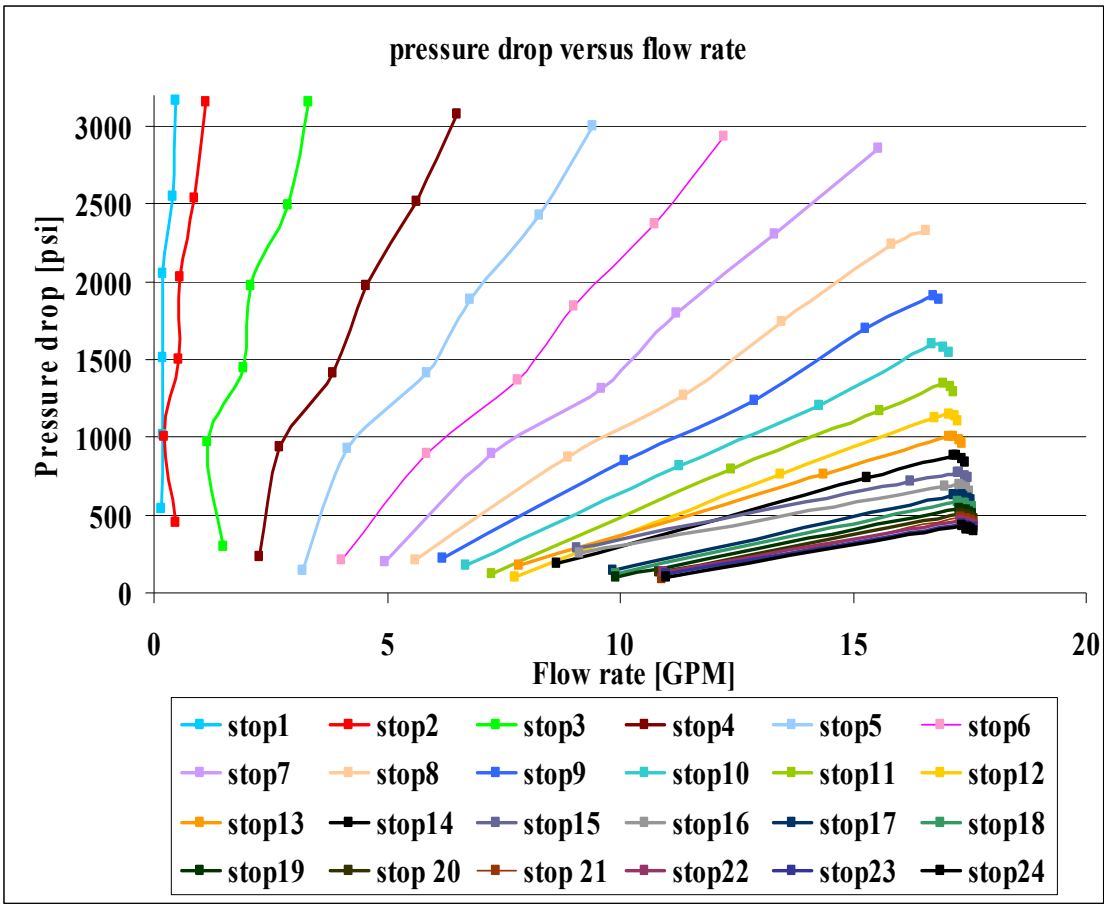

Figure 77: A plot of pressure drop vs. flow rate at each spool stop of test 3.

The opening area (A_{spool}) along with the wetted perimeter (P_{spool}) values at each spool stop of spool #2/ curved side are listed in Table 17.

Table 17: The opening area (A_{spool}) along with the wetted perimeter (P_{spool}) values at each spool stop of spool #2/curved side.

Spool- stop Number	**Spool displacement (x) [inch]**	**Opening area (A_{spool}) [inch^2]**	**Wetted perimeter (P_{spool}) [inch]**
1	0.007813	0.000067	0.026164
2	0.015625	0.000251	0.049606
3	0.023438	0.000533	0.071334
4	0.031250	0.000898	0.091862
5	0.039063	0.001337	0.111494
6	0.046875	0.001842	0.130433
7	0.054688	0.002405	0.148813
8	0.062500	0.003021	0.166739
9	0.070313	0.003684	0.184286
10	0.078125	0.004391	0.201514
11	0.085938	0.005137	0.218469
12	0.093750	0.005918	0.235194
13	0.101563	0.006731	0.251720
14	0.109375	0.007572	0.268074
15	0.117188	0.008439	0.284281
16	0.125000	0.009328	0.300362
17	0.132813	0.010237	0.316335
18	0.140625	0.011164	0.332218
19	0.148438	0.012104	0.348026
20	0.156250	0.013057	0.363772
21	0.164063	0.014019	0.379469
22	0.171875	0.014988	0.395133
23	0.179688	0.015962	0.410772
24	0.187500	0.016937	0.426376

The opening area (A_{spool}) along with the wetted perimeter (P_{spool}) values at each spool stop of spool #2/curved side were calculated from the CAD model of spool #2, as shown in Figure 78.

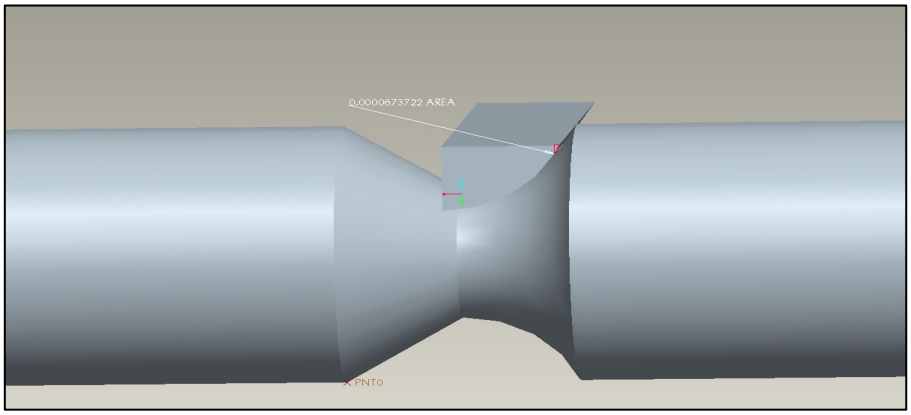

(a)

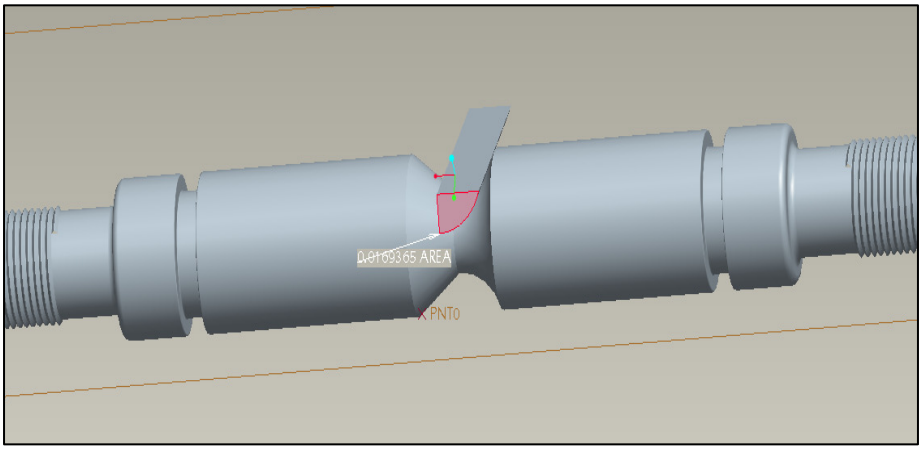

(b)

Figure 78: CAD model of spool #2/curved side that was used to calculate the opening area (A_{spool}) and the wetted perimeter (P_{spool}) at each spool stop. a) area calculation at the first spool stop b) area calculation at the twenty fourth spool stop.

According to the testing procedure shown in Figure 79, the flow was not completely internal, in other words, the flow was not completely bounded by solid surfaces when it passed the spool land region. Thus, it was assumed that the flow passes the spool land region was a flow inside a hydraulic channel for which the wetted perimeter (P_{spool}) will not be the whole circumference of the aforementioned opening areas in Figure 78.

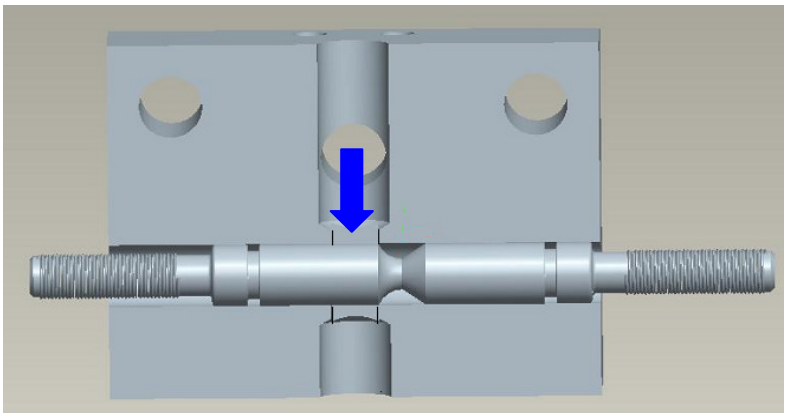

(a)

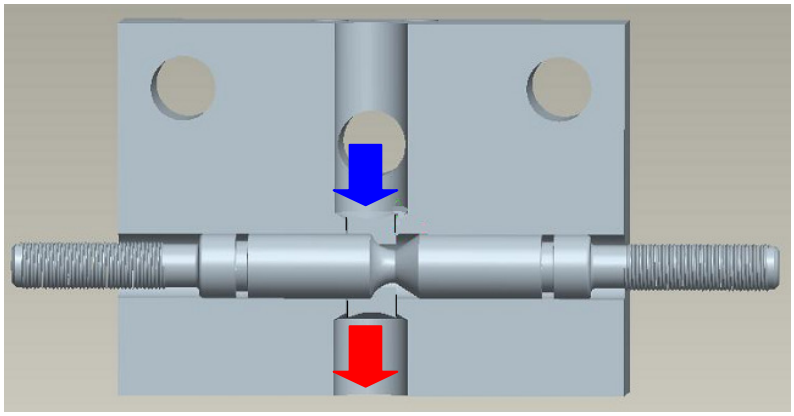

(b)

Figure 79: CAD model of the test valve (Bottom view) shows the location of spool #2/ curved side inside the manifold at a) fully closed position b) at 24 spool stop position.

The results of the calculations for mean velocities, Reynolds numbers and Mach numbers of test 3 are shown below:

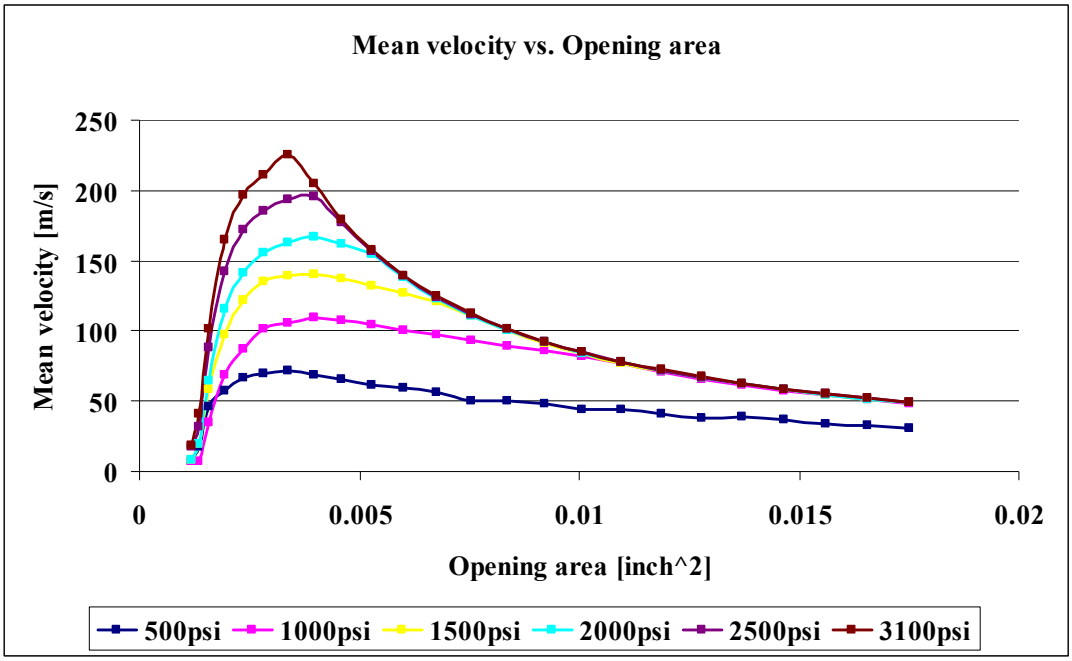

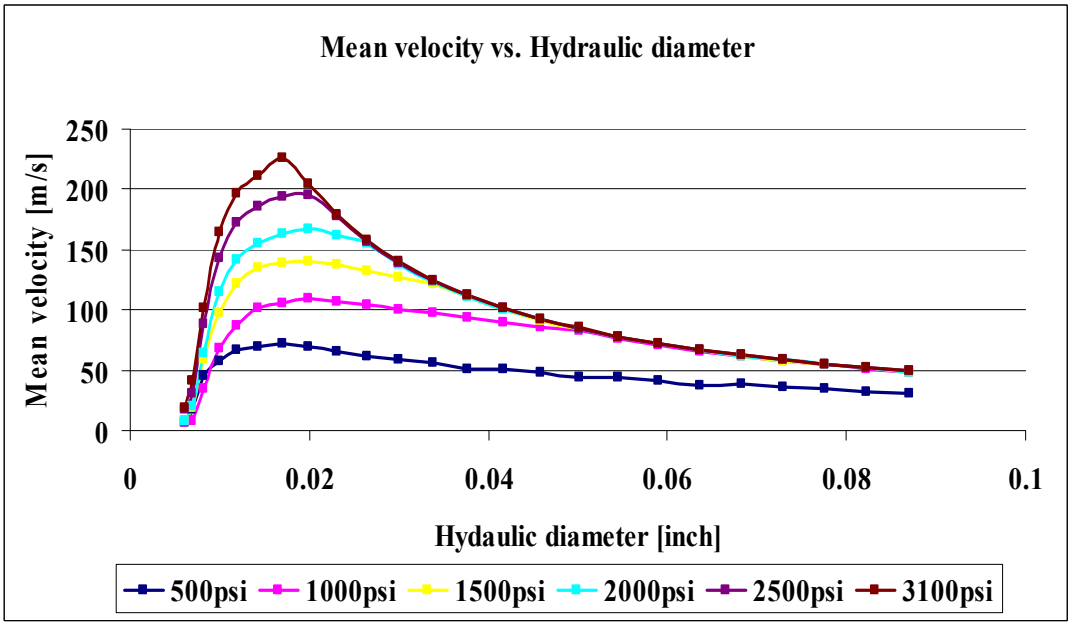

Figure 80: Plots of the flow mean velocity at different spool stops versus the opening area and the hydraulic diameter respectively. (test 3)

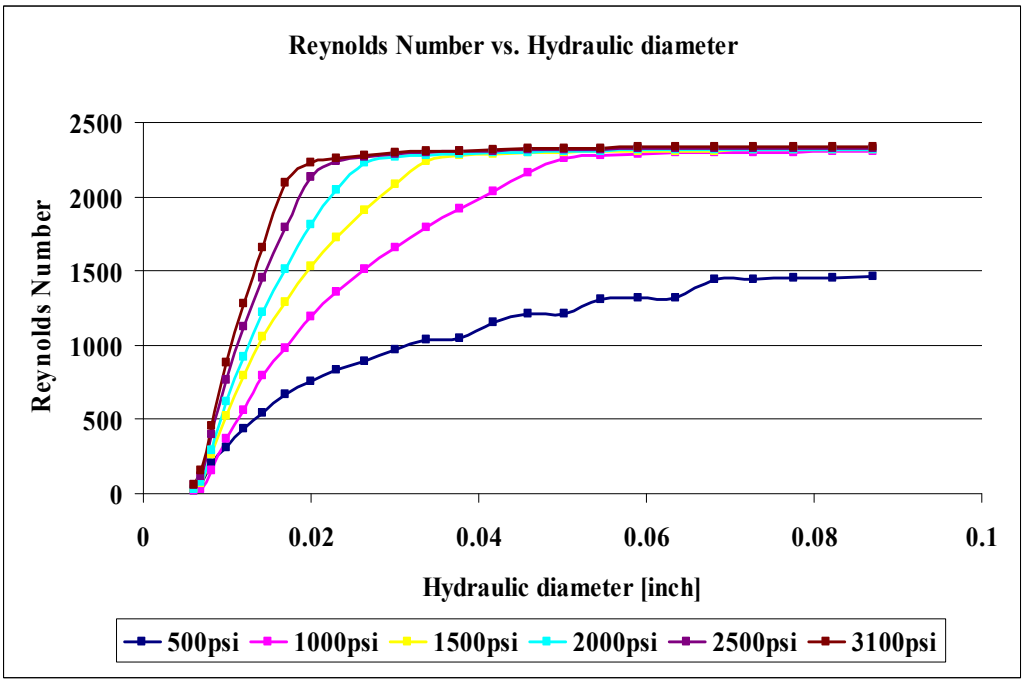

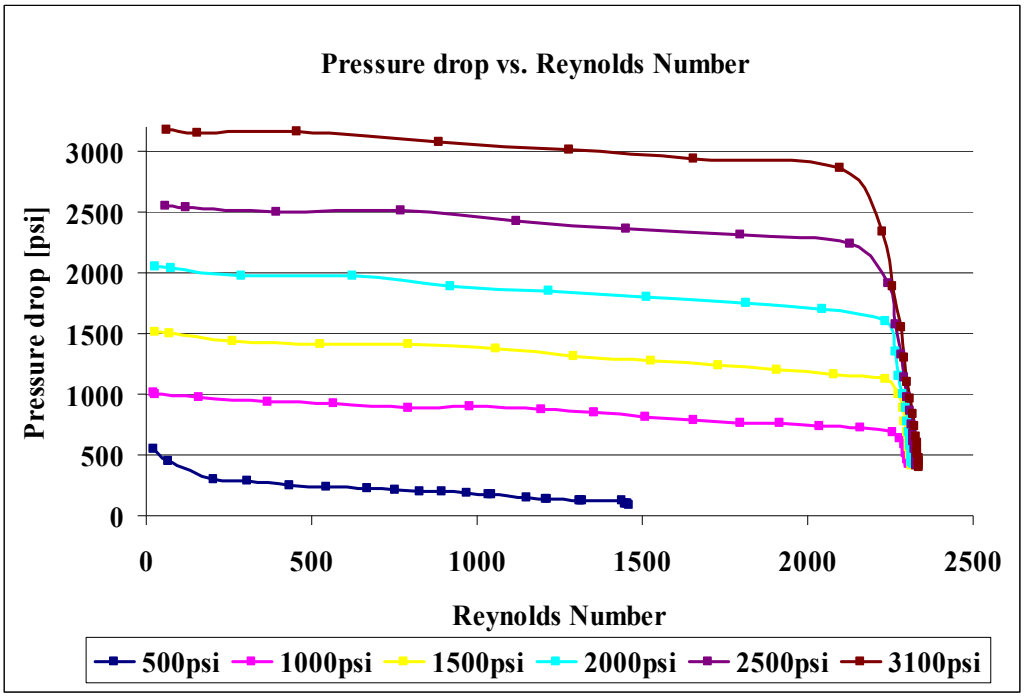

Figure 81: Plots of the flow Reynolds number at different spool stops versus the hydraulic diameter and the pressure drop respectively. (test 3)

As shown in Figure 80, the mean velocity of the flow starts to decrease at earlier spool stop as the applied pressure increases, since the flow rate is reaching its limit of 18 GPM faster. And so, there is no significant increase in the flow rate corresponding to significant increase to both opening area and hydraulic diameter. In addition, Reynolds number reaches a finite value at earlier spool stop as the applied pressure increases due to decrease in the mean velocity accompanied with increase in the hydraulic diameter at the same spool stop, as shown in Figure 81.

As shown in Figure 82, the Mach numbers are less than 0.3 for all the spool stops of test 3. As a result, the flow is incompressible for this test.

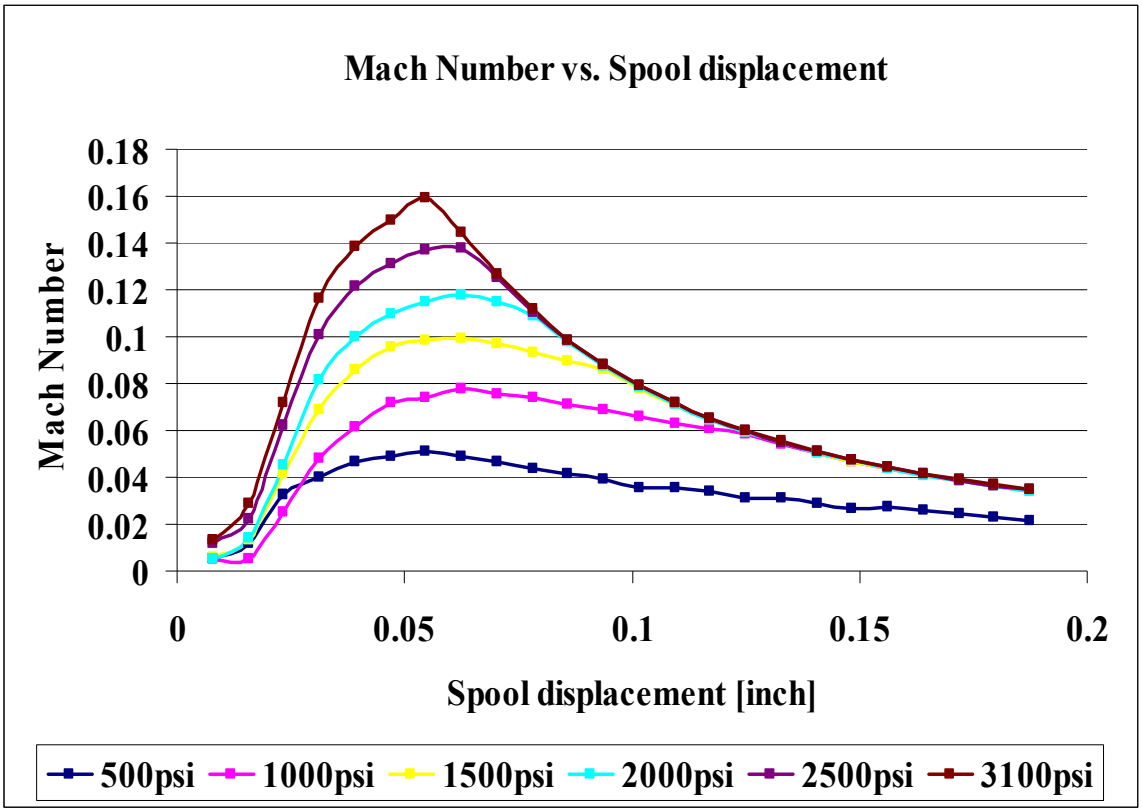

Figure 82: Plot of Mach number versus spool displacement of test 3.

Experimental Results for Spool #3/J-Side

After the experimental testing for spool #3/J-side was completed, the text file associated with each sub-experiment (six sub-experiments in total with different pressure applied) was imported in Microsoft Excel to generate columns of flow rate, pressure drop and valve position values. The total number of spool stops was 24 for each sub-experiment, with each stop corresponding to one quarter turn of both the trailing and the lead wheel of the test valve. The results of test 4 are shown Figure 83, 84 and 85.

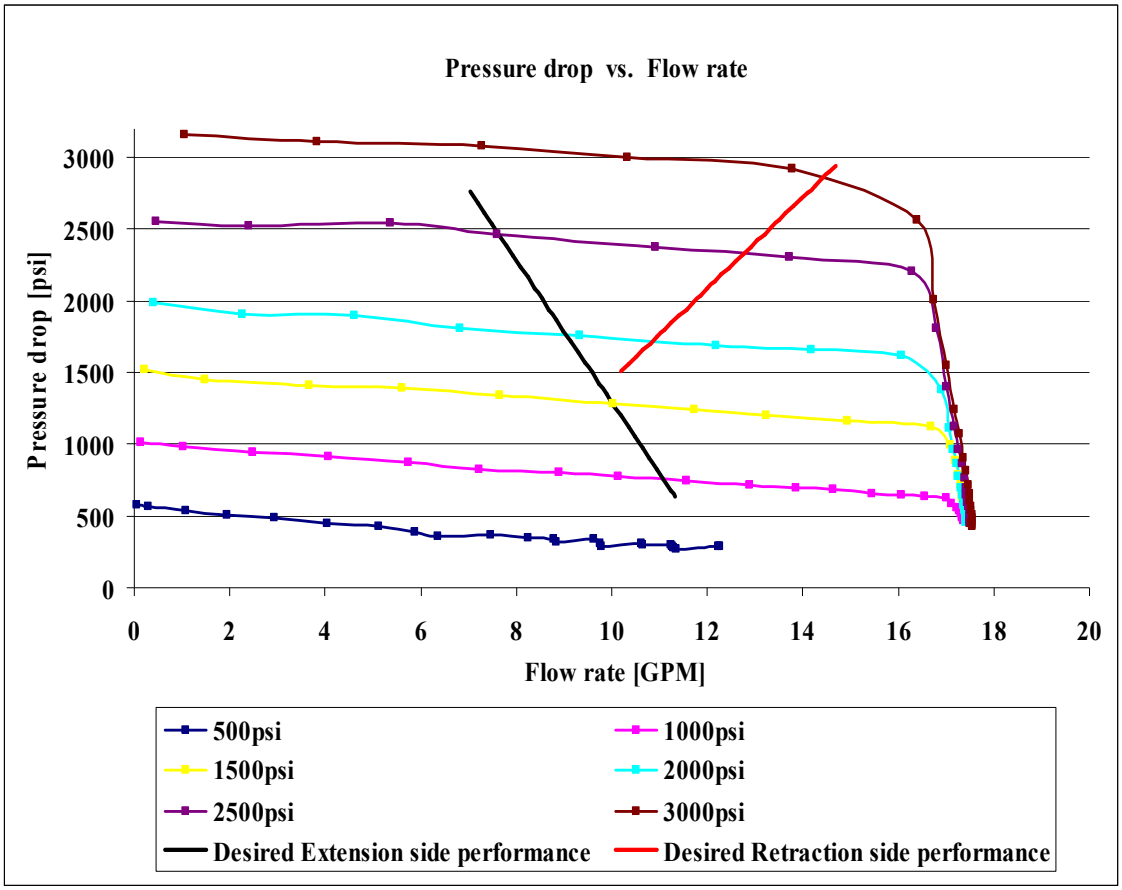

Figure 83: A plot of the pressure drop versus flow rate for the six sub-experiments of test 4. (The results were overlaid with the desired linear performance of the hydraulic damper for comparison).

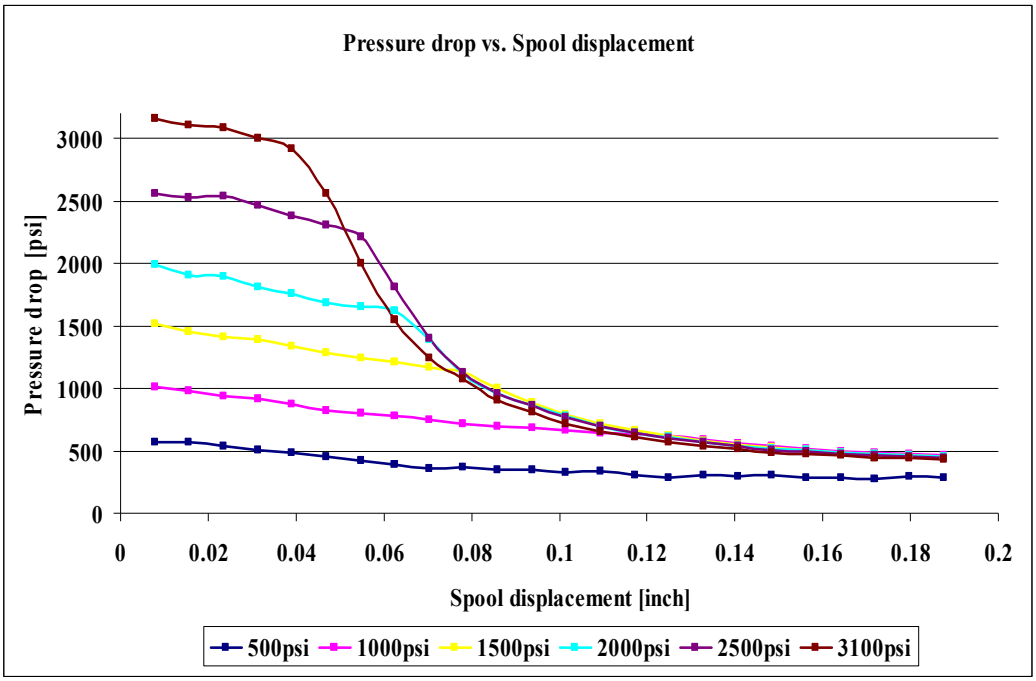

Figure 84: A plot of the pressure drop versus spool displacement for the six sub-experiments of test 4.

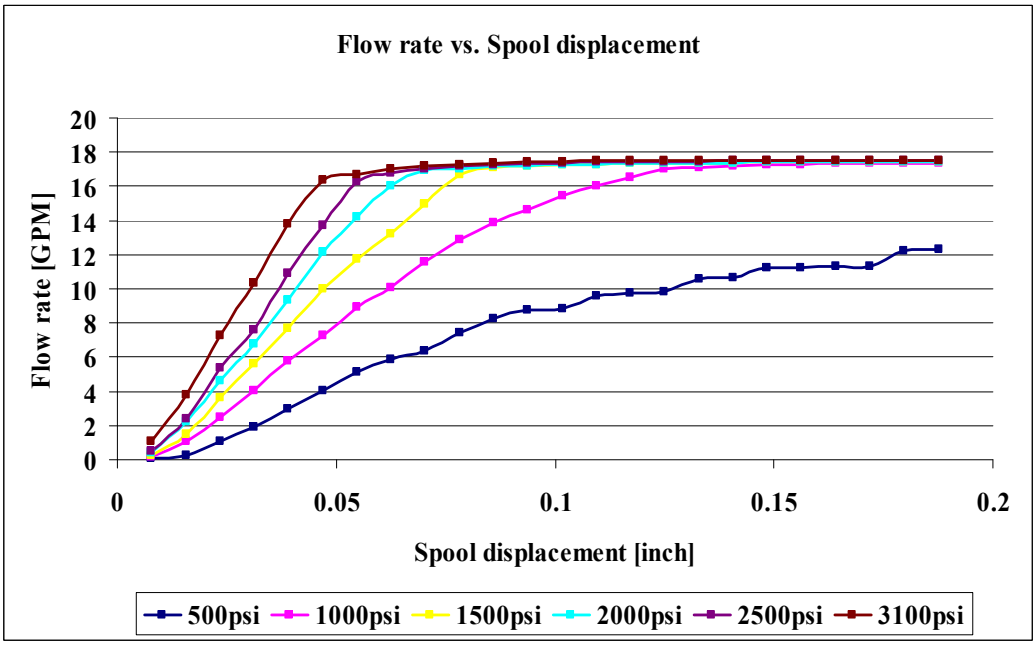

Figure 85: A plot of the flow rate versus spool displacement for the six sub-experiments of test 4.

It is important to mention that the applied pressure in each sub-experiment of test 4 was not constant throughout making the sub-experiment due to the influence of the test valve opening. In addition, the applied pressure performance lines for the six sub-experiments of test 4 were found to have the same trend as the pressure drop performance lines and with small differences between both values.

The total average percentage difference between the applied pressure and the pressure drop values for the six sub-experiments of test 4 was found to be 11.82%. The pressure drop performance lines start to decline as the flow rate approaches its maximum value of 18 GPM as shown in Figure 83, since the hydraulic power unit can not sustain the applied pressure settings.

Furthermore, the pressure drop performance line with higher starting applied pressure will start to decrease at earlier spool stops as the spool displaces from the fully closed position as shown in Figure 84.

In Figure 85, the flow rate is almost linear with the spool's position for all the six sub-experiments as was not predicted for spool #3/J-side since it does not have a straight cut as in spool #1. The cause behind this behavior is that the clearance area, which is a straight cut opening area, influences the flow at earlier spool stops.

In order to characterize the flow at each spool stop of test 4, constant spool stop's performance lines of pressure drop and flow rates were generated in Figure 86.

As shown in Figure 86, the pressure drop increases as the flow rate increases at the same spool stop. In addition, the slope of the performance line decreases as the spool opening increases. In other words, a larger opening area needs more flow rate in order to cause the same pressure drop as a smaller opening area.

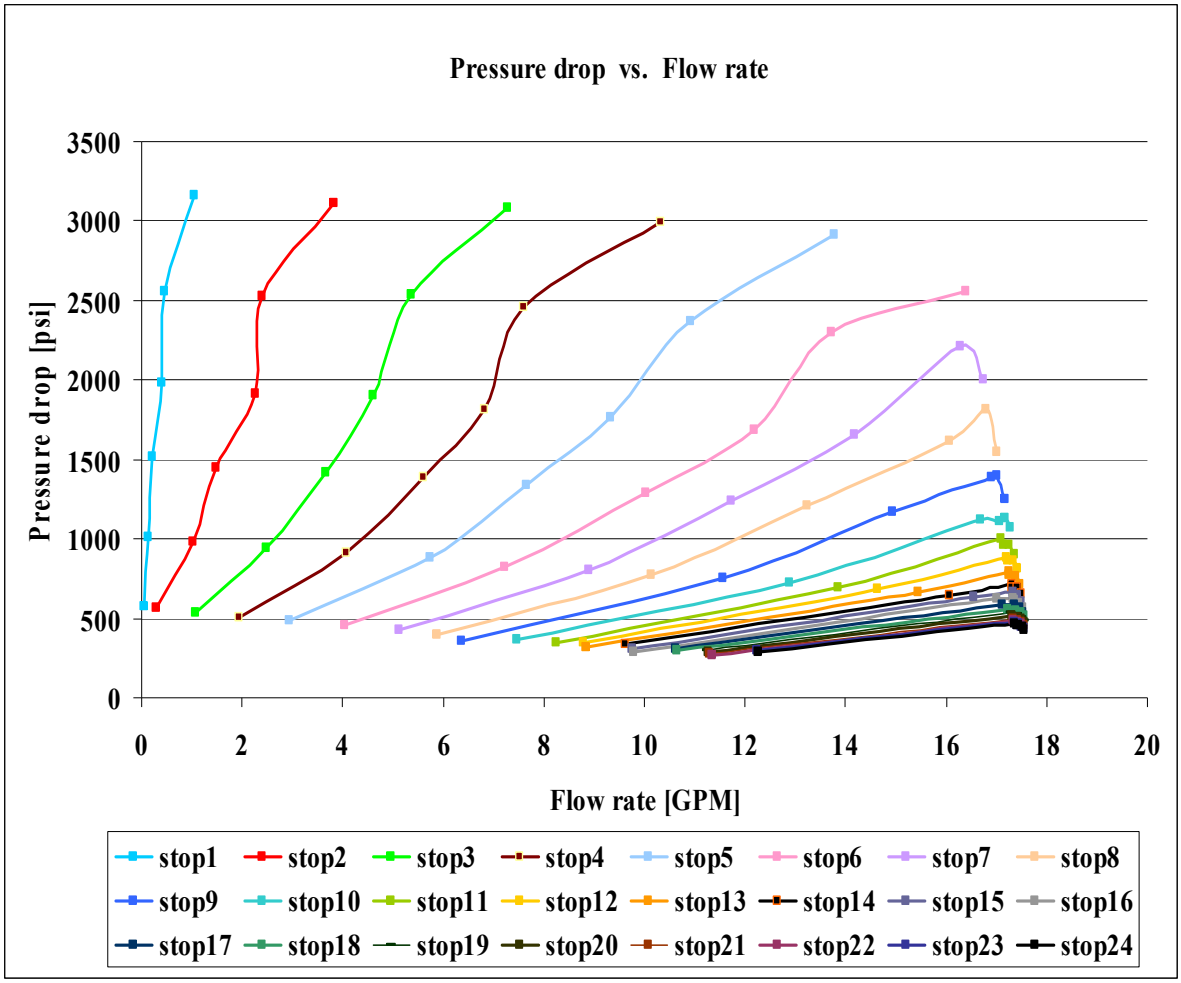

Figure 86: A plot of pressure drop vs. flow rate at each spool stop of test 4.

The opening area (A_{spool}) along with the wetted perimeter (P_{spool}) values at each spool stop of spool #3/ J-side are listed in Table 18.

Table 18: The opening area (A_{spool}) along with the wetted perimeter (P_{spool}) values at each spool stop of spool #3/J-side.

Spool- stop Number	**Spool displacement (x) [inch]**	**Opening area (A_{spool}) [inch^2]**	**Wetted perimeter (P_{spool}) [inch]**
1	0.007813	0.000192	0.057570
2	0.015625	0.000768	0.115140
3	0.023438	0.001706	0.158574
4	0.031250	0.002755	0.174799
5	0.039063	0.003796	0.192404
6	0.046875	0.004767	0.213239
7	0.054688	0.005657	0.234074
8	0.062500	0.006467	0.254867
9	0.070313	0.007217	0.271313
10	0.078125	0.007959	0.287097
11	0.085938	0.008701	0.302723
12	0.093750	0.009443	0.318349
13	0.101563	0.010186	0.333975
14	0.109375	0.010928	0.349601
15	0.117188	0.011670	0.365227
16	0.125000	0.012412	0.380853
17	0.132813	0.013155	0.396479
18	0.140625	0.013897	0.412105
19	0.148438	0.014639	0.427731
20	0.156250	0.015381	0.443357
21	0.164063	0.016123	0.458983
22	0.171875	0.016866	0.474609
23	0.179688	0.017608	0.490235
24	0.187500	0.018349	0.505849

The opening area (A_{spool}) along with the wetted perimeter (P_{spool}) values at each spool stop of spool #3/J-side were calculated from the CAD model of spool #3, as shown in Figure 87.

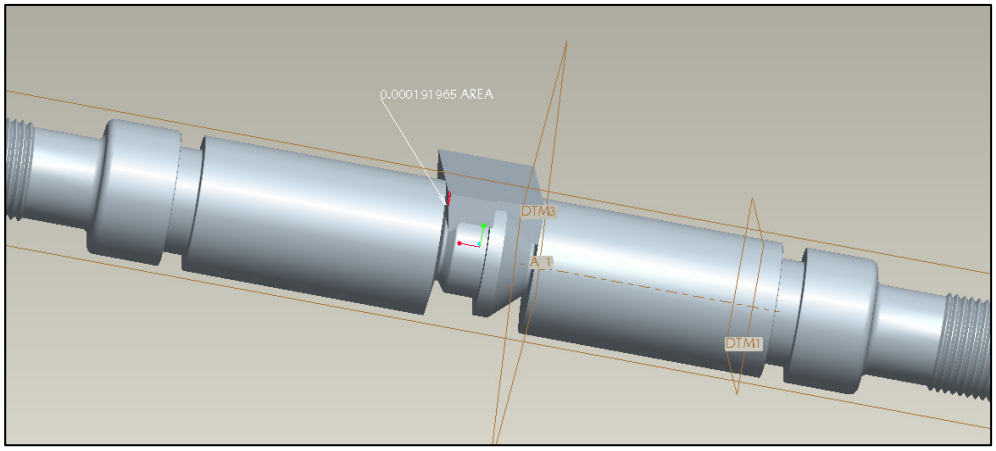

(a)

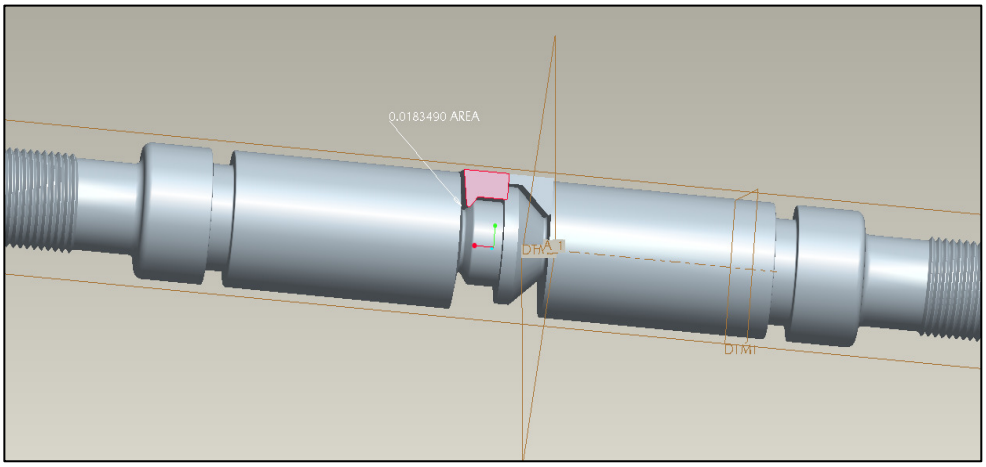

(b)

Figure 87: CAD model of spool #3/J-side that was used to calculate the opening area (A_{spool}) and the wetted perimeter (P_{spool}) at each spool stop. a) area calculation at the first spool stop b) area calculation at the twenty fourth spool stop.

According to the testing procedure shown in Figure 88, the flow was not completely internal, in other words, the flow was not completely bounded by solid surfaces when it passed the spool land region. Thus, it was assumed that the flow passes the spool land region was a flow inside a hydraulic channel for which the wetted perimeter (P_{spool}) will not be the whole circumference of the aforementioned opening areas in Figure 87.

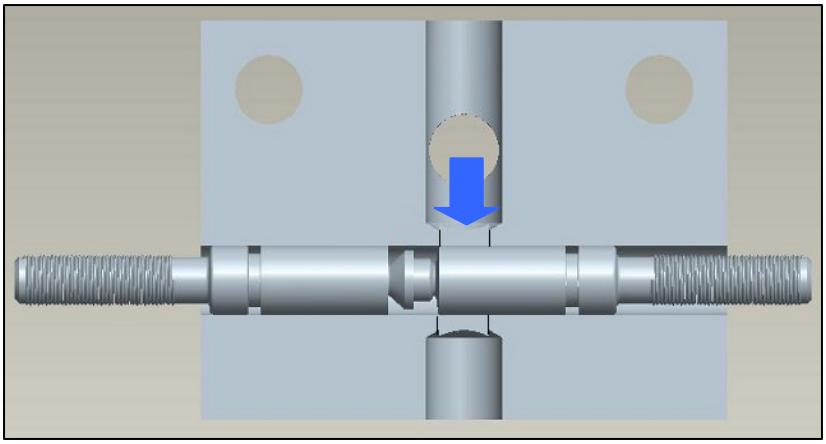

(a)

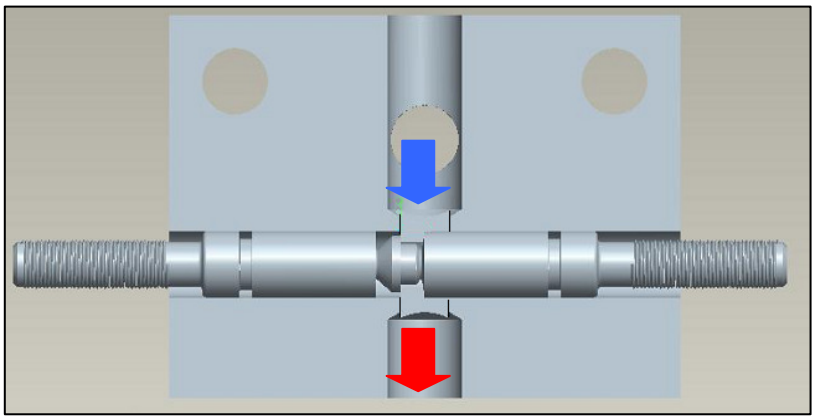

(b)

Figure 88: CAD model of the test valve (Bottom view) shows the location of spool #3/J-side inside the manifold at a) fully closed position b) at 24 spool stop position.

The results of the calculations for mean velocities, Reynolds numbers and Mach numbers of test 4 are shown below:

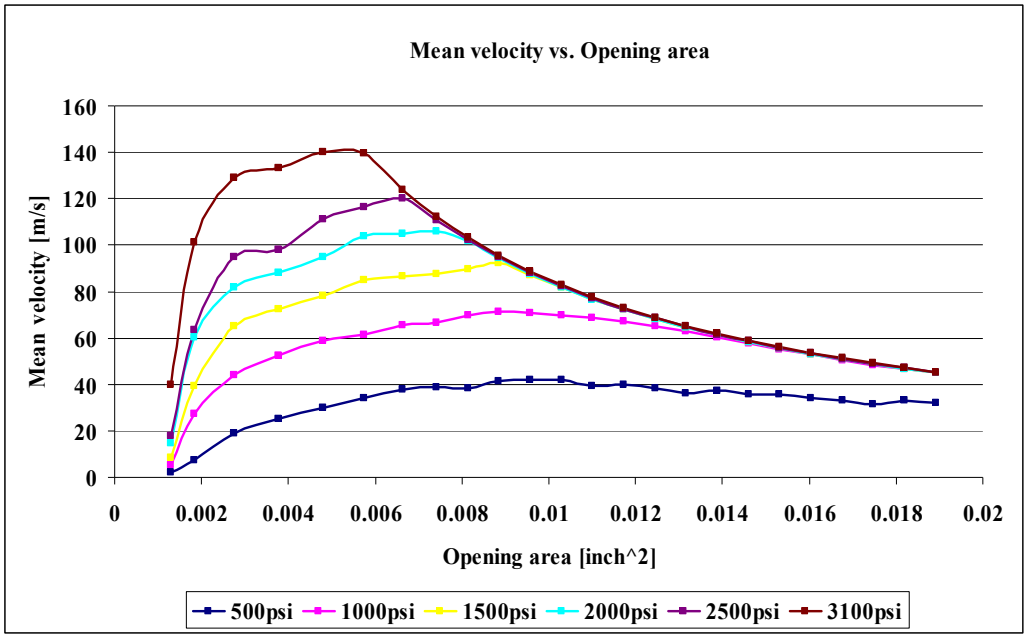

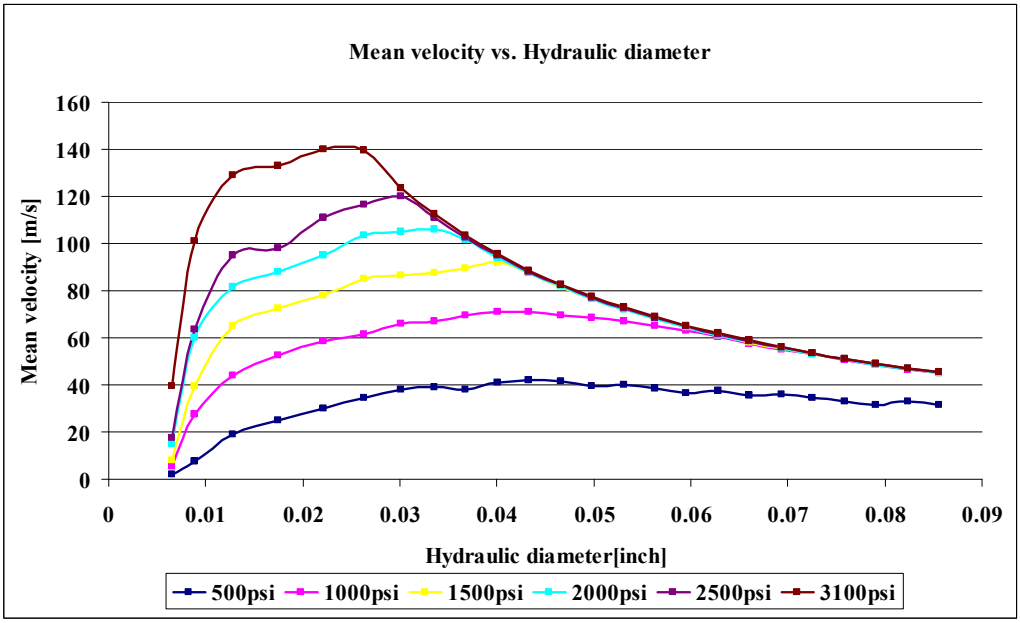

Figure 89: Plots of the flow mean velocity at different spool stops versus the opening area and the hydraulic diameter respectively. (test 4)

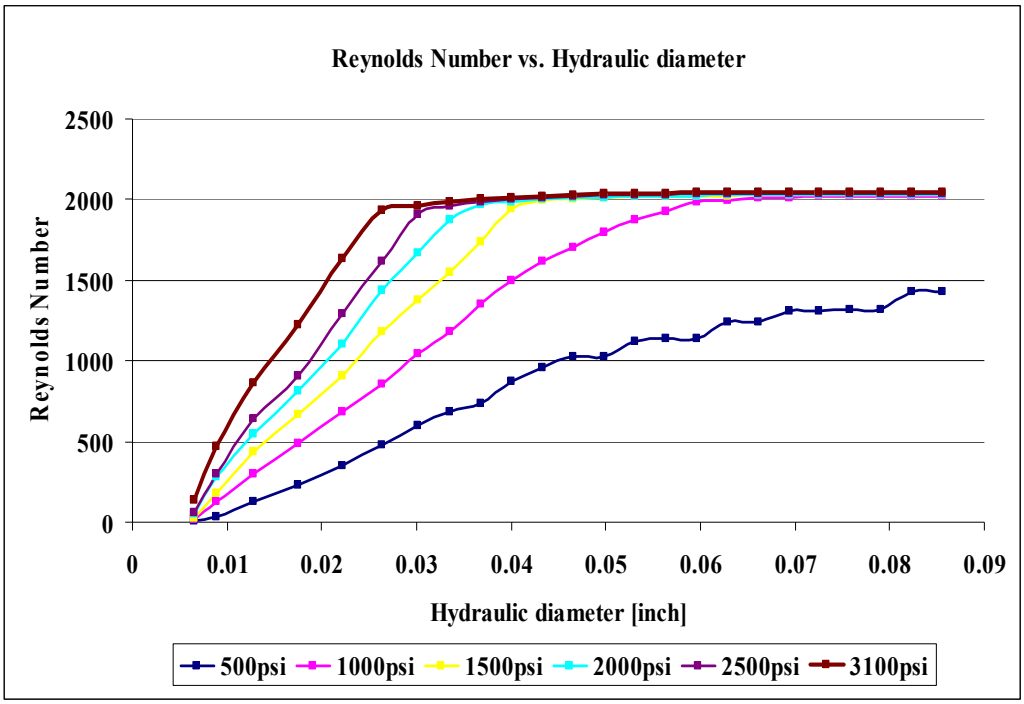

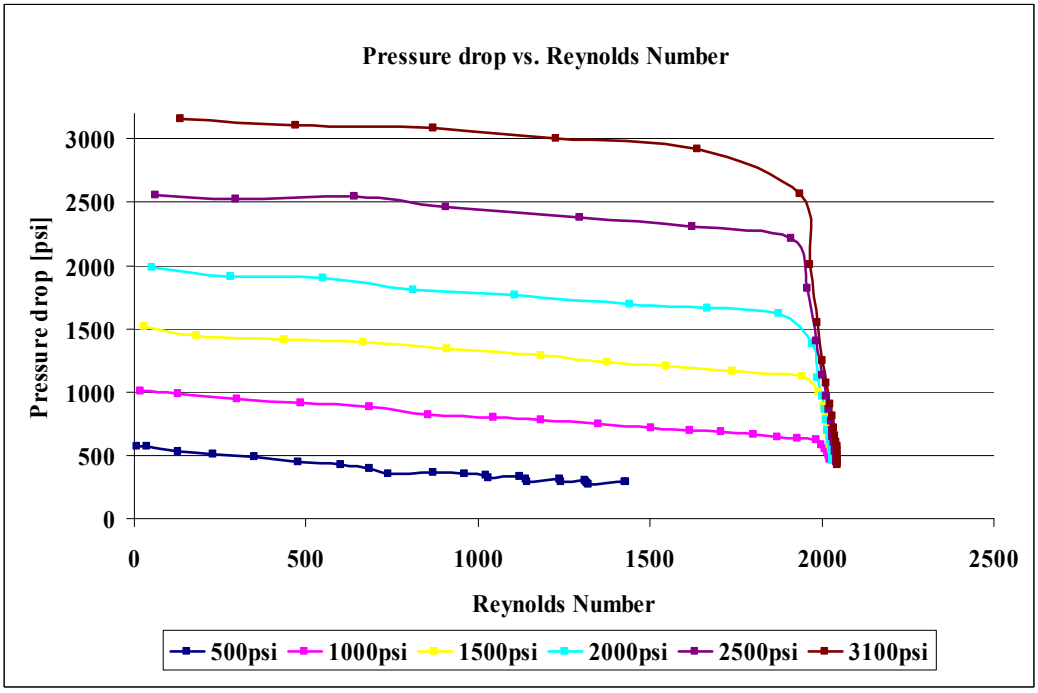

Figure 90: Plots of the flow Reynolds number at different spool stops versus the hydraulic diameter and the pressure drop respectively. (test 4)

As shown in Figure 89, the mean velocity of the flow starts to decrease at earlier spool stop as the applied pressure increases, since the flow rate is reaching its limit of 18 GPM faster. And so, there is no significant increase in the flow rate corresponding to significant increase to both opening area and hydraulic diameter. In addition, Reynolds number reaches a finite value at earlier spool stop as the applied pressure increases due to decrease in the mean velocity accompanied with increase in the hydraulic diameter at the same spool stop, as shown in Figure 90.

As shown in Figure 91, the Mach numbers are less than 0.3 for all the spool stops of test 4. As a result, the flow is incompressible for this test.

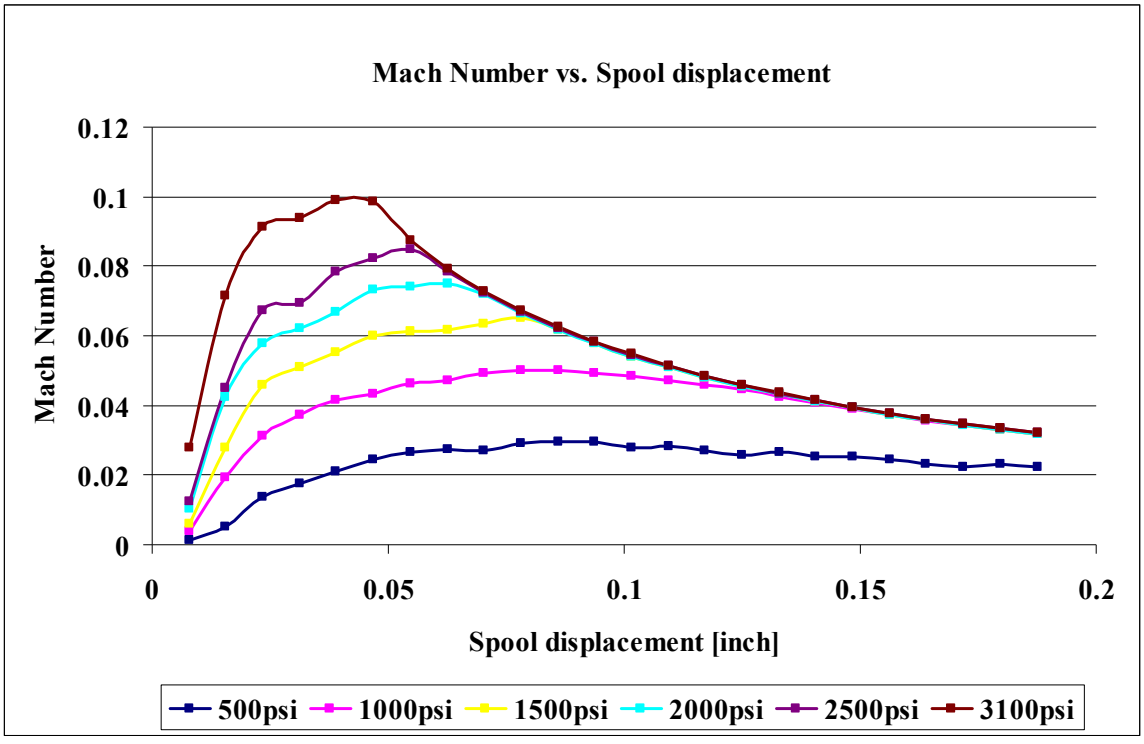

Figure 91: Plot of Mach number versus Spool displacement of test 4.

Experimental Results for Spool #3/ Slope side

After the experimental testing for spool #3/slope side was completed, the text file associated with each sub-experiment (six sub-experiments in total with different pressure applied) was imported in Microsoft Excel to generate columns of flow rate, pressure drop and valve position values. The total number of spool stops was 24 for each sub-experiment, with each stop corresponding to one quarter turn of both the trailing and the lead wheel of the test valve. The results of test 5 are shown in Figure 92, 93 and 94.

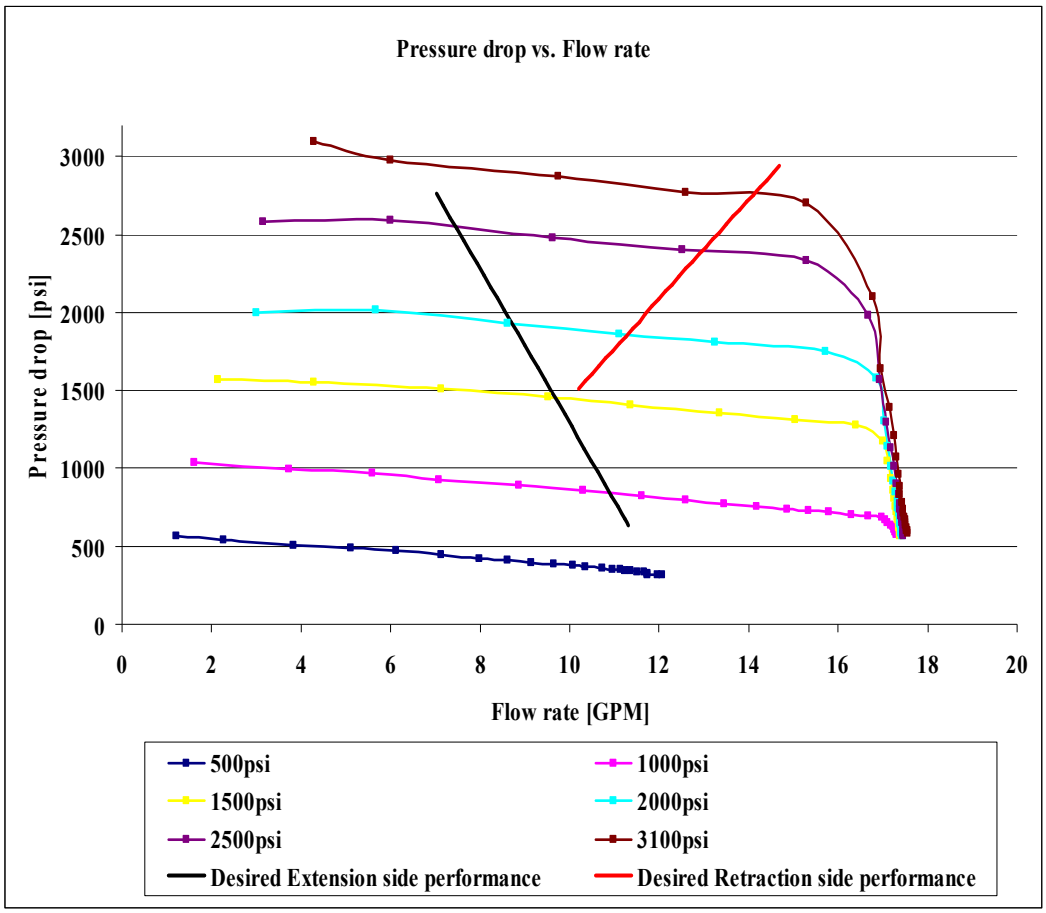

Figure 92: A plot of the pressure drop versus flow rate for the six sub-experiments of test 5. (The results were overlaid with the desired linear performance of the hydraulic damper for comparison).

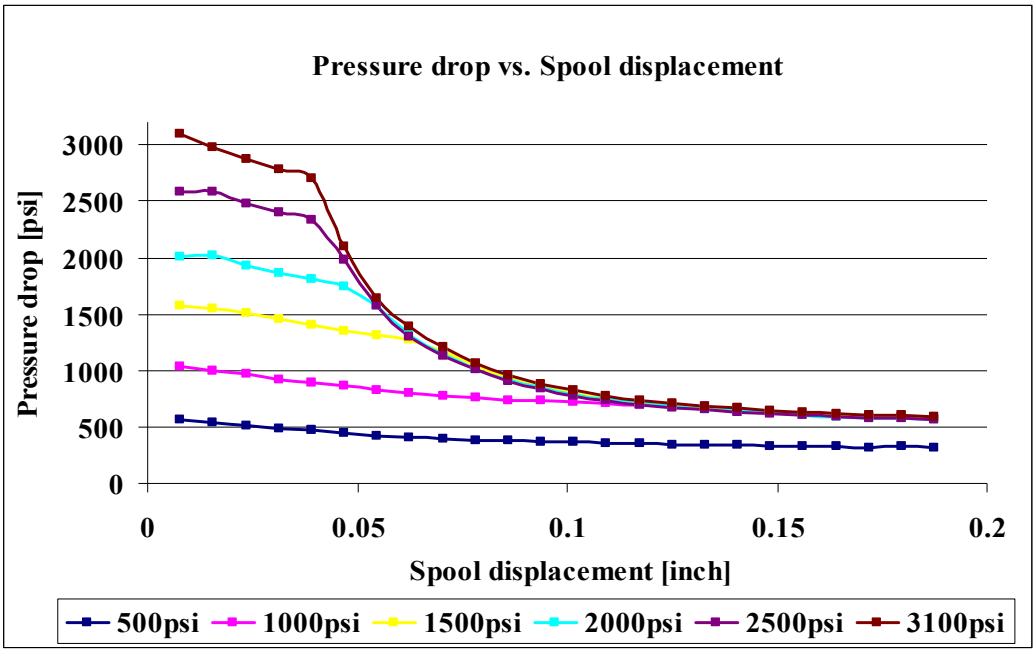

Figure 93: A plot of the pressure drop versus spool displacement for the six sub-experiments of test 5.

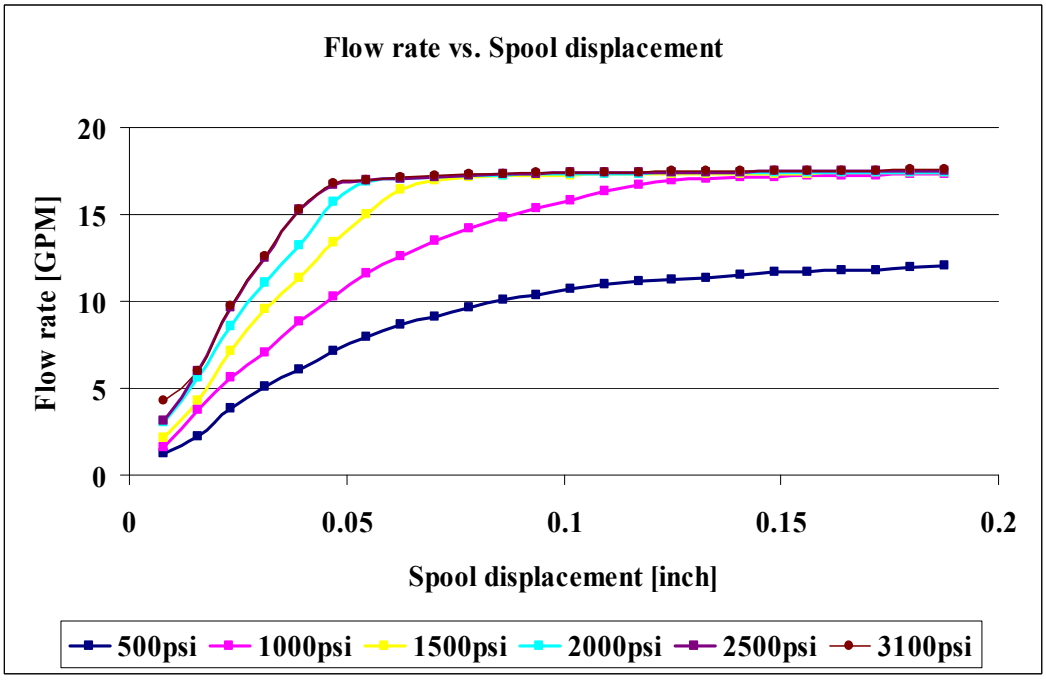

Figure 94: A plot of the flow rate versus spool displacement for the six sub-experiments of test 5.

It is important to mention that the applied pressure in each sub-experiment of test 5 was not constant throughout making the sub-experiment due to the influence of the test valve opening. In addition, the applied pressure performance lines for the six sub-experiments of test 5 were found to have the same trend as the pressure drop performance lines and with small differences between both values.

The total average percentage difference between the applied pressure and the pressure drop values for the six sub-experiments of test 5 was found to be 10.87%. The pressure drop performance lines start to decline as the flow rate approaches its maximum value of 18 GPM as shown in Figure 92, since the hydraulic power unit can not sustain the applied pressure settings.

Furthermore, the pressure drop performance line with higher starting applied pressure will start to decrease at earlier spool stops as the spool displaces from the fully closed position as shown in Figure 93.

In Figure 94, the flow rate is almost linear with the spool's position for all the six sub-experiments as was not predicted for spool #3/slope side since it does not have a straight cut as in spool #1. The cause behind this behavior is that the clearance area, which is a straight cut opening area, influences the flow at earlier spool stops.

In order to characterize the flow at each spool stop of test 5, constant spool stop's performance lines of pressure drop and flow rates were generated in Figure 95.

As shown in Figure 95, the pressure drop increases as the flow rate increases at the same spool stop. In addition, the slope of the performance line decreases as the spool opening increases. In other words, a larger opening area needs more flow rate in order to cause the same pressure drop as a smaller opening area.

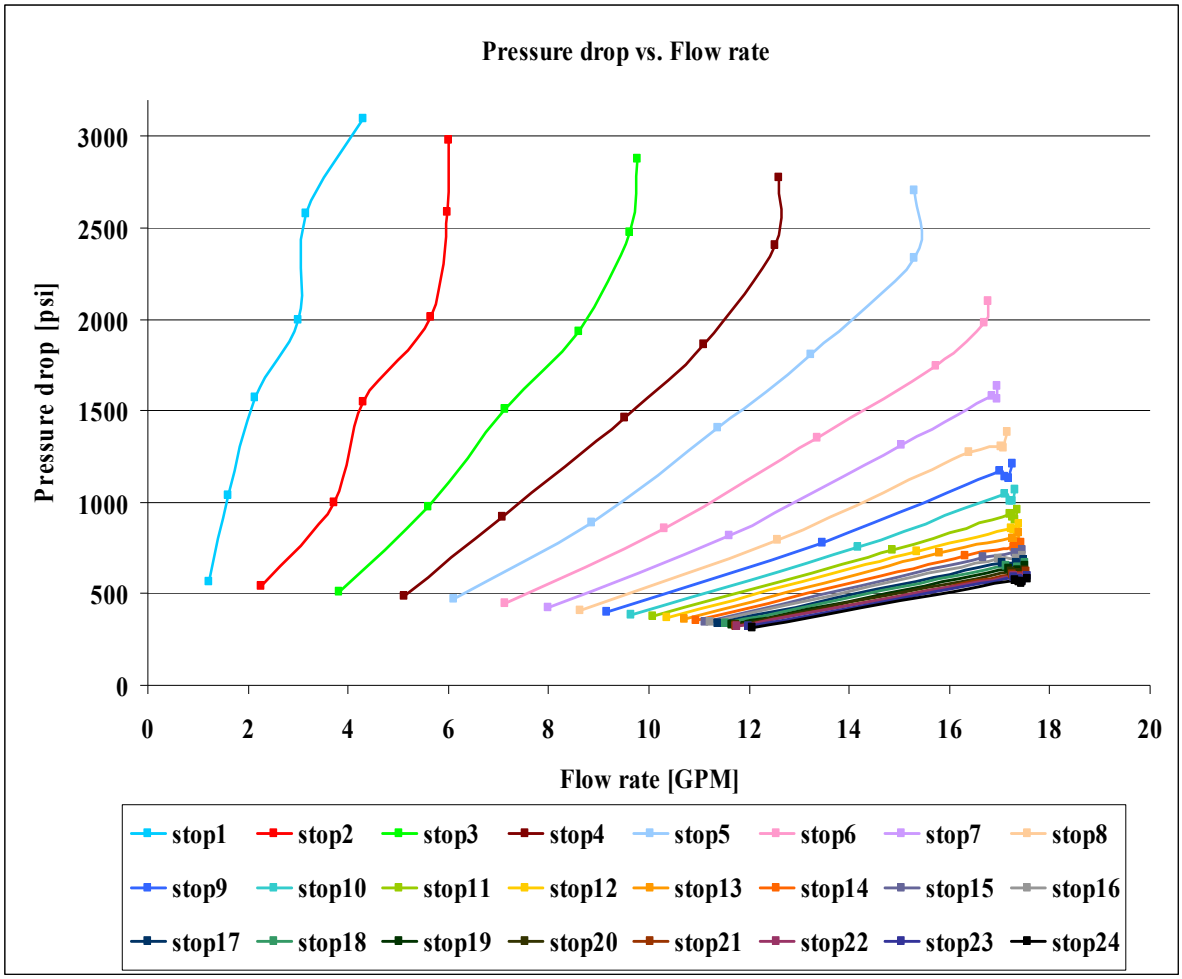

Figure 95: A plot of pressure drop vs. flow rate at each spool stop of test 5.

The opening area (A_{spool}) along with the wetted perimeter (P_{spool}) values at each spool stop of spool #3/ slope side are listed in Table 19.

Table 19: The opening area (A_{spool}) along with the wetted perimeter (P_{spool}) values at each spool stop of spool #3/slope side.

Spool- stop Number	**Spool displacement (x) [inch]**	**Opening area (A_{spool}) [inch^2]**	**Wetted perimeter (P_{spool}) [inch]**
1	0.007813	0.002135	0.883691
2	0.015625	0.003163	0.884060
3	0.023438	0.004155	0.886543
4	0.031250	0.005094	0.889084
5	0.039063	0.005979	0.891625
6	0.046875	0.006812	0.894166
7	0.054688	0.007592	0.896708
8	0.062500	0.008318	0.899249
9	0.070313	0.008992	0.901790
10	0.078125	0.009612	0.904332
11	0.085938	0.010180	0.906874
12	0.093750	0.010694	0.909415
13	0.101563	0.011155	0.911957
14	0.109375	0.011563	0.914498
15	0.117188	0.011918	0.917039
16	0.125000	0.012220	0.919580
17	0.132813	0.012476	0.920798
18	0.140625	0.012726	0.920799
19	0.148438	0.012976	0.920800
20	0.156250	0.013226	0.920801
21	0.164063	0.013476	0.920802
22	0.171875	0.013726	0.920803
23	0.179688	0.013976	0.920804
24	0.187500	0.014226	0.920793

The opening area (A_{spool}) along with the wetted perimeter (P_{spool}) values at each spool stop of spool #3/ slope side were calculated from the CAD model of spool #3, as shown in Figure 96.

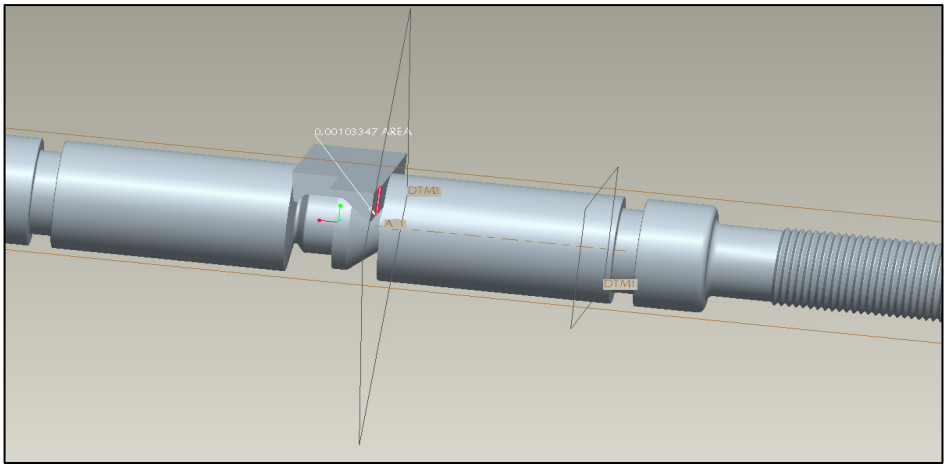

(a)

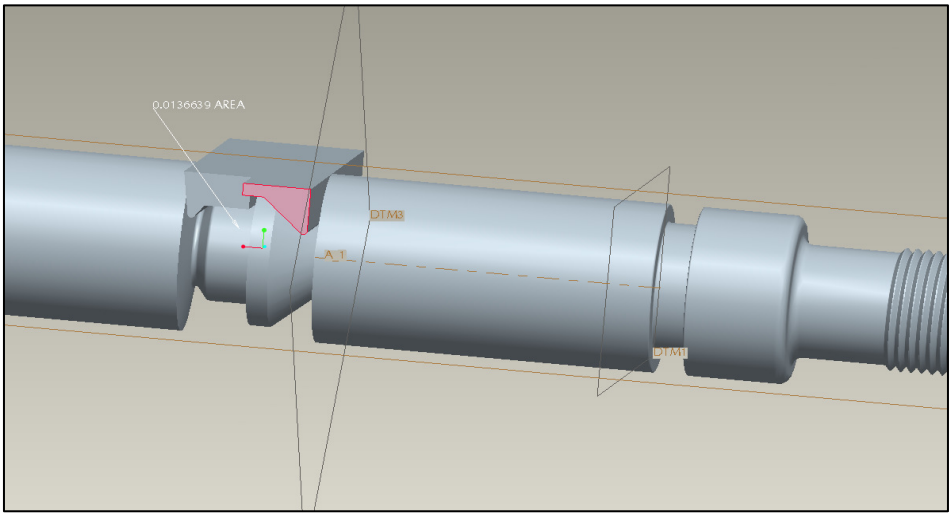

(b)

Figure 96: CAD model of spool #3/ slope side that was used to calculate the opening area (A_{spool}) and the wetted perimeter (P_{spool}) at each spool stop. a) area calculation at the first spool stop b) area calculation at the twenty fourth spool stop.

According to the testing procedure shown in Figure 97, the flow was not completely internal, in other words, the flow was not completely bounded by solid surfaces when it passed the spool land region. Thus, it was assumed that the flow passes the spool land region was a flow inside a hydraulic channel for which the wetted perimeter (P_{spool}) will not be the whole circumference of the aforementioned opening areas in Figure 96.

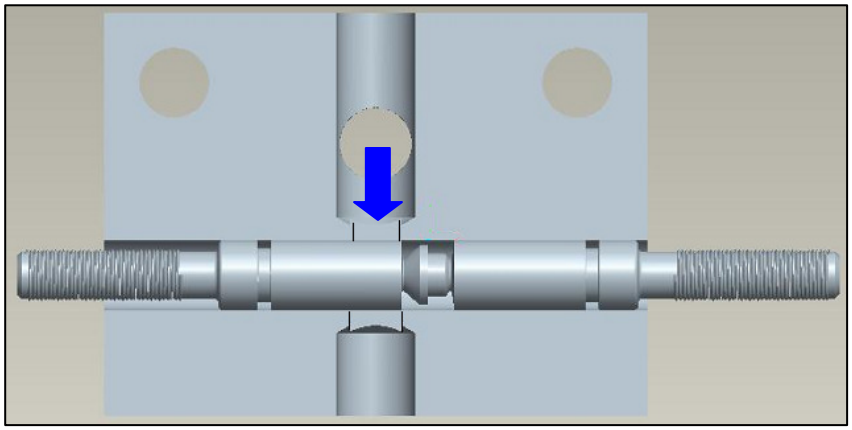

(a)

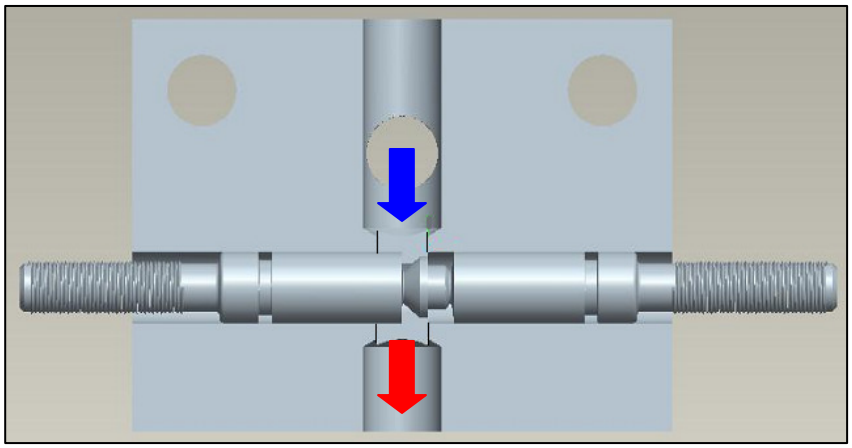

(b)

Figure 97: CAD model of the test valve (Bottom view) shows the location of spool #3/ slope side inside the manifold at a) fully closed position b) at 24 spool stop position.

The results of the calculations for mean velocities, Reynolds numbers and Mach numbers of test 5 are shown below:

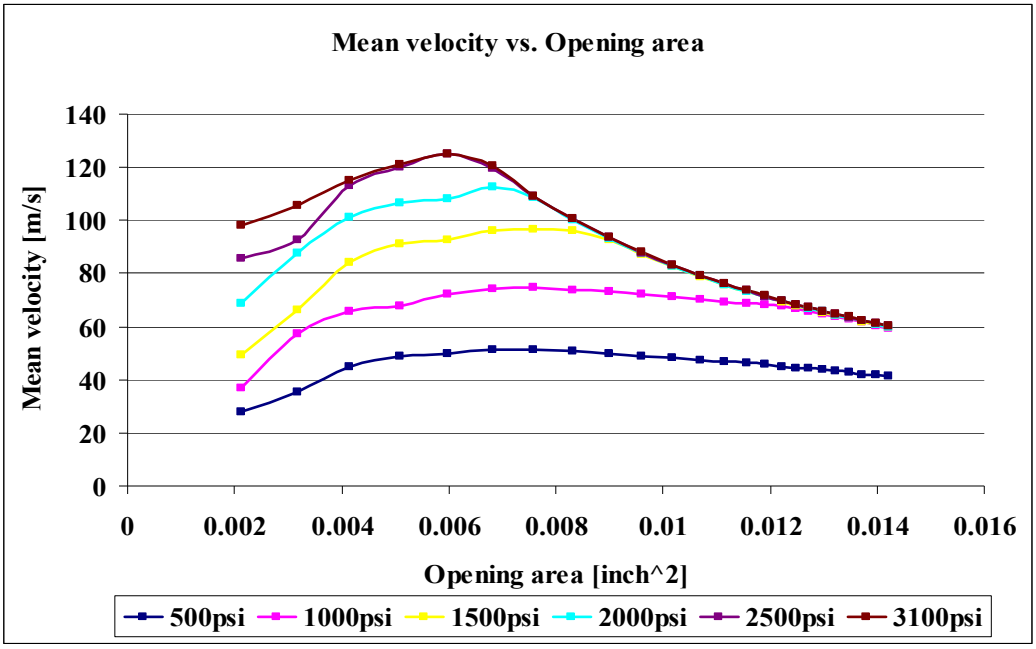

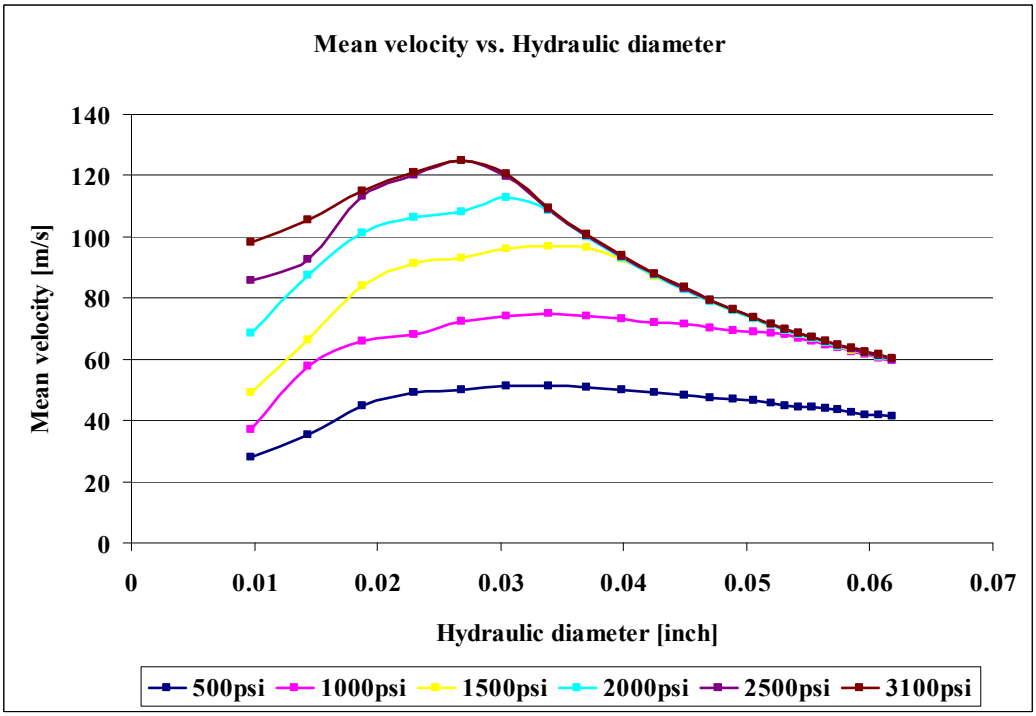

Figure 98: Plots of the flow mean velocity at different spool stops versus the opening area and the hydraulic diameter respectively. (test 5)

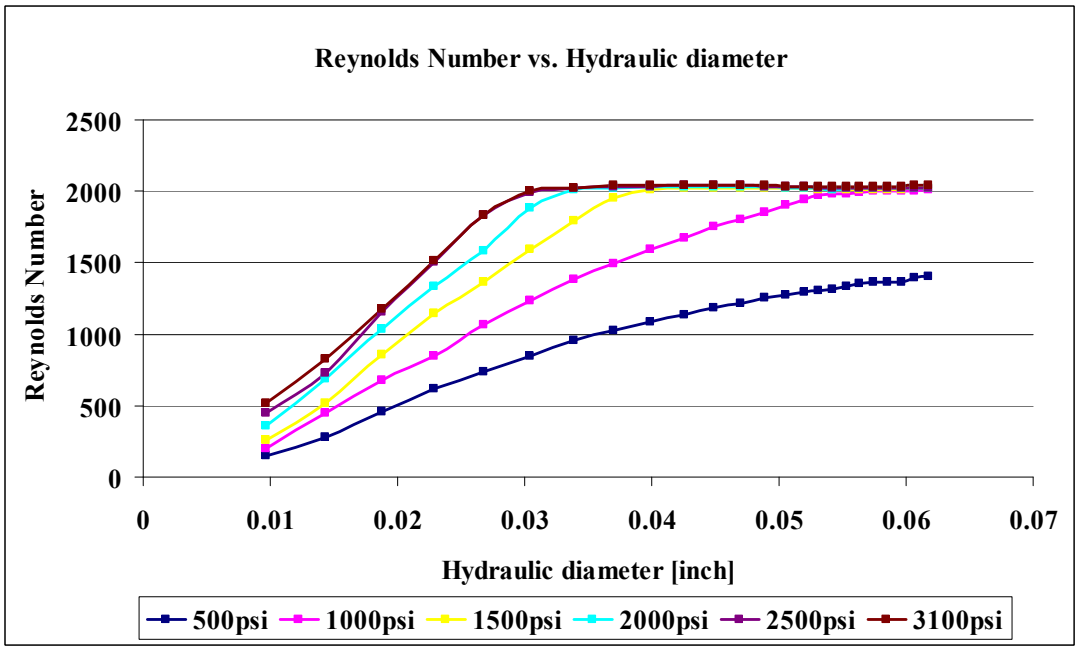

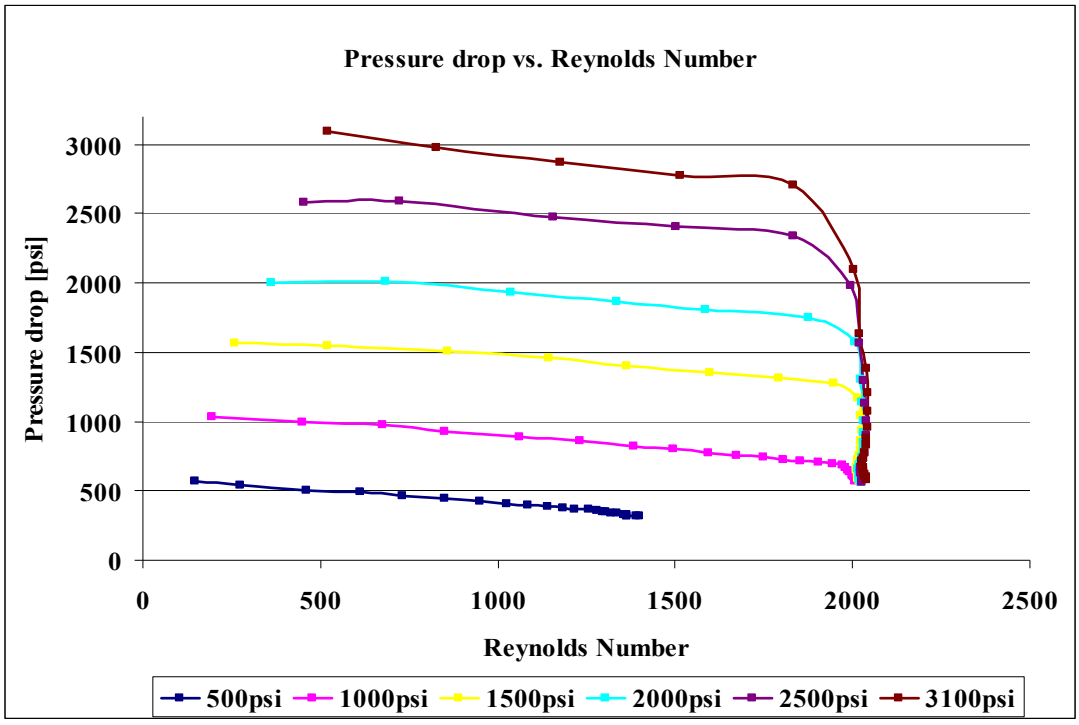

Figure 99: Plots of the flow Reynolds number at different spool stops versus the hydraulic diameter and the pressure drop respectively. (test 5)

As shown in Figure 98, the mean velocity of the flow starts to decrease at earlier spool stop as the applied pressure increases, since the flow rate is reaching its limit of 18 GPM faster. And so, there is no significant increase in the flow rate corresponding to significant increase to both opening area and hydraulic diameter. In addition, Reynolds number reaches a finite value at earlier spool stop as the applied pressure increases due to decrease in the mean velocity accompanied with increase in the hydraulic diameter at the same spool stop, as shown in Figure 99.

As shown in Figure 100, the Mach numbers are less than 0.3 for all the spool stops of test 5. As a result, the flow is incompressible for this test.

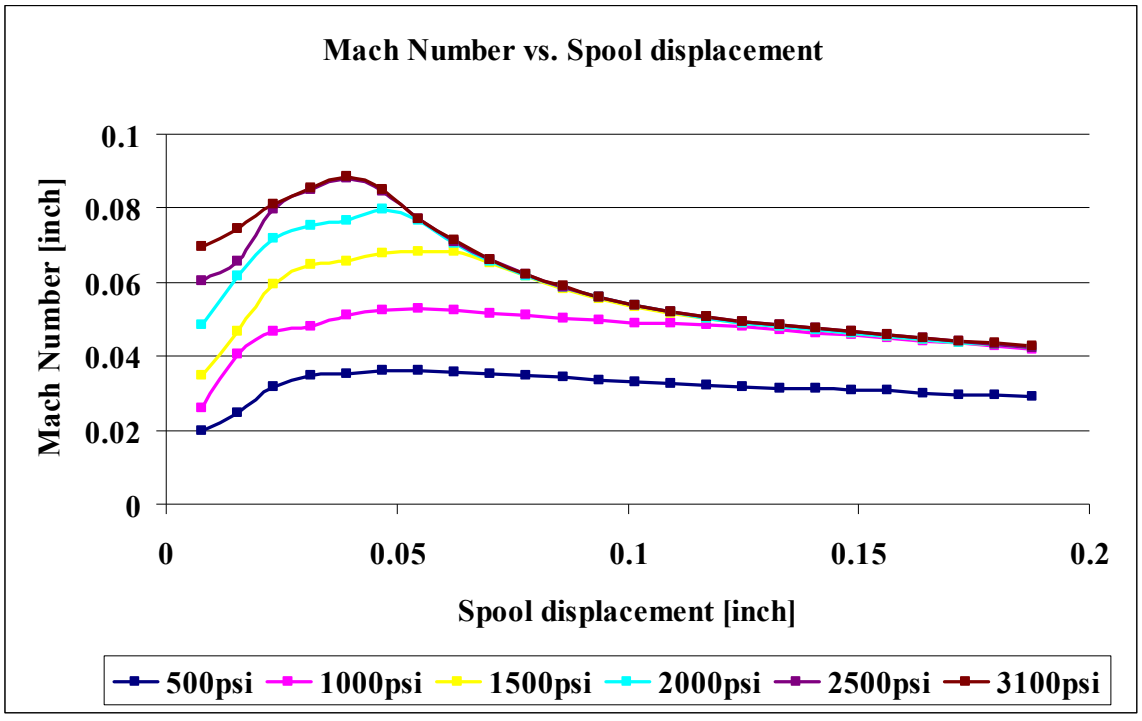

Figure 100: Plot of Mach number versus spool displacement of test 5.

Initial Proposed Spool Type Control Valves

Amsted Rail's proposed hydraulic damper has two distinct functionalities. These functions depend on the reaction of the suspension system to the track irregularities. Two spool valves were initially developed based on the results of the aforementioned tests.

Initial Retraction Performance Spool

As described earlier in Chapter I, the retraction performance spool should provide an increasingly linear relation between pressure drop, flow rate and spool position. Thus, as the applied pressure on the spool pilot increases, the spool will travel from normally closed position to a specific location with certain opening area in order to let more flow in and dampen the total applied pressure.

It was noticed that most of the desired retraction performance line was enclosed by stop #5 of spool #1 in test 1 as shown in Figure 101. Thus, a spool with a straight cut land of certain diameter was adopted initially as the proposed retraction performance spool.

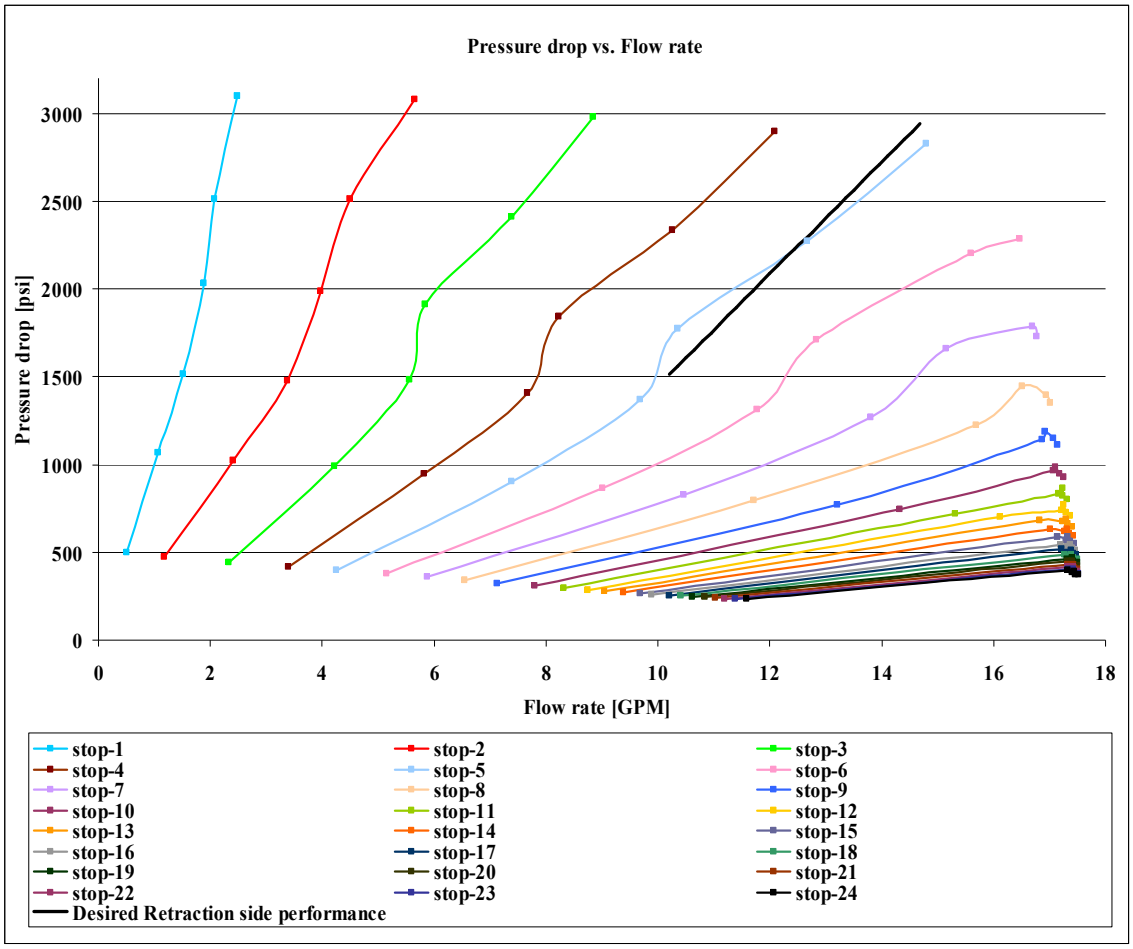

Figure 101: A plot of pressure drop vs. flow rate at each spool stops of test 1. (The results were overlaid with the desired retraction performance of the hydraulic damper for comparison)

In order to enclose all the desired retraction line within a series of stops, the opening area of spool #1 at stop #5 (*i.e.* area #5) was initially broken down into a series of areas that change the total spool openings of spool #1 to two- third of area #5 over the first half of the spool land length, 1875 in., and to four- third of area #5 over the second half of the spool land length.

The calculations of the new two diameters of cut of spool #1 are shown below

$$\phi 1 = 0.5 - 2 \times \left[\frac{(2/3) \times 0.004883}{0.1875} \right] = 0.465''$$

$$\phi 2 = 0.5 - 2 \times \left[\frac{(4/3) \times 0.004883}{0.1875} \right] = 0.431''$$

This new version of spool #1, which was called spool #7, has an opening area that ranges from 3% to 200% of area #5 of spool #1; in order to have enough domain to tweak the opening areas around the one of stop #5 of spool #1 to fully enclose the retraction side performance. A CAD model of spool #7 is shown in Figure 102.

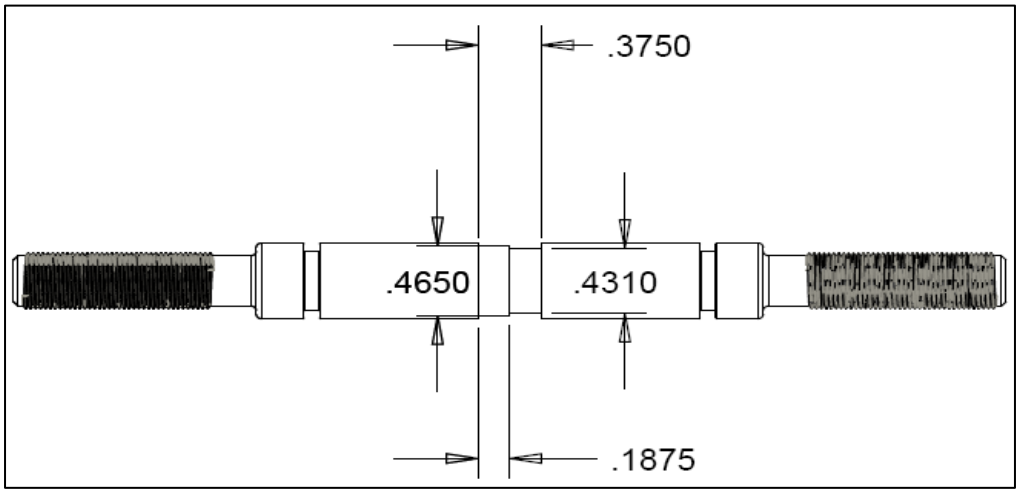

Figure 102: CAD model of spool #7 (retraction side performance spool)

Initial Extension Performance Spool

As described earlier in Chapter I, the extension performance spool should provide a decreasingly linear relation between pressure drop and flow rate. In addition, the same spool should provide a decreasingly linear relation between pressure drop and spool position. Thus, as the applied pressure on the spool pilot increases, the spool will travel from normally open position to a specific location with less opening area in order to let less flow in and damp the total applied pressure.

The aperture that was used to develop the initial extension performance spool was chosen based on two criteria: capability of damping more pressure at initial stops along with linearity between pressure drop and spool position.

To test the damping capability at initial stops of all the tested spools; a plot of the orifice flow coefficient (k) versus the percentage of spool opening ($A_{t,x} / A_{t,24} \times 100\%$) at each spool stop was generated for all the aforementioned spools as shown in Figure 103, the orifice flow coefficient was calculated using the orifice plate equation assuming steady incompressible flow [100]:

$$Q = 77.5780 \times k \times A_t \times \sqrt{\frac{2 \times \Delta p}{\rho}} \tag{23}$$

where Q is the flow rate at each spool stop in GPM, k is the orifice flow coefficient, A_t is the total spool opening at each spool stop in inch^2, Δp is the pressure drop across each spool stop in psi and ρ is the flow density in Ibm/GAL. The density value used in the orifice flow coefficient calculations was 7.28 Ib/GAL (872.34 kg/m^3).

The k values were calculated using the least square type optimization command in Matlab to fit the experimental data of flow rate, pressure drop and total opening area values at each spool stop to Eq. (23).

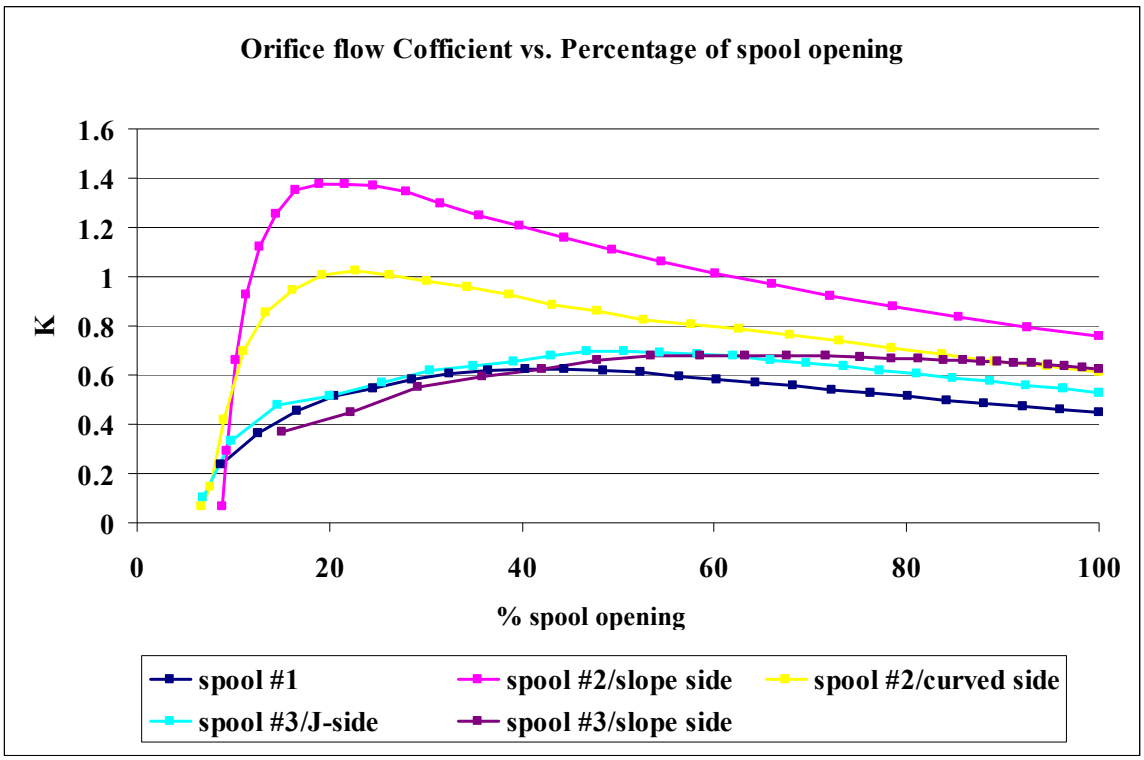

Figure 103: A plot of the orifice flow coefficient (k) versus percentage of spool opening ($A_{t,x} / A_{t,24} \times 100\%$) for all the tests (*i.e.* test 1, 2, 3, 4 and 5).

As shown in Figure 103, spool #2/ slope side has the highest k values among the other spools at the same percentage of the spool opening; thus it is more efficient than the other spools at allowing fluid flow through the same opening areas. As a result, spool #2/slope side has the capacity to cause more pressure drop than the other tested apertures at initial stops.

Another plot of the intersection points between the spool stop's performance lines and the desired extension performance line for all the aforementioned tests was generated in order to evaluate the linearity of the pressure drop versus spool stop performance lines for all the tested spools as shown in Figure 104.

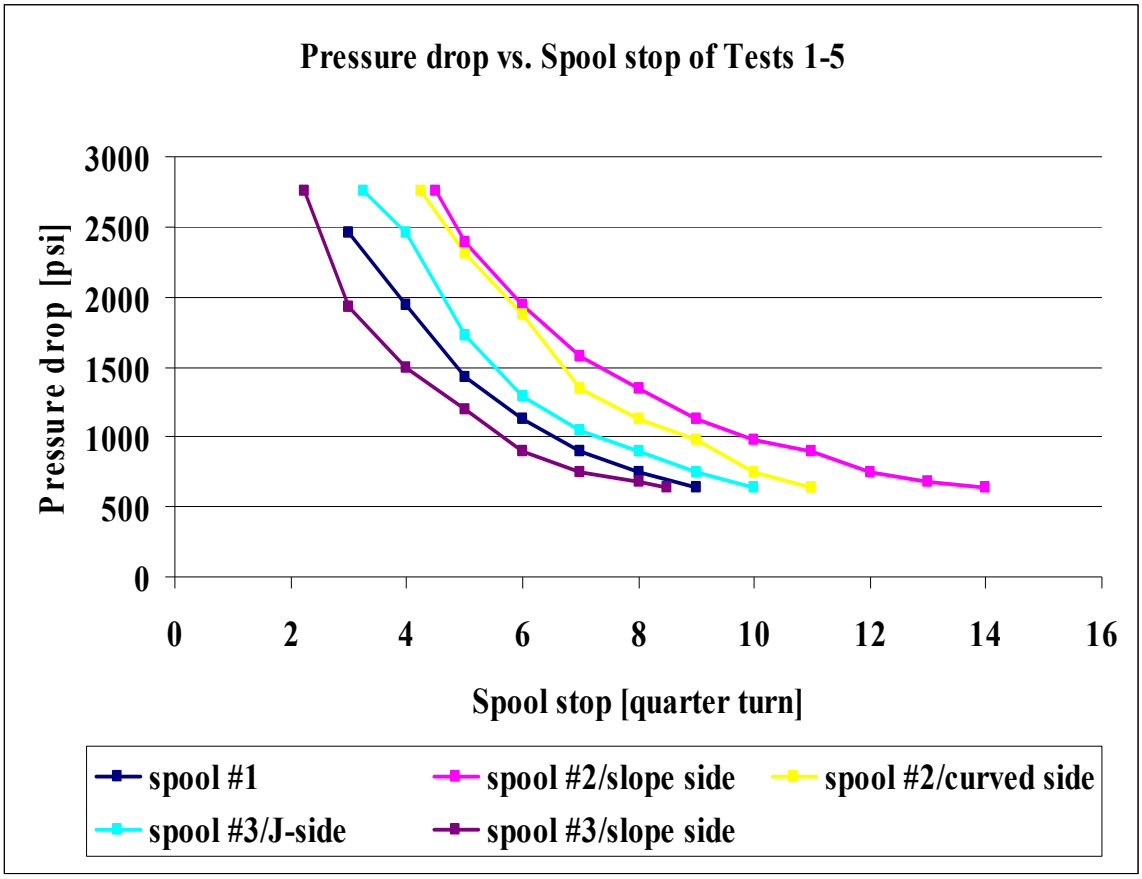

Figure 104: A plot of pressure drop versus spool stop for all the tests (*i.e.* test 1, 2, 3, 4 and 5). (The plot was generated using the intersection points between the spool stop's performance lines and the desired extension performance line)

According to Table 20, all the tested spools have a close goodness of linear fit. But spool #2/slope side has more points of intersections than the other tested spools; thus, more of the aperture land of spool #2/slope side were used for the extension performance relative to the other spools.

Table 20: A summary table shows the statistics of the intersection points associated with each trend line shown in Figure 104.

Spool Name	**Statistics of the Intersection Points of each Test**	
	Number of intersection points	**Coefficient of determination Based on linear Fit (R^2)**
Spool #1 (Test #1)	7	0.9264
Spool #2/slope side (Test #2)	11	0.8930
Spool #2/curved side (Test #3)	8	0.9348
Spool #3/J-side (Test #4)	8	0.9026
Spool #3/slope side (Test #5)	8	0.8658

According to the results shown in Figure 103 and 104, spool #2/slope side was used to develop the initial extension side performance spool which was called spool #8.

The development of the initial spool for the extension performance side, spool #8, was based on linearizing the pressure drop, flow rate data that was obtained experimentally from spool #2/slope side with the new spool displacement. The linearization methodology was started by first assigning a lower and upper end for the new spool displacement domain where the desired performance is enclosed. The new spool has a total land length of 0.1875 in. with its position at stop #4 was assigned to the upper limit of the desired pressure drop, Δp =2759 psi, and its position at stop #21 was assigned to the lower limit of the desired pressure drop, Δp = 637 psi.

Since a linear relation between the pressure drop and the spool stop is required; the two aforementioned data sets of the pressure drop and spool stop were fitted using a linear fit with the following equation:

$$\Delta p = -124.82 \times s + 3258.3 \tag{24}$$

where Δp is the pressure drop in psi and s is the new spool stop number in quarter turn.

Another eight spool stops were chosen arbitrary within the new displacement domain (between spool stop # 4 and 21) and the corresponding pressure drop of each chosen spool stop was calculated using Eq. (24).

Figure 68 was overlaid with the desired extension performance line provided by Amsted Rail as shown in Figure 105, and the calculated values of the pressure drop were located on the desired extension line to find the corresponding stop numbers of spool #2/slope side.

In addition, the corresponding opening areas were found from Table 16 using the previously found spool #2/slope side stop numbers as inputs.

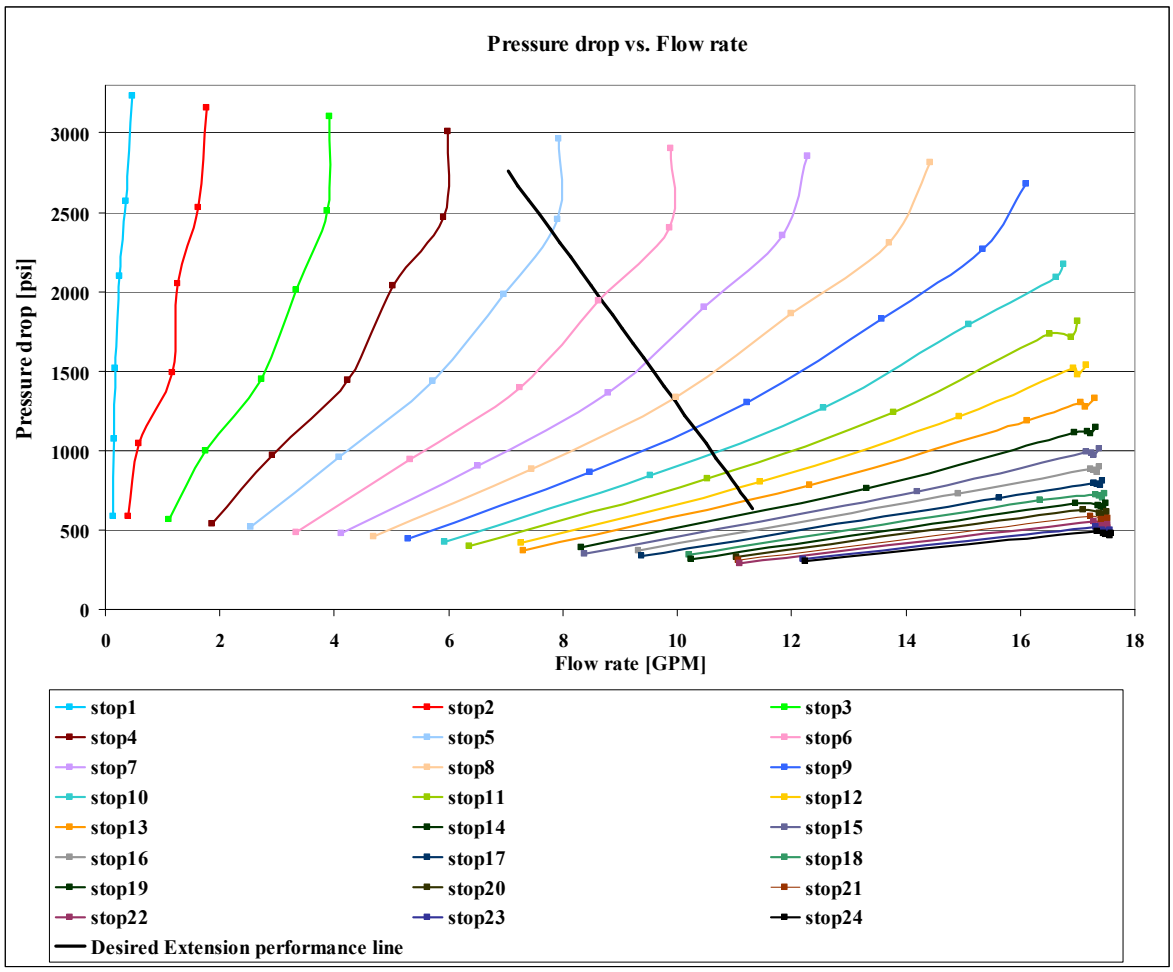

Figure 105: A plot of the pressure drop vs. flow rate at each spool stop of test 2 overlaid with the desired extension performance line.

All the results obtained using the linearization methodologies are summarized in Table 21, see below.

Stop #4 was chosen to be the stop where the linear performance starts, since it was close from spool #2/slope side stop at which the upper limit of the desired pressure drop was obtained (*i.e.* stop # 4.5, see Table 21).

It is important to mention that a side flow on the open side of the flow area of spool #2/slope side impacts the flow, and since stop #24 does not have an open side, stop #21 was chosen instead of stop #24 so that the entire range is similarly impacted by the side flow.

Table 21: A summary of the results obtained from the linearization methodology for spool #2/slope side in order to obtain the required opening areas for the extension side initial spool based on the aforementioned spool displacement domain.

Stop Number of Spool #8 (s) [quarter turn]	**Calculated pressure drop (Δp) (From Eq.(24)) [psi]**	**Stop Number of Spool #2/slope side (from Figure 105) [quarter turn]**	**Required opening area (A_{spool}) (From Table 16) [inch^2]**
4	2759.00	4.50	0.000405
6	2509.40	4.75	0.000480
8	2259.70	5.25	0.000594
10	2010.10	5.75	0.000708
12	1760.50	6.50	0.000845
14	1510.80	7.50	0.001100
16	1261.20	8.50	0.001400
18	1011.50	9.75	0.002000
20	761.900	11.75	0.002900
21	637.100	13.50	0.003900

Since the actual opening areas of spool #2/slope side that were used to develop spool #8 have a trapezoidal shapes (see Figure 106), the calculated opening areas for spool #8 (see Table 21) have the same shapes at stop #6 to 21 in order to keep the same boundary conditions.

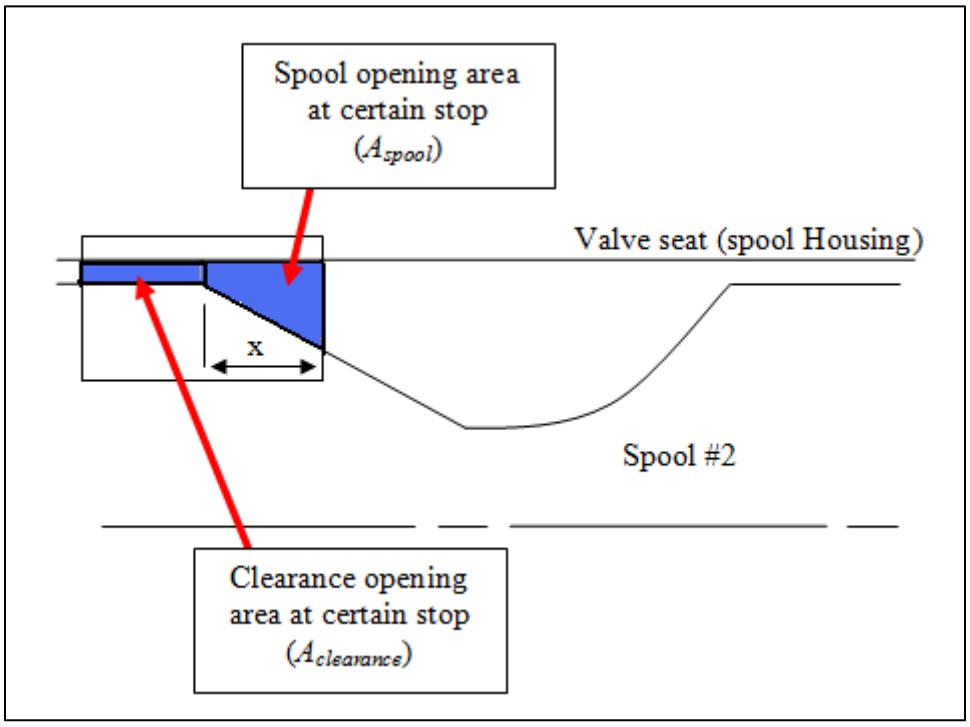

Figure 106: A schematic of spool #2 while making test #2 that shows the total opening area at a certain spool stop (x).

The opening area shape for spool #8 at stop #4 was chosen as a rectangular one, since it has nothing to do with linearizing the flow. Its main function is to initiate enough flow to cause the initial pressure drop described by the desired extension line provided by Amsted Rail.

The corresponding X-Y coordinates of spool # 8 profile (see Figure 107) were extracted from its spool stop number data along with the its opening areas, based on the proposed areas shapes at each stop.

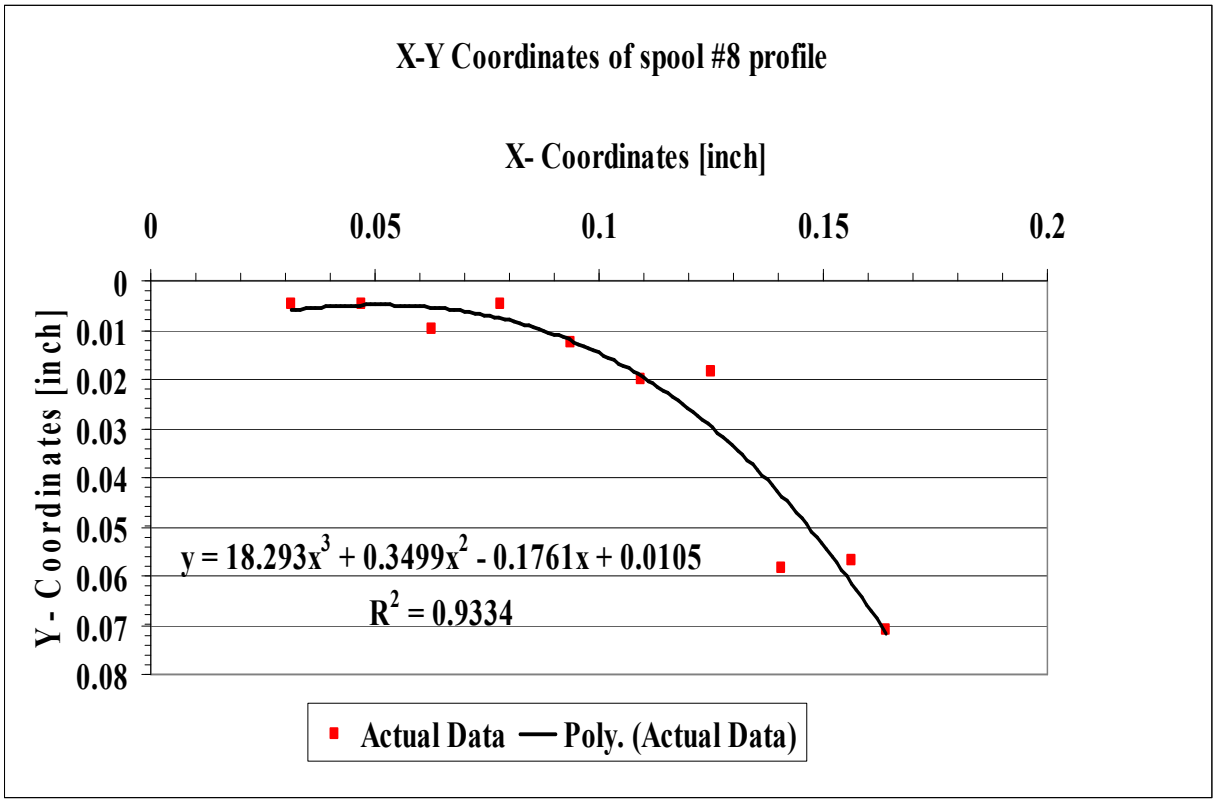

Figure 107: X-Y coordinates of spool #8 profile. (The initial spool for the extension side)

The actual X-Y data of spool #8 profile were fitted using a third degree polynomial in order to come up with a smoother surface that can be manufactured easily. The initial design of spool #8 land is shown in Figure 108 (see below).

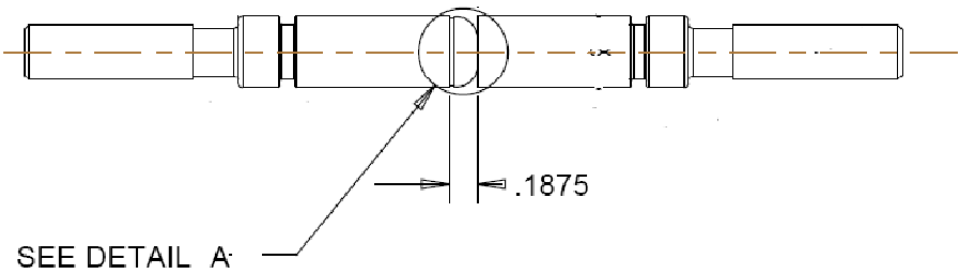

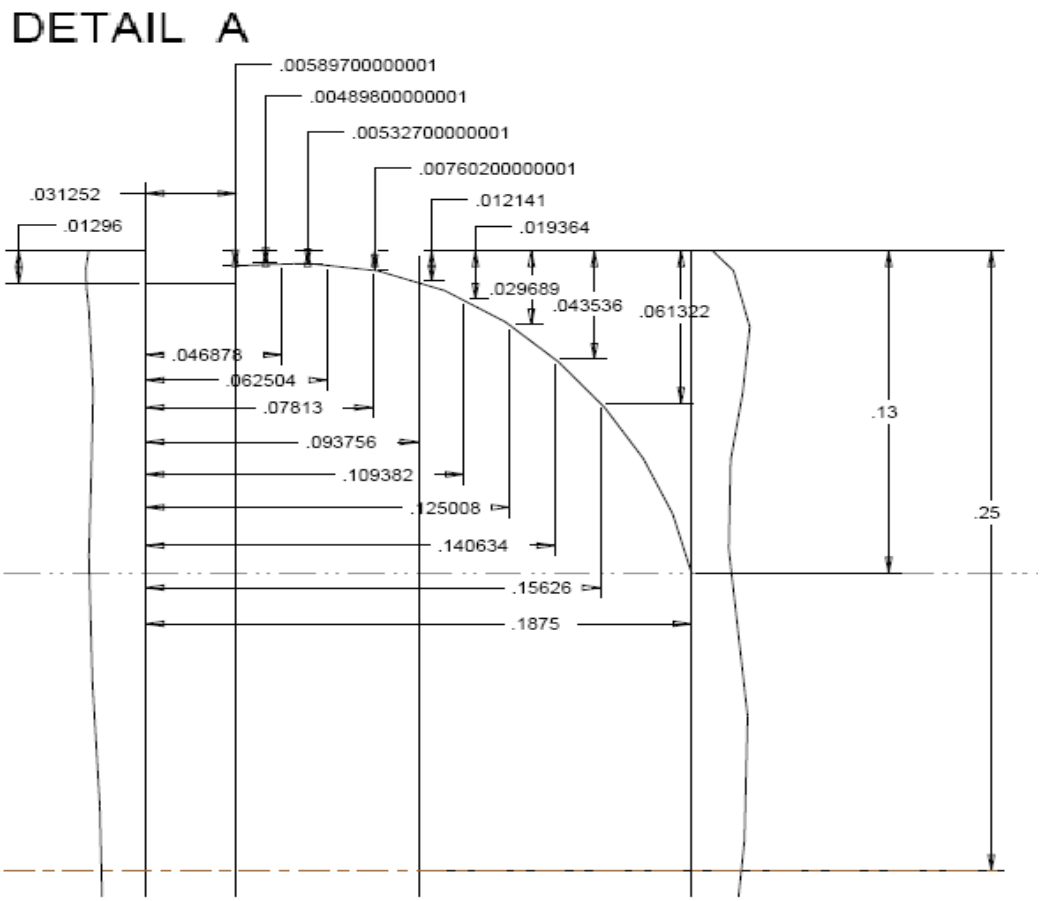

Figure 108: CAD drawing of the initial design of spool #8 land.

(All the dimensions are in inchs)

Amsted Rail Engineering provided another three spools (see Figure 109) after the aforementioned tested three two-sided spools (spool #1, 2 and 3), in order to evaluate the flow characteristics across their aperture and see if they can contribute in the development of the desired two spools. But it was not possible to test them, since the sizing of their threads did not match the sizing of the threads of the test valve hand wheels.

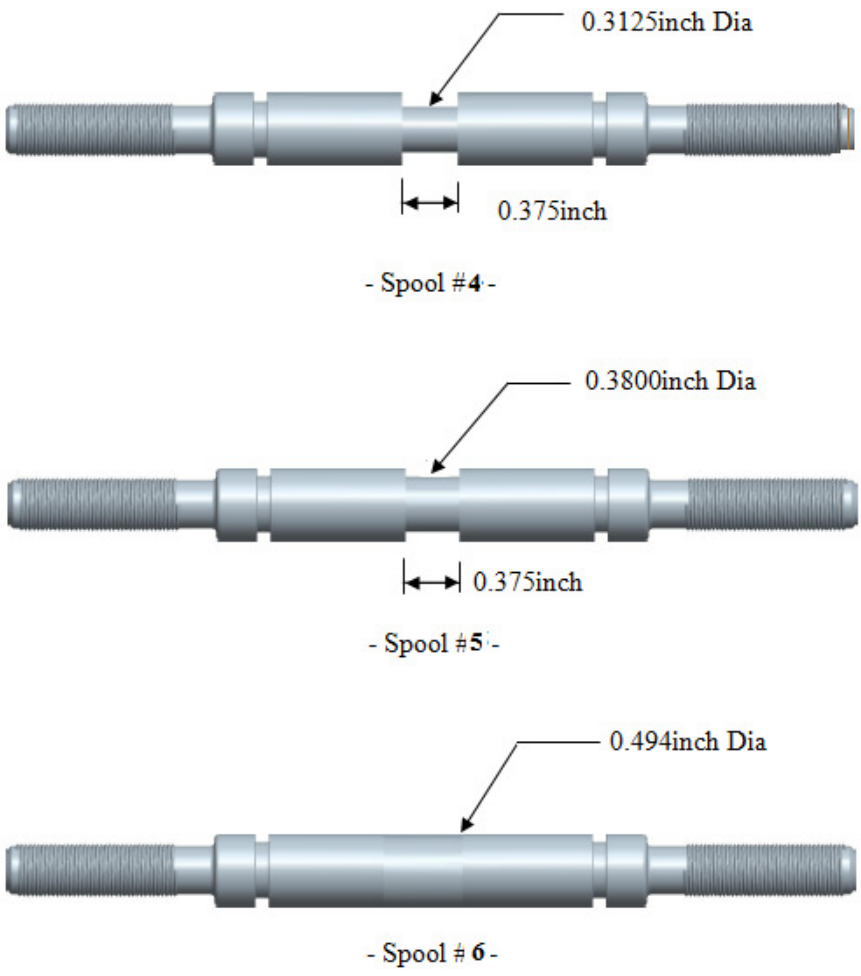

Figure 109: CAD drawing of spool #4, 5 and 6.

At the time that the three new spools (spool #4, 5 and 6) was sent to a local machine shop to modify the sizing of their threads, spool #7 and 8 were already made and ready to be tested. Thus spool #4, 5 and 6 did not contribute to the design of the initial proposed spools (spool #7 and 8) and the discussion of their testing results is mentioned in Chapter V.

CHAPTER V

TEMPERATURE EFFECT ON SPOOL PERFORMANCE

In this Chapter, test #2 was repeated three different times with three different temperature settings for the thermostat mounted on the hydraulic power unit (see Table 22). Two temperature calibrated multimeters (FLUKE) were initially used for each repeation of test 2 to measure the temperature of the flow before and after the test valve as will be shown later in this Chapter.

The results of this phase of testing shows that the performance lines of pressure drop and flow rate at constant spool stop shifts to the right as the temperature increases, flow increases with temperature. Some of the measured behavior was caused by errors in the turbine flow rate readings due to its sensitivity to viscosity changes of the flow as the temperature changes. As a result, a coriolis flow meter from the fluid laboratory of the engineering department at the University of Texas Pan American was installed on the downstream side of the test valve.

The coriolis flow meter was capable to do three independent measurements of mass flow rate, flow density and flow temperature. In addition, this coriolis flow meter was more accurate than the turbine flow meter, since the coriolis flow meter eliminates any uncertainty in the volumetric flow rate due to variations in temperature, entrained air, viscosity and pressure changes.

Table 22: A brief description of the three laboratory tests conducted to study the temperature effect on the spool #2/slope side performance. (Temperature of the flow was recorded at each spool stop manually using a two calibrated multimeters with one was mounted before and the other was mounted after the test valve)

Test #	Hydraulic Power Unit's Thermostat setting ($T_{thermostat}$) [°C]	Experimental Description
6	40	Total of six Experiments. Applied pressure values were {500, 1000, 1500, 2000, 2500, 3200} psi. Tested length of the spool land was 0.1875 inch. (5.30-hour test)
7	70	Total of six Experiments. Applied pressure values were {500, 1000, 1500, 2000, 2500, 3200} psi. Tested length of the spool land was 0.1875 inch. (6.30-hour test)
8	100	Total of six Experiments. Applied pressure values were {500, 1000, 1500, 2000, 2500, 3200} psi. Tested length of the spool land was 0.1875 inch. (7.30-hour test)

Test #6 (see Table 22) was repeated again with the same thermostat setting (*i.e.* $T_{thermostat=}$ 40°C), but this time the flow rate readings were based on the coriolis flow meter instead of the turbine flow meter ones. As it will be shown later; the intersection points for test #2 when using the turbine flow meter and test #6 when using the coriolis one are close (less than 10% error).

This comparison of the intersection points of both the aforementioned tests gave the author more confidence about the initial proposed design for spool #8 in the temperature range of

18-40°C with some doubts about the possibility of the flow temperature influencing the linearity of the spool performance.

While still waiting for spool #7 and spool #8 to be made, absolute viscosity data for AW46 Hydraulic oil in the temperature range of 0-100°C were gathered using three different sources. In addition, density data for the same oil was collected using the coriolis flow meter. This collected data of absolute viscosity and density of the flow was so helpful in the recalibration of the turbine flow meter based on the UVC principles (Universal Viscosity Curve) over a temperature range of 0 to 100°C. The recalibration of the turbine flow meter was necessary to get more accurate flow rate reading; in case the coriolis flow meter has to be returned back to the fluid lab and the turbine flow meter is the only source of getting a flow rate readings.

The test of spool #7 with the thermostat setting at 40°C was the turning point; the results of this test showed that the desired retraction performance can be achieved at one spool stop if the temperature of the flow kept constant at 50°C during the test.

Since the two desired spools (*i.e.* the retraction and extension performance spools) are placed in the same housing, they should have the same flow temperature. Thus, spool #8 was tested with the thermostat setting at 40°C and the temperature of the flow was kept close to

50°C. The results of this test showed that spool #8 could not deliver enough flow to intersect with the desired extension performance line at applied pressures lower than 1500 psi. The main source of this flow shortage at lower applied pressures came from underestimating the side flow that the curved side of spool #2 supplied while testing the slope land side of the same spool. Thus, spool #8 land diameter along with its land length were modified based on spool #7 test results when they were overlaid with the desired extension side performance as will be shown later in this chapter. When the modified version of spool #8 (which was called spool #8A) was tested again at the same flow temperature conditions (*i.e.* at T_{flow}=50°C), the results showed a performance that is close from the targeted one described previously in Chapter IV.

Two spring loaded omega RTDs were mounted inside two thermo wells before and after the test valve. In addition, a SPRTX signal converter was used in series with each RTD to convert the temperature signal captured by the RTD to DC current signal (*i.e*. 4-20 mA analog output signal). As a result, it was possible to interface the temperature signal recorded by the RTD with the developed labview program mentioned previously in Chapter III, in order to get a real time data of the flow temperature before and after the test valve.

The latter test of spool #7 was repeated again at only the same stop where the desired performance is achieved (*i.e.* stop #15), in order to see how much temperature difference between the inlet and the outlet flow at the aforementioned stop. The results show that there was a temperature increase across the test valve of 5°C for spool #7 test when the temperature of the outlet flow from the test valve was 50°C. Thus, it was more reasonable to base the performance

of the spools on the inlet flow temperature rather than to the temperature of the outlet flow being measured by the RTD built inside the coriolis flow meter.

Thus, the test of spool #7 and spool #8A were repeated based on an inlet flow temperature of 45°C. The results of both new tests were close from those obtained earlier (*i.e.* when T_{flow}=50°C based on coriolis flow meter) for the same aforementioned spools. As a result, those tests were repeatable within 3%.

After the aforementioned tests results of spool #7 and spool #8A were sent to Amsted Rail Engineering, they decide to set the design temperature of both spools at 25°C.

Since it was not possible to keep the inlet flow temperature for a reasonable time at 25°C while making the test with only using the heat exchanger mounted on the hydraulic power unit (*i.e.* waiting for 20-30 minutes for the flow to cool down in order to record two data points before the flow heats up significantly again), a cooling setup using a 13 kW water chiller, multiple fans and radiator was implemented to enhance the performance of the power unit's heat exchanger. As a result the cooling setup increases the testing capability of recording data points at constant flow temperature from 2 to 12 data points.

All The aforementioned tests that were conducted on spool #7, spool #8 and spool #8A are summarized in Table 23 and 24 respectively, along with the source of flow temperature

measurements, applied pressure values, the tested land length of each spool profile and the total duration of each test.

Another two tests were conducted on spool #4 and 5 with the inlet flow temperature kept at 25°C (see Table 25). The results of both tests showed that the desired retraction side performance was achieved at stop 6 of spool #4 and at stop 5 of spool #5. When the results of the both tests were compared with the ones obtained from test 12 (see Table 34), it was found that all the stops where the desired retraction performance was obtained have a close wetted perimeter value (*i.e.* within 6%).

The objective of spool #6 was to justify the possibility of a flow rate when any of the previously tested spools (*i.e.* spool #1 to spool #8A) were at a fully closed position. When spool #6 was tested at 25°C inlet flow temperature, it was found that a flow rate in a range of 0.470 to 1.870 GPM was obtained when the applied pressure went from 500 to 3100 psi.

Since there was a temperature increase of the flow while it was crossing the test valve (due to frictional heating of the flow while it passes the valve), the turbine flow meter was recalibrated again based on the temperature of the upstream flow this time using UVC method (see Figure 147 and Table 35).

It is obvious that spool #8A needs more modifications to decrease the discrepancy between its performance and the targeted performance as shown in Figure 144. But no further modifications were made since Amsted rail Engineering changed their design criteria for both the retraction and the extension side performances as will be shown later in Chapter VI.

Table 23: A brief description of the four laboratory experiments conducted on spool #7. (Coriolis flow meter was used to record the flow rate data at each spool stop while making all the tests)

Test #	Source of Flow Temperature Measurements	Experimental Description
9	RTD built inside the Coriolis flow meter	Total of 15 Experiments. Applied pressure values were in increments of 200 psi starting from 500 psi and ending at 3250 psi. All spool land was tested (0.375 in.). Downstream flow temperature range of 18-55°C (8.00-hour test)
10	RTD built inside the Coriolis flow meter	Total of 15 Experiments. Applied pressure values were in increments of 200 psi starting from 500 psi and ending at 3250 psi. All spool land was tested (0.375 in.). Downstream flow temperature kept at 50°C ± 3°C (9.00-hour test)
11	RTD mounted before the test valve	Total of 9 Experiments. Applied pressure values were in increments of 200 psi starting from 1700 psi and ending at 3250 psi. All spool land was tested (0.375 in.). Upstream flow temperature kept at 45°C ± 3°C (6.50-hour test)
12	RTD mounted before the test valve	Total of 9 Experiments. Applied pressure values were in increments of 200 psi starting from 1500 psi and ending at 3100 psi. All the spool land was tested for {1500, 1700, 2900 and 3100 psi} experiments. Stop # 15 to 22 of the spool land were tested for {1900, 2100, 2300, 2500, 2700 psi} experiments. Upstream flow temperature kept at 25°C ± 3°C (7.00-hour test)

Table 24: A brief description of the one laboratory experiment conducted on spool #8 and of the other three experiments conducted on its modified version (*i.e.* spool #8A). (Flow rate data at each spool stop was recorded based on coriolis flow meter)

Spool #8		
Test #	**Source of Flow Temperature Measurements**	**Experimental Description**
13	RTD built inside the Coriolis flow meter	Total of 13 Experiments. Applied pressure values were in increments of 200 psi starting from 500 psi and ending at 2900 psi. All spool land was tested (0.1875 in.). Downstream flow temperature kept at 50°C ± 3°C (8.00-hour test)
Spool #8A		
Test #	**Source of Flow Temperature Measurements**	**Experimental Description**
14	RTD built inside the Coriolis flow meter	Total of 13 Experiments. Applied pressure values were in increments of 200 psi starting from 500 psi and ending at 2900 psi. All spool land was tested (0.3125 in.). Downstream flow temperature kept at 50°C ± 3°C (7.50-hour test)
15	RTD mounted before the test valve	Total of 11 Experiments. Applied pressure values were in increments of 200 psi starting from 900 psi and ending at 2900 psi. All spool land was tested (0.3125 in.). Upstream flow temperature kept at 45°C ± 3°C (7.00-hour test)
16	RTD mounted before the test valve	Total of 11 Experiments. Applied pressure values were in increments of 200 psi starting from 900 psi and ending at 2900 psi. All spool land was tested (0.3125 inch). Upstream flow temperature kept at 25°C ± 3°C (12.00-hour test)

Table 25: A brief description of the experiments conducted on spool #4, 5 and 6. (Coriolis flow meter was used to record the flow rate data at each spool stop while making all the tests)

Spool #4 (0.3125 inch Dia.)		
Test #	**Source of Flow Temperature Measurements**	**Experimental Description**
17	RTD mounted before the test valve	Total of 9 Experiments. Applied pressure values were in increments of 200 psi starting from 1500 psi and ending at 3100 psi. A 0.07813 in. of the spool land was tested (*i.e.* stop #1 to stop #10). Upstream flow temperature kept at 25°C ± 3°C (3.50-hour test)
Spool #5 (0.3800 inch Dia.)		
Test #	**Source of Flow Temperature Measurements**	**Experimental Description**
18	RTD mounted before the test valve	Total of 9 Experiments. Applied pressure values were in increments of 200 psi starting from 1500psi and ending at 3100 psi. A 0.07813 in. of the spool land was tested (*i.e.* stop #1 to stop #10). Upstream flow temperature kept at 25°C ± 3°C (3.50-hour test)
Spool #6 (0.4940 inch Dia.)		
Test #	**Source of Flow Temperature Measurements**	**Experimental Description**
19	RTD mounted before the test valve	Total of 2 Experiments. Applied pressure values were 500psi and 3100psi. All spool land was tested (*i.e.* 0.375 in.). Upstream flow temperature kept at 25°C ± 3°C (30 minutes test)

Experimental Results of Test 6, 7 and 8

Test 6, 7 and 8 were conducted on spool #2/slope side in order to identify any significant change on the spool performance due to change in flow temperature. The flow temperature was measured at two different locations (*i.e.* one multimeter was mounted upstream of the test valve and the other was mounted at downstream side) using a two calibrated multimeters (FLUKE brand) as shown in Figure 110.

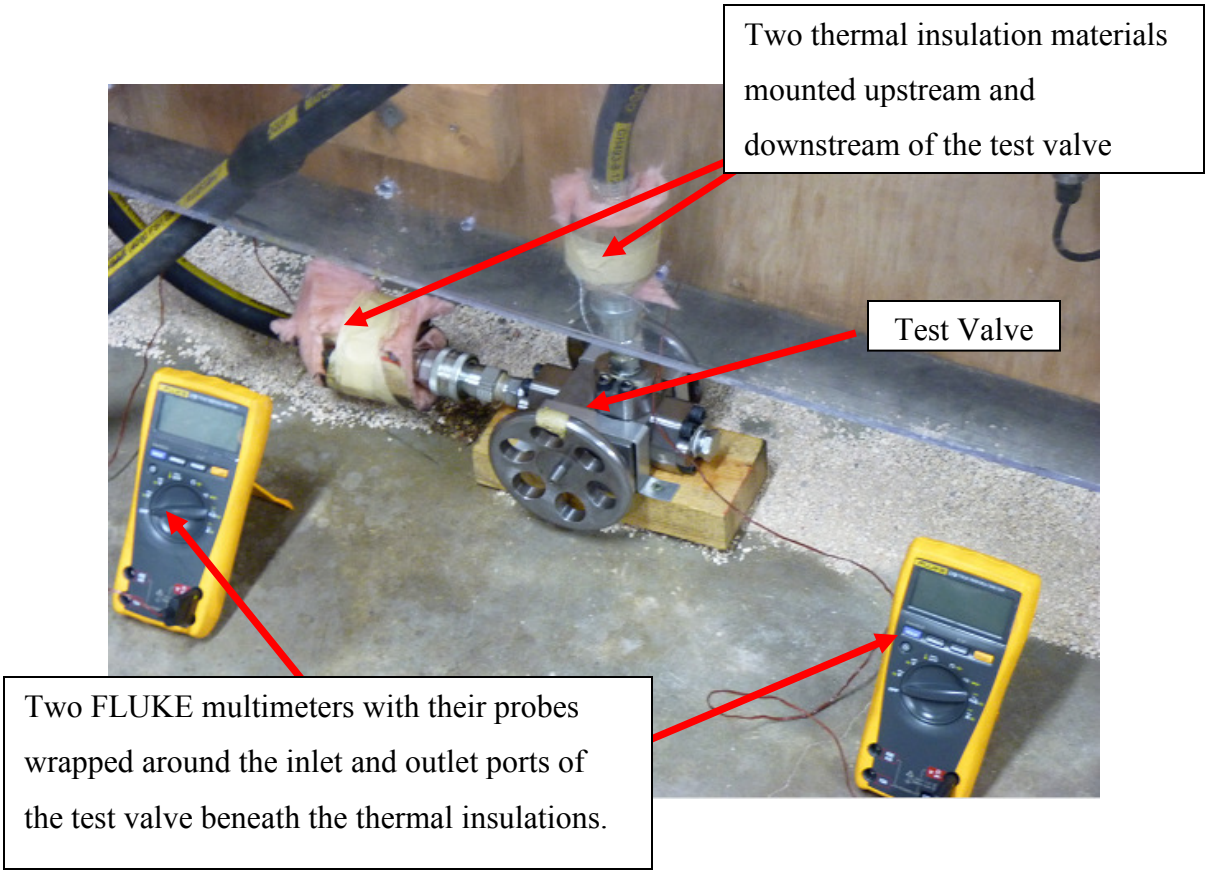

Figure 110: A picture of the two calibrated multimeters used to measure the temperature of the flow while making test 6, 7 and 8.

The results of test 6, 7 and 8 are shown in Figure 111. It can be noticed that the performance lines of pressure drop versus flow rate of the sub experiments that have the same starting applied pressure have the same trend even though the flow temperatures are not the same. In addition, the initial stops of the sub experiments with higher flow temperatures have more corresponding flow rate values; thus, its performance lines start to decline faster since the flow rate reaches its limit of 18 GPM faster.

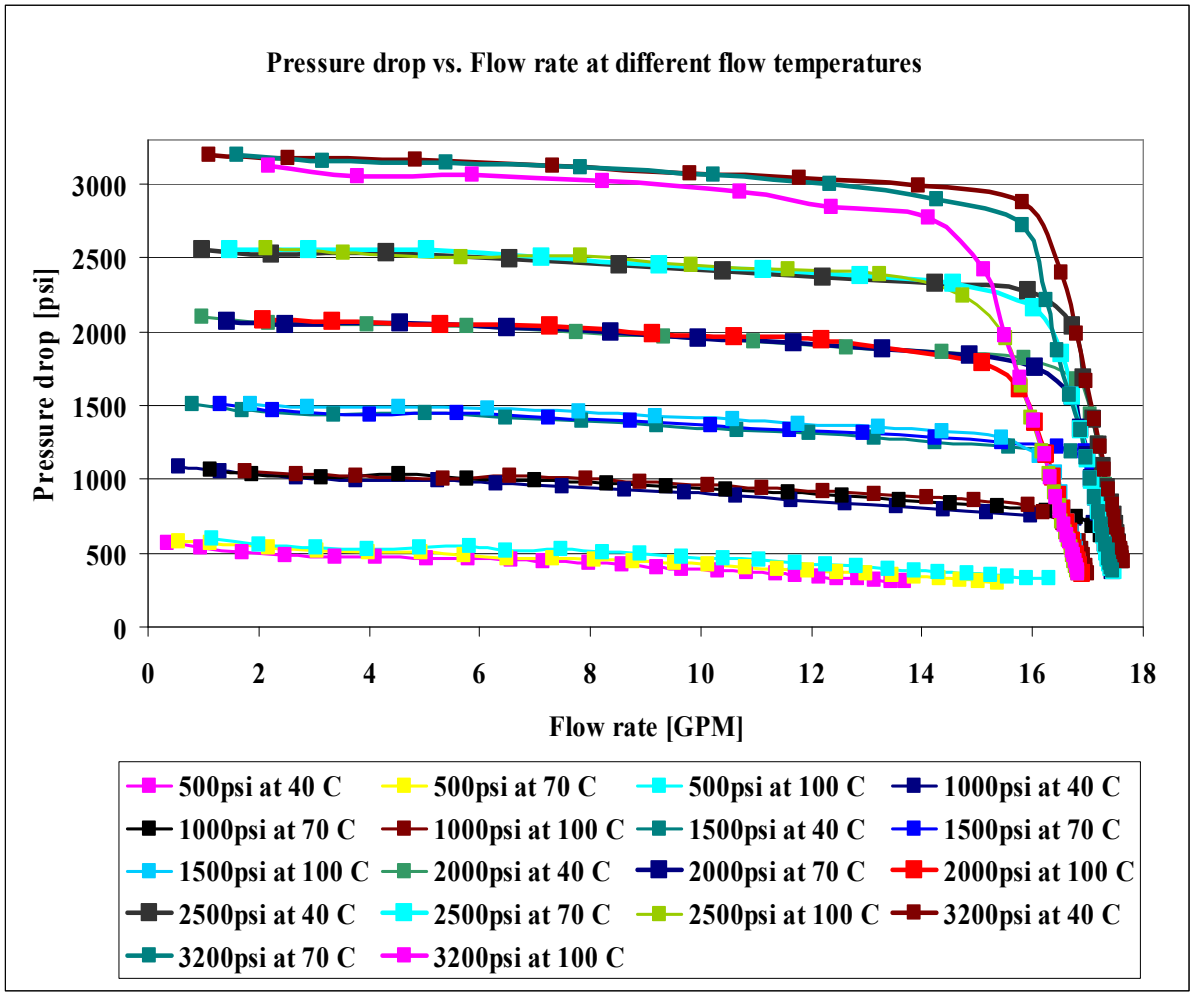

Figure 111: A plot of the pressure drop vs. flow rate results of test 6, 7 and 8.

Stop #7 of the tested spool in test 6, 7 and 8 was chosen to see the effect of the flow temperature on the performance at constant spool stop. As shown in Figure 112, the same spool stop has more flow rate as the flow temperature increases (*i.e.* the same spool stop performance shifts to the right as the flow temperature increases).

It was found that for 60°C temperature increase of the flow at stop #7, the percentage increase in the flow rate is 13.85%. The same behavior was noticed for the other tested spool stops as the flow temperature increases.

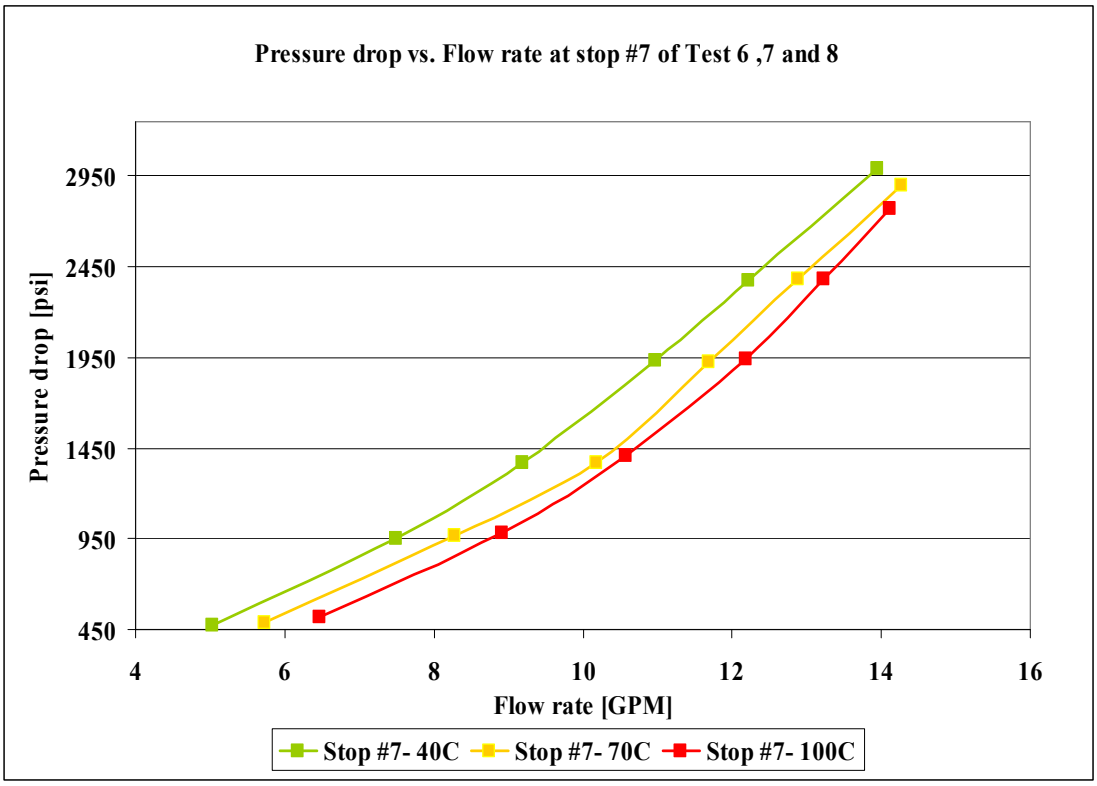

Figure 112: A plot of the pressure drop vs. flow rate performance lines for stop #7 of the tested spool in test 6, 7 and 8.

This shift in the spool stop performance as the flow temperature increases was initially believed to be caused by errors in the turbine flow rate readings due to its sensitivity to viscosity changes of the flow as the temperature changes. Thus, a coriolis flow meter that was available at the engineering fluid laboratory of the University of Texas Pan America was used, since its readings are not sensitive to the viscosity changes of the flow due to changes in the flow temperatures. Table 26 lists the specifications of the flow sensor of the coriolis flow meter.

The maximum downstream pressure obtained while making the initial tests (test 1-5) was 250 psi. Thus, the coriolis flow meter was mounted on the downstream side of the test valve, since the pressure rating for its flow sensor is 1800 psi.

Table 26: A summary of the ABB K-Flow coriolis mass flow sensor specifications.

Specification	**Description**
Sensor Model	K250
Operating Temperature	-95°C to 204°C
Pressure Rating	1800 psi
Minimum to Maximum Flow Rate	(2.50 lbs/min) to (250 lbs/min) or (1.13 kg/min) to (113 kg/min)
Accuracy of Flow rate	0.2% of mass flow rate ± 0.03
Flow Sensor Weight	35 lbs(16 kg)

Two GH493-12 Aeroquip hoses were used to connect the inlet and outlet ports of the ABB coriolis mass flow meter to the initial experimental setup through the coriolis flanged process connections (see Figure 113 and 114).

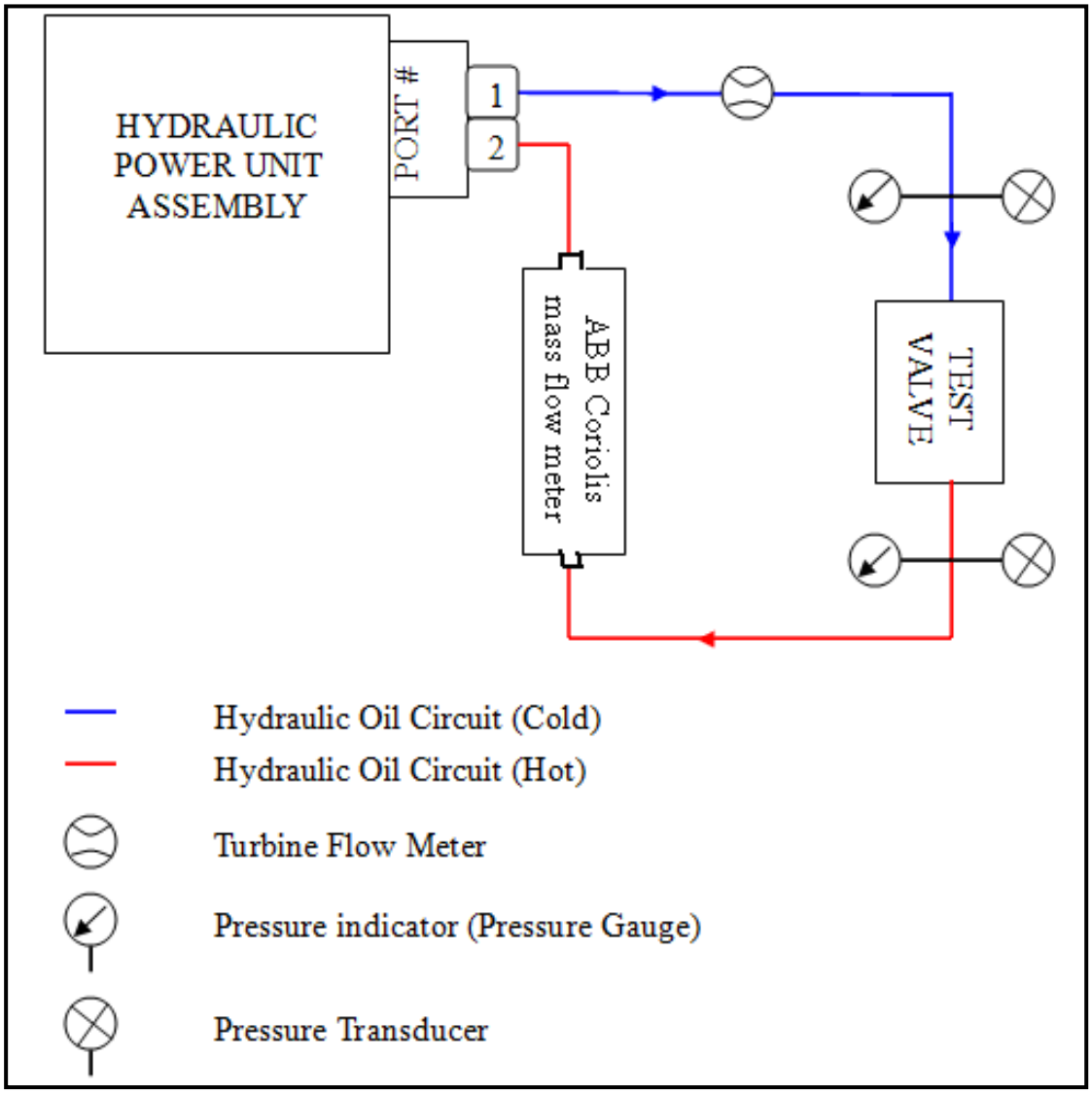

Figure 113: A schematic of the new test setup that uses the ABB K-Flow coriolis mass flow meter on the downstream side of the test valve.

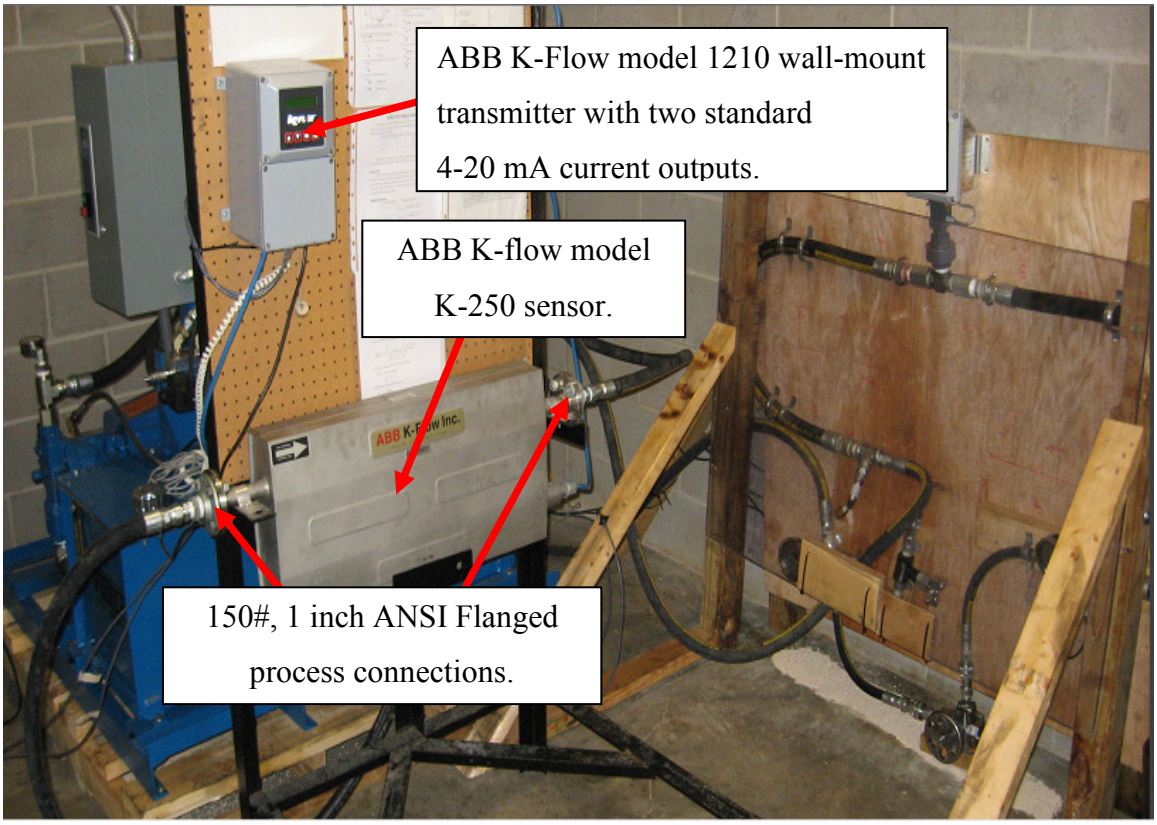

Figure 114: A picture of the new test setup that uses the ABB K-Flow coriolis mass flow meter on the downstream side of the test valve.

Since the ABB K-flow transmitter has two standard 4-20 mA current output channels; the measured temperature of the flow within its chosen range (*i.e.* [0-120]°C) was assigned to one channel and the volumetric flow rate within its chosen range (*i.e.* [0-20] GPM) was assigned to the other channel. It is important to mention that the coriolis meter does independent measurements of both mass flow rate and density; thus, the volumetric flow rate can be computed inside the transmitter memory once activating its function ID.

Figure 115 shows how the transmitter was connected electrically to the USB DAQ; in order to get a real time data of the flow temperature and volumetric flow rate while making a test.

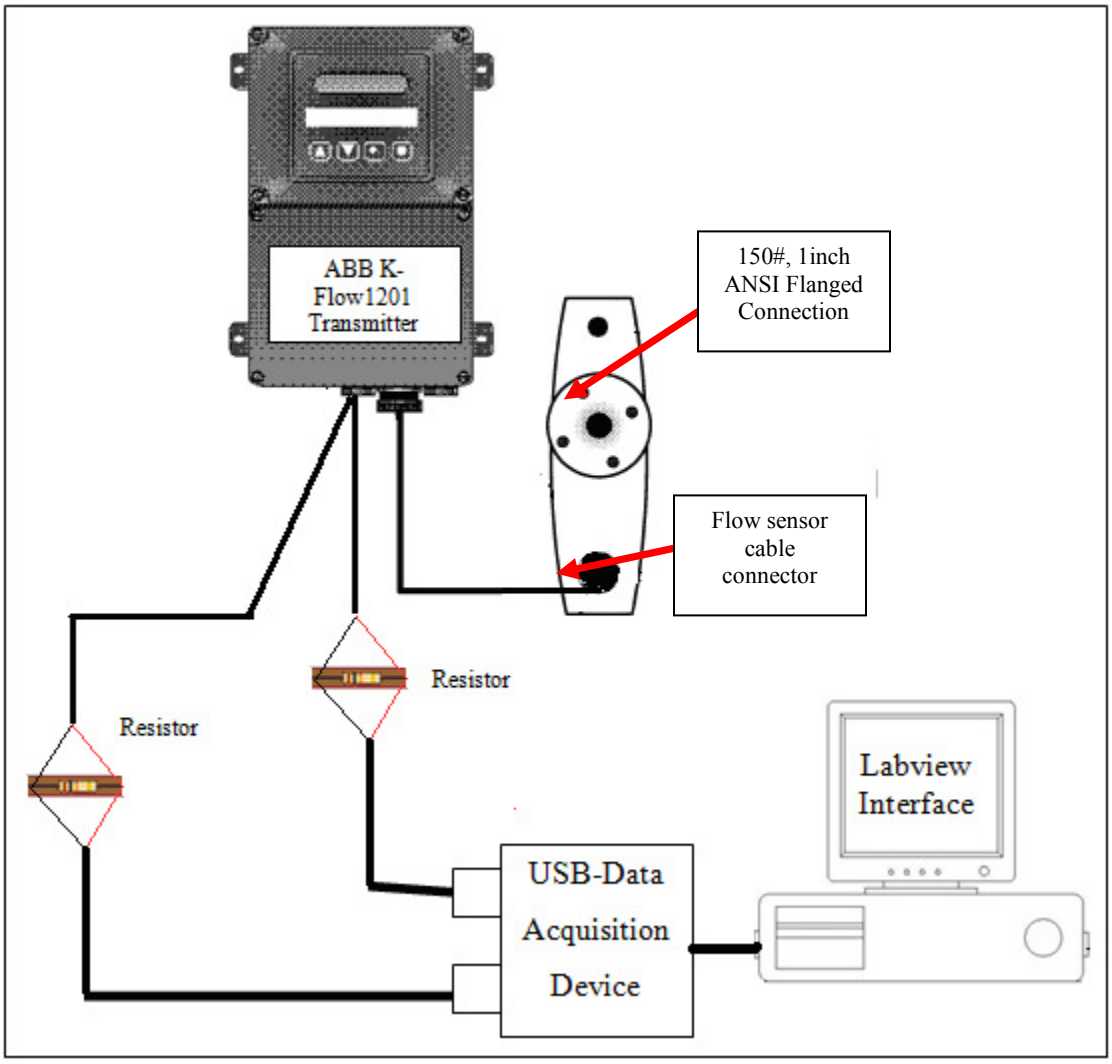

Figure 115: A schematic of the ABB K-Flow 1201 transmitter with its three electrical connections. (One connection is between the transmitter and the flow sensor with the other ones are between the two 4-20 mA output channels and the USB DAQ)

Two 270 Ω resistors were used to convert the 4-20 mA current output of the transmitter channels to voltage signal that the USB DAQ can acquire while making the tests (see Figure 115). Three new equations were added to the previously mentioned labview program to convert the voltage signals acquired by the DAQ from the ABB K-Flow transmitter into its corresponding values of the recorded data of flow temperature and volumetric flow rate. The three equations are given by

$$I = \frac{V}{270} \times 1000 \tag{25}$$

$$T_{flow} = \frac{[120 - 0]}{[20 - 4]} \times (I - 4) \tag{26}$$

$$Q = \frac{[20 - 0]}{[20 - 4]} \times (I - 4) \tag{27}$$

where I is the output current from the ABB K-Flow transmitter channels in milliampere, V is the voltage drop across the 270 Ω resistor in volts, T_{flow} is the temperature of the flow in degree Celsius (°C) and Q is the volumetric flow rate in GPM.

Test #6 was repeated again with the same thermostat setting (*i.e.* $T_{thermostat=}$ 40°C), but this time the ABB K-Flow coriolis mass flow meter was used to record the volumetric flow rate and the flow temperature at each spool stop of spool #2/slope side.

The results of the aforementioned test are shown in Figure 116. It can be noticed that the performance lines of pressure drop versus flow rate have the same trend as those obtained in the previously conducted tests (test 1 to 8); where the turbine flow meter was the only tool to get flow rate data while making the test. In addition, the temperature of the flow recorded by the coriolis flow meter for this test was found to be between 20 and 52°C.

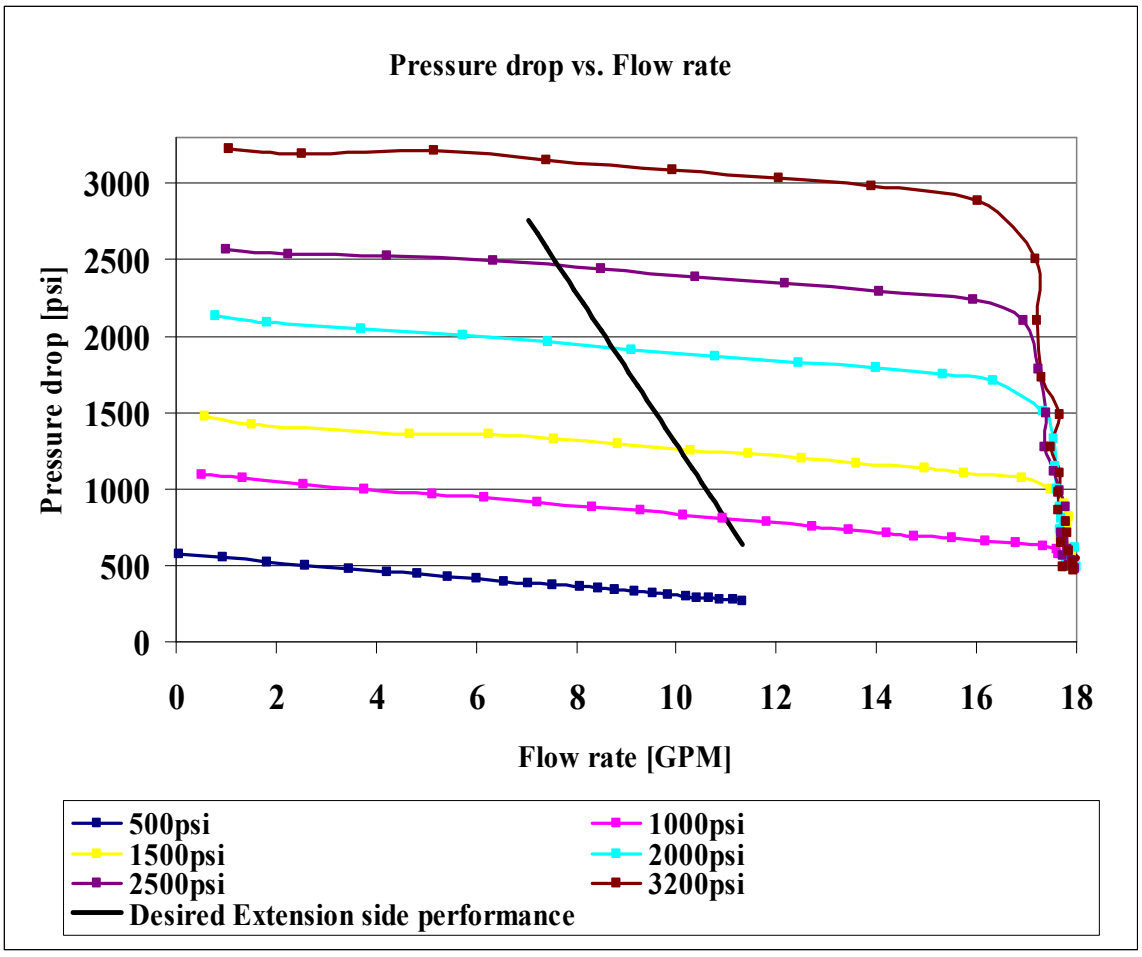

Figure 116: A plot of the pressure drop vs. flow rate for test 6, as the ABB K-Flow coriolis mass flow meter was being used to record the flow rate data while conducting the test.

Another plot of the pressure drop versus flow rate at each spool stop of the same test was generated as shown in Figure 117. It was noticed that there is one point where the performance of the spool stop shifts abruptly to the right relative to the other points on the same spool stop performance line. It was found that the flow temperature at this point is ten degree Celsius higher than the other points which lie on the same performance line for each spool stop.

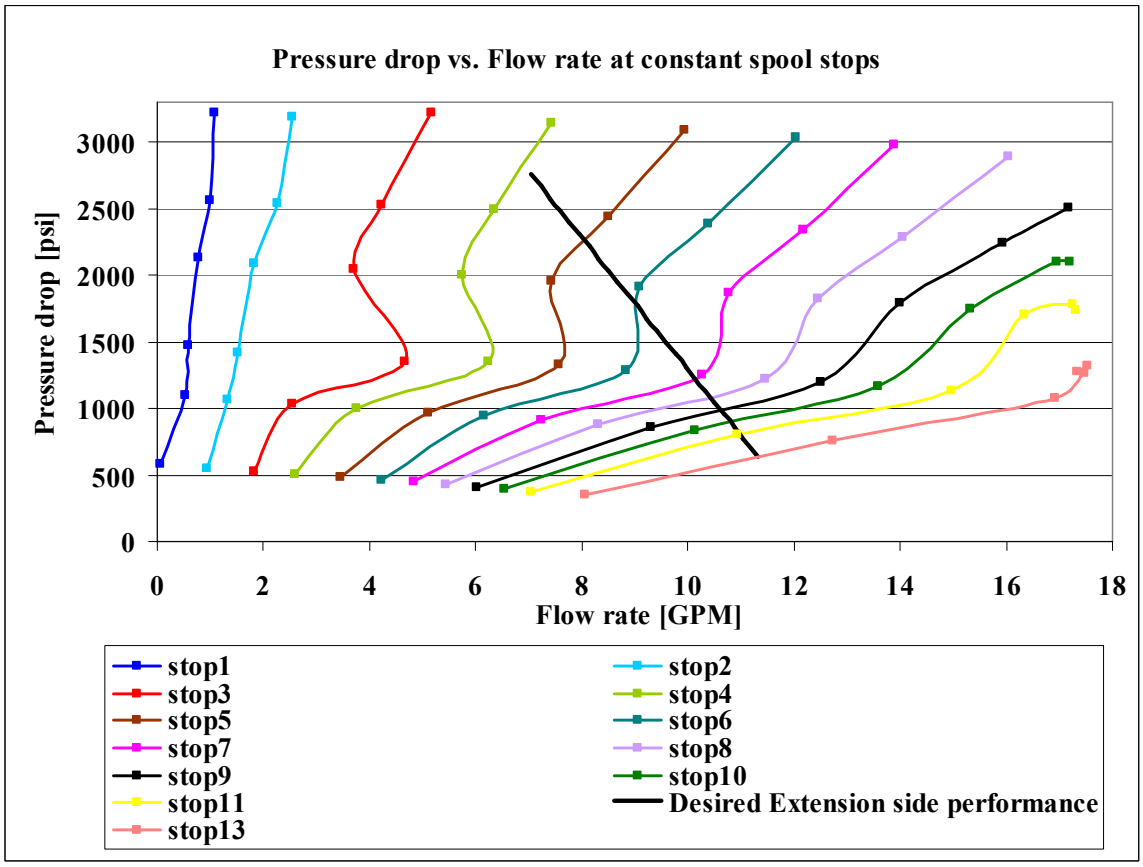

Figure 117: A plot of the pressure drop vs. flow rate at constant spool stops of test 6, as the ABB K-Flow coriolis mass flow meter was being used to record the flow rate data while conducting the test.

The intersection points between the experimental performance lines of "test 6 with coriolis" and the desired extension performance line provided by Amsted Rail engineering were found based on Figure 118.

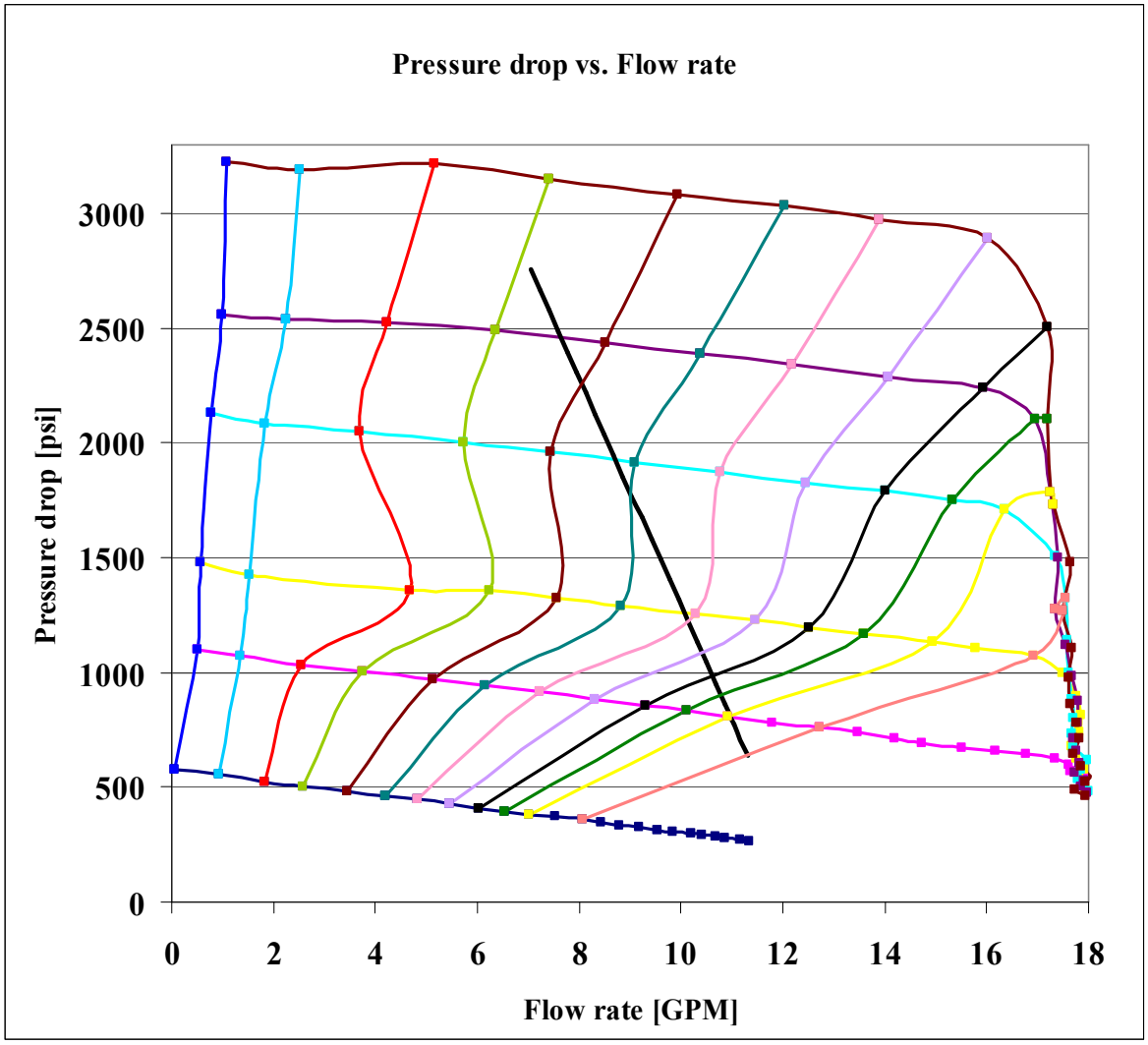

Figure 118: A plot combines the experimental results of "test 6 with coriolis" showed in "Figure 116"with the ones showed in "Figure 117".

All The intersection points that were found based on Figure 118 are summarized in Table 27. The average flow temperature of the collected intersection points is 32°C.

Table 27: A summary of all the intersection points that were found based on Figure 118.

Intersection points of " Test 6 with coriolis"		
Spool stop [quarter turn]	**Pressure drop [psi]**	**Temperature of the flow [^{o}C]**
4.00	2759.1	31.68
4.50	2488.2	35.87
5.00	2262.0	34.39
5.75	1946.0	32.69
6.00	1765.8	33.92
7.00	1256.0	35.60
8.00	1088.0	31.29
9.00	953.1	31.73
11.00	807.0	27.16
13.00	637.0	25.46

The intersection points of "test 6 using coriolis" with the intersection points of test 2 overlay to compare between them are shown in Figure 119 . It was found that the average percentage error between both sets of data is less than 10%. The source of the error was the faulty flow rate readings recorded using the turbine flow meter since it is sensitive to the viscosity changes of the flow as the temperature changes.

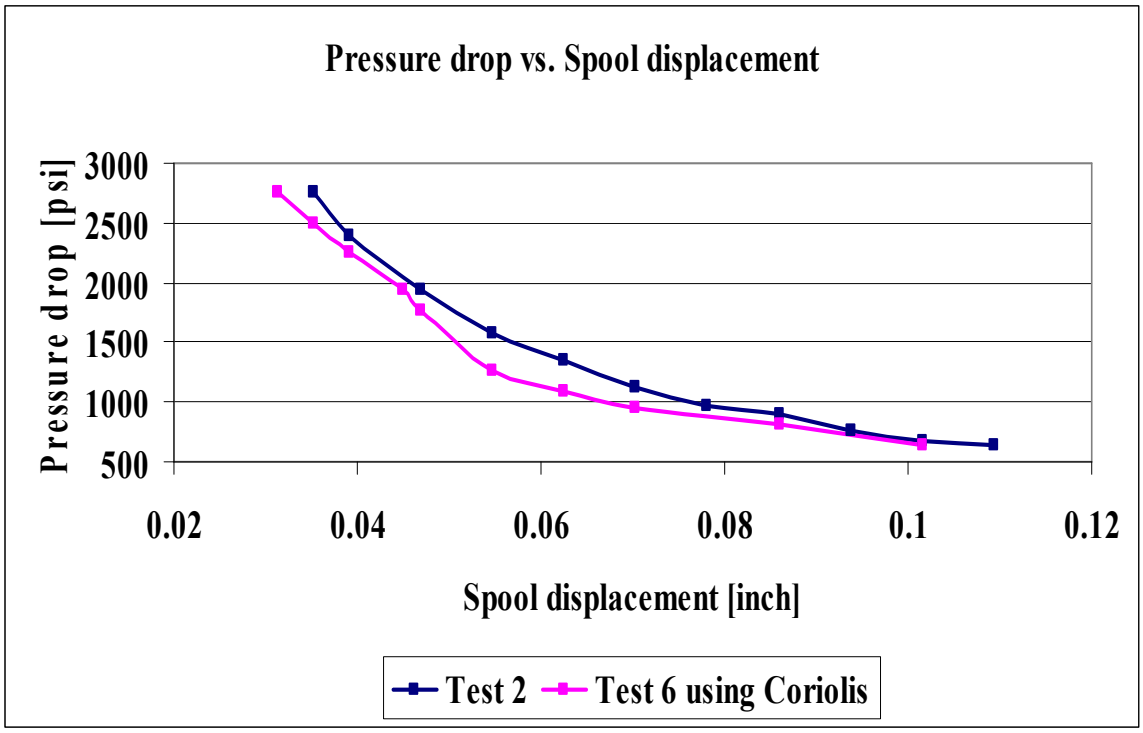

Figure 119: A plot of the pressure drop vs. spool displacement for "test 2" and "test 6 using coriolis."

Two steps were followed to ensure that all the recorded data from the coriolis meter while making the test are as accurate as possible; firstly, the AW46 oil was being passed through the coriolis flow meter for at least 10 minutes at a flow rate greater than 20% of the rated capacity of the K-250 model sensor flow meter (*i.e.* 50 lb/min or 22.6 kg/min); in order to ensure that all the air has been purged from the system. Secondly, the flow was stopped and the coriolis meter was zero calibrated automatically using zero- calibration function provided by its transmitter interface.

Recalibration of the Turbine Flow Meter Based on UVC

In order to compensate for the sensitivity of the turbine flow meter readings to the temperature variation of the flow while making a test, a recalibration of the turbine meter was done based on the UVC principles along with the flow temperature data that were recorded using coriolis flow meter.

The under mentioned steps were followed to recalibrate the turbine flow meter based on the UVC principles over temperature range of 20 to70°C:

1. Density data of the AW46 Hydraulic oil were collected at 20, 25, 30, 40, 50, 60, 70, 80, 90 and 100°C flow temperatures (see Table 28).

2. Absolute viscosity data of the AW46 Hydraulic oil were collected at 0, 20, 25, 40, 60, 70, 80 and 100°C using three different sources (see Table 29).

2. A relationship was established between the kinematic viscosities of the AW46 hydraulic oil (calculated based on the density and absolute viscosity data that were collected in step #1 and 2) and the corresponding flow temperature data recorded using coriolis meter (see Figure 123).

3. The corrected K-factor of the turbine flow meter was found over a coriolis flow rate range of 0.53 to 17.87 GPM at 20, 30, 40, 50, 60 and 70°C flow temperatures

4. A plot of the corrected K-factor versus the coriolis flow rate at different flow temperature was generated based on step #3 data (see Figure 124).

5. The output frequencies of the turbine flow meter (f) corresponding to the corrected K-factor data in step #3 were calculated using Hochreiter equation.

6. A plot of the corrected K-factor versus (output frequency/flow kinematic viscosity) was generated from step #3 data in order to have one curve for the corrected K-factor different flow temperatures (see Figure 125).

7. A parametric fit was found for the curve generated in step #6 using the parametric fitting tool box (*i.e.* CFtool) in Matlab.

8. An algorithm that uses the aforementioned data to get a real time data of flow rate at different flow temperatures (see Figure 126) was programmed in labview.

The algorithm uses the flow temperature (recorded by the coriolis flow meter) and the corresponding output frequency of the turbine flow meter (calculated using Hochreiter equation) as inputs, in order to calculate the actual volumetric flow rate through the turbine flow meter.

Density and Absolute Viscosity Data of AW46 Hydraulic Oil

The density data of AW46 oil were recorded at different flow temperatures using the coriolis flow meter as shown below.

Table 28: Density data of AW46 hydraulic oil at different flow temperatures.

Flow Temperature recorded using coriolis meter [^{o}C]	**Density of the flow [kg/m^{3}]**
20	864.4999
25	861.9808
30	860.0000
40	848.4866
50	843.0000
60	837.1786
70	830.0605
80	827.9819
90	825.5000
100	821.4487

The absolute viscosity data of AW46 hydraulic oil were collected using three different sources:

1. Absolute viscosity tests conducted at the engineering fluid laboratory at the University of Texas Pan American. The tests were conducted on an AW46 oil sample using Brookfield DV-III Ultra Rheometer with a TC-102 water bath to heat or cool the oil sample to the temperature where the viscosity need to be recorded. All the data of absolute viscosity and flow temperature were collected using Rheocalc software.
2. Viscosity tests conducted on the same aforementioned sample of AW46 oil at Brookfield Engineering using a thermosel with an SC4-18 spindle, LVDV-III instrument and Rheocalc software (see Figure 120). The results show that this type of oil is a pseudo plastic at temperatures higher than 40°C.
3. Online chart shows the absolute viscosity of ISO-46 oil (*i.e.* another standard name for the AW46 hydraulic oil) as a function of temperature (see Figure 121).

A summary of all the viscosity data that were extracted using each of aforementioned sources along with kinematic viscosity data that supplied by the oil manufacturer (Warren oil company) is provided in Table 29 for comparison. Absolute viscosity data at 0 and 20°C of the first source along with viscosity data at 25, 40, 60, 70, 80 and 100°C of the second source were used for kinematic viscosity calculations of AW46 hydraulic oil (see Table 30), since it was believed that these data are the most accurate among the other ones listed in Table 29.

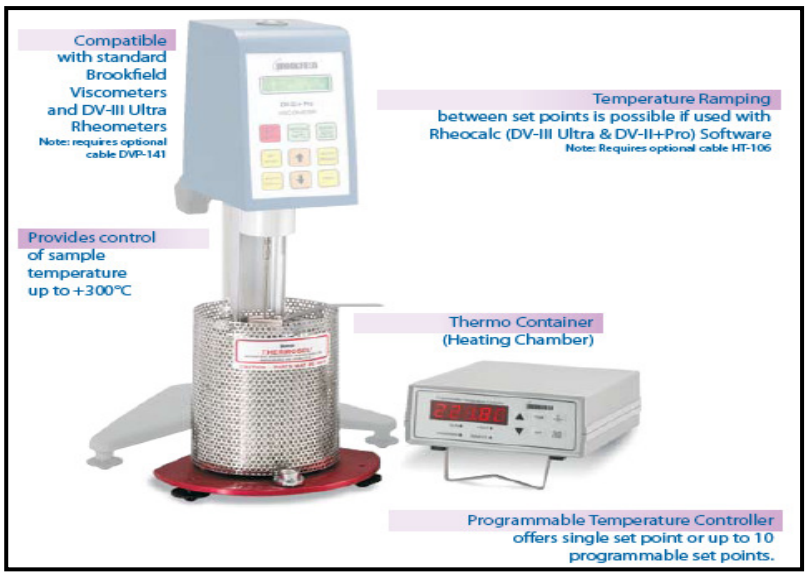

Figure 120: A picture of the Brookfield thermosel with an SC4-18 spindle, LVDV-III instrument. (Courtesy of Brookfield engineering)

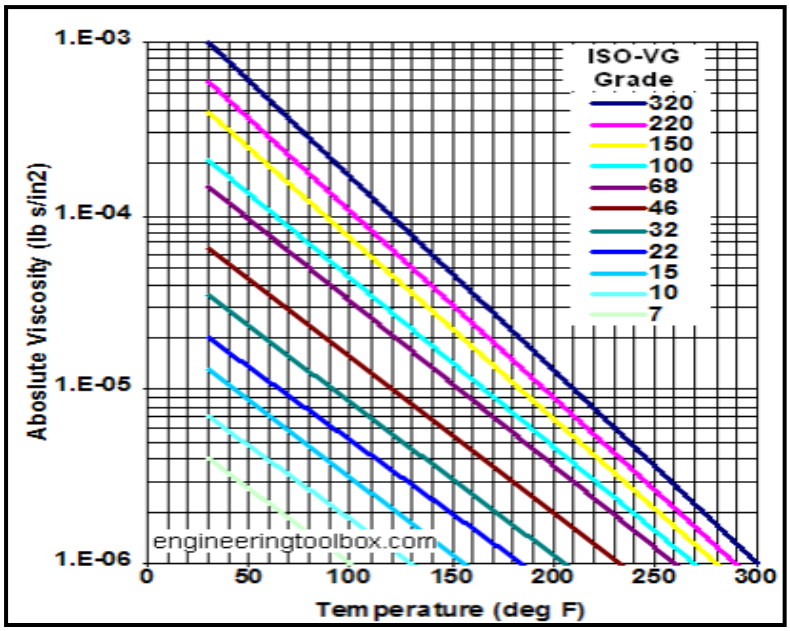

Figure 121: A picture of a chart shows the absolute viscosity of ISO-VG grade oil as a function of its temperature.

(Courtesy of http://www.engineeringtoolbox.com)

Table 29: A summary of all the viscosity data that were extracted using each of aforementioned sources along with kinematic viscosity data that supplied by the AW46 oil manufacturer (Warren Oil Company).

Temperature of the flow [°C]	**Warren Oil Company Kinematic viscosity [cSt]**	**Source**		
		UTPA Research team	**Brookfield Engineering**	**Chart from a website**
		Absolute viscosity [cP]		
0	-	412.0	-	400.0
20	-	110.0	-	200.0
25	-	-	84.85	-
40	46.50 cSt	50.72 **(59.77cSt)**	43.62 **(51.40cSt)**	100.0 **(117.8cSt)**
60	-	33.60	18.68	40.00
70	-	29.00	14.26	30.00
80	-	26.00	10.61	20.00
100	6.800 cSt	23.00 **(28.00 cSt)**	7.510 **(9.150cSt)**	10.00 **(12.18 cSt)**

The chosen absolute viscosity data from Table 29 are tabulated along with their corresponding density and calculated kinematic viscosity values in Table 30 . The kinematic viscosity was calculated using the following equation

$$\nu = \frac{\mu}{\rho} \times 10^3 \tag{28}$$

where υ is the Kinematic viscosity in cSt, μ is the absolute viscosity in cP and ρ is the density in kg/m3.

Table 30: A summary of the selected absolute viscosity data of AW46 hydraulic oil along with its corresponding flow temperature, flow density and kinematic viscosity values.

Flow Temperature recorded using coriolis meter [°C]	**Density of the flow (see Table 28) [kg/m^3]**	**Absolute Viscosity (see Table 29) [cP]**	**Kinematic Viscosity (From Eq.(28)) [cSt]**
0	890.0000	412.00	462.9213
20	864.4999	110.00	127.2412
25	861.9808	84.850	98.43607
40	848.4866	43.620	51.40918
60	837.1786	18.680	22.31304
70	830.0605	14.260	17.17947
80	827.9819	10.610	12.81429
100	821.4487	7.5100	9.142385

It is important to mention that the density of AW46 oil at 0°C could not be measured since it was impossible to reach that temperature using the current testing setup. Thus, the specific gravity of AW46 oil that was mentioned previously in Chapter III (*i.e.* 0.89) was used to calculate the density of the oil at 0°C (it was assumed that water has ρ=1000kg/m^3 at 0°C).

A plot of the kinematic viscosity data versus its corresponding flow temperature (see Table 30) was generated as shown in Figure 122 and 123.

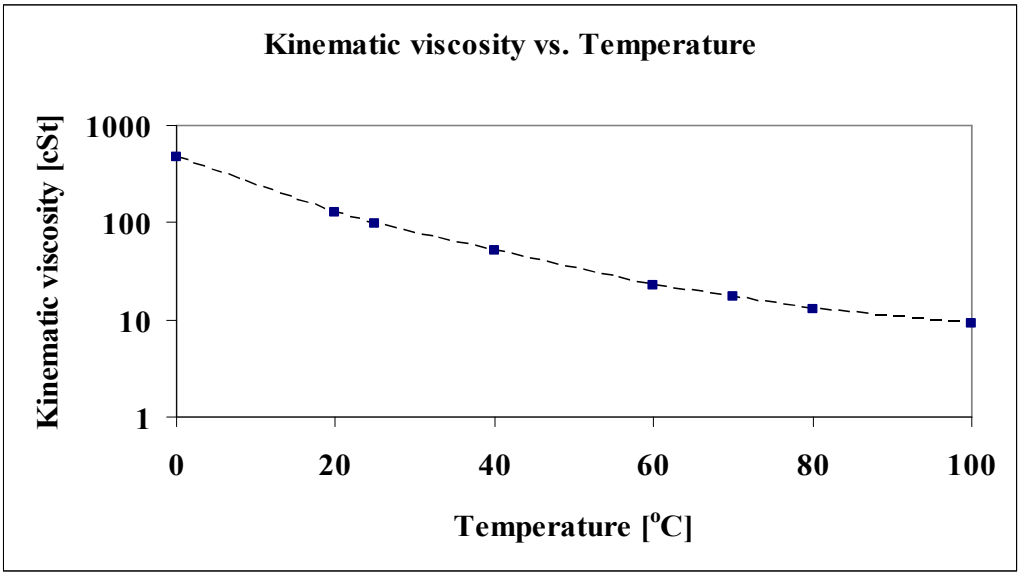

Figure 122: A plot of the kinematic viscosity of AW46 hydraulic oil versus the flow temperature.

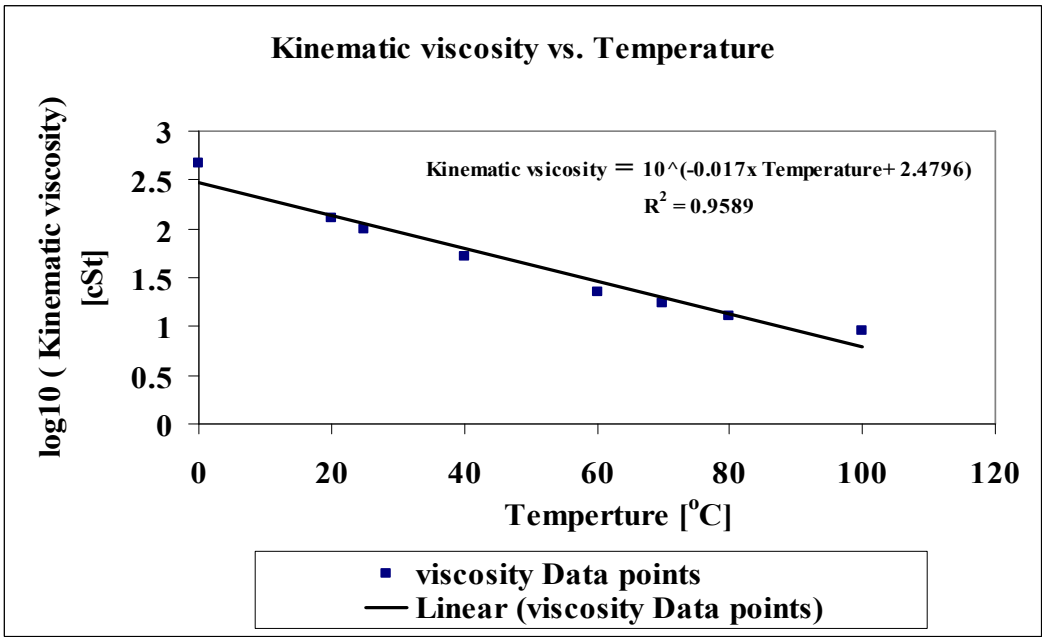

Figure 123: A plot of the logarithmic of the kinematic viscosity vs. temperature.

Based on Figure 122, the kinematic viscosity of the AW46 Oil (*i.e.* υ) decreases linearly (only when the kinematic viscosity is plotted on the logarithmic scale) as the temperature of the flow increases as predicted initially from the behavior of the ISO-VG grade oils shown in Figure 121. In addition, a power function that relates between both the aforementioned variables numerically was found as shown in Figure 123.

Corrected K-Factor Calculations of the Turbine Flow Meter

The experimental setup shown in Figure 114 was used to record different flow rate readings from both the turbine flow meter and the coriolis one (master flow meter) at different flow temperatures. Spool #2 was mounted and centered inside the test valve in order to obtain the maximum flow rate of 18 GPM from the hydraulic power unit. In addition the pressure setting on the power unit was 1500 psi (which is the lowest pressure setting that can give the maximum flow rate without heating the flow significantly while making the test). The HEDLAND flow meter (see Chapter III) was used to control the flow rate that was passing through the turbine and the coriolis flow meter while making the test. As a result, different flow rate readings were recorded from the turbine flow meter and compared to the coriolis ones at constant flow temperature. Thus, the corrected K-factor values at this constant flow temperature were calculated using the same technique that was mentioned previously in Chapter III to do the first calibration of the turbine flow meter.

A plot of the corrected K-factor of the turbine flow meter versus the flow rate recorded using the coriolis flow meter was generated in Figure 124 for 20, 30, 40, 50, 60 and 70°C flow temperatures.

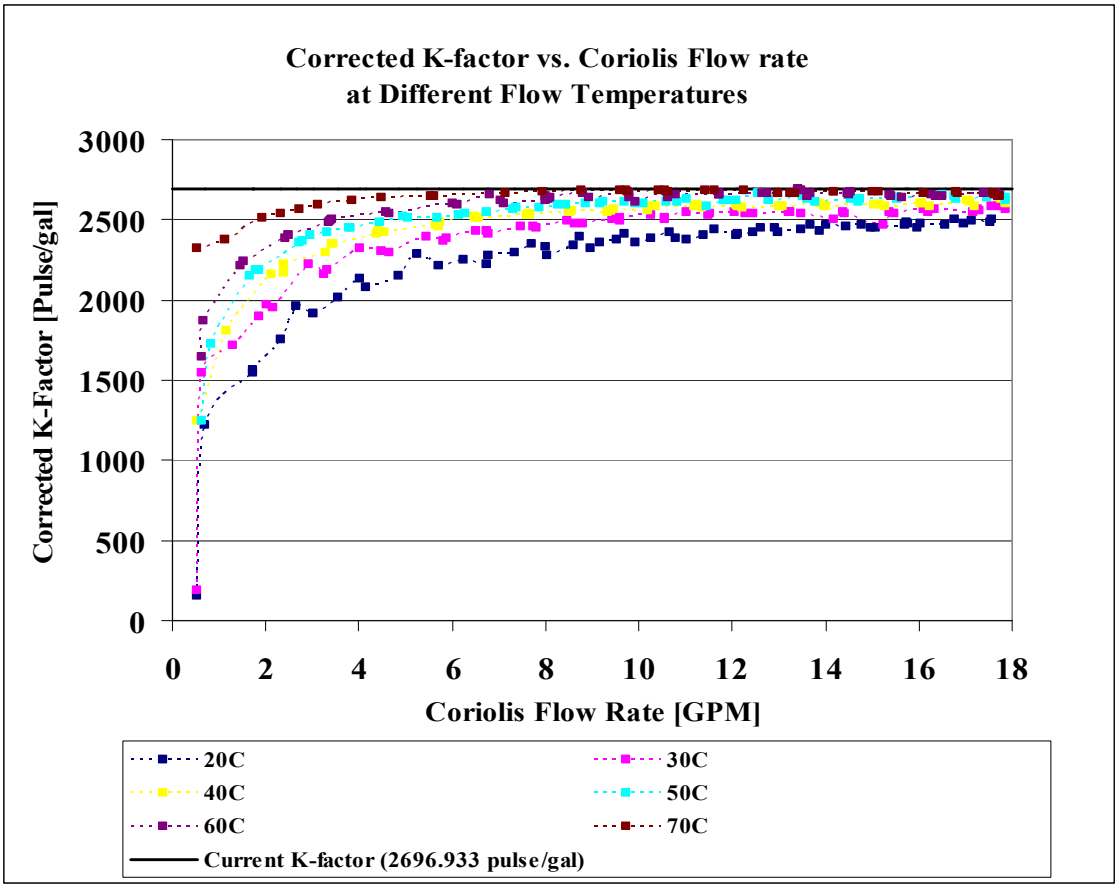

Figure 124: A plot of the corrected K-factor of the turbine flow meter versus the flow rate recorded using the coriolis flow meter at different flow temperatures.

It can be noticed from the above figure that the discrepancy between the meter corrected K-factor values and the current one stored inside the turbine flow meter memory (*i.e.* K-factor value obtained from the first calibration of the turbine flow meter, see Chapter III) increases at lower flow rates and/or at lower flow temperatures.

In order to get one continuous curve of the meter corrected K-factor covering the range of the possible flow temperatures (*i.e.* 20 to 70°C) and thus covering the range of possible turbine flow meter frequencies and viscosities, the data in Figure 124 was represented on a plot called a

Universal Viscosity Curve (UVC). The UVC is formed by plotting the meter corrected K-factor versus the output frequency divided by kinematic viscosity.

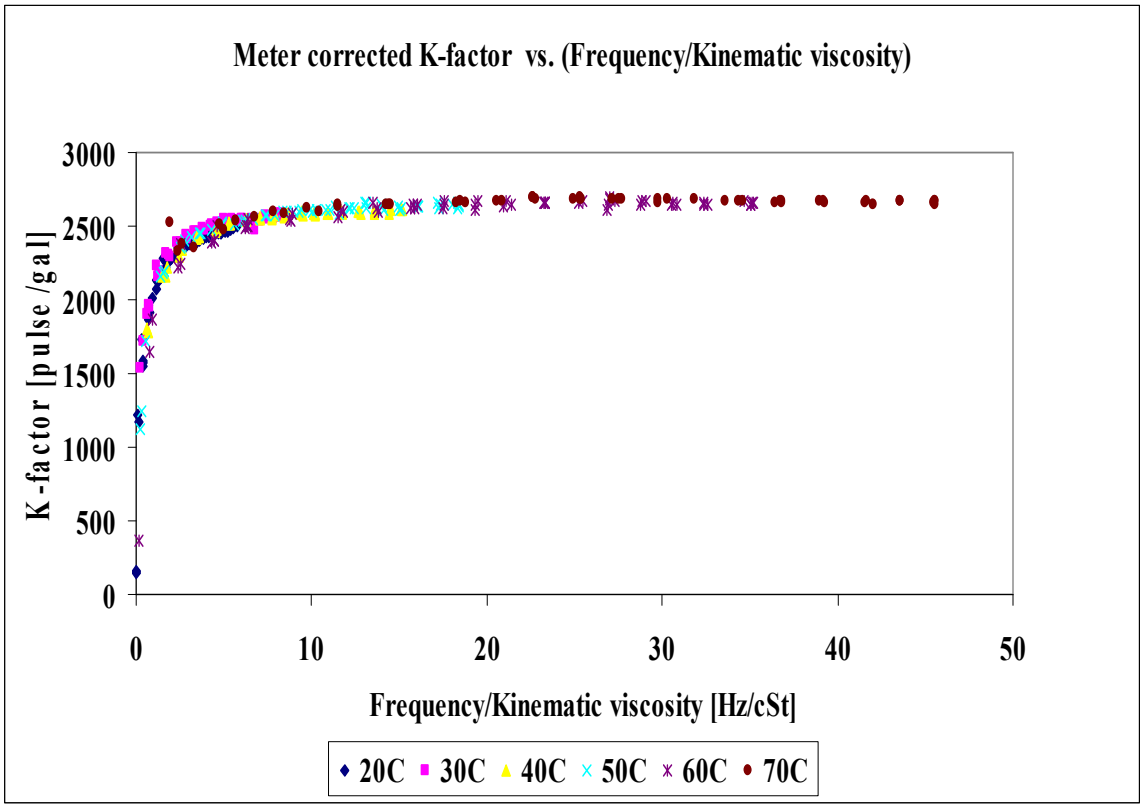

Figure 125: A plot of the UVC for B2800 KIMRAY turbine flow meter when using AW46 hydraulic oil.

Since no absolute viscosity tests were conducted at 30 and 50°C flow temperatures (see Table 29), the power function shown in Figure 123 (*i.e.* the numerical function that relates the kinematic viscosity of the AW46 Oil with the flow temperature) was used to compute the kinematic viscosities of the oil at both aforementioned temperatures.

The output frequency of the turbine flow meter was calculated using Hochreiter equation [101]:

$$f = \left(\frac{K1 \times Q1}{60} \right)_{turbine} = \left(\frac{K2 \times Q2}{60} \right)_{coriolis} \tag{29}$$

where f is the turbine meter output frequency in Hz, *K1* is the current K-factor programmed inside the memory of the turbine flow meter (*i.e.* 2696.933 pulse/gal) in pulse/gal, *Q1* is the turbine meter flow rate readings in GPM, *Q2* is the coriolis meter flow rate readings in GPM and *K2* is the corrected meter K-factor corresponding to *Q2* in pulse/gal.

Using Matlab parametric fittings tool box, a rational function (cubic/cubic) was found to be the best fit for the curve shown in Figure 125. The equation of this fit is described by the following

$$K = \frac{2668 \times y^3 - 6231 \times y^2 + 1943 \times y + 20.57}{y^3 - 2.012 \times y^2 - 0.02945 \times y + 0.2488} \tag{30}$$

and

$$y = \frac{f}{\upsilon} \tag{31}$$

All the best fit models along with their Goodness of fit values are summarized in Table 31 (see below).

Table 31: A summary of all the best fit models of the curve shown in Figure 125 along with their R-square values.

Fit-Model Type	R-Square
Rational fit(cubic/cubic)	0.982
Power fit	0.978
Cubic polynomial	0.968
Gaussian fit	0.89
9th degree polynomial	0.83
Sum of sin functions	0.80

The algorithm that was programmed in the labview in order to calculate the actual flow rate passes through the turbine meter at different flow temperatures is shown below.

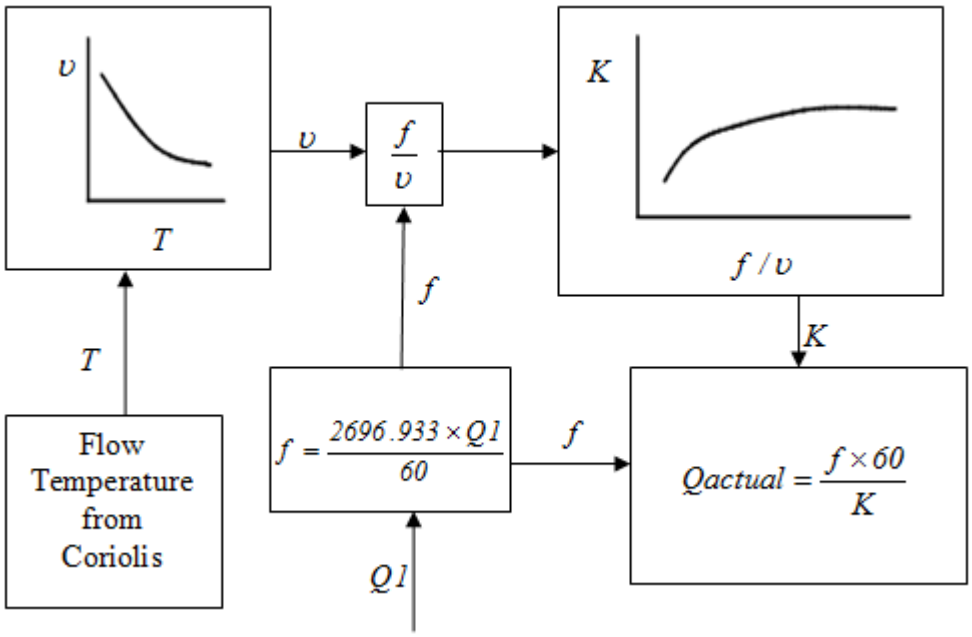

Figure 126: A flow chart that shows how the actual flow rate of the turbine meter is calculated based on flow temperature measured by coriolis meter.

To test the aforementioned algorithm, an experiment was conducted with spool #2 was mounted and centered inside the test valve. In addition, the pressure setting was kept at 1500 psi and the flow rate coming out from the power unit was controlled using the HEDLAND flow meter. Furthermore, the thermostat was set at 70°C to allow the flow to heat up from the room temperature (*i.e.* 18°C) while making the test. Table 32 shows a summary of results obtained for this test.

Table 32: A summary of the results of the experiment that was conducted to test the algorithm shown in Figure 126.

Temperature range [^{o}C]	**Coriolis flow rate [GPM]**		**Turbine meter %error before correction**	**Turbine meter %error after correction**
	Minimum	**Maximum**		
18-30	0.42	10.72	31.28	5.76
31-40	0.86	13.93	17.42	4.87
41-50	0.73	18.29	7.790	1.87
51-60	1.33	17.87	4.150	1.30
61-70	1.89	17.85	3.730	1.21

It can be noticed from the above table that the used algorithm reduces the discrepancy significantly between the turbine meter flow rate readings and the coriolis ones. In addition, this discrepancy between flow rate readings before and after correction decreases as the flow temperature increases.

Experimental Results of Test 9, 10, 13 and 14

Test 9 and 10 were the initial conducted tests on spool #7. The results of both tests showed that the desired linear performance for the retraction side of the Amsted Rail hydraulic damper can be achieved at one spool stop if the flow temperature at the downstream side of the test valve is kept constant at 50°C (see Figure 128 and 129).

The same flow temperature conditions of test 10 were used in test 13 for spool #8, but the results of this test showed that spool #8 could not deliver enough flow to intersect with the desired extension performance line at applied pressures lower than 1500 psi (see Figure 130). As a result, spool #8 was modified to have the same starting land diameter as spool #7 (*i.e.* 0.465 in. diameter) and extra land length of 0.125 inch; since the results of test 10 when overlaid with the desired extension side performance, the intersection between both performances happened at earlier spool stop compared to spool #8 test results (test 13) as shown in Figure 131.

The results of the initial conducted test on the modified version of spool #8 (test 14) showed an agreement with the targeted pressure drop/spool displacement performance described previously in Chapter IV (see Figure 134).

Experimental Results of Test 9 and 10

At the beginning of each sub -experiment of both test 9 and 10, the flow window is fully closed and as spool # 7 moves inside the valve test as shown in Figure 127, the larger diameter land of spool #7 (0.465 in. diameter) appears first inside the window and after 24 spool stops the smaller diameter land of the same spool (0.431 in. diameter) appears in the same flow window.

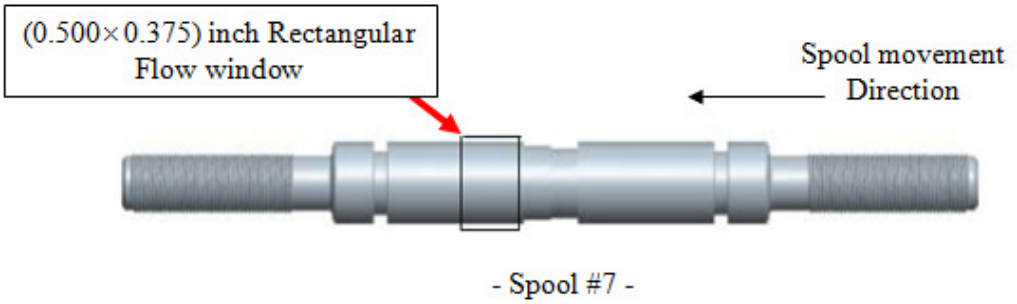

Figure 127: A CAD drawing of spool #7 shows the testing procedure of each sub-experiment for test 9 and 10.

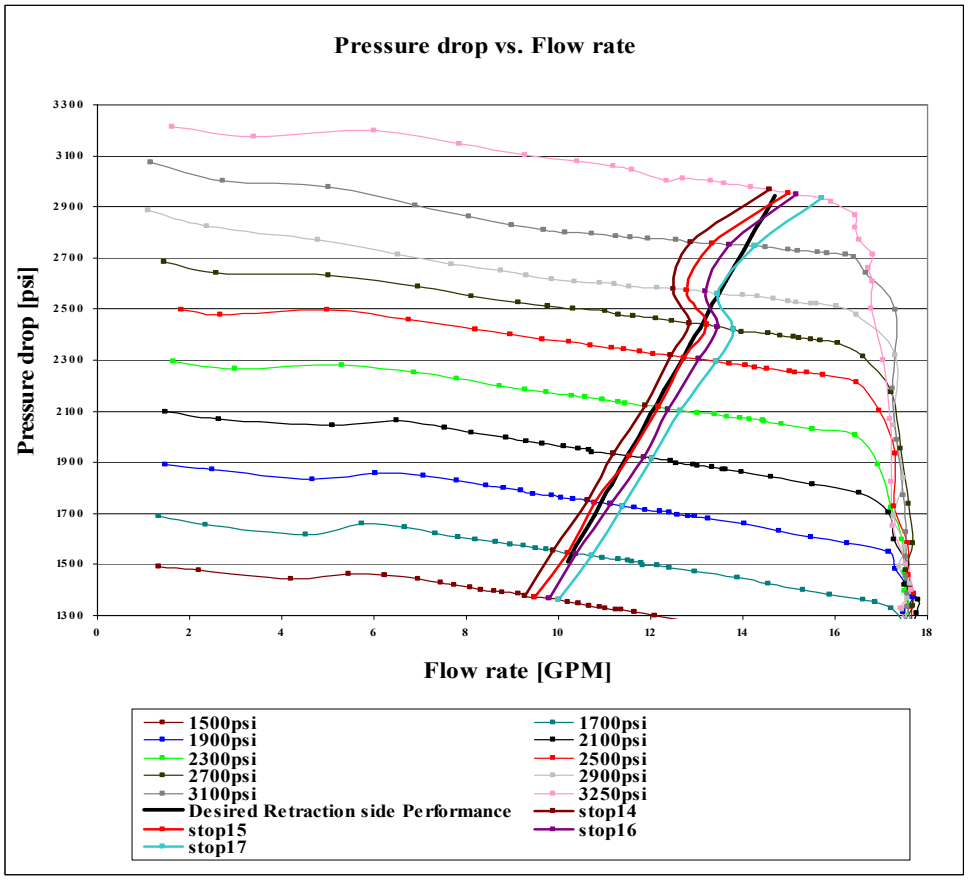

Figure 128: A plot of the pressure drop versus flow rate results of test 9. (The 500 to 1300 psi sub-experiments were excluded from the figure since they did not have any contribution to the desired performance)

The downstream flow temperature was found to be 50 ± 3°C along the straight portion of the performance lines of stop #14, 15, 16 and 17 (see Figure 128). In addition, the last three points of each performance line of the same stops (*i.e.* the portion of the performance line where it starts to curve) was found to have three different flow temperatures of 40, 38 and 62°C respectively. Thus, it was concluded that the flow temperature has an influence on the linearity of the spool performance.

As a result, test 9 was repeated again with the downstream flow temperature was kept at 50 ± 3°C throughout the test. Thus, the desired retraction performance was fully achieved at spool stop #15 as shown in Figure 129.

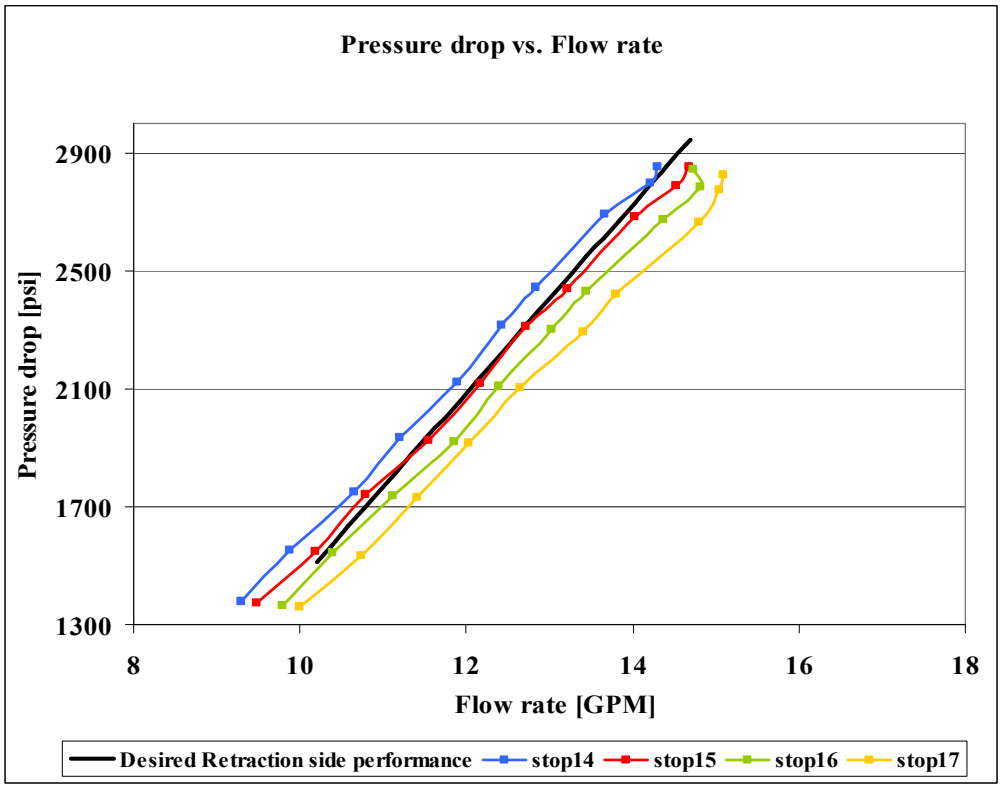

Figure 129: A plot of the pressure drop versus flow rate results of test 10 at spool stop #14, 15, 16 and 17.

Experimental Results of Test 13 and 14

The results of test 13 are shown in Figure 130. It can be noticed that spool #8 could not deliver enough flow to intersect with the desired extension performance line at applied pressures lower than 1500 psi.

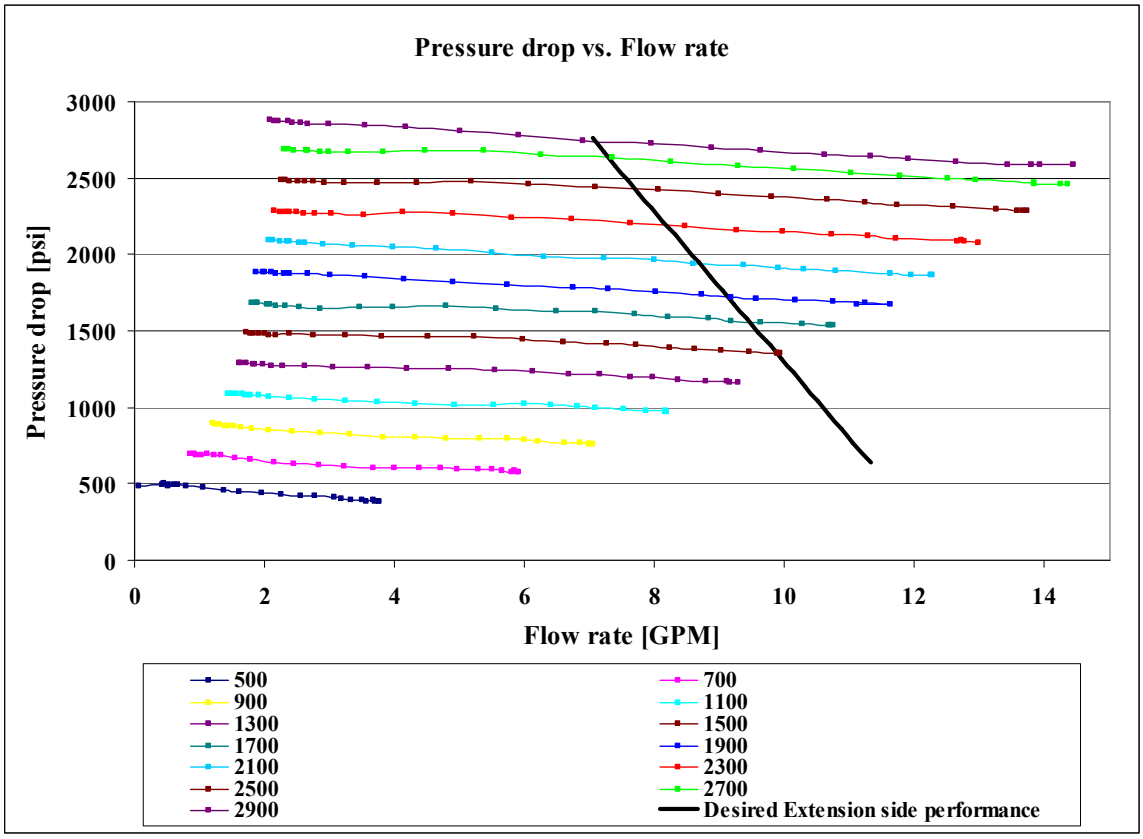

Figure 130: A plot of the pressure drop versus flow rate results of test 13 for spool #8.

Since spool #7 intersects with the desired extension performance line at earlier stop (the same starting stop as spool #2/slope side and spool #2/curved side) compared to spool #8 as shown in Figure 131, the starting land diameter of spool #8 was modified to match the one of spool #7 (see Figure 132).

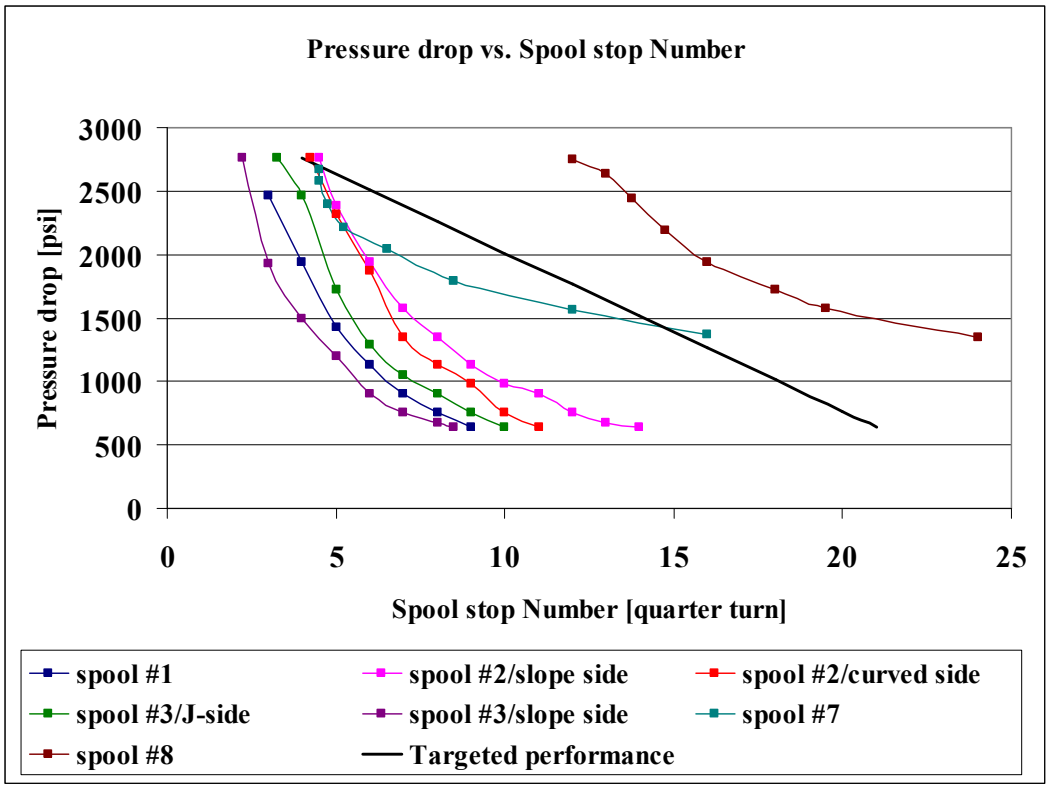

Figure 131: A plot of the pressure drop versus spool stop number for test 1-5, 10 and13. (The plot was generated using the intersection points between the spool stop's performance lines and the desired extension performance line)

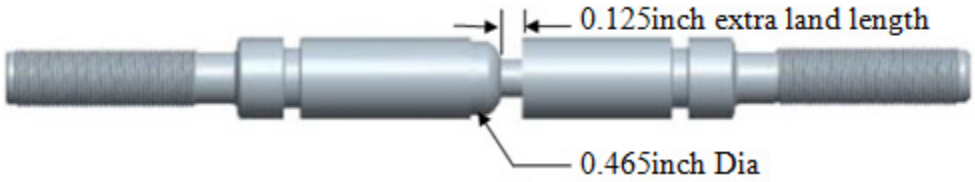

Figure 132: A CAD drawing of the modified version of spool #8 (*i.e.* spool #8A).

The experimental results of test 14 are shown below.

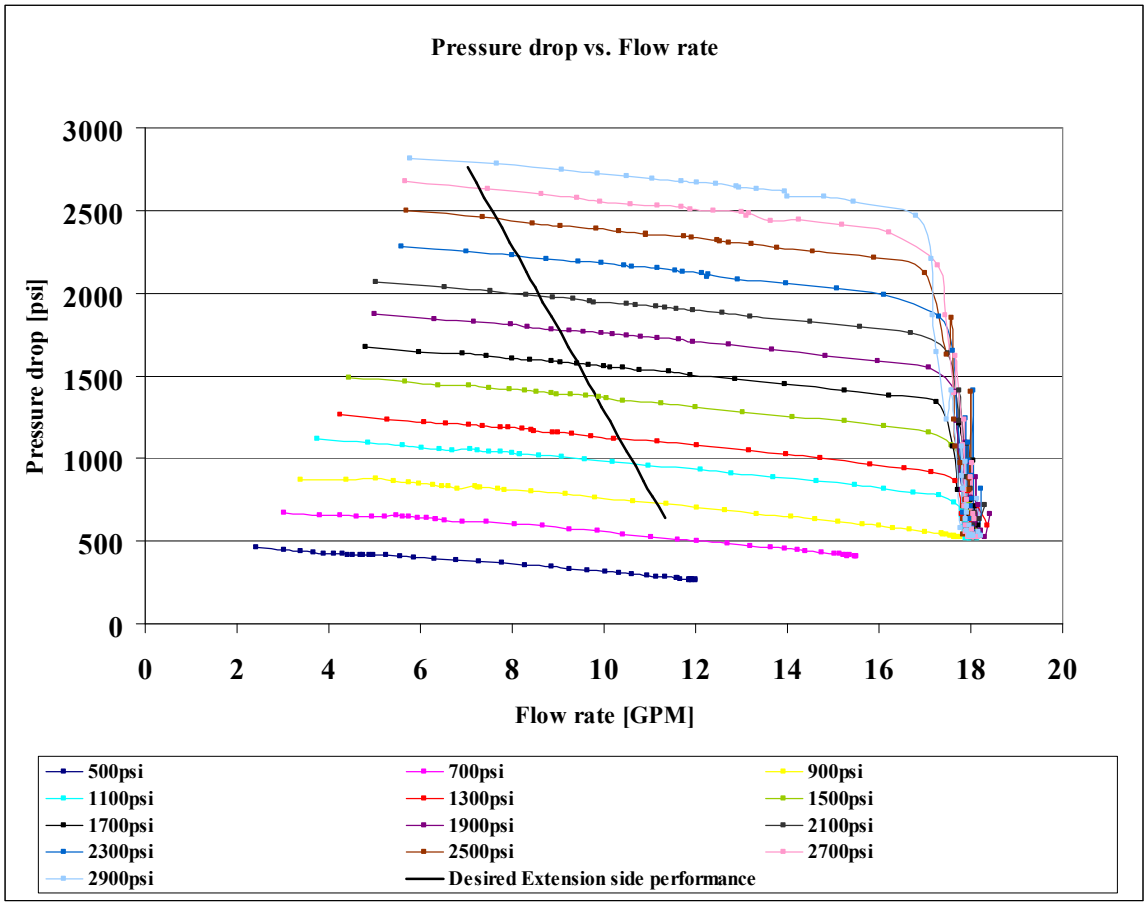

Figure 133: A plot of the pressure drop versus flow rate results of test 14 for spool #8A.

The intersection points between the experimental performance lines of spool #8A shown above and the desired extension performance line are shown in Figure 134, along with the targeted performance for the pressure drop versus the spool stop number that was developed previously in Chapter IV.

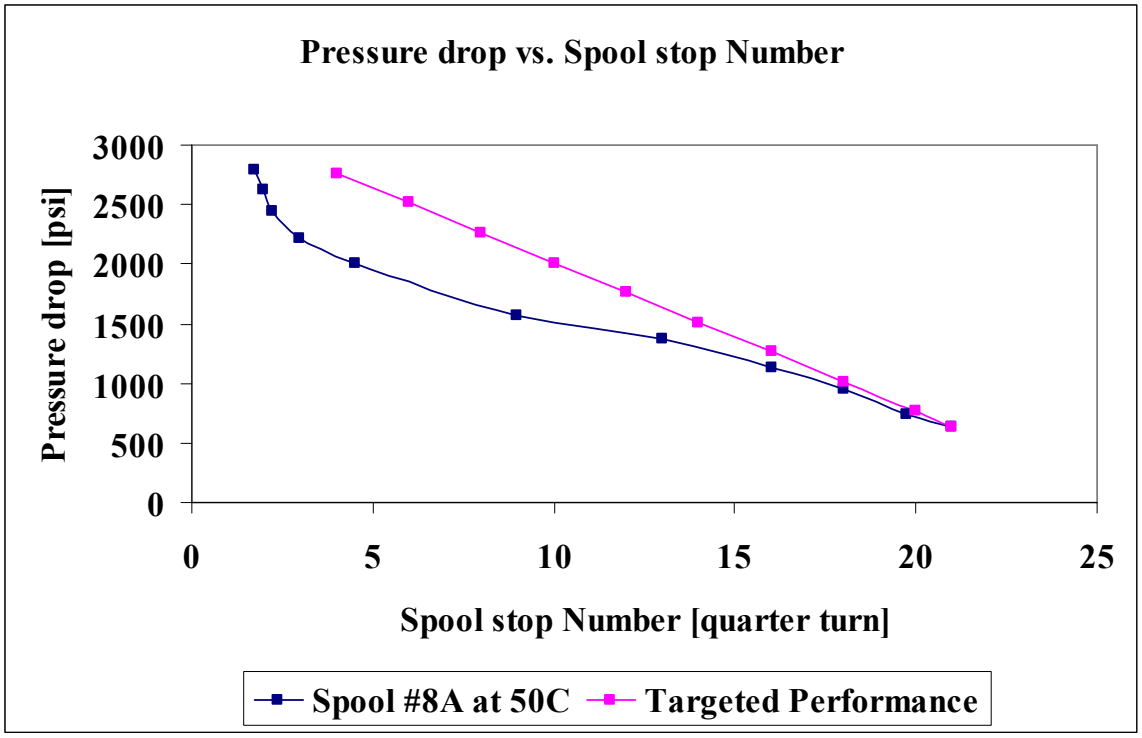

Figure 134: A plot of the pressure drop versus spool stop number for test 14.

Experimental Results of Test 11, 12, 15 and 16

Two spring-loaded Omega RTDs were mounted inside two Omega thermo wells before and after the test valve (see Figure 135). A bushing placed above each RTD followed by a spring and bolt with hole for the RTD wire (see Figure 136). Thus, the spring keeps each RTD in contact with bottom of the well at all the time, in order to eliminate any delay in the RTD readings caused by any possible gap between the two. In addition, each thermo well was filled with thermal grease to enhance the thermal conductivity between the RTD and its corresponding thermo well surfaces.

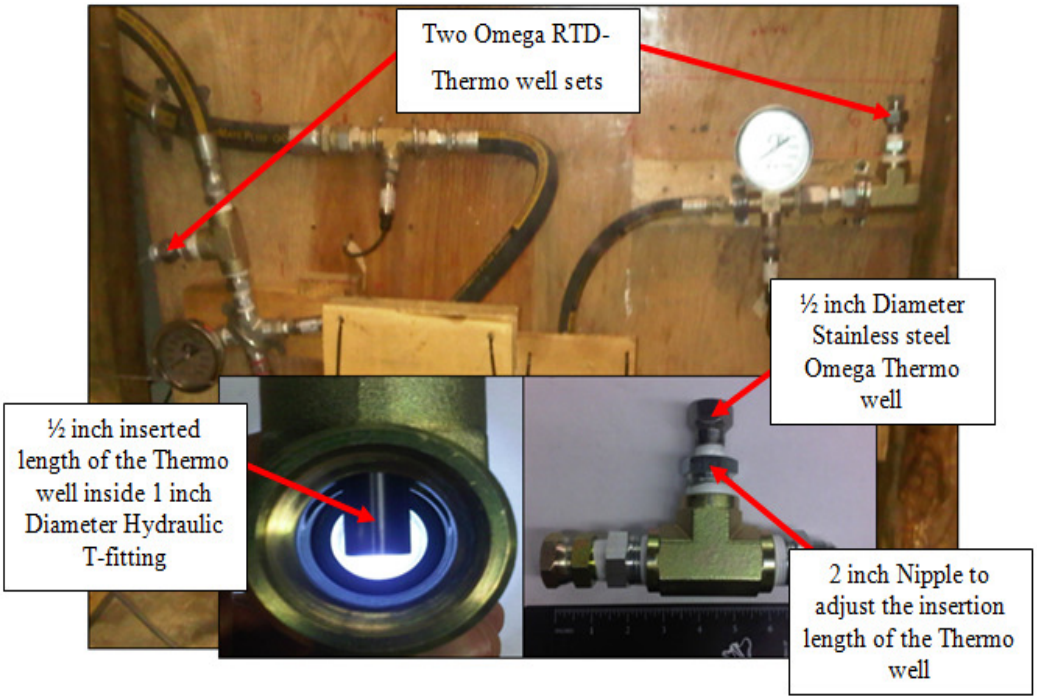

Figure 135: A picture of the same setup shown in Figure 114 with the two RTD-thermo well assemblies were added to measure the flow temperature before and after the test valve.

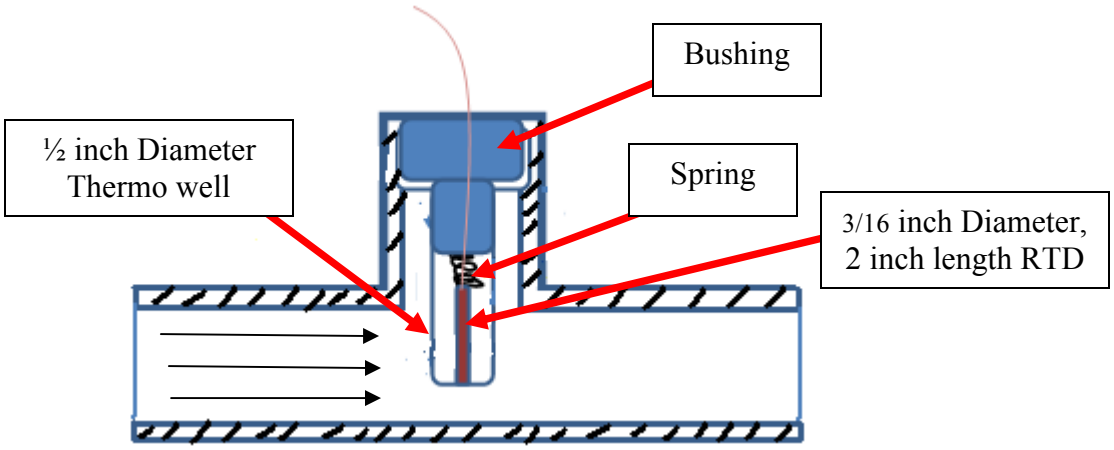

Figure 136: A schematic shows how the RTD was mounted inside the thermo well.

Table 33: A summary of the RTD sensor specifications as given from Omega.

Specification	Description
Omega RTD Model	PR-20-2-100-3/16-2-E-G
Operating Temperature	-200 to 260°C (-328 to 500°F)
Probe Diameter	3/16 in.
Probe length	2 in.
Accuracy	± 0.5% of full scale
Response Time	120 ms

It can be noticed from Figure 135 that one RTD-thermo well assembly was installed before the upstream pressure transducer and the other one was installed after the downstream pressure transducer, in order to prevent any additional pressure drop that both RTD-thermo well sets could cause beside the one caused by the test valve.

A thermo well was used with each RTD, because it gives a pressure allowance of 5000 psi since the RTDs by itself do not have the required pressure rating. In addition, An Omega SPRTX signal converter was used in series with each RTD to convert the temperature signal captured by the RTD to DC current signal (*i.e.* 4-20 mA analog output signal). As a result, it was possible to get real time data of the flow temperature before and after the test valve using the previously developed labview program.

The electric power requirements of both three wire model RTDs that were being used are similar to those of the pressure transducers (see Chapter III).

A 270 Ω resistor was used to change the 4-20 mA current output of each SPRTX signal converter to voltage signal that the USB DAQ can acquire while making the tests. The equation that was programmed in labview to convert the 4-20 mA current input from the SPRTX signal convertor into temperature reading was provided from Omega and is given by:

$$T_{flow} = 19.186 \times I - 175.73 \tag{32}$$

where I is the output current from the SPRTX signal converter in milliamperes and T_{flow} is the temperature of the flow in degree Celsius (°C). It is important to mention that I was calculated using Eq. (25).

Since it was more reasonable to base the performance of spool #7 and spool #8A on the inlet flow temperature rather than to the downstream temperature that was measured initially by the RTD built inside the coriolis flow meter, test 10 (for spool #7) and test 14 (for spool #8A) were repeated based on an inlet flow temperature of 45°C.

An upstream flow temperature of 45°C was chosen, since the results of an abbreviated test done on spool #7 at stop #15 (*i.e.* the same stop where the desired retraction side was achieved in test 10, see Figure 129) shows that the RTD mounted before the test valve was reading a temperature of 45°C when the downstream temperature was at 50°C.

Thus, test 10 of spool #7 was repeated based on an inlet flow temperature of 45°C and this new test was called test 11. In addition, test 14 of spool #8A was repeated based on the same aforementioned upstream temperature and this new test was called test 15.

After the aforementioned tests results of spool #7, spool #8 and spool #8A (*i.e.* tests 9, 10, 11, 13, 14 and 15) were sent to Amsted Rail Engineering, they decide to set the design temperature of spool #7 and spool #8A at 25°C.

Thus, test 11 of spool #7 was repeated based on an inlet flow temperature of 25°C and this new test was called test 12. In addition, test 15 of spool #8A was repeated based on the same aforementioned upstream temperature and this new test was called test 16.

Experimental Results of Test 11 and 15

The results of test 11 are shown in Figure 137. It can be seen from test results that the desired retraction side performance is enclosed between stop #14 and 15 of spool #7 with the inlet flow temperature of the test valve kept at 45 ± 3°C.

As mentioned previously, the inlet flow temperature of 45°C was picked for test 11; since an abbreviated test was conducted using the setup shown in Figure 135 at stop #15 of spool #7 to see the temperature difference across the test valve at this spool stop if the downstream temperature was kept at 50°C. This temperature difference was found to be 5°C. Thus, in order

to get the same results of test 10 with downstream flow temperature of 50°C, test 11 was conducted with upstream flow temperature of 45°C.

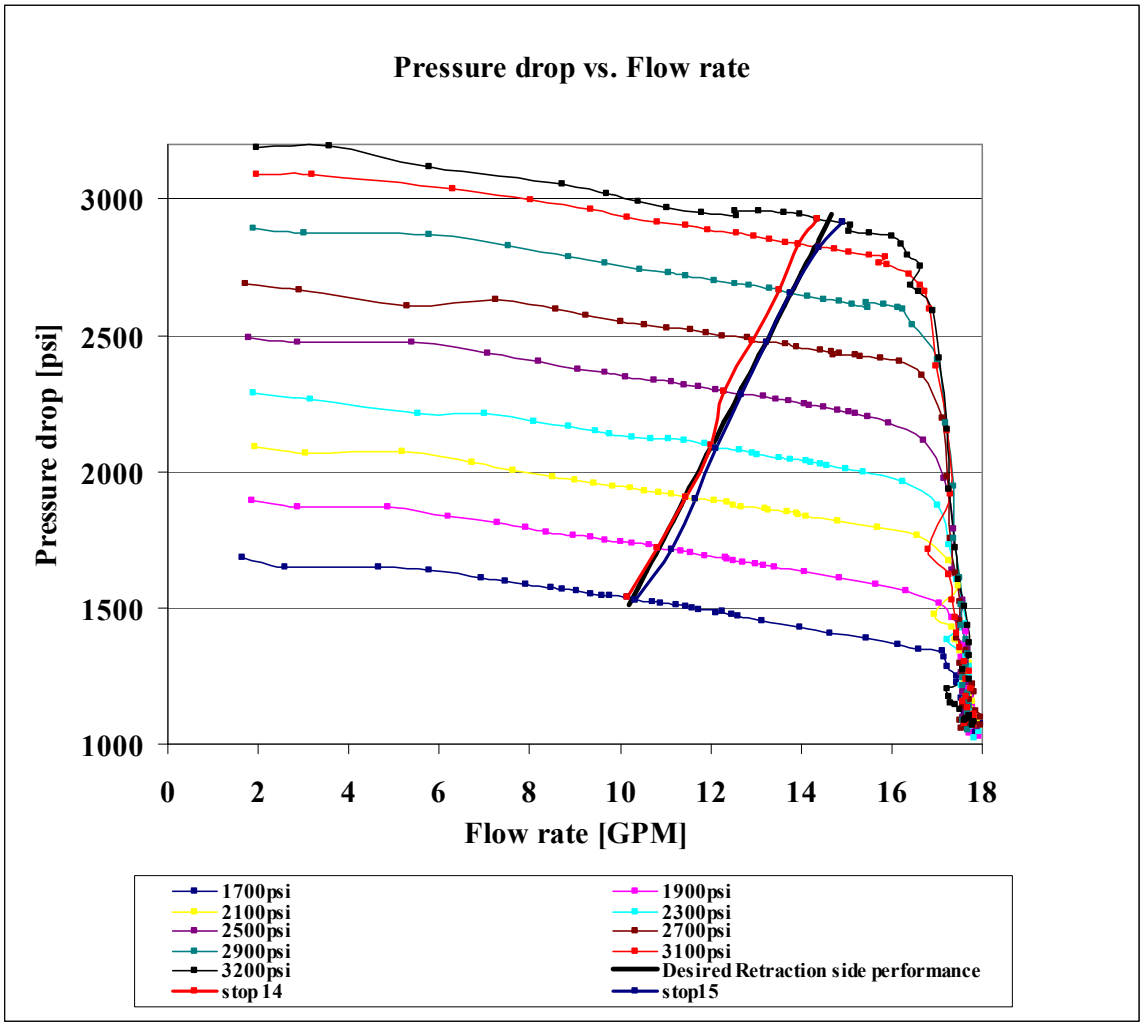

Figure 137: A plot of the pressure drop versus flow rate results of test 11 for spool #7.

In order to quantify the temperature influence on stop #15 of spool #7, stop #15 was tested for four different applied pressures of 1817, 2200, 2400 and 2536 psi along with three different inlet flow temperature of 35, 45 and 55°C. The results are shown in Figure 138.

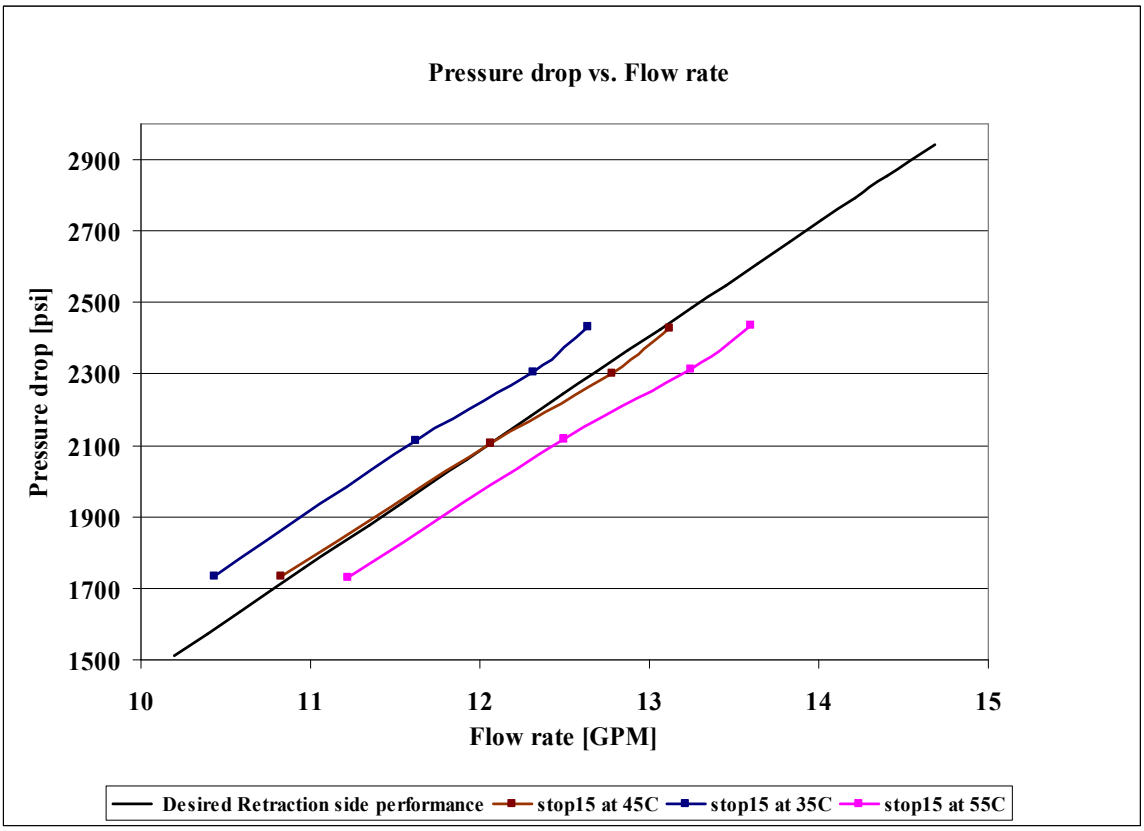

Figure 138: A plot of the pressure drop versus flow rate results for stop #15 of spool #7 at three different inlet flow temperatures of 35, 45 and 55°C.

From the above Figure, the percentage increase in the flow rate was found to be 7.57% for 20°C temperature increase.

The results of test 15 are shown in Figure 139 and 140.

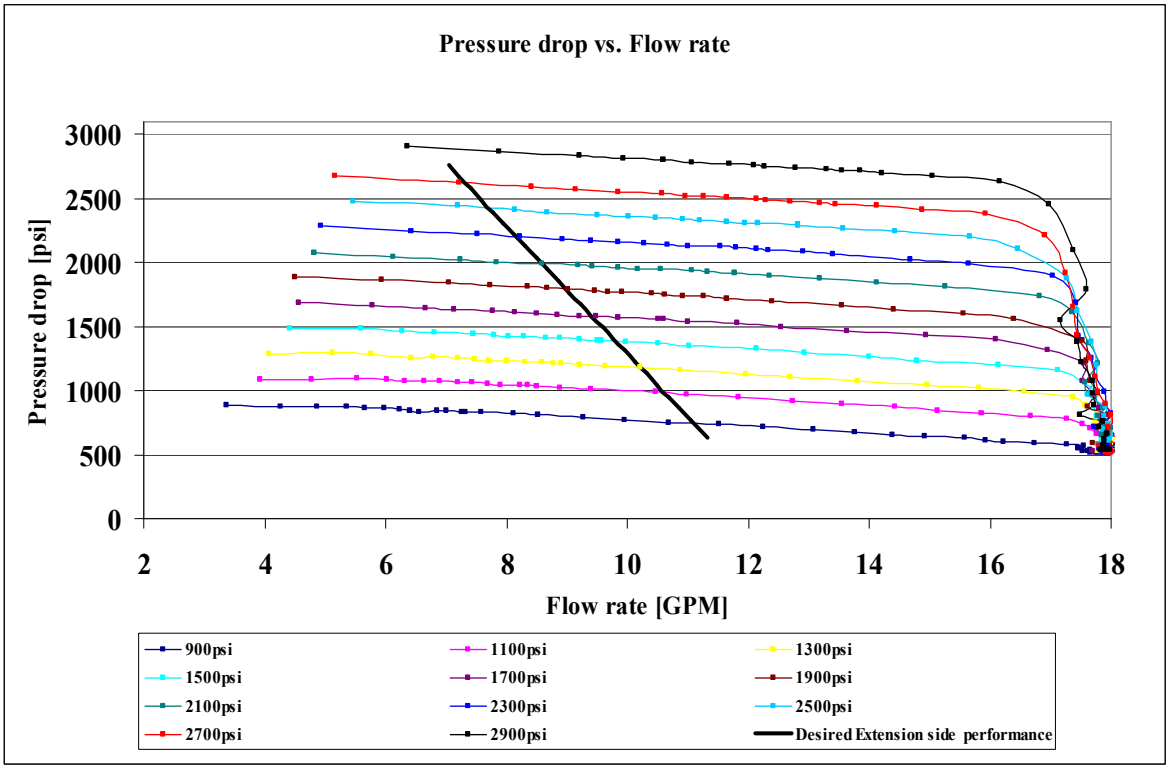

Figure 139: A plot of the pressure drop versus flow rate results of test 15 for spool #8A.

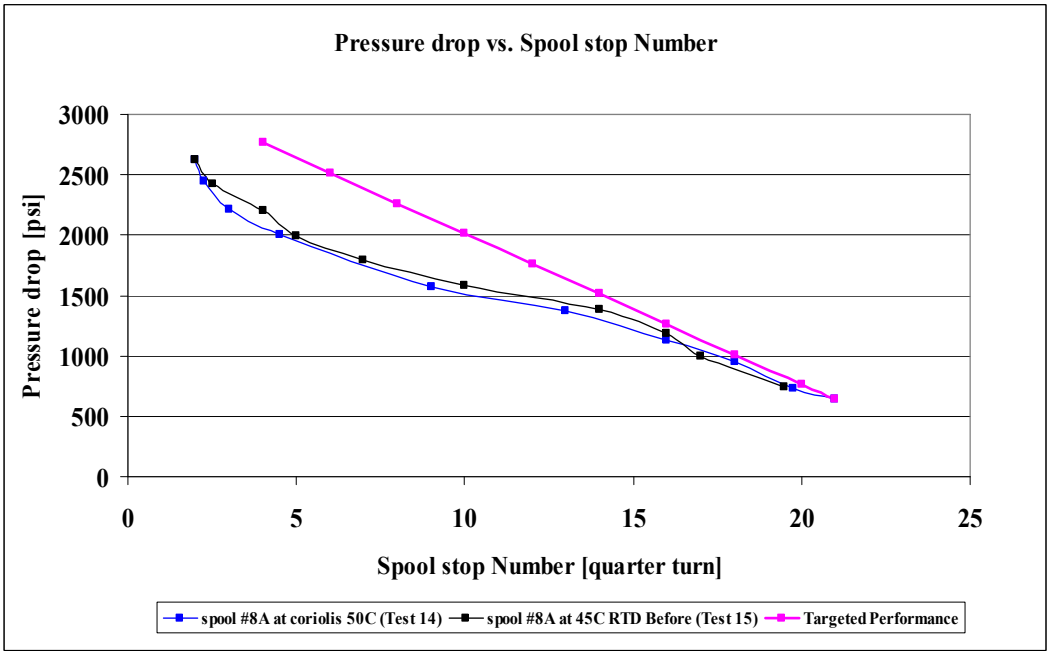

Figure 140: A plot of the pressure drop versus spool stop number for test 14 and 15.

Based on the results of test 11 and 15, it was found that test 10 and 14 were repeatable within 3%.

Experimental Results of Test 12 and 16

After the aforementioned tests results of spool #7, spool #8 and spool #8A (*i.e.* test 9, 10, 11, 13, 14 and 15) were sent to Amsted Rail Engineering, they decide to set the design temperature of the extension and the retraction performance spools at 25°C.

Since it was not possible to keep the inlet flow temperature for a reasonable time at 25°C while making the test with only using the heat exchanger mounted on the hydraulic power unit (*i.e.* waiting for 20-30 minutes for the flow to cool down in order to record two data points before the flow heats up significantly again), a cooling setup (see Figure 141) uses a 13 kW water chiller, multiple fans and radiator was implemented to enhance the performance of the power unit's heat exchanger. As a result the cooling setup increases the testing capability of recording data points at constant flow temperature from 2 to 12 data points.

The results of test 12 are shown in Figure 142. This time the desired retraction performance was achieved at stop 18 of spool #7 instead of stop 15, as the flow temperature was changed from 45°C to 25°C. Thus, as the flow temperature decreases, its viscosity increases and a larger opening area is needed in order to cause the same pressure drop as it was less viscous. The same behavior was noticed for spool #8A stops in test 16 results, when the flow temperature was lowered to 25°C (see Figure 144) and the performance was closer from the target one this time within 8%.

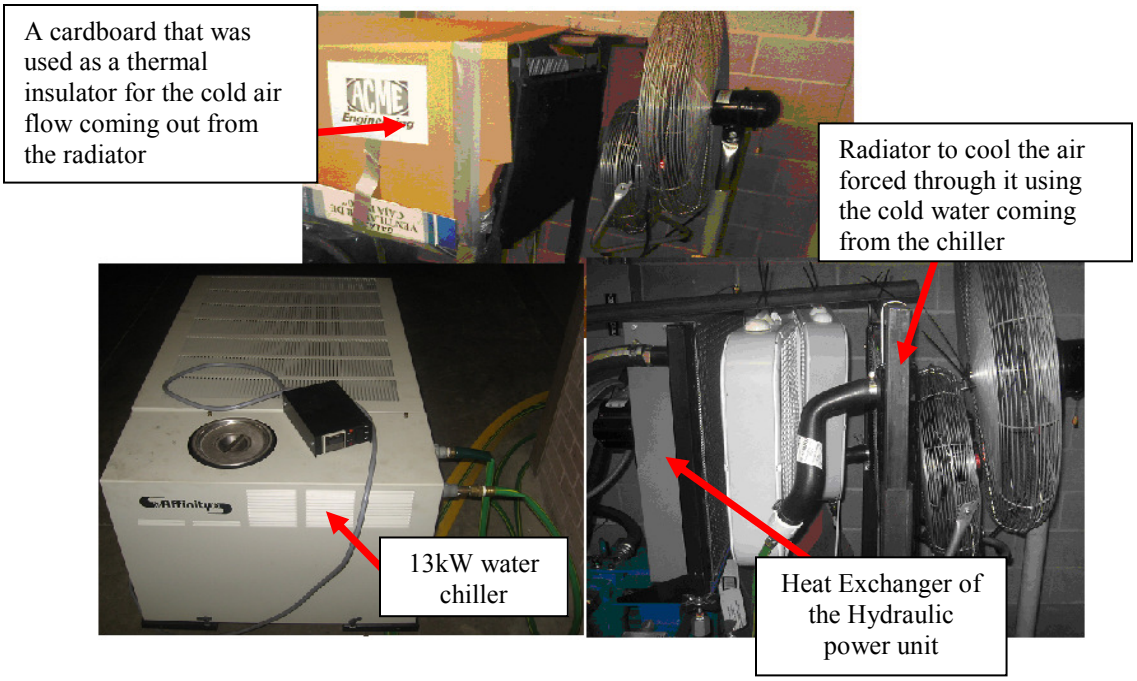

Figure 141: The cooling setup that was used to keep the inlet flow temperature at 25°C while making test 12 and 16.

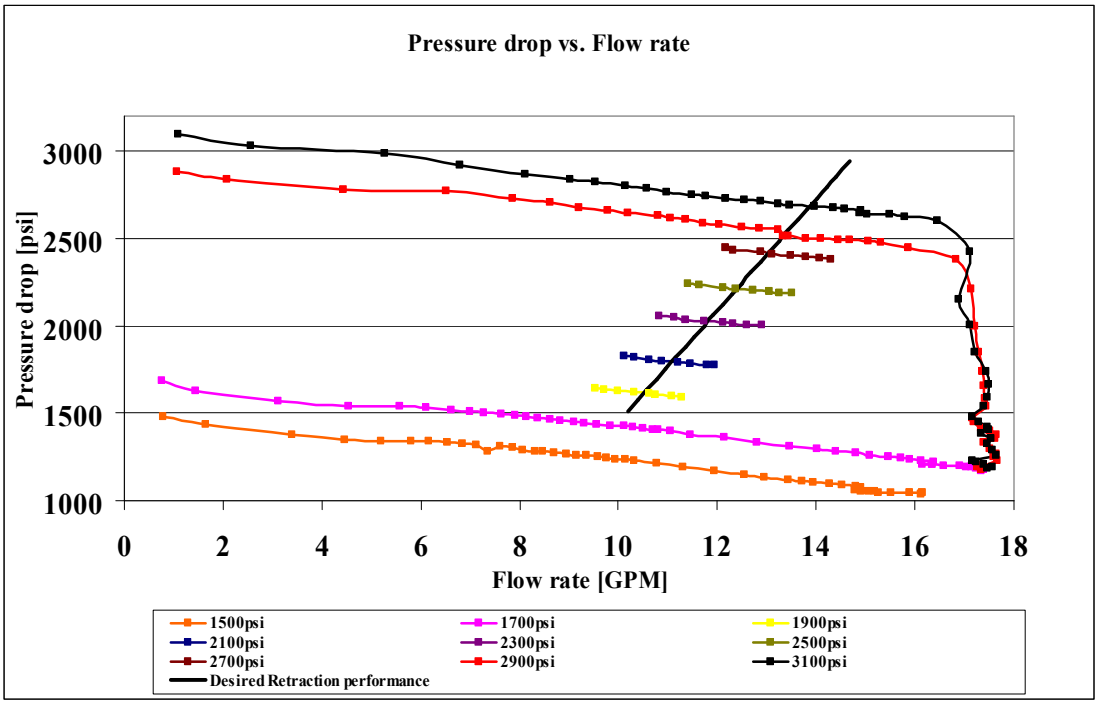

Figure 142: A plot of the pressure drop versus flow rate results of test 12 for spool #7.

The results of test 16 are shown in Figure 143 and 144.

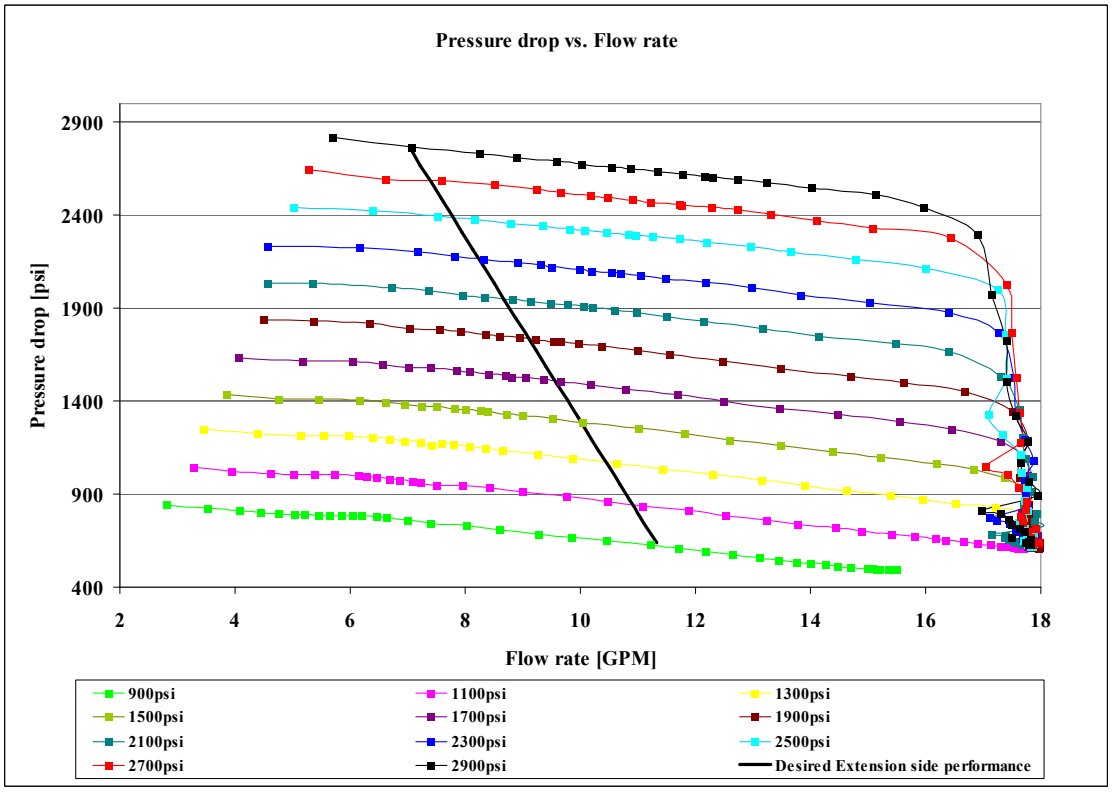

Figure 143: A plot of the pressure drop versus flow rate results of test 16 for spool #8A.

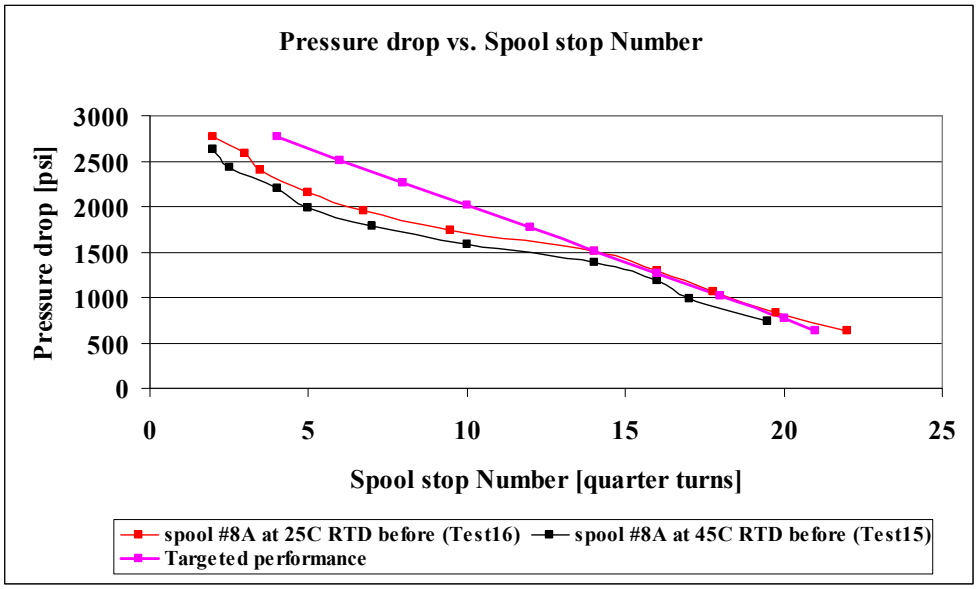

Figure 144: A plot of the pressure drop versus spool stop number for test 15 and 16.

Experimental Results of Test 17 and 18

Two tests were conducted on spool #4 and spool #5, tests 17 and 18, respectively. The results of these tests were compared with the ones obtained from test 12 of spool #7 (see Figure 142), in order to compare the spool stop number at which the desired retraction performance was achieved and to draw a conclusion about if the spool performance is an area driven or geometry driven.

The results of test 17 are shown below in Figure 145.

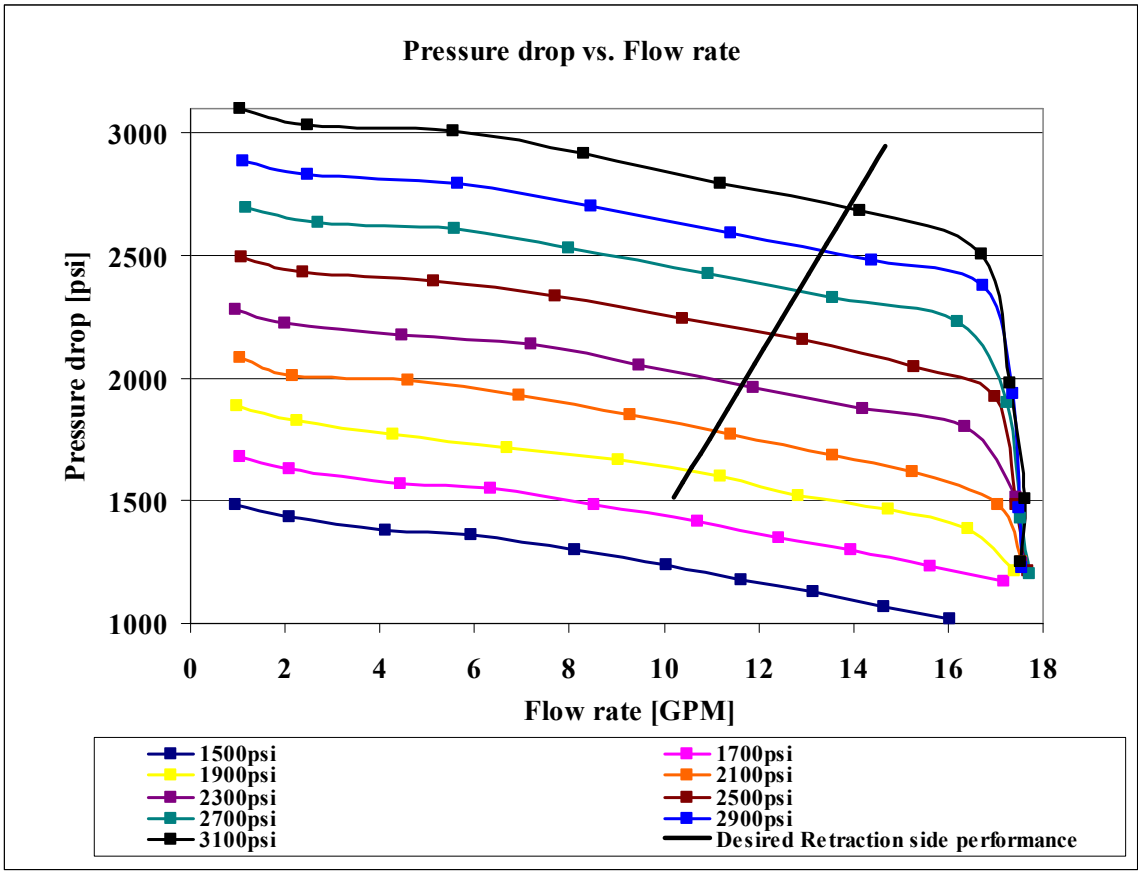

Figure 145: A plot of the pressure drop vs. flow rate results of test 17 for spool #4.

From the Figure above, the desired retraction side performance was achieved at stop 6 of spool #4.

The results of test 18 are shown below in Figure 146.

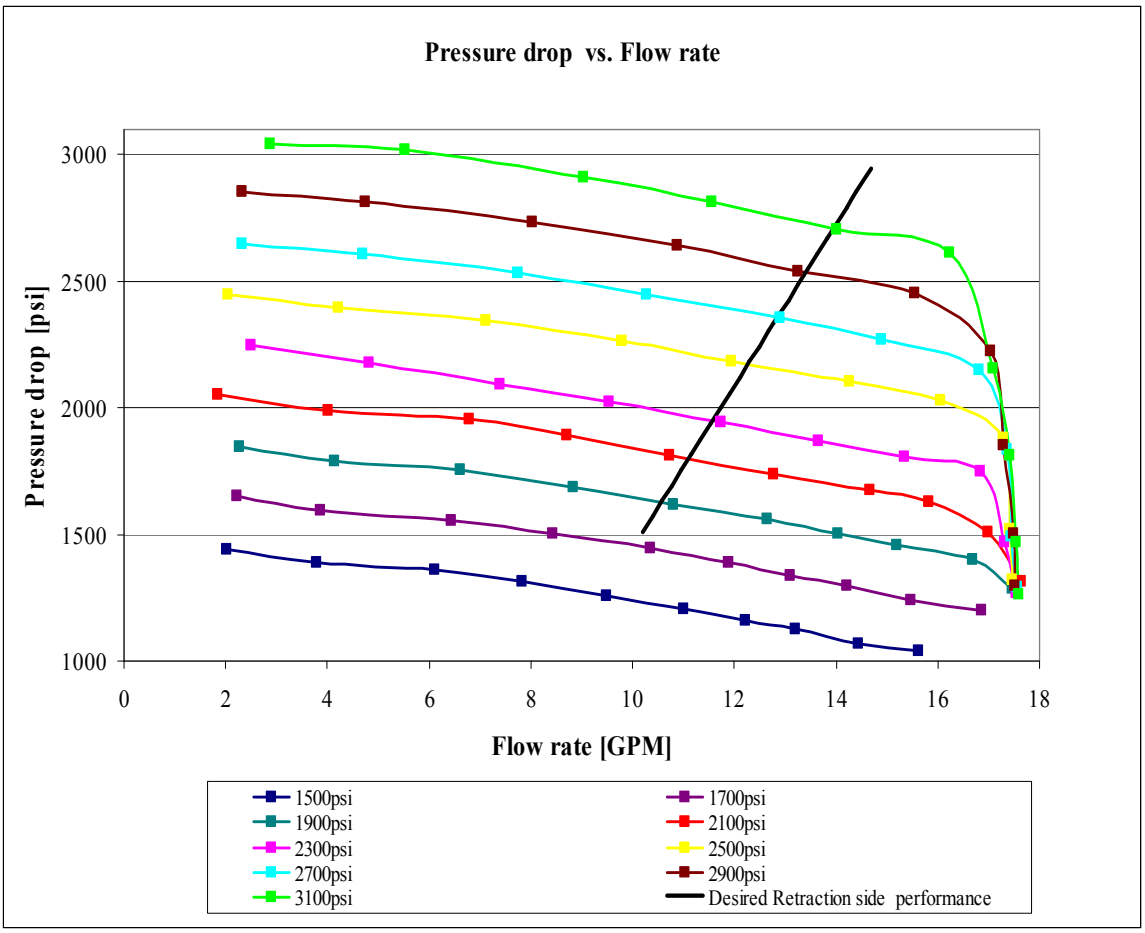

Figure 146: A plot of the pressure drop vs. flow rate results of test 18 for spool #5.

From the Figure above, the desired retraction side performance was achieved at stop 5 of spool #5.

A summary for the flow characteristics at the stop where the desired retraction side performance was achieved for spool #4, 5 and 7 are listed in Table 34.

Table 34: A summary of the flow characteristics at stop 6 of spool #4 (test 17), stop 5 of spool #5 (test 18) and stop 18 of spool #7 (test 12).

Spool Number	Total opening area (A_t) [inch^2]	Total wetted perimeter (P_t) [inch]	Hydraulic Diameter (D_h) [inch]	Maximum mean velocity (U) [m/s]	Maximum Reynolds Number	Maximum Mach Number
Spool #4	0.005202	0.7530	0.027633	132.9399	947.9028	0.093950
Spool #5	0.003352	0.8130	0.016491	204.5540	870.4083	0.144561
Spool #7	0.002930	0.7695	0.015230	233.1071	921.1176	0.164740

From the above table, a 77.6% increase of the total opening area of stop 18 of spool #7 (see Figure 102 for the CAD model of spool #7) along with only 2.14% decrease in its wetted perimeter gives a spool stop aperture that is the same spool stop aperture as the one of stop 6 of spool #4 where the desired retraction performance is obtained. In addition, a 14.4% increase of the total opening area of stop 18 of spool #7 along with only 5.65% increase in its wetted perimeter gives a spool stop aperture that is the same spool stop aperture as the one of stop 5 of spool #5 where the desired retraction performance is obtained again. Thus, the wetted perimeter has a bigger influence on the spool stop's aperture performance compared to its opening area; see Figure 109 for the CAD model of spool #4 and 5.

Turbine Meter Recalibration Based on Upstream Flow Temperatures

The same UVC procedure that was followed to recalibrate the turbine flow meter based on downstream flow temperatures (based on the flow temperature data recorded by coriolis flow meter mounted after the test valve) was used again to recalibrate the same flow meter based on the upstream flow temperatures (based on the flow temperature data recorded by the RTD mounted before the test valve).

The new UVC plot is shown in Figure 147.

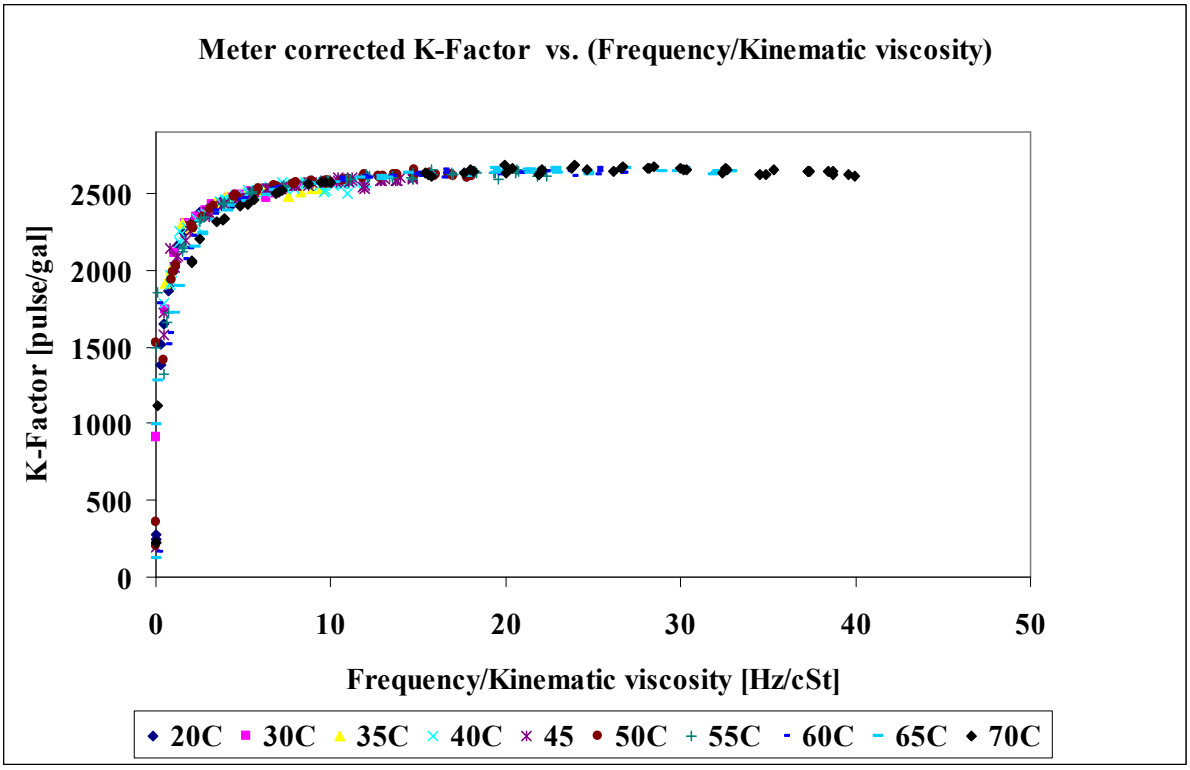

Figure 147: A plot of the new UVC for B2800 KIMRAY turbine flow meter when using AW46 hydraulic oil. (Based on the upstream flow temperature data)

Using Matlab parametric fittings tool box, a power function was found to be the best fit for the curve shown in Figure 147 (*i.e.* goodness of fit =0.9933). The equation of this fit is described by the following

$$K = -779.6 \times \left(\frac{f}{\upsilon} \right)^{-0.2874} + 2966 \tag{33}$$

The new algorithm that was programmed in the labview in order to calculate the actual flow rate passes through the turbine meter at different inlet flow temperatures is the same as the one shown in Figure 126, but the source of the temperature input was changed from the coriolis flow meter to the RTD mounted before the test valve.

An experiment was conducted with spool #7 mounted and centered inside the test valve. In addition, the pressure setting was kept at 1500 psi and the flow rate coming out from the power unit was controlled using the HEDLAND flow meter. Furthermore, the thermostat was set at 70°C to allow the flow to heat up from the room temperature (*i.e.* 18°C) while making the test. Table 35 shows a summary of results obtained for this test.

Table 35: A summary of the results of the experiment that was conducted using spool #7 to test the new algorithm that uses the RTD mounted before the test valve as a source of the temperature input for the algorithm.

Temperature range [^{o}C]	**Coriolis flow rate [GPM]**		**Turbine meter %error before correction**	**Turbine meter %error after correction**
	Minimum	**Maximum**		
18-30	0.670	16.76	18.97	4.930
31-40	0.640	17.71	11.22	2.810
41-50	1.670	17.48	7.110	1.360
51-60	1.160	17.54	7.220	1.650
61-70	0.964	17.51	7.622	2.150

CHAPTER VI

PROPOSED SPOOLS DESIGN BASED ON THE REVSIED SIMULATION DATA

Amsted Rail Engineering did changes for both desired retraction and extension side performances that were shown previously in Chapter I. To eliminate any confusion with the initial desired performance; the revised retraction side performance was called blind side performance and the revised extension one was called rod side performance. Both of the revised performances are shown in Figure 148 and summarized in Table 36.

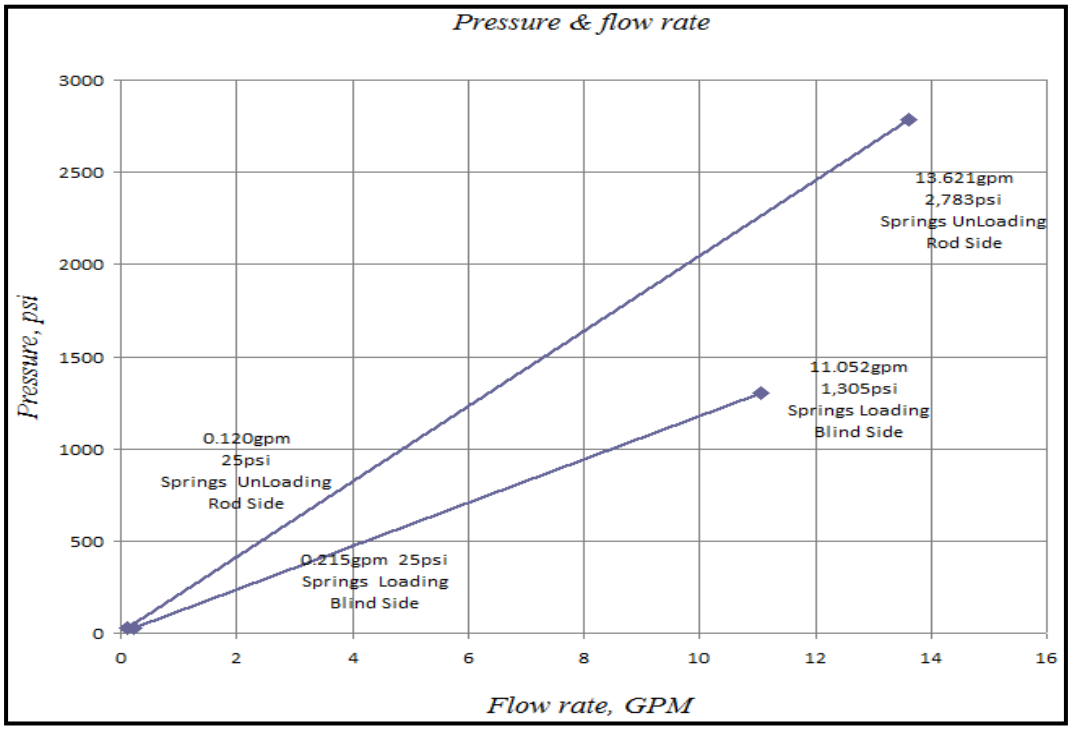

Figure 148: A plot of the pressure drop versus flow rate data for the desired blind and rod side performances (Courtesy of Amsted Rail).

Table 36: The end points (*i.e.* pressure drop and flow rate values) of the desired linear performance for both blind and rod sides. (Provided by Amsted Rail).

Spool Type Control Valve Desired Performance			
Blind side performance		**Rod side performance**	
Flow rate [GPM]	Pressure drop [psi]	Flow rate [GPM]	Pressure drop [psi]
Starting Value		**Starting Value**	
0.2150	25.00	0.1200	25.00
Ending Value		**Ending Value**	
11.052	1305.00	13.621	2783.00

Summary Tables and Experimental Results of the Tested Spools

This time both rod and blind side performance spools should provide an increasingly linear relation between pressure drop, flow rate and spool position (see Figure 148). Thus, as the applied pressure on the spool pilot increases, the spool will travel from a normally closed position to a specific location with certain opening area in order to let more flow in given a specified pressure drop.

Since the new required performances (rod and blind side performances) are similar to the old required retraction side performance (see Figure 10) that was achieved using a straight cut spool (spool #7), straight cut land spools of different diameters were tested in order to get two spools that give the desired performances for the rod and the blind side (see Table 37).

Table 37: A summary of all the tested spools along with their corresponding land diameter, body diameter and land length.

Test Number	Spool designated Number	Spool land Diameter [inch]	Spool body Diameter [inch]	Spool land Length [inch]
20	5	0.3800	0.494	0.375
21	7	0.4650	0.494	0.375
22	7- Reversed side	0.4310	0.494	0.375
23	9	0.4780	0.494	0.375
24	10	0.4715	0.494	0.375
25	11	0.4670	0.494	0.375
26	12	0.4730	0.494	0.375

Before conducting any of the aforementioned tests, the 40 gallon of AW46 oil that was being used in previous tests was replaced with a new one; since there were doubts about the oil was burnt when the flow temperature exceeded 70°C in some of the conducted experiments that mentioned previously in Chapter V. In addition, a PARKER gate valve (see Figure 42) was installed on the upstream side of the test valve in order to test the spools at applied pressures less than 275 psi. All the aforementioned tests are summarized in Table 38, 39 and 40.

Table 38: A brief description of the conducted tests on spool #5, 7 and 7-reversed side. (The flow rate data were recorded using the coriolis flow meter mounted on the down stream side of the test valve)

Spool #5 (0.3800 inch Dia.)		
Test #	**Source of Flow Temperature Measurements**	**Experimental Description**
20	RTD mounted before the test valve	Total of 15 Experiments. Applied pressure values were {275, 500 to 3100 in increments of 200} psi All the spool land was tested (0.375 inch) Upstream flow temperature kept at 25°C ± 3°C (13.00-hour test)
Spool #7 (starting with 0.4650 inch Dia.)		
Test #	**Source of Flow Temperature Measurements**	**Experimental Description**
21	RTD mounted before the test valve	Total of 15 Experiments. Applied pressure values were {200 to 3000 in increments of 200} psi. All the spool land was tested (0.375 inch) Upstream flow temperature kept at 25°C ± 3°C (14.50-hour test)
Spool #7-reversed side (starting with 0.4310 inch Dia.)		
Test #	**Source of Flow Temperature Measurements**	**Experimental Description**
22	RTD mounted before the test valve	Total of 15 Experiments. Applied pressure values were {275, 500 to 3100 in increments of 200} psi. All the spool land was tested (0.375 inch) Upstream flow temperature kept at 25°C ± 3°C (14.00-hour test)

Table 39: A brief description of the conducted tests on spool #9 and 10.

(The flow rate data were recorded using the coriolis flow meter mounted on the downstream side of the test valve)

Spool #9 (0.4780 inch Dia.)		
Test #	**Source of Flow Temperature Measurements**	**Experimental Description**
23	RTD mounted before the test valve	Total of 6 Experiments. Applied pressure values were {200, 275, 500, 700, 900, 3100} psi. All the spool land was tested (0.375 inch) Upstream flow temperature kept at 25°C ± 3°C (3.50-hour test)
Spool #10 (0.4715 inch Dia.)		
Test #	**Source of Flow Temperature Measurements**	**Experimental Description**
24	RTD mounted before the test valve	Total of 17 Experiments. Applied pressure values were {150, 200, 275, 500 to 3100 in increments of 200} psi. All the spool land was tested (0.375 inch) Upstream flow temperature kept at 25°C ± 3°C (18.50-hour test)

Table 40: A brief description of the conducted tests on spool #11 and 12.
(The flow rate data were recorded using the coriolis flow meter mounted on the downstream side of the test valve)

Spool #11 (0.4670 inch Dia.)		
Test #	**Source of Flow Temperature Measurements**	**Experimental Description**
25	RTD mounted before the test valve	Total of 17 Experiments. Applied pressure values were {150, 200, 275, 500 to 3100 in increments of 200} psi. All the spool land was tested (0.375 inch) Upstream flow temperature kept at 25°C ± 3°C (17.00-hour test)
Spool #12 (0.4730 inch Dia.)		
Test #	**Source of Flow Temperature Measurements**	**Experimental Description**
26	RTD mounted before the test valve	Total of 17 Experiments. Applied pressure values were {150, 200, 275, 500 to 3200 in increments of 200} psi. All the spool land was tested (0.375 inch) Upstream flow temperature kept at 25°C ± 3°C (19.00-hour test)

The results of all the aforementioned tests were overlaid with the two revised performances (the desired rod and blind side performances) as shown in Figure 149 through Figure 156.

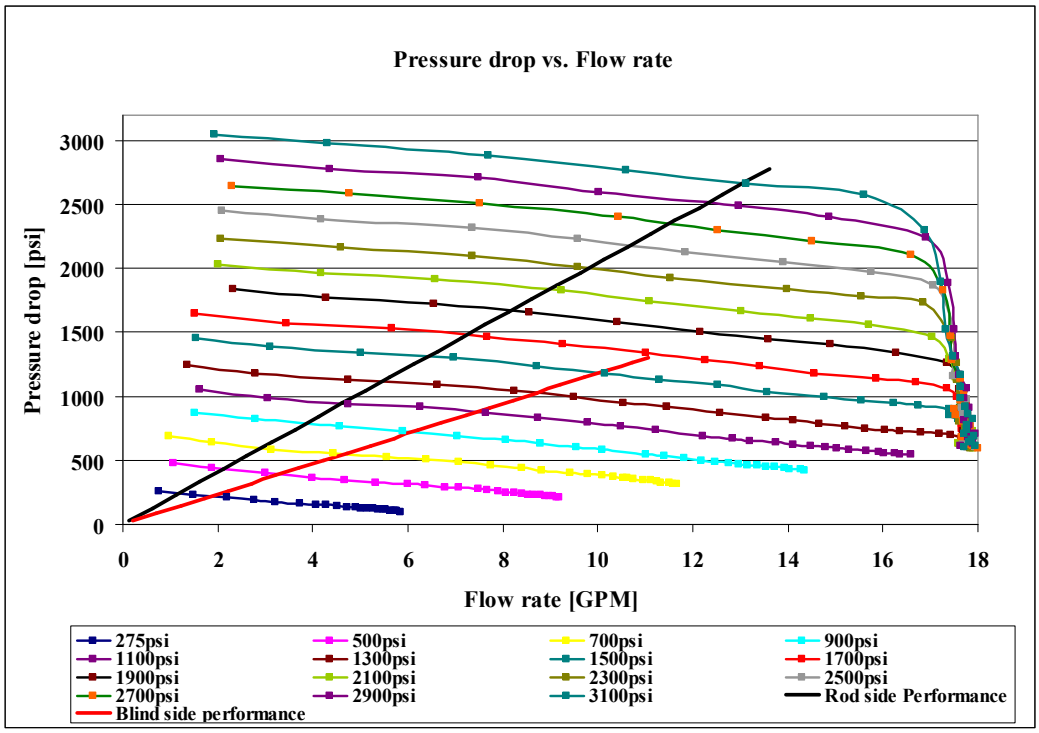

Figure 149: A plot of the pressure drop vs. flow rate results of test 20 (spool #5).

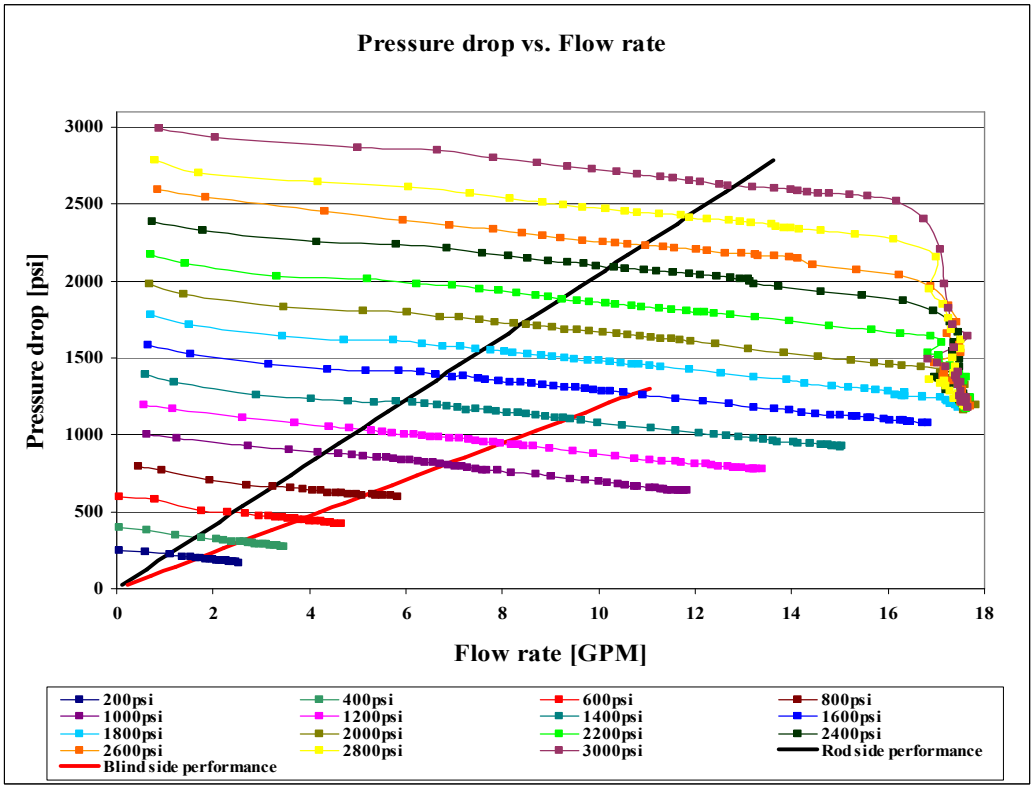

Figure 150: A plot of the pressure drop vs. flow rate results of test 21(spool #7).

The results of spool #5 using the old AW46 Oil (test 18) were compared with the results of test 20 as shown in Figure 151. The difference in the performance of spool #5 between using the old oil and the new one was within 4%.

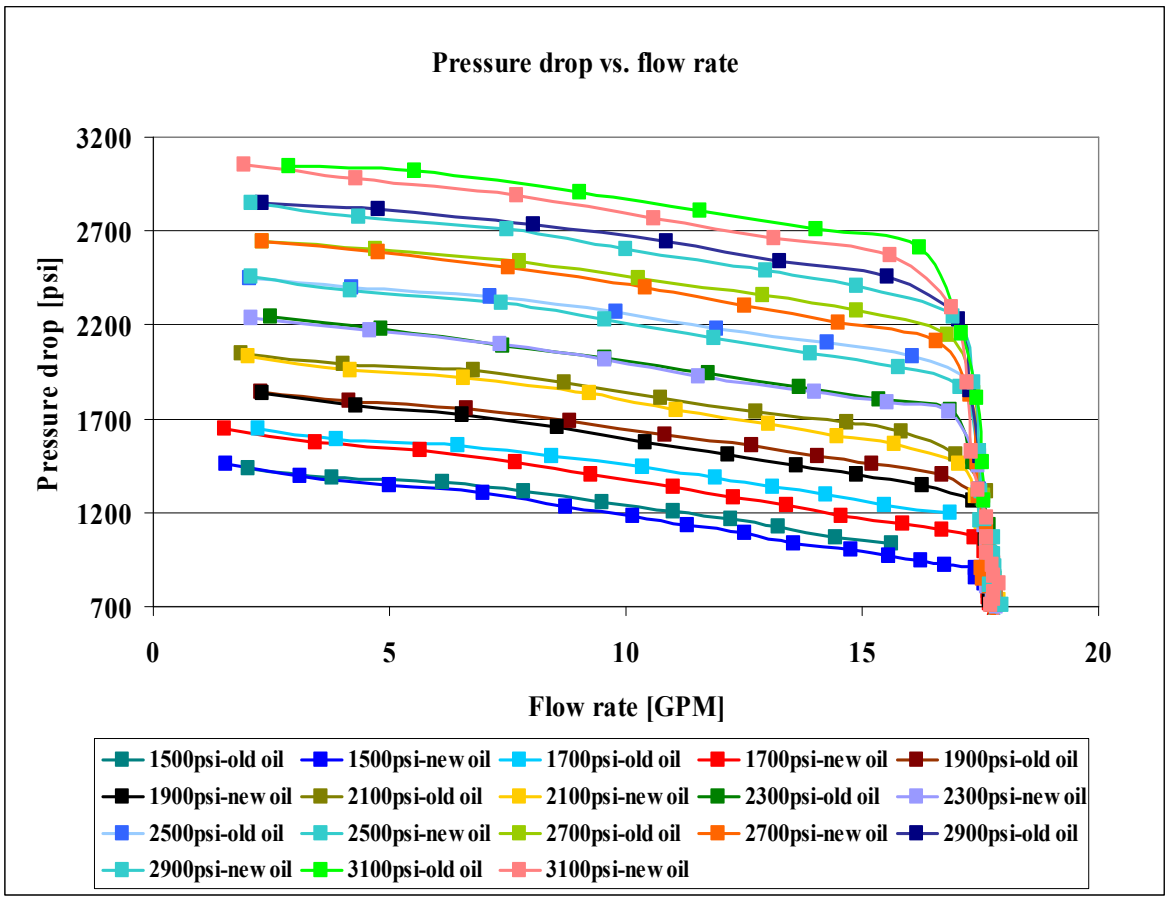

Figure 151: A plot of the pressure drop versus flow rate results of test 18 and 20 for spool #5.

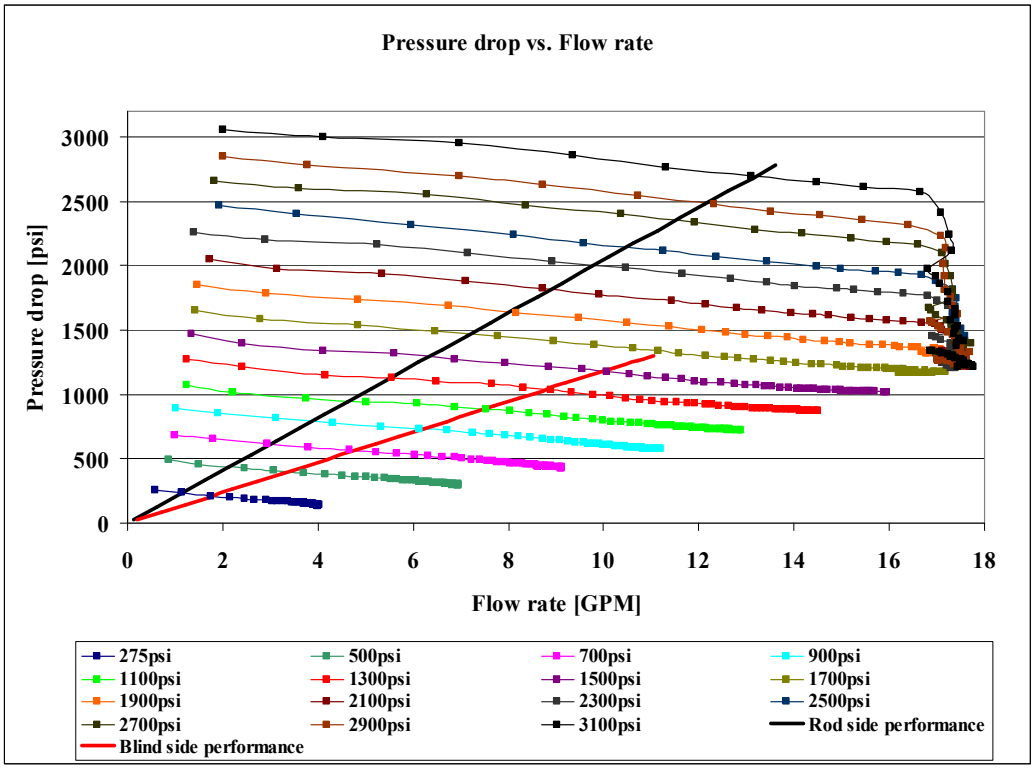

Figure 152: A plot of the pressure drop vs. flow rate results of test 22 (spool #7-reversed side).

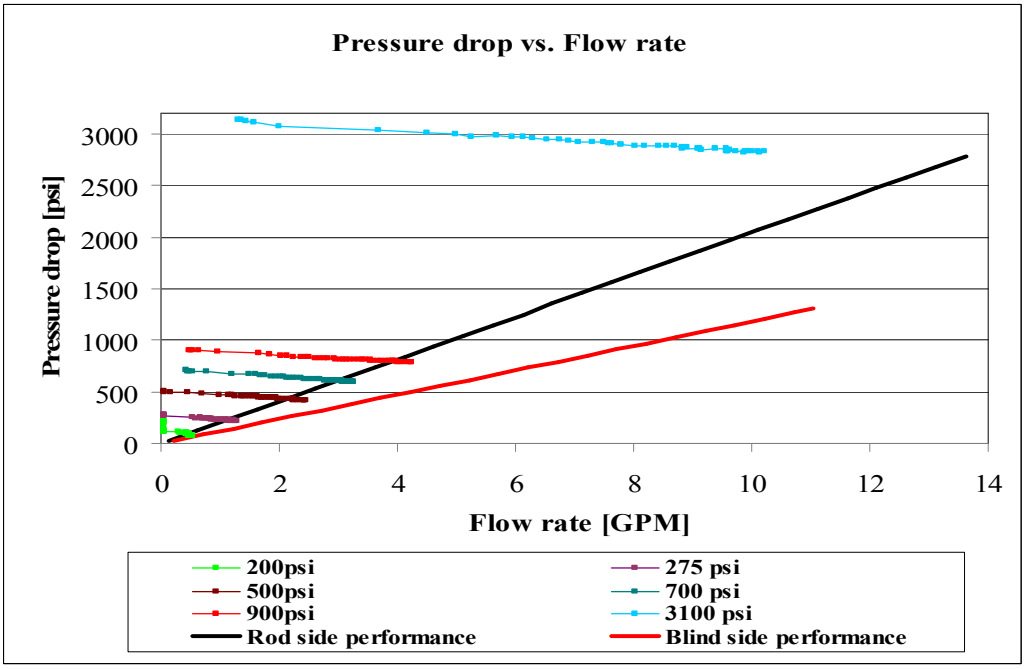

Figure 153: A plot of the pressure drop vs. flow rate results of test 23 (spool #9).

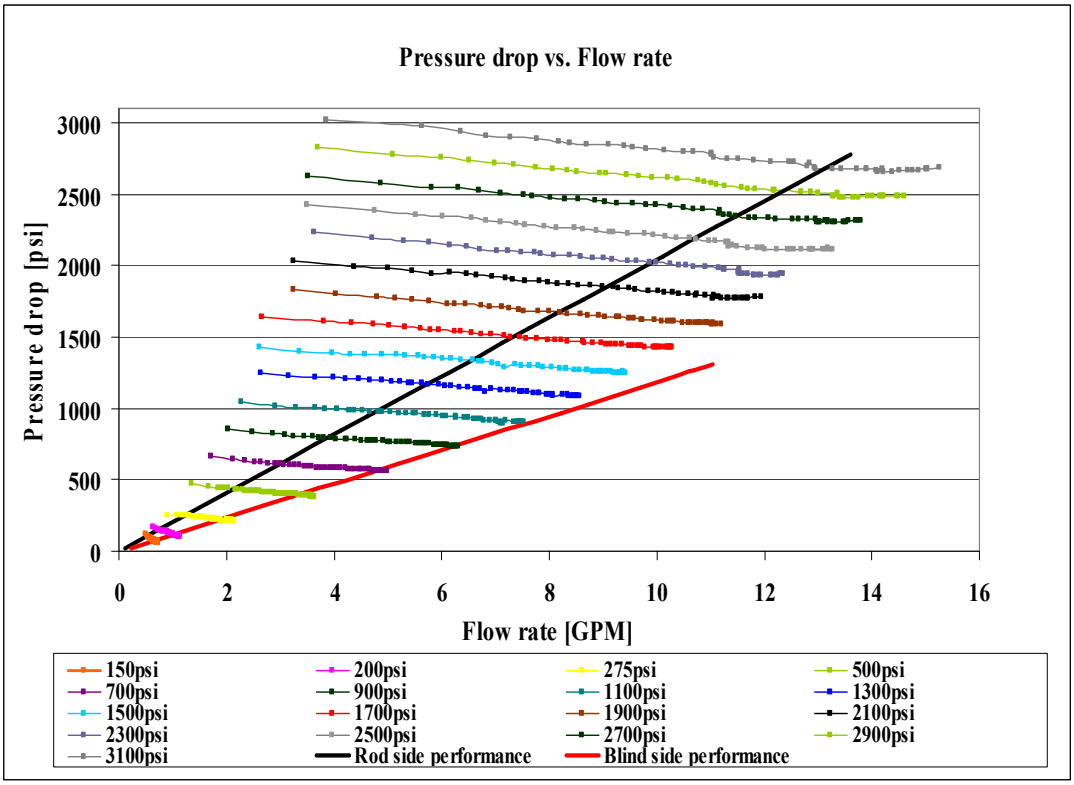

Figure 154: A plot of the pressure drop versus flow rate results of test 24 (spool #10).

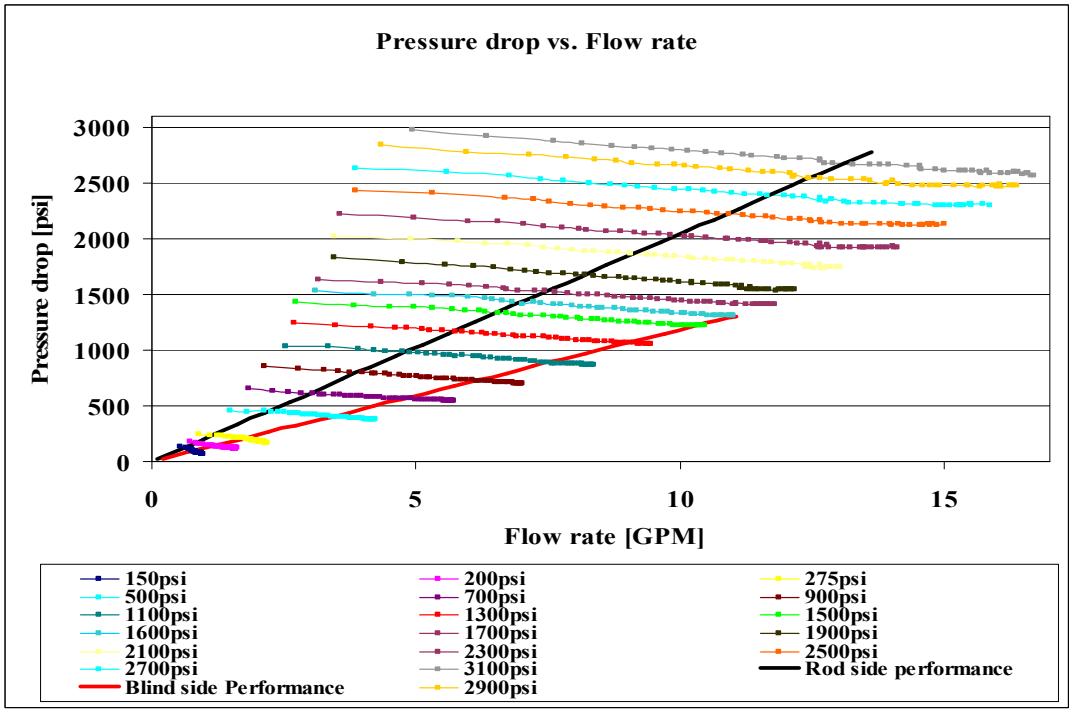

Figure 155: A plot of the pressure drop versus flow rate results of test 25 (spool #11).

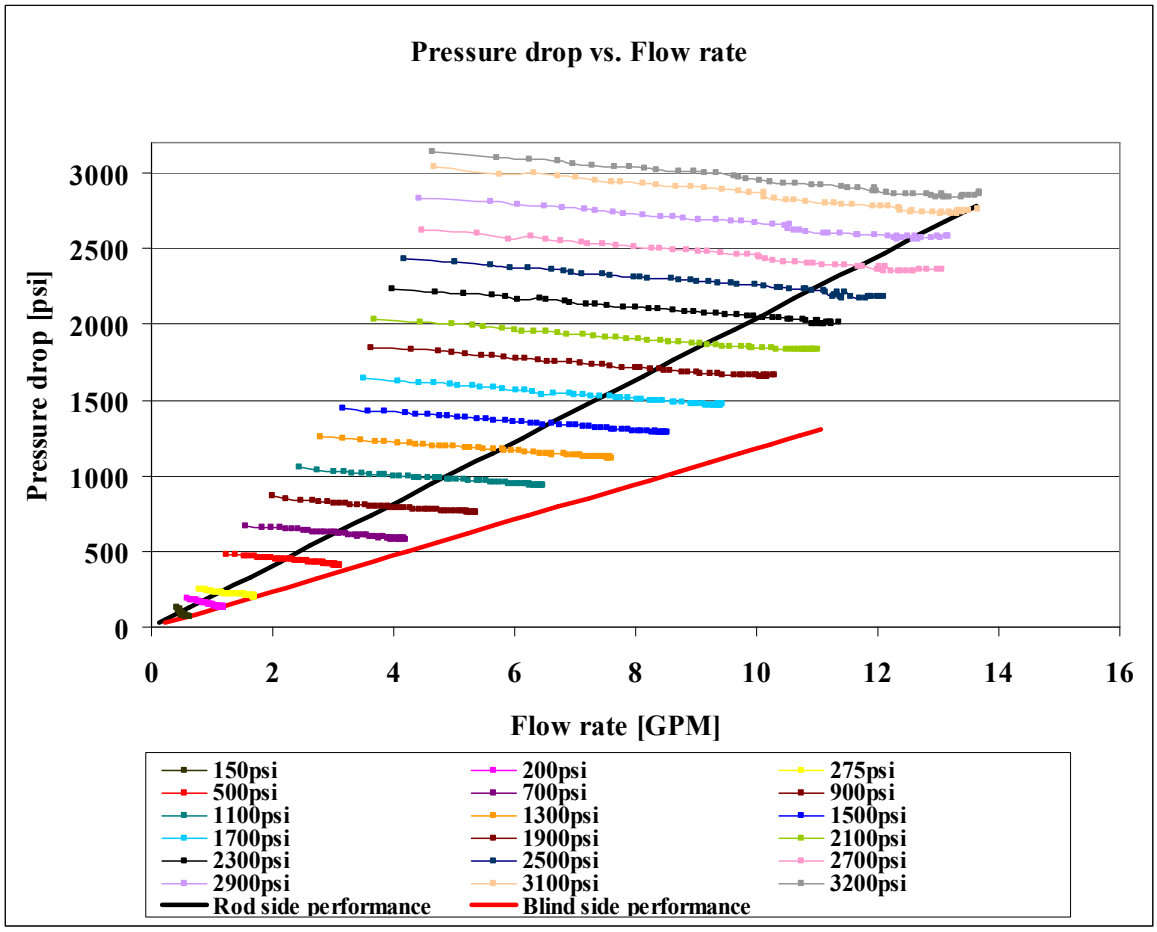

Figure 156: A plot of the pressure drop versus flow rate results of test 26 (spool #12).

In order to evaluate the performance of each tested spool, evaluation plots were generated for the intersection points between the experimental performance of each tested spool and the two desired performances (the rod side and blind side performances).

As shown in Figure 153, the experimental performance lines of spool #9 did not intersect at all with the desired blind side and intersect with the rod side at applied pressures lower than 900 psi. Thus, spool #9 was excluded from the evaluation plots for both the blind and the rod side. In addition, the experimental performance lines of both spool # 10 and 12 did not intersect

with all the blind side performance as shown in Figure 154 and 156. Thus, spool # 10 and 12 were excluded from the evaluation plots for the blind side.

Evaluation Plots for the Rod side

Three different evaluation plots were generated for the intersection points of all the aforementioned tested spools with the desired rod side performance; the first plot was to compare the linearity of the pressure drop versus the spool stop number (see Figure 157), the second plot was to compare the pressure drop versus the spool stop hydraulic diameter (see Figure 158) and the third was to compare the pressure drop versus Reynolds number performance for all the tested spools (see Figure 159).

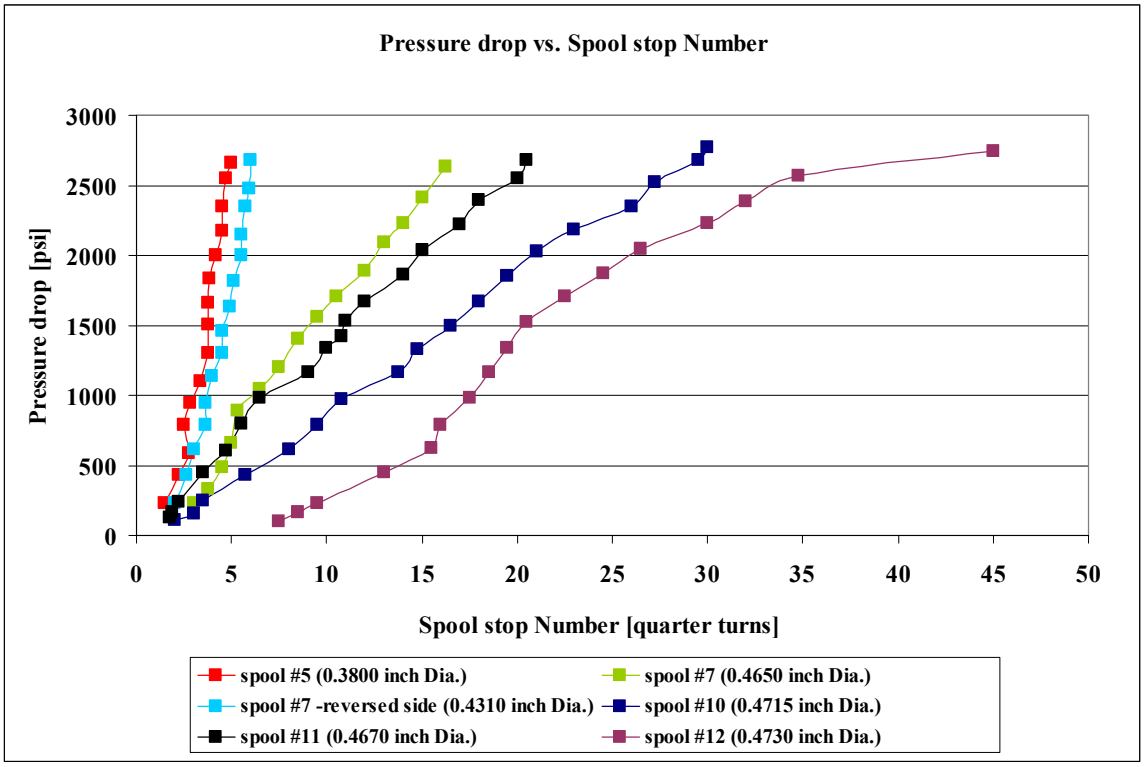

Figure 157: A plot of the pressure drop versus spool stop number results for spool #5 to 12.

Each data set of each spool in Figure 157 was fitted using a linear regression type fit. The goodness of the fit of each tested spool along with its starting and ending spool stop are listed in Table 41.

Table 41: A summary of the results shown in Figure 157.

Spool Designated Number	**Goodness of a linear Fit**	**Starting spool stop [quarter turn]**	**Ending spool stop [quarter turn]**
5	0.9482	1.50	5.00
7	0.9878	3.00	16.25
7-reversed side	0.9669	2.00	6.00
10	0.9970	2.00	30.00
11	0.9941	1.75	20.50
12	0.9319	7.50	45.00

From the above table, all the tested spools have a strong linear relation between both its pressure drop and position, but almost all the spool land of spool #12 was used for the rod side performance. Thus, spool #12 has better sensitivity response than the other spools and required less stiff springs to be attached to it (since it has the largest stroke among the other spools for the same required applied forces). As a result spool #12 was chosen to be the rod side performance spool.

From Figure 158, each spool reaches the desired rod side performance at a group of hydraulic diameter values that is different from those associated with the other spools. But still they all have the same flow regime in common as shown in Figure 159.

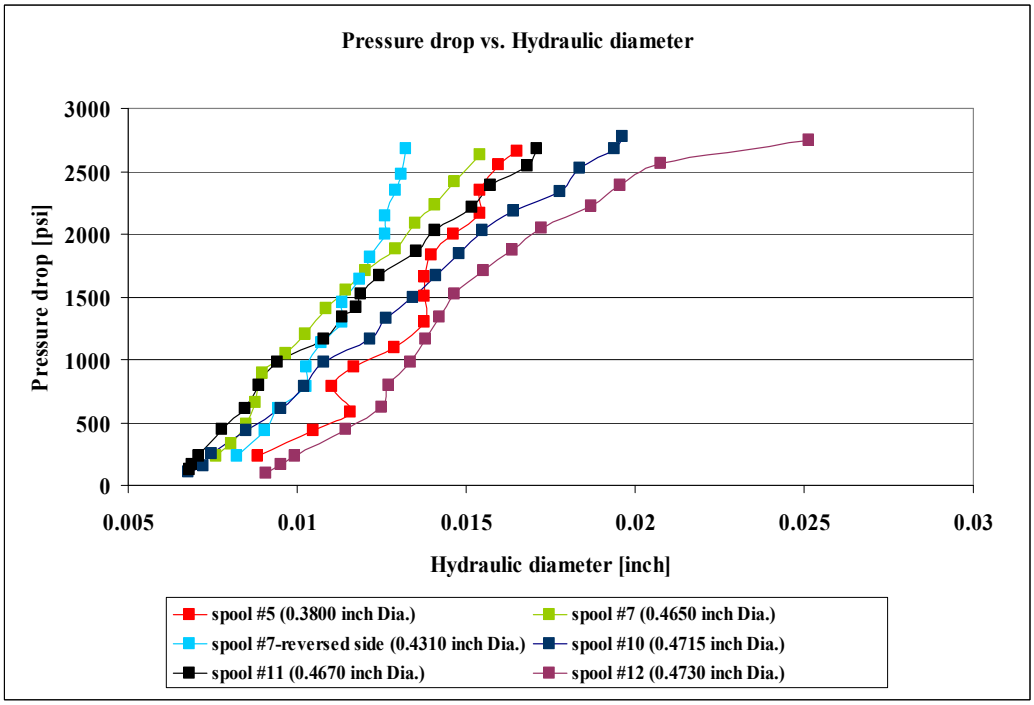

Figure 158: A plot of pressure drop versus the spool stop hydraulic diameters results for spool #5 to 12.

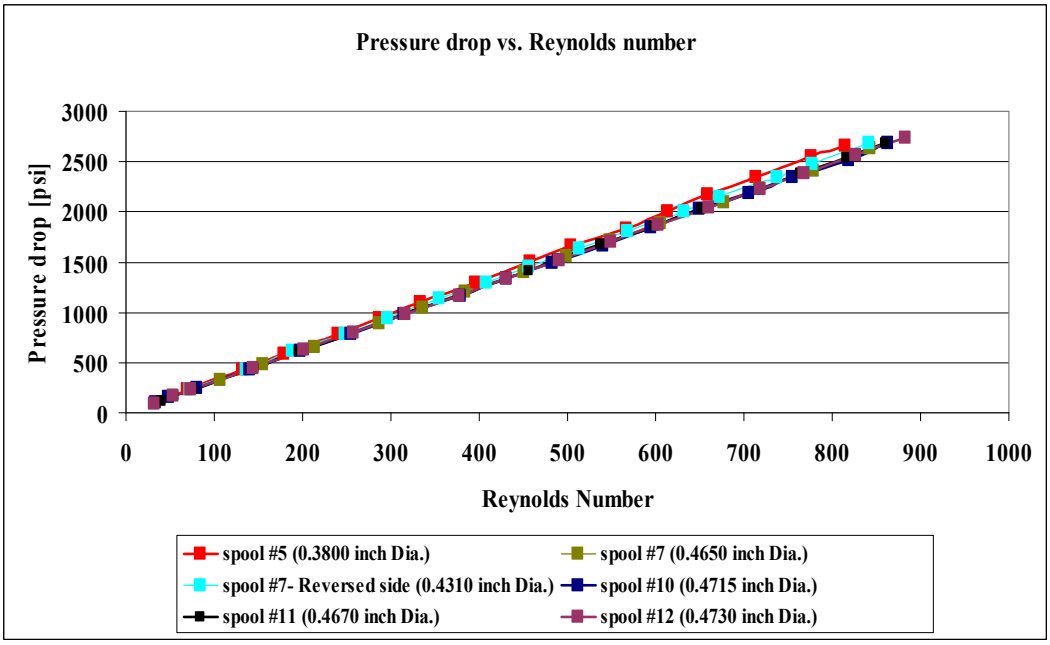

Figure 159: A plot of the pressure drop versus Reynolds number results for spool #5 to 12.

Evaluation Plots for the Blind side

Three different evaluation plots were generated for the intersection points of all the aforementioned tested spools with the desired blind side performance; the first plot was to compare the linearity of the pressure drop versus the spool stop number (see Figure 160), the second plot was to compare the pressure drop versus the spool stop hydraulic diameter (see Figure 161) and the third was to compare the pressure drop versus Reynolds number performance for all the tested spools (see Figure 162).

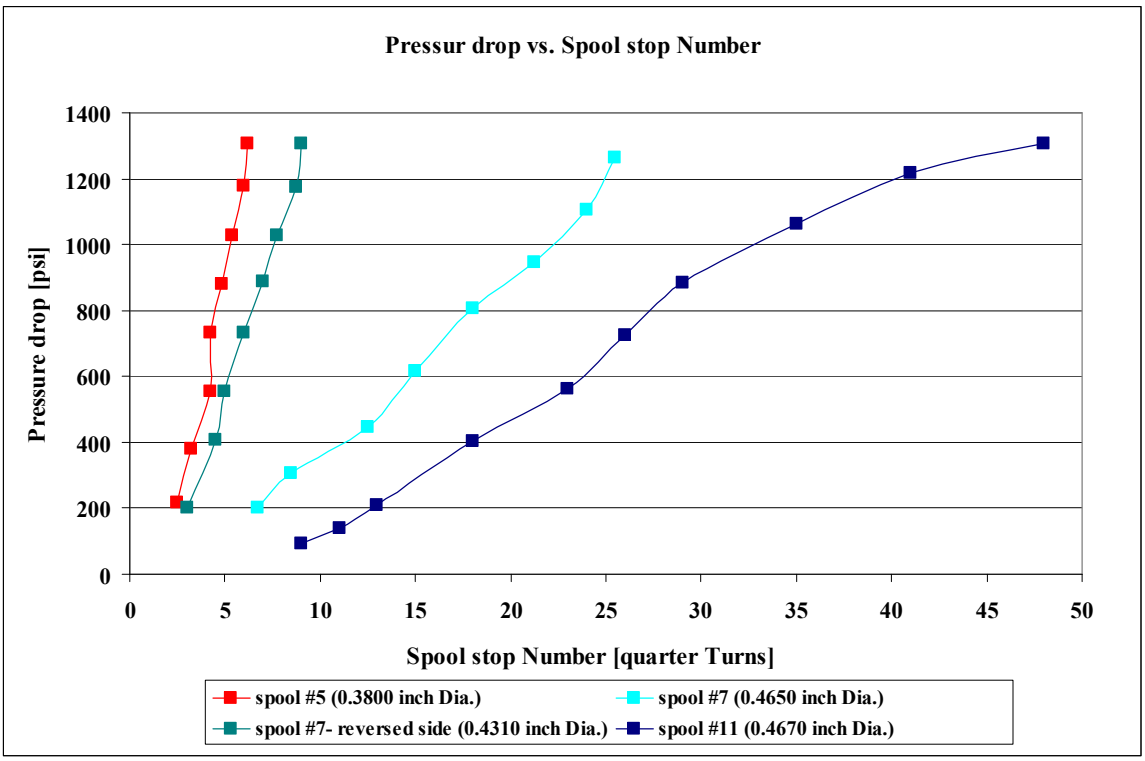

Figure 160: A plot of the pressure drop versus spool stop number results for spool #5 to 11.

Each data set of each spool in Figure 160 was fitted using a linear regression type fit. The goodness of the fit of each tested spool along with its starting and ending spool stop are listed in Table 42.

Table 42: A summary of the results shown in Figure 160.

Spool Designated Number	**Goodness of a linear Fit**	**Starting spool stop [quarter turn]**	**Ending spool stop [quarter turn]**
5	0.9751	2.50	6.00
7	0.9916	6.75	25.5
7-reversed side	0.9937	3.00	9.00
11	0.9796	9.00	48.00

From the above table, all the tested spools have a strong linear relation between both its pressure drop and position, but almost all the spool land of spool #11 was used for the blind side performance. Thus, spool #11 has better sensitivity response than the other spools and required less stiff springs to be attached to it, since it has the largest stroke among the other spools for the same required applied forces. As a result spool #11 was chosen to be the blind side performance spool.

From Figure 161, each spool reaches the desired blind side performance at a group of hydraulic diameter values that is different from those associated with the other spools. But still they all have the same flow regime (*i.e.* laminar flow) in common as shown in Figure 162.

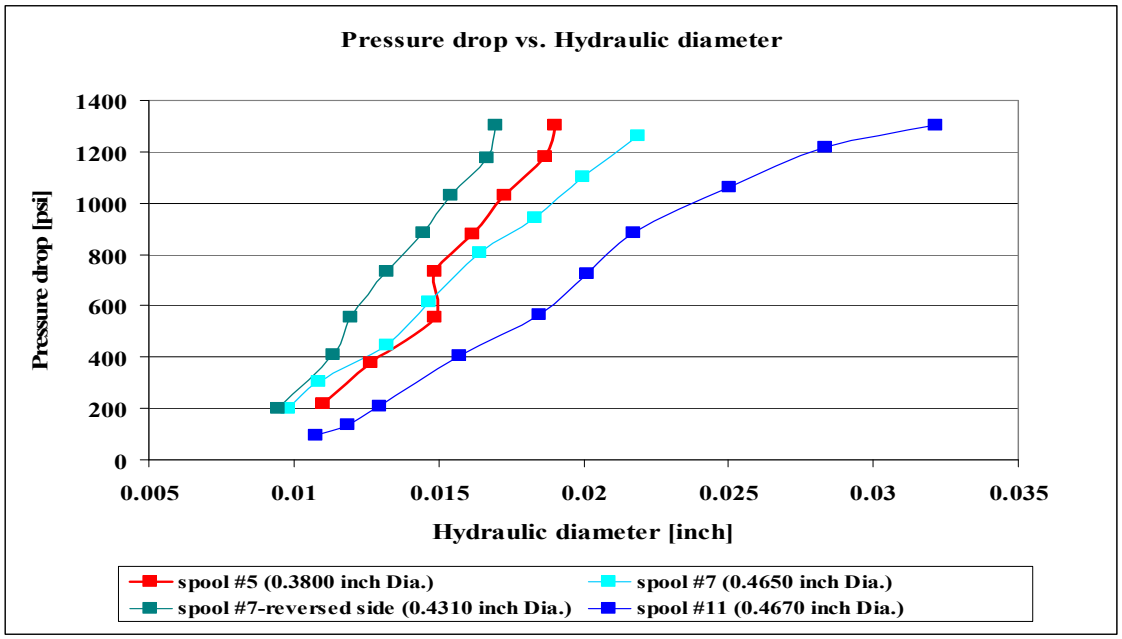

Figure 161: A plot of pressure drop versus the spool stop hydraulic diameters results for spool #5 to 11.

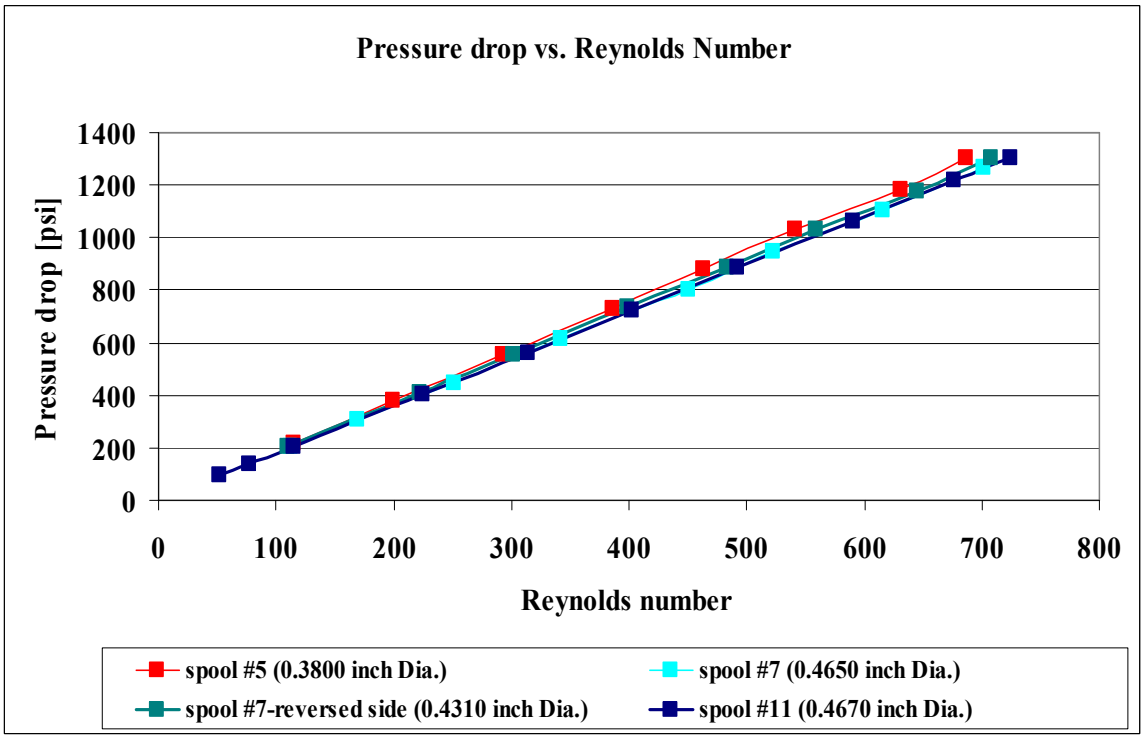

Figure 162: A plot of the pressure drop versus Reynolds number results for spool #5 to 11.

Linearity Check of Spool #12 Performance

In order to check the linearity of spool #12 performance (*i.e.* the proposed rod side performance spool); two tests were conducted where the applied pressure was controlled to give the calculated pressure drop values at the selected spool stops and the corresponding flow rate values were found experimentally using coriolis flow meter. The pressure drop values at the selected spool stops were calculated using the linear fit equation shown in Figure 163.

The two tests that were conducted to check the linearity of spool #12 performance are summarized in Table 43.

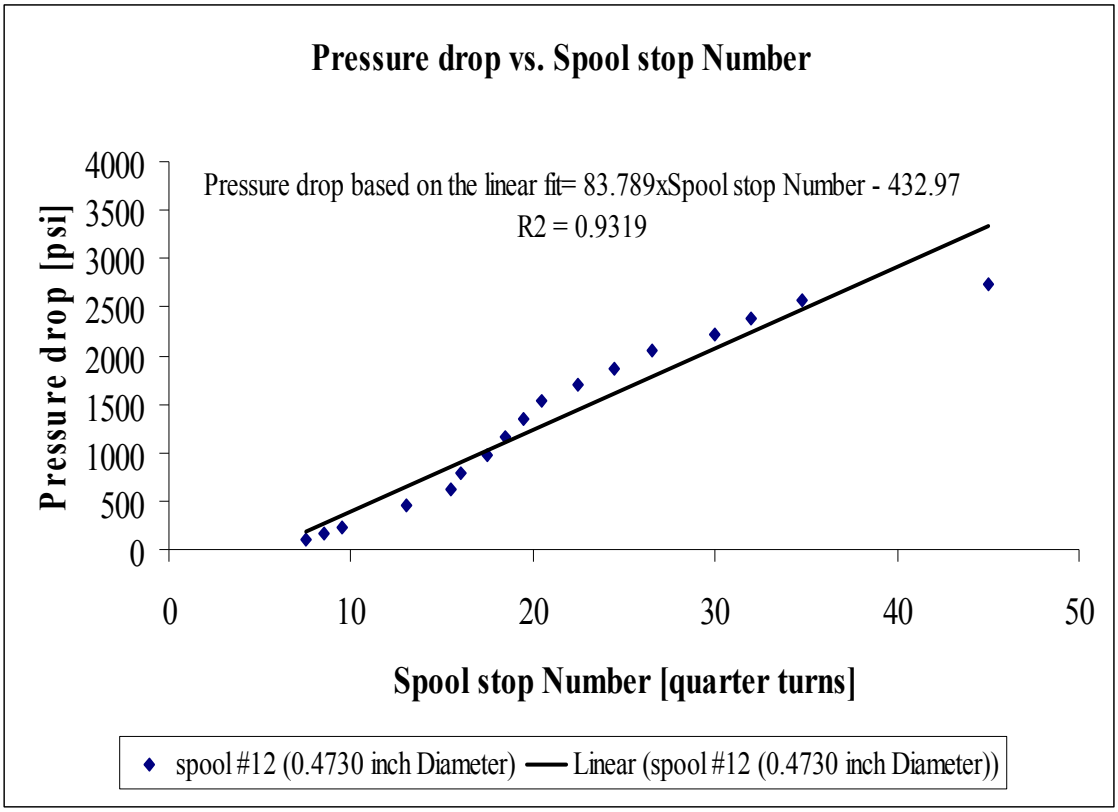

Figure 163: A plot of the pressure drop versus Spool stop number results of test 26 of spool #12 for the rod side performance along with its linear fit.

Table 43: A summary of the linearity check tests that were conducted on spool #12.

Linearity Check for Spool #12 (0.4730 in. Dia.) Performance		
Test #	**Source of Flow Temperature Measurements**	**Experimental Description**
27	RTD mounted before the test valve	Only one experiment. Random spool stops were chosen to calculate the required pressure drop using Figure 163. The test starts at spool stop #6 and ends at spool stop #42. The applied pressure was controlled to give the aforementioned calculated pressure drop at each spool stop. The corresponding flow rate of each calculated pressure drop at each chosen spool stop was measured using coriolis flow meter. Upstream flow temperature kept at 25°C ± 3°C (1.00-hour test)
28	RTD mounted before the test valve	Only one experiment. Random spool stops were chosen to calculate the required pressure drop using Figure 163. The test starts at spool stop #7.5 and ends at spool stop #38.5. The applied pressure was controlled to give the aforementioned calculated pressure drop at each spool stop. The corresponding flow rate of each calculated pressure drop at each chosen spool stop was measured using coriolis flow meter. Upstream flow temperature kept at 25°C ± 3°C (1.00-hour test)

Table 44: Linearity check test results for test 27 of spool #12.

spool stop Number [quarter turn]	Pressure drop based on linear fit [psi]	Actual pressure drop [psi]	Flow rate [GPM]	Temperature [^{o}C]
6	69.764	70.24864	0.056609	22.73446
7	153.553	153.8202	0.813113	23.04425
8	237.342	237.7527	1.209369	23.29415
9	321.131	320.6086	1.606942	23.39315
10	404.920	404.7150	2.000038	23.51571
11	488.709	488.5333	2.390596	23.52050
12	572.498	572.7411	2.796309	23.44984
13	656.287	656.3034	3.207049	23.36880
14	740.076	740.6622	3.599570	23.35523
15	823.865	823.8709	4.054675	23.37958
16	907.654	907.3971	4.445711	23.51890
17	991.443	991.3290	4.925739	23.81272
18	1075.232	1075.2030	5.369519	24.00713
19	1159.021	1159.9520	5.758928	24.42550
20	1242.810	1242.4310	6.234909	24.71413
21	1326.599	1326.7160	6.598940	25.11453
22	1410.388	1410.7420	7.078488	25.63470
23	1494.177	1494.7530	7.559976	26.31615
24	1577.966	1577.8160	7.954844	26.86545
25	1661.755	1660.8590	8.406668	27.50179
26	1745.544	1744.5320	8.855188	28.30260
27	1829.333	1830.0130	9.174161	25.01513
28	1913.122	1913.6160	9.431030	26.04987
29	1996.911	1996.7250	9.948885	26.71216
30	2080.700	2081.5410	10.43179	28.02595
31	2164.489	2166.3340	10.74683	25.34847
32	2248.278	2247.6890	11.08046	26.74729
33	2332.067	2330.5870	11.56630	27.37764
34	2415.856	2415.4550	11.87103	27.89980
35	2499.645	2498.7480	12.12438	26.11534
36	2583.434	2583.9090	12.43658	26.59679
37	2667.223	2668.2040	12.91160	27.61596
38	2751.012	2751.4220	13.05374	25.78760
39	2834.801	2835.8550	13.59645	26.83791
40	2918.590	2916.4950	13.89323	28.17126
41	3002.379	3003.0270	14.06520	24.85904
42	3086.168	3087.1830	14.45688	26.49699

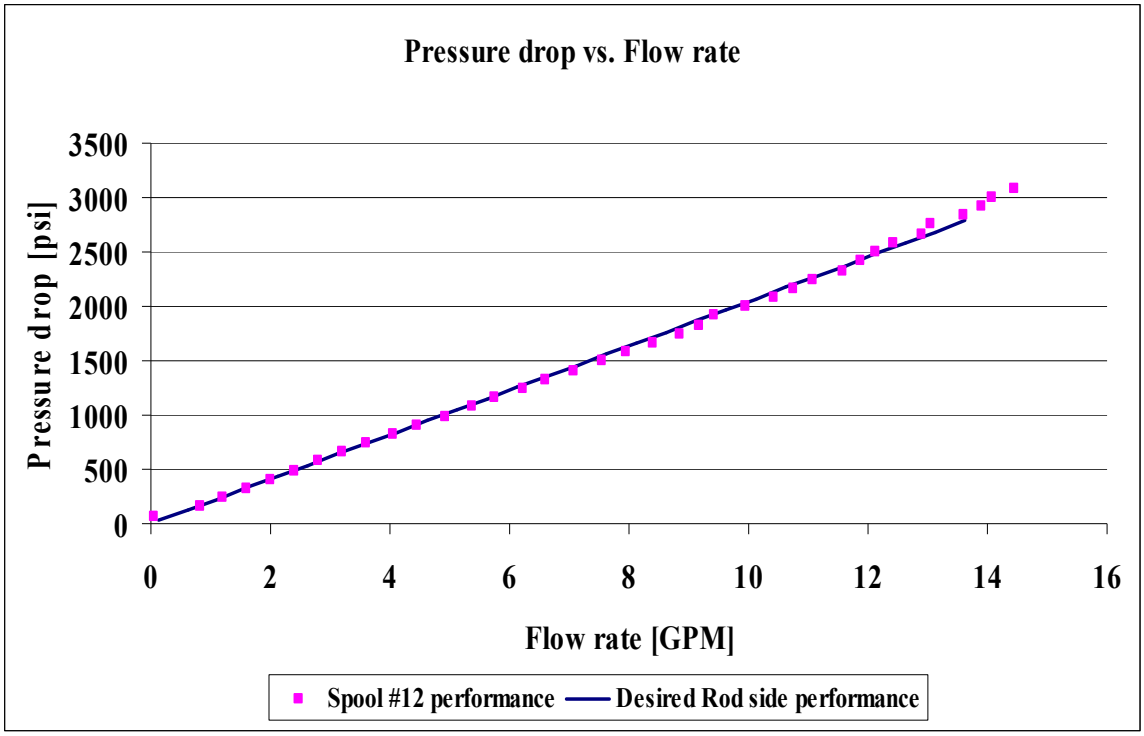

Figure 164: A comparison between the linearity check test results for test 27of spool #12 (*i.e.* the actual pressure drop vs. flow rate results shown in "Table 44") and the desired rod side performance provided by Amsted Rail.

From the above figure the difference in the flow rate data between test #27 results and the desired rod side performance provided by Amsted Rail was found to be 1%.

Based on the equation shown in Figure 163, zero pressure drop corresponds to spool stop of 5.137 (the stop where the linear performance starts). Thus, the linearity check test started at stop 6, since it is the closest stop from the starting one which has a flow rate that could be measured using the current test setup. In addition, the ending value for the pressure drop of the desired Rod side performance (see Table 36) is achieved at spool stop of 38.380 based on the same aforementioned linear fit equation.

The stop number of spool #12 where the desired rod side performance ends at for both test #26 results and the ones obtained from test #27 are listed in Table 45 along with its corresponding pressure drop, flow rate and flow temperature values.

Table 45: A comparison between the results of spool #12 for the rod side performance obtained from both test #26 and 27.

Spool # 12 results based on	**Spool stop Number [quarter turn]**	**Pressure drop [psi]**	**Flow rate [GPM]**	**Flow Temp. [^{o}C]**
Test #26	45.00 out of 48	2743.1 out of 2783.0	13.41 out of 13.621	26.72
Test #27	38.38 out of 48	2783.0 out of 2783.0	13.26 out of 13.621	26.31

It can be noticed from the above table that the desired rod side performance is reached at earlier spool stop using the linear model fit of spool #12 than the intersection points results obtained in test #26 (see Figure 163). Thus, to check the repeatability of spool #12 performance; the linearity check test was repeated in test # 28, since it is easier and less time consuming compared to the repeation of test #26. The results of the repeation of test 27 are listed in Table 46.

Table 46: The results of the repeated linearity check test for spool #12 (test #28)

spool stop Number [quarter turn]	Pressure drop based on linear fit [psi]	Actual pressure drop [psi]	Flow rate [GPM]	Temperature [^{o}C]
7.50	195.4475	195.6275	1.066965	23.85504
8.50	279.2365	279.4165	1.431163	24.09376
9.50	363.0255	363.2055	1.738931	22.91291
13.00	656.2870	656.4670	3.068763	21.55281
15.50	865.7595	865.9395	4.117880	21.35121
16.00	907.6540	907.8340	4.361365	21.57157
17.50	1033.3380	1033.5180	4.988537	21.86778
18.50	1117.1270	1117.3070	5.515466	22.31889
19.50	1200.9160	1201.0960	5.934227	22.75283
20.50	1284.7050	1284.8850	6.438053	23.23387
22.50	1452.2830	1452.4630	7.271816	24.28578
24.50	1619.8610	1620.0410	8.198688	25.13569
26.50	1787.4390	1787.6190	9.063503	26.19000
30.00	2080.7000	2080.8800	10.35694	26.49699
32.00	2248.2780	2248.4580	11.22765	26.74529
34.75	2478.6980	2478.8780	12.17660	26.74968
38.50	2792.9070	2797.3900	13.41340	26.85504

From the above table, the desired rod side performance was obtained at stop number of 38.5 of spool #12. In addition, the pressure drops versus flow rate results listed in the above table were compared to the ones provided by Amsted Rail (see Figure 165) and the difference in the flow rate was found to be within 2%. Thus, it was concluded that the linear fit model represents spool #12 performance better than the intersection points collected from test #26 results. Since the latter may have a means of experimental error introduced to the spool performance while conducting the test such as the heating and cooling cycles of the hydraulic oil while collecting data points.

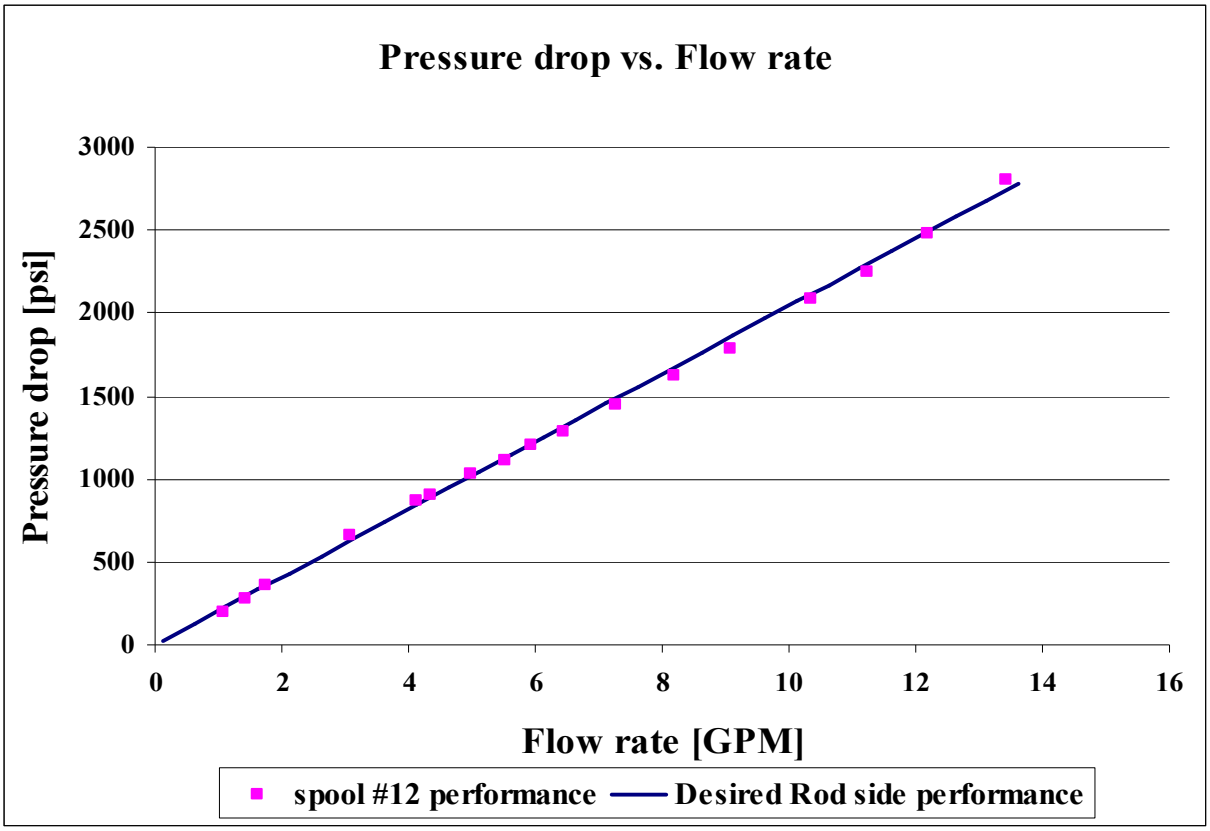

Figure 165: A comparison between the results of test #28 of spool #12 (*i.e.* the actual pressure drop vs. flow rate results shown in "Table 46") and the desired rod side performance provided by Amsted Rail.

Linearity Check of Spool #11 Performance

In order to check the linearity in spool #11 performance (*i.e.* the proposed blind side performance spool); two tests were conducted where the applied pressure was controlled to give the calculated pressure drop values at the selected spool stops and the corresponding flow rate values were found experimentally using coriolis flow meter. The pressure drop values at the selected spool stops were calculated using the linear fit equation shown in Figure 166.

The two tests that were conducted to check the linearity of spool #12 performance are summarized in Table 47.

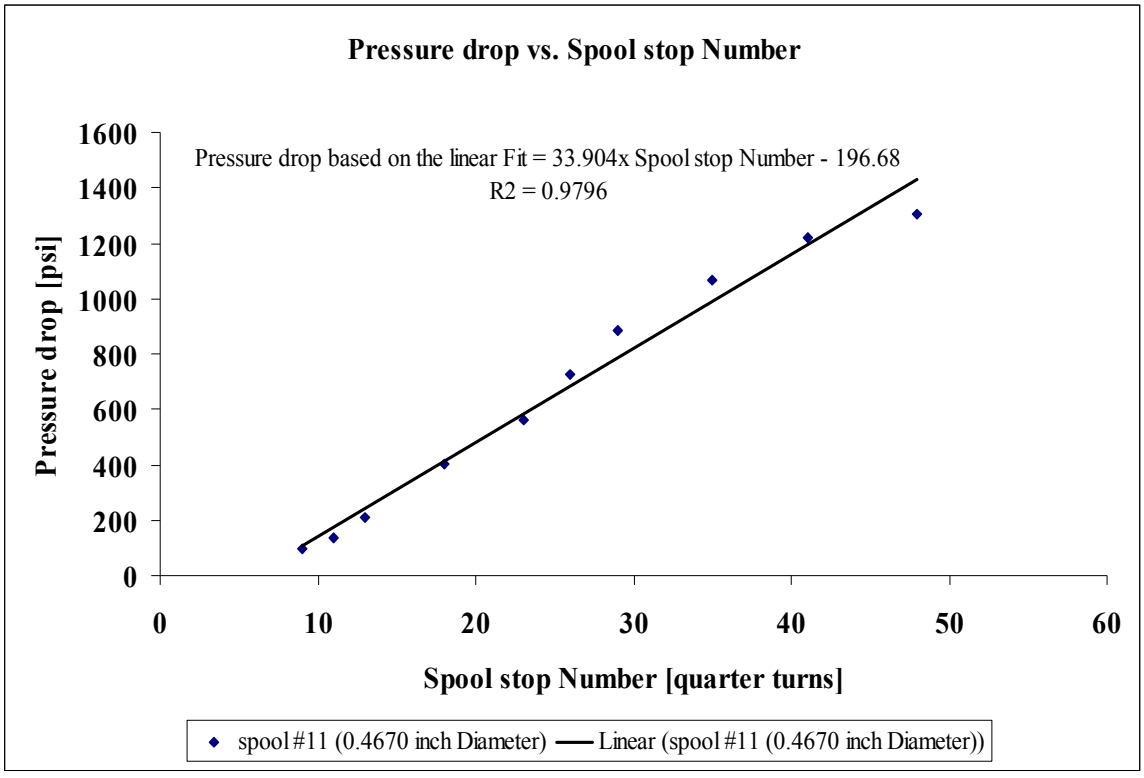

Figure 166: A plot of the pressure drop versus spool stop number results for test 25 of spool #11 for the blind side performance along with its linear fit.

Table 47: A summary of the linearity check tests of spool #11.

Linearity Check of Spool #11 (0.4670 in. Dia.) Performance		
Test #	**Source of Flow Temperature Measurements**	**Experimental Description**
29	RTD mounted before the test valve	Only one experiment. Random spool stops were chosen to calculate the required pressure drop using Figure 166. The test starts at spool stop #6 and ends at spool stop #48. The applied pressure was controlled to give the aforementioned calculated pressure drop at each spool stop. The corresponding flow rate of each calculated pressure drop at each chosen spool stop was measured using coriolis flow meter. Upstream flow temperature kept at 25°C ± 3°C (1.00-hour test)
30	RTD mounted before the test valve	Only one experiment. Random spool stops were chosen to calculate the required pressure drop using Figure 166. The test starts at spool stop #9 and ends at spool stop #48. The applied pressure was controlled to give the aforementioned calculated pressure drop at each spool stop. The corresponding flow rate of each calculated pressure drop at each chosen spool stop was measured using coriolis flow meter. Upstream flow temperature kept at 25°C ± 3°C (1.00-hour test)

Table 48: Linearity check test results for test 29 of spool #11/ part I.

spool stop Number [quarter turn]	Pressure drop based on linear fit [psi]	Actual pressure drop [psi]	Flow rate [GPM]	Temperature [^{o}C]
6	6.744	7.055989	0.056824	22.04583
7	40.648	40.85906	0.088714	22.03944
8	74.552	74.56826	0.678921	22.76760
9	108.456	107.8641	0.956307	23.50693
10	142.360	142.4913	1.233263	23.76002
11	176.264	175.6078	1.547878	23.97001
12	210.168	210.6106	1.800701	23.92530
13	244.072	243.8714	2.080936	23.89615
14	277.976	276.1572	2.332753	23.53607
15	311.880	311.8828	2.623594	23.36361
16	345.784	345.2298	2.884844	23.20513
17	379.688	379.8769	3.185693	23.16081
18	413.592	413.1509	3.465139	23.12329
19	447.496	447.2856	3.760433	23.15363
20	481.400	481.3982	4.068010	23.17239
21	515.304	514.8154	4.354973	23.23507
22	549.208	549.6658	4.747662	23.89895
23	583.112	583.4744	5.045279	23.96322
24	617.016	617.4280	5.329680	24.08298
25	650.920	650.9479	5.672571	24.21073
26	684.824	685.1107	5.971480	24.36762
27	718.728	718.5065	6.327946	24.53129
28	752.632	752.4887	6.645458	24.78319
29	786.536	786.1098	6.940872	25.18400
30	820.440	821.0242	7.250580	25.61713
31	854.344	854.7317	7.596271	25.94967
32	888.248	888.4753	7.911198	26.35247
33	922.152	922.4000	8.231512	26.70138
34	956.056	956.1725	8.511580	27.03711
35	989.960	989.1493	8.728178	27.43432
36	1023.864	1023.032	9.076480	27.73932
37	1057.768	1058.459	9.095561	23.63028
38	1091.672	1091.233	9.308904	24.68938
39	1125.576	1127.533	9.638603	24.85704
40	1159.480	1159.285	9.872008	25.58799
41	1193.384	1194.340	10.26470	26.46465

Table 49: Linearity check test results for test 29 of spool #11/ part II.

spool stop Number [quarter turn]	Pressure drop based on linear fit [psi]	Actual pressure drop [psi]	Flow rate [GPM]	Temperature [^{o}C]
42	1227.288	1226.633	10.40930	27.23193
43	1261.192	1261.210	10.75816	27.84191
44	1295.096	1296.468	10.68284	24.57441
45	1329.000	1329.152	10.93602	25.50536
46	1362.904	1363.057	11.22542	25.83071
47	1396.808	1397.471	11.56580	27.06546
48	1430.712	1430.372	11.76131	28.03313

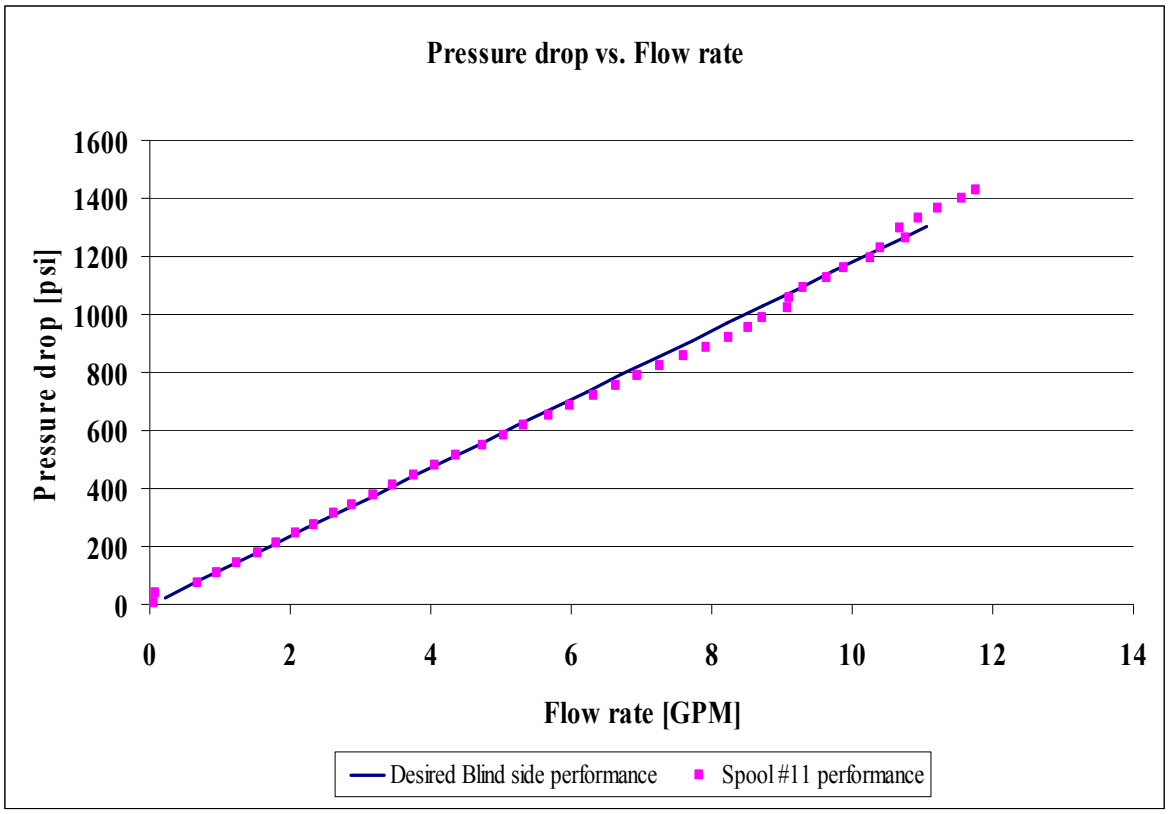

Figure 167: A comparison between the linearity check test results for test 29 of spool #11 (*i.e.* the actual pressure drop vs. flow rate results shown in "Table 48 and 49") and the desired rod side performance provided by Amsted Rail.

From the above figure the difference in the flow rate data between test #29 results and the desired rod side performance provided by Amsted Rail was found to be 2%.

Based on the equation shown in Figure 166, zero pressure drop corresponds to spool stop of 5.8 (the stop where the linear performance starts). Thus, the linearity check test started at stop 6, since it is the closest stop from the starting one which has a flow rate that could be measured using the current test setup. In addition, the ending value for the pressure drop of the desired blind side performance (see Table 36) is achieved at spool stop of 44.3 based on the same aforementioned linear fit equation.

The stop number of spool #11 where the desired blind side performance ends at for both test #25 results and the ones obtained from test #29 are listed in Table 50 along with its corresponding pressure drop, flow rate and flow temperature values.

Table 50: A comparison between the results of spool #11 for the blind side performance obtained from both test #25 and test #29.

Spool # 11 results based on	**Spool stop Number [quarter turn]**	**Pressure drop [psi]**	**Flow rate [GPM]**	**Flow Temp. [^{o}C]**
Test #25	48.00 out of 48	1305.0 out of 1305	11.052 out of 11.052	28.14
Test #29	44.30 out of 48	1305.0 out of 1305	10.812 out of 11.052	25.04

It can be noticed from the above table that the desired blind side performance is reached at earlier spool stop using the linear model fit of spool #11 than the intersection points results obtained in test #25 (see Figure 166). Thus, to check the repeatability of spool #11 performance; the linearity check test was repeated in test 30, since it is easier and less time consuming compared to the repetition of test # 25. The results of the repetition of the linearity check test are listed in Table 51.

Table 51: The results of the repeated linearity check test for spool #11 (test #30).

spool stop Number [quarter turn]	**Pressure drop based on linear fit [psi]**	**Actual pressure drop [psi]**	**Flow rate [GPM]**	**Temperature [^{o}C]**
9.0	108.456	109.0920	0.824102	21.01548
11.0	176.264	177.2679	1.426542	21.94802
13.0	244.072	245.8863	1.942530	22.25901
18.0	413.592	413.4577	3.324530	22.23266
23.0	583.112	583.8014	4.773207	21.52526
26.0	684.824	684.3050	5.670128	21.69453
29.0	786.536	786.6254	6.602268	21.94683
35.0	989.96	989.6169	8.377531	22.72089
41.0	1193.384	1194.4330	9.759364	23.97759
44.0	1295.096	1296.6990	10.595380	25.23669
44.3	1305.267	1305.6800	10.616300	24.15125
48.0	1430.712	1432.4180	11.536690	26.88541

From the above table, the desired blind side performance was obtained at stop number of 44.3 of spool #11. In addition, the pressure drops versus flow rate results listed in the above table were compared to the ones provided by Amsted Rail (see Figure 168) and the difference in the flow rate was found to be within 2%. Thus, it was concluded that the linear fit model represents spool #11 performance better than the intersection points collected from test #25 results. Since the latter may have a means of experimental error introduced to the spool performance while conducting the test such as the heating and cooling cycles of the hydraulic oil while collecting data points.

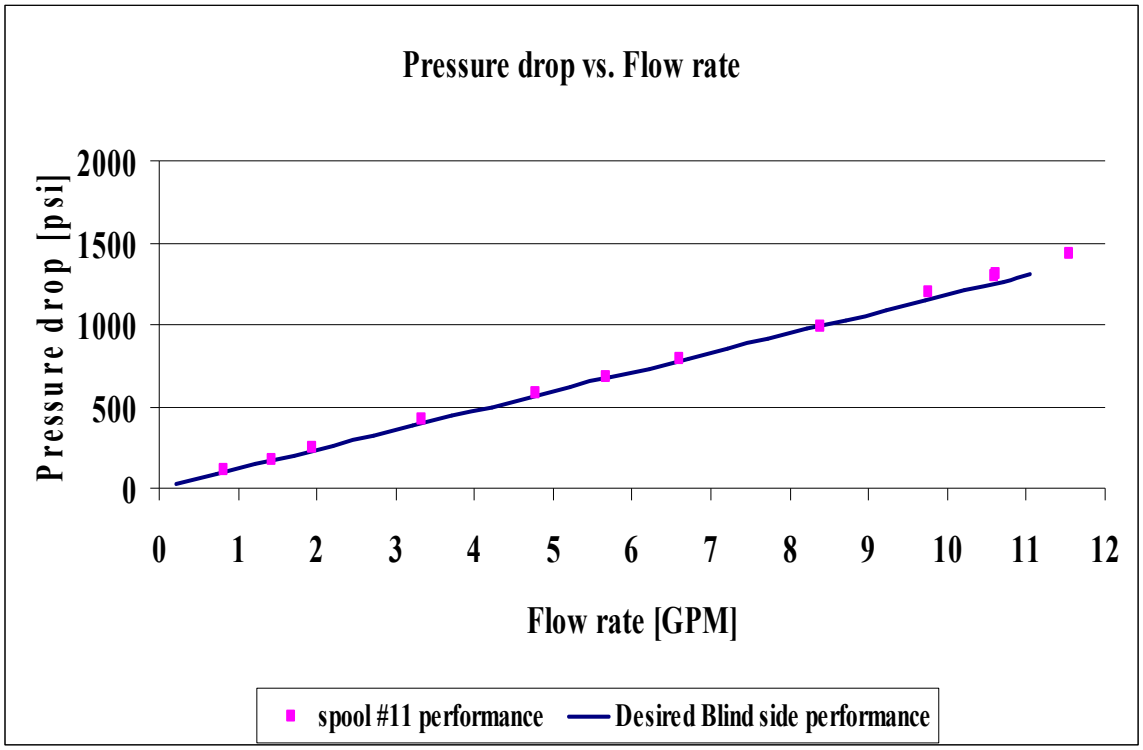

Figure 168: A comparison between the linearity check test results for test 30 of spool #11 (*i.e.* the actual pressure drop vs. flow rate results shown in "Table 51") and the desired blind side performance provided by Amsted Rail.

CHAPTER VII

CONCLUSIONS AND FUTURE WORK

In conclusion, the work presented in this thesis determines the required design of the two spool type control valves that will be part of Amsted Rail's innovative hydraulic damper which will be used as a means of vertical suspension for Amtrak's modified truck assembly as shown previously in Chapter I. The objective of this research was to prove that spools with specific aperture sizing could have a linear relation between pressure drop, flow rate and position, as requested by Amsted Rail engineering based on their simulation data. To this effect, several tests were conducted initially (using the static test setup and following an experimental procedure that was described previously in Chapter III) on different spools to quantify their flow characteristics and in order to find out the optimum apertures that produce the desired linear flow performance for both retraction and extension actions of Amtrak's truck suspension system. Chapter IV has the results of this phase of testing along with the initial correlations for the optimum apertures that would give the required initial performance.

Other tests that included the use of a coriolis flow meter were conducted to see the effect of the flow temperature on the linearity of the initial proposed spools. It was found that a temperature difference of ± 10°C (± 18°F) could change the linearity of the spool performance

significantly as concluded from test 6 and 9 results shown previously in Chapter V. As a result, Amsted Rail engineering set their design temperature to 25°C (77°F).

Based on the aforementioned design temperature information, $T_{flow} = 25^{\circ}C$, and according to the initial simulation data provided by Amsted Rail, the required retraction performance was achieved at only one stop of spool #7. In addition, spool #8A came within 8% of the required extension performance when the operating flow temperature was kept at 25°C. No further modifications were done to spool #8A in order to decrease the discrepancy between its performance and the targeted one, since Amsted Rail engineering revised their simulation data for both retraction and extension performances.

Based on the revised simulation data provided by Amsted Rail, the required rod side performance (the revised extension performance) was achieved using spool # 5, 7, 10, 11 and 12 for flow temperature of 25°C. But it was noticed from the test results of these spools that as the spool land diameter increases the required performance is covered using more length of the spool land; on the other hand, the flow regime stays the same for all the spools. Thus, spool #12 was chosen since it covers the required performance using more of its land length. In addition, the required blind side performance (the revised retraction performance) was achieved using Spool #5, 7 and 11 for flow temperature of 25°C. But spool #11 was chosen since it covers the required performance using more of its land.

The only drawback of the adopted spools design for both rod and blind side (Spool #12 and 11 respectively) is that their land diameters must have tight tolerances. Since the difference in diameter between spool #10 and 12 is only 0.0015 in., yet their performances are different. In addition, the difference in diameter between spool #7 and 11 is only 0.002 in., yet their

performances are also different. This kind of behavior, where a slight change in spool diameter makes dramatic changes in its performance, is caused by the spool performance sensitivity to slight changes in its wetted perimeter as concluded earlier in Chapter V (see Table 34).

Next, one must look at the sizing of the required springs that will be attached to both spool #11 and 12. The sizing of the springs for 0.496 in. diameter spools will be based on the starting and ending positions for both spool #11 and 12 (see Table 52) that were attained from the linearity fit for both spool performances as shown previously in Figure 163 and 166 respectively.

Table 52: A summary for the starting and ending positions along with stroke calculations for both Spool #12 and 11 respectively based on their linear fits.

Spool Designated Number	Starting Position		Ending Position		Stroke [inch]
	[quarter turn]	[inch]	[quarter turn]	[inch]	
Spool #12	5.137	0.0401	38.38	0.300	0.2599
Spool #11	5.800	0.0453	44.30	0.346	0.3007

Other future work will be building a new tester (see Figure 169) for the whole valve assembly along with its cylinder and connecting hoses. This new tester will be used to evaluate the performance of the total hydraulic damper for different track profiles. The tester will have an actuator, a driving cylinder, which is coupled with the hydraulic damper. The actuator force

being measured from a load cell along with its stroke being measured from an LVDT will be adjusted using a controller and a servo valve to match any track profile of interest.

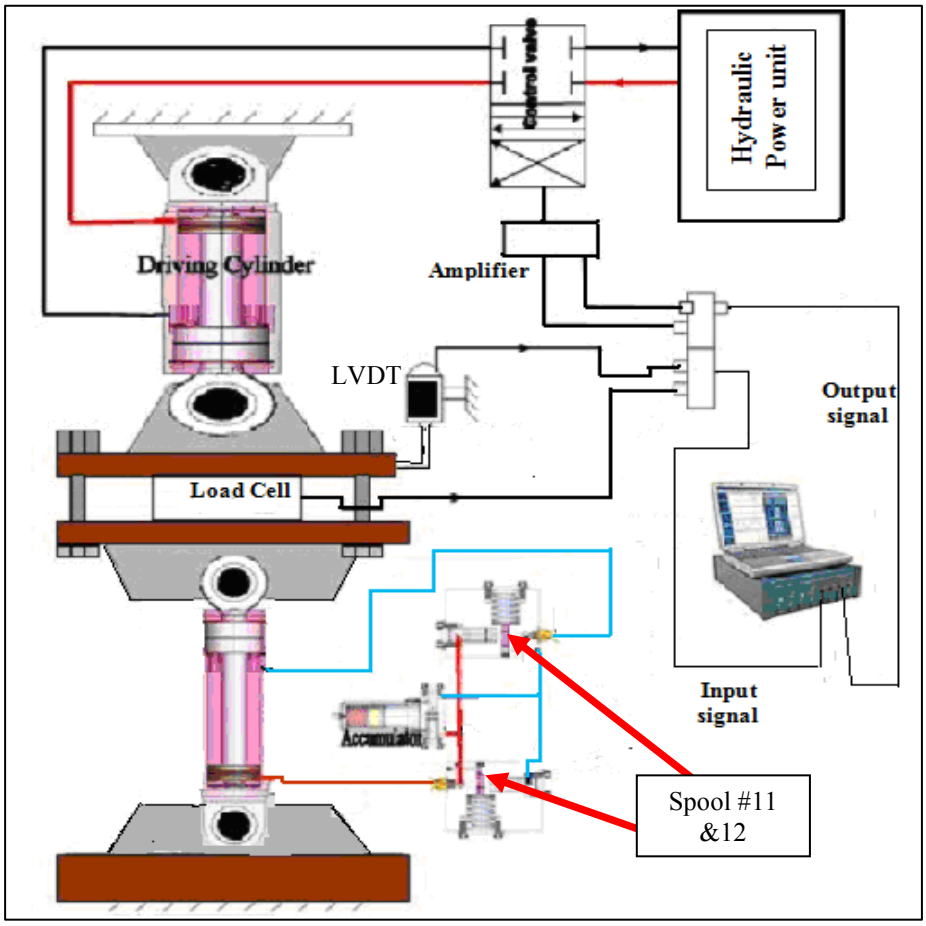

Figure 169: A schematic of the new tester that will be used to test Amsted Rail hydraulic damper for different track profile scenarios.

REFERENCES

1. B.M. Eickhoff; J.R. EVANS; A.J. Minnis, A Review of Modeling Methods for Railway Vehicle Suspension Components, Vehicle System Dynamics, Vol.24 (1995), pp.469-496.

2. Iwnicki, S. Handbook of Railway Vehicle Dynamics. ISBN -10: 0-8493-3321-0 (2006).

3. Nishimura, K. and Perkins, N.C., Suspension Dynamics And Design optimization of a high speed railway vehicle, in: proceedings of the 2004 ASME/IEEE joint Rail Conference April 6-8, 2004, Baltimore, Maryland, USA.

4. L.R. Miller, Tuning passive, semi-active and fully active suspension system, in: IEEE Proceedings of 27th conference on Decision and control, pages 2047-2053, 1988.

5. E. Esmailzadeh; H.D. Taghirad, Active Vehicle Suspensions with Optimal state-feedback Control, International Journal of modeling & simulation, Vol.18 (1998), pp.228-238.

6. Den Hartog, Mechanical Vibration, (1947), McGraw-Hill.

7. JSME (Taniguchi O. ed.), Handbook of vibration Engineering, (In Japanese), (1985), Yokendo.

8. Iba, D., et al., Vibration Control of structures by Using Multi-Degree-of-Freedom Dynamic Absorber, ASME/JSME pressure vessels and piping Conference, Vol.486 (2004), pp.85-91.

9. Elbeheiry, E.M., Karnopp, D.C., Elaraby, M.E., and Abdelraaouf, A.m., in: Advanced Ground Vehicle Suspension Systems-a Classified Bibography, Vehicle System Dynamics (1995), pp.231-258.

10. Hedrick, J.k. and Wormely, D.N., in: Active Suspension for Ground Support Transportation-a Review, ASME-AMD 15 (1975), pp.21-40.

11. Sharp, R.S. and Crolla, D.A., in: Road Vehicle Suspension Systems Design- a Review, Vehicle System Dynamics, 16(1987), pp. 167-192.

12. Hrovat, D., in: Survey of advanced Suspension Developments and related Optimal Control Applications, Automatica, 33(10) (1997), pp.1781-1817.

13. Zuo, L. and Nayfeh, S.A., Design of Passive Mechanical Systems via Decentralized Control Techniques, in: 43rd AIAA/ASME/ASCE/AHS/ASC Structures, Structural Dynamics, and Materials Conference, (2002), AIAA2002-1282, pp.1-9.

14. Zuo, L.et al., Structured H2 Optimization of vehicle Suspensions Based on Multi-Wheel Models, Vehicle System Dynamics, Vol.40(2003), pp.351-371.

15. Zuo, L.et al., The Two –Degree-of-Freedom Tuned-Mass Damper for suppression of Single-Mode Vibration under Random and Harmonic Excitation , ASME Journal of vibration and acoustics (2006), pp. 56-65.

16. Iba, D. et al., Robust Design Method of Multi-Degree-of-Freedom Passive Tuned Mass Damper by control Theory, ASME pressure vessels and piping Conference (2006), pp. 1-8.

17. Iba, D. et al., Vibration Control of Nuclear Components Using Simply Supported Dynamic Damper, International Conference on Global environment and Advanced Nuclear power Plants – Kyoto (2003), paper 1056,pp. 1-8.

18. Li, T. H. and pin, K.Y., Evolutionary Algorithms for passive Suspension system, JSME Int. J. Ser. C. 43(3) (2000), pp.537-544.

19. Corriga, G., Giua, A. and Usai, G., An H2 Formulation for the Design of a passive Vibration –Isolation System for Cars, Vehicle System Dynamics, 26 (1996), pp.381-393.

20. Camino, J.F., Zampieri, D.E. and peres, P.I., Design of a Vehicular Suspension Controller by Static Output Feedback, in: Proc.of the American Control Conference, 1999, pp.3168-3172.

21. Elbeheiry, E.M., Karnopp, D.C., Elaraby, M.E. and Abdelraaouf, A.M, Suboptimal Control Design of Active and Passive Suspensions based on a full Car Model, Vehicle System Dynamics, 26(1996),pp.197-222.

22. Lin, Y. and Zhang, Y., Suspension Optimization by Frequency Domain Equivalent Optimal Control Algorithm, J.Sound Vib. , 133(2) (1989), pp.239-249.

23. Elmadany, M.M., A procedure for Optimization of truck Suspensions, Vehicle System Dynamics 16(1987), pp.297-312.

24. Castillo, J.M.D., Pintado, P. and Benitez, F.G., Optimization for Vehicle Suspension II: Frequency Domain, Vehicle System Dynamics, 19(1990), pp.331-352.

25. Demic, M., Optimization of characteristics of Elasto-Damping Elements of Cars from the Aspect Comfort and Handling, Int.Vehicle design, 13(1992), pp.29-46.

26. Spentzas, C.N., Optimization of Vehicle Ride Characteristics by Means of Box's Method, Int. J. Vehicle Design, 14(1993), pp.539-551.

27. Demic, M., Optimization of the characteristics of the Elasto-Damping elements of a passenger Car by means of a modified Nelder-Mead Method, Int.J.Veh.Design, 10(2), (1989), pp.136-152.

28. Pintado, P., and Benitez, F.G., Optimization for Vehicle Suspension: Part I-Time Domain, Veh.Syst. Dyn., 19, (1990), 273-288.

29. Kodiyalam, S. and Sobieski, J., 'Multidisciplinary design optimization-some formal methods, framework requirments, and application to vehicle design', International Journal of Vehicle Design, Special Issue, 25(1/2), 2001, 3-22.

30. Bestle, D. and Eberhard, P., 'Dynamic system design via Multicriteria Optimization, in Multiple Criteria Decision Making', in: Proceedings of the Twelfth International Conference on Multiple Criteria Decision Making, Fandel, G. and Gal, T.(eds.), Springer-Verlag,1995, pp.467-478.

31. Miettinen, K., Nonlinear Multiobjective Optimization, 1999 (Kluwer Academic Publishers, Boston).

32. Grierson, D. and Hajela, P. Emergent Computing Methods in Engineering Design, 1996 (Springer- Verlag, Berlin).

33. Ng, W.Y., Interactive Multi-Objective Programming as a Framework for Computer-Aided Control System Design, 1989 (Springer-Verlag).

34. Stadler, w., Multicriteria Optimization in Engineering and in Sciences, 1988 (Plenum Press, New York).

35. Eschenauer, H., et al. Multicriteria Design Optimization, 1990 (Springer-Verlag).

36. Mastinu, G., A method for the optimal design of railway vehicles, in: world Congress on Railway Research, Florence, 1997.

37. Gobbi, M., et al. Optimal and robust design of a road vehicle suspension system, in: Proceedings of 16th IAVSD Symposium, Supplement of Veh.Syst.Dynamics, 1999.

38. G.Mastinu, A method to design optimal railway vehicles, in: Proceedings of World Congress Railway Research, Florence, 1997.

39. T.X. Mei, R.M. Goodall, Use of Multiobjective genetic algorithms to optimize inter-Vehicle active suspensions, Journal of Rail and Rapid Transit 216 (2002), pp.53-63.

40. G.R.M. Mastinu, M. Gobbi, on the optimal design of railway passenger vehicles, Journal of Rail and Rapid Transit 215 (2001), pp.111-124.

41. H.Li, R.M. Goodall, Linear and non-linear skyhook damping control laws for active railway suspensions, Control Engineering Practice, 7 (1999), pp. 843-850.

42. G.R.M. Mastinu, M. Gobbi and G D Pace, Analytical formulae for the design of a railway Vehicle Suspension System, in: proc. Instn. Mech. Engrs., Vol.215 part C (2001), pp.683-697.

43. YUPING HE, JOHN McPHEE, Multidisciplinary Optimization of Multibody Systems with Application to the Design of Rail Vehicles, Multibody System Dynamics(2005) 14, pp.111-135.

44. Niahn-Chung Shieh, Chun-Liang Lin, Yu-Chen Lin and Kuo-zoo Liang, Optimal design for passive suspension of a light rail vehicle using constrained multiobjective evolutionary search, Journal of Sound and vibration, 285 (2005), pp.407-424.

45. Hung Chi NGUYEN, Akira SONE, Daisuke IBA and Arata MASUDA, Design of passive Suspension System of Railway Vehicles via Control Theory, Journal of System Design and Dynamics, Vol.2, No.2 (2008), pp.518-527.

46. Guglielmino, E. and Sireteanu, T., Semi-active suspension control, ISBN 978-1-84800-230-2 (2008).

47. Hedrick, J.K. and Wormely, D.N., 1975, Active Suspensions- A State of the Art Review, ASME Book No.100095, AMD-Vol.15, Mechanics of Transportation Systems.

48. Goodall, R.M. and Kortum, W., Active control in ground transportation- a review of the state-of-the Art and future potential, Vehicle System Dynamics, Vol.12 (1983), pp. 225-257.

49. Goodall, R., Active Railway Suspensions: Implementation Status and Technological Trends, Vehicle System Dynamics, Vol.28 (1997), pp.87-117.

50. S. BRUNI and R. GOODALL, Control and monitoring for railway vehicle dynamics, Vehicle System Dynamics, Vol.45 (2007), pp.743-779.

51. Goodall, R.M. and Kortum, W., Mechatronic developments for railway vehicles of the future, Control Engineering Practice, Vol.10 (8), pp.887-898.

52. a) Suda, Y., 2006, Collaborative research for railway vehicle systems possibility of innovative and attractive system, in: Proceedings of International Symposium on Speed-up and Service Technology for Railway and Maglev Systems, STECH'06, Chengdu Sichuan, P.R. China, pp. 17–25.
b) Katsuya Tanifuji; Satoshi Koizumi; Ryo-hei Shimamune, "Mechatronics in Japanese rail vehicles: active and semi-active suspensions", Control Engineering Practice, Vol.10 (2002), pp.999-1004.

53. Anneli Orvnas, Active Secondary Suspension in Trains, ISBN 978-91-7415-144-2 (2008).

54. Jalili N., Semi-Active suspension systems, the mechanical Systems Design Handbook-Modeling, Measurement and control, CRC Press LLC, 2002.

55. Hedrick J. K., Railway Vehicle Active Suspensions, Vehicle System Dynamics, Vol.10 (1981), pp.267-283.

56. Anton Stribersky; Andreas Kienberger; Gunther Wanger and Herbert Muller, Design and Evaluation of a Semi-Active Damping System for Rail Vehicles, Vehicle System Dynamics, Vol.28 (1998), pp.669-681.

57. Norino H., Active and semi-Active Suspensions smooth 300 km/h Ride, Railway Gazette International, pp.241-242, April, 1997.

58. Homepage of University of Pretoria (Electronic Theses and Dissertations): Document title " Analysis of a four state switchable hydro-pneumatic spring and damper system" /chapter 2 / http://upetd.up.ac.za/thesis/available/etd-01242006-111737/.

59. J. PAUL TULLIS, Hydraulics of Pipelines, ISBN 0-471-83285-5 (1989).

60. Control valve Handbook, Fisher controls International 4th Edition (2005).

61. FRANK YEAPLE, Fluid Power Design Handbook, ISBN 0-8247-9562-8(1995).

62. Kleinig, A.R., Ide, B.H. & Middelburg, A.P.J. (1995). High-Pressure homogenizer valve mechanics, in: CHEMECA '95', 23rd Aust.Chem.Eng.Conf. Vol.3, pp.50-55.

63. Kleinig, A. R. & Middelberg, A.P.J. (1996). Fluid mechanics of a high-pressure homogenizer, in: the 1996 IChemE Res.Event, 2nd Euro. Conf. For Young Res. In Chem. Eng., Vol.1, pp.109-111.

64. Phipps, L. W. (1975). The fragmentation of oil drops in emulsions by a high-pressure homogenizer, Journal of physics D: Applied Physics, 8, pp.448-462.

65. Nakayama, Y. (1964). Action of the fluid in the air-micrometer (3rd report, characteristics of double-disc nozzle no.1, in the case of compressibility being ignored). Bull. JSME, 7, 698-707.

66. Kawaguchi, T. (1971). Entrance loss for turbulent flow without swirl between parallel discs. Bull. JSME, 14, pp.355-363.

67. Matthew J. Stevenson & Xiao Dong Chen, Visualization of the flow patterns in a High-pressure Homogenizing Valve Using a CFD package, Journal of food Engineering, 33(1997), pp.151-165.

68. Amirante, R., Moscatelli, P.G. and Catalano, L.A., Evaluation of the flow forces on a direct (single stage) proportional valve by means of computational fluid dynamic analysis, Energy Conversion and Management Vol.48,2007, pp.942-953.

69. Amirante, R., Del Vescovo, G. and Lippolis, A., Evaluation of flow forces on an open center directional control valve by means of a computational fluid dynamics analysis, Energy Conversion and Management, Vol.47,2006, pp.1748-1760.

70. Beeson, H.D., Stewart, W. F., and Woods, S. S., "Safe Use of Oxygen and Oxygen Systems: Guidelines for Oxygen System Design, Materials Selection, Operations, Storage and Transportation", ASTM Manual 36, ASTM International, West Conshohocken, PA,2000.

71. Chern, M. and Wang, C., "Control of Volumetric Flow Rate of Ball Valve using V-port", Journal of fluids Engineering (ASME), Vol.126, 2004, pp.471-481.

72. Vu, B., and Wang, T., "Navier-Stokes Flow Field Analysis of Compressible Flow in a High pressure safety Relief Valve", Applied Mathematics and computation, Vol.65, 1994, pp.345-353.

73. Choudhury, S. M. A. A, Thornhill, N.F. and Shah, S.L., "Modeling Valve stiction", Control Engineering Practice, Vol.13 (2005), pp.641-658.

74. Choudhury, S. M. A. A, Thornhill, N.F. and Shah, S.L., "Automatic detection and quantification of stiction in control valves", Control Engineering Practice, Vol.14 (2006), pp.1395-1412.

75. FLUENT, 2005, "User's Guide," Fluent Incorporated, Centra Resource Park, 10 Cavendish Court, Lebanon, NH 03766.

76. Forder, A., Thew, M. and Harrison, D., "A numerical investigation of solid particle erosion experienced within oilfield control valves", Wear, Vol. 216 (1998), pp.184-193.

77. Kalsi, M.S., Eldiwany, B., Sharma, V. and Simonyi, D., "Dynamic Torque Models for Quarter –Turn Air-operated Valves", NRC/ASME Symposium on Valve and Pump Testing, Vol.3 (1999), pp.47-59.

78. Newton, B. E. and Forsyth, E., "Cause and origin analyses of two large industrial gas oxygen valve fires", Flammability and Sensitivity of Materials in Oxygen Enriched Atmospheres, 10th Volume, ASTM STP 1454, T. A. Steinberg, H.D. Beeson and B.E. Newton, Eds., ASTM International, west Conshohocken, PA, 2003, pp.268-289.

79. Oza, A. and Chowdhury, K., "Safe Design of Oxygen System Components: A Review", presented at twenty First National Symposium on Cryogenics, New Delhi, 22nd-24th Nov.2006.

80. Parslow, G.I., Stephenson, D.J., Strutt, J.E. and Tetlow, S., "Investigation of solid particle erosion in components of Complex geometry", Wear, Vol.233, 1999, pp.737-745.

81. Slockers, M. J. and Robles-Culbreth, R., "Ignition of Metals at High Temperatures in Oxygen", Flammability and Sensitivity of Materials in Oxygen-Enriched Environments, 11th Vol., STP 1479, David B. Hirsch; Robert Zawierucha; Theodore A. Steinberg; Hervve Barthelmey Eds, ASTM International, 2006, Pp. 62-79.

82. Ahuja, V., Hosangadi, A., Shipman, J., Daines, R. and Woods, J., "Multi-Element Unstructured Analyses of Complex Valve Systems", Journal of Fluids Engineering, Vol. 128 (2006), pp. 707-716.

83. Davis, J. A., and Stewart, M., ''Geometry Effects when using CFD Analysis as a Design Tool to Predict Control Valve Performance,'' Nineteenth Southeastern Conference on Theoretical and Applied Mechanics, Deerfield Beach, FL, 1998, pp. 38–45.

84. Forsyth, E. T., Newton, B. E., Rantala, J., and Hirschfeld, T., "Using ASTM Standard Guide G 88 to Identify and Rank System-Level Hazards in Large-Scale Oxygen Systems", Flammability and Sensitivity of Materials in Oxygen-Enriched Atmospheres: 10th Volume, ASTM STP 1454, T. A. Steinberg, H. D. Beeson, and B. E.Newton, Eds., ASTM International, West Conshohocken,PA, 2003, pp. 211 - 229.

85. Mazur, Z., Campos-Amezcua, R., Urquiza-Beltrán, G. and García-Gutiérrez, A.,"Numerical 3D simulation of the erosion due to solid particle impact in the main stop valve of a steam turbine", Applied Thermal Engineering Vol. 24, 2004, pp.1877–1891.

86. Aditi Oza, Sudipto Ghosh and Kanchan Chowdhury, CFD Modeling of Globe Valves for Oxygen Application, in: 16th Australasian Fluid Mechanics Conference, Crown Plaza, Gold Coast, Australia, 2-7 December 2007.

87. Cao Bingang, Numerical study on fluid flow in poppet valve by boundary element method, Machine Tool and Hydraulics, Vol.2 (1991).

88. Kazumi ITO, Flow in poppet Valve, Proc of 1st international symposium on FPTC, 1991 Beijing China.

89. BORGHI M, MILANI M, PAOLUZZI R. Stationary axial flow Forces analysis on compensated spool valves [J]. International Journal of Fluid Power, 2000, 1(1), pp.13−22.

90. YUAN Q H, LI P Y. Using Viscosity to improve spool agility[C]//The 2002 Bath workshop on Power Transmission and Control, University of Bath, UK, September 12−14, 2002,pp. 101−106.

91. YUAN Q H, LI P Y. An Experimental Study on the Use of Unstable Electro hydraulic Valves for Control[C], in: Proceedings of the 2002 American Control Conference, Anchorage Alaska, USA, May 16-20, 2002, pp. 178−184.

92. BAO M, FU X, CHEN Y. Computational fluid dynamic approach to pressure loss analysis of hydraulic spool valve[C], in: Proceedings of the 5th International Conference of Fluid Power Transmission and Control, Hangzhou, China, April 3−5, 2001, pp. 467−471.

93. WANG L X, CHEN Y, RUAN X D, et al. Experimental study on Fluid Flow in Fluid Power system[C], in: Proceedings of the 4th International Conference of Fluid Power Transmission and Control, Hangzhou, China, September 9-11, 1997,pp. 6-9.

94. RUAN X D, SONG X Q, YAMAMOTO F, et al. PIV experiment of flow field in spool valve chamber[C], in: Proceedings of the 4th International Conference of Fluid Power Transmission and Control, Hangzhou, China, September 9−11, 1997, pp. 42−45.

95. VAUGHAN N D, JONSTON D N, BURNELL L R. The use of computational dynamics in hydraulic valve design: design, circuit, component and system design [M]. New York: John Wiley and Sons Inc., 1992.

96. BORGHI M, "Hydraulic Locking-in spool- type valves: tapered clearance analysis", in: Proc. Instn. Mech. Engrs, Vol.215 Part I, pp.157-168.

97. GAO Dianrong, QIAO Haijun and LU Xianghui, " Finite Element Numerical Simulation and PIV Measurement of Flow Field inside Metering-in Spool Valve", CHINESE JOURNAL OF MECHANICAL ENGINEERING, Vol.22, No.1,2009, pp. 1-7.

98. J.Emura, S.Kakizaki, F.Yamaoka, and M.Nakamura, "Development of the Semi-Active Suspension System Based on the sky-hook Damper Theory", SAE 940863, 1994.

99. Se Kyung Oh, Young Hwan Yoon, and Ary Bachtiar Krishna, " A Study on the performance Characteristics of Variable Valve for Reverse Continuous Damper", World Academy of Science, Engineering and Technology, Vol 32(2007), pp.123-128.

100. R.W. Fox, P.J. Pritchard and A.T. McDonald, Introduction to Fluid Mechanics, wiley, 7th edition, New York, 2009.

101. Hochreiter, H.M. - Dimensionless correlation of coefficients of turbine type flow meters, Trans. ASME, October 1958, pp. 1363-1368.

APPENDIX A

APPENDIX A

TRUCK ASSEMBLY, CONTROL VALVE AND CYLINDER DRAWINGS

TRUCK ASSEMBLY

	DESCRIPTION	QUANTITY	PART NO.
1	SIDE FRAME ASSEMBLY	2	2764-20
2	BOLSTER ASSEMBLY	1	2764-21
3	TRAMSOM	1	2901-24
4	HYDRAULIC CYLINDER ASSEMBLY	4	2901-17
5	D7 OUTER SPRING	12	
6	GUDGON BLOCK	4	2901-21
7	SIDE BEARING	2	
8	LATERAL STOP	2	2901-23

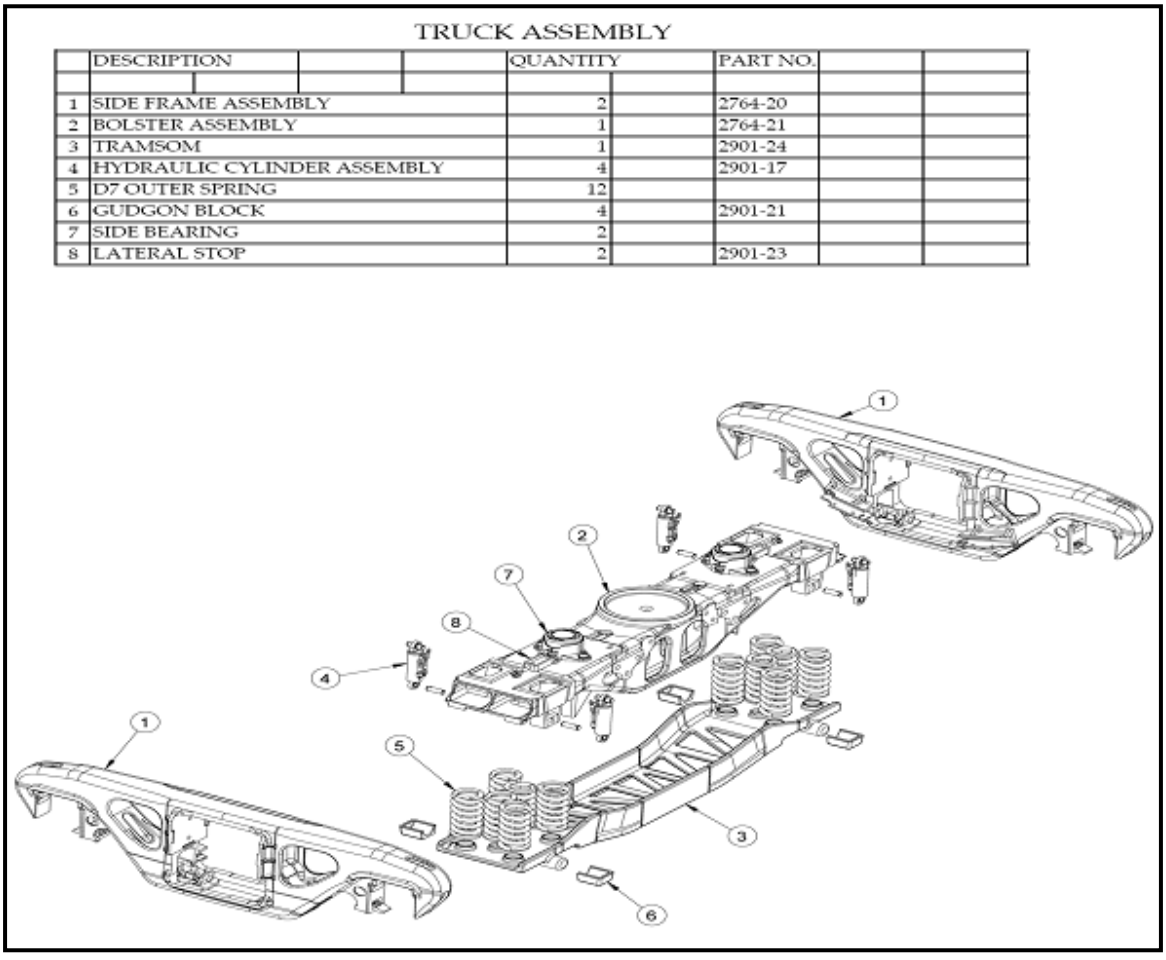

Figure A1: Truck Assembly (Courtesy of Amsted Rail).

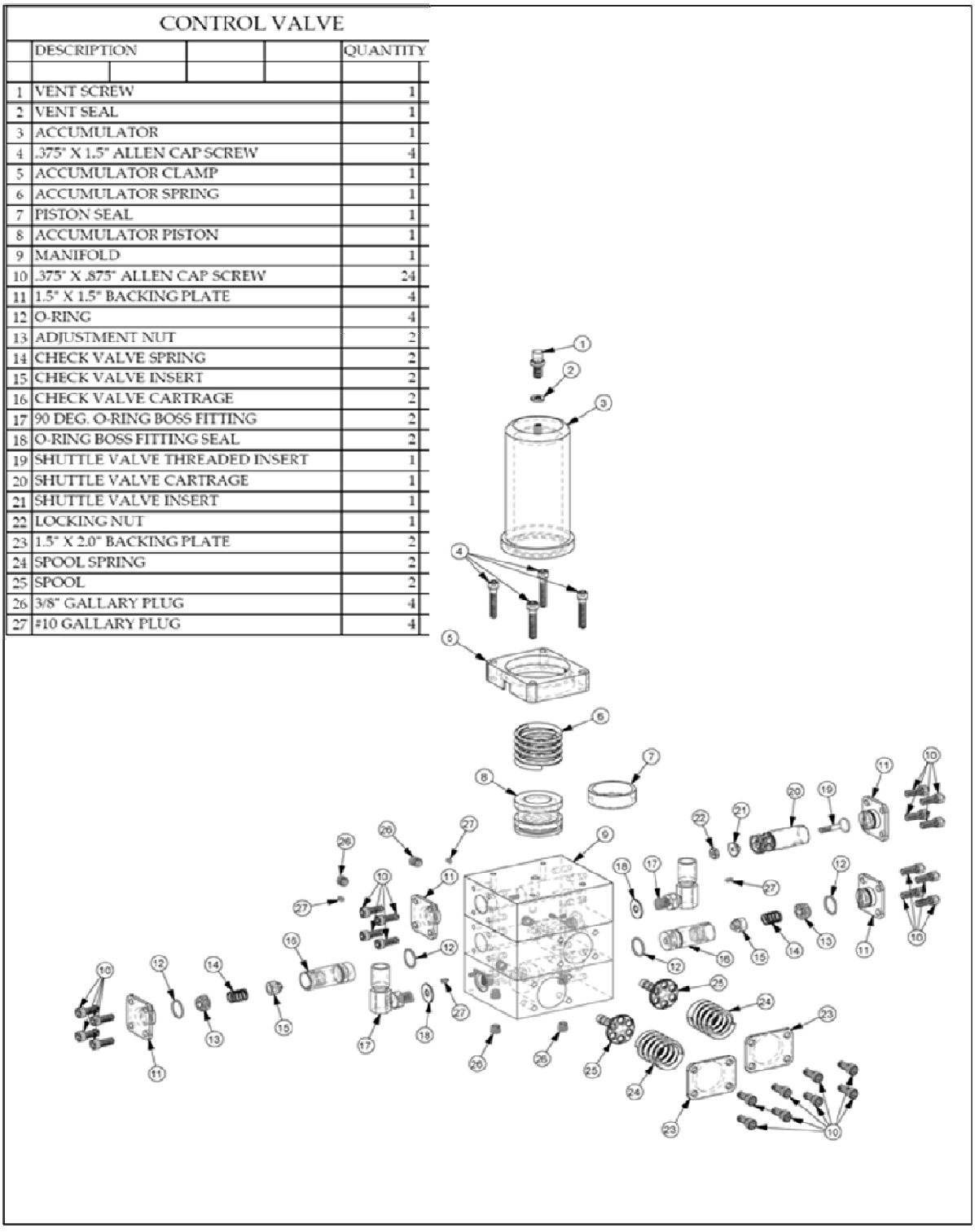

CONTROL VALVE

	DESCRIPTION	QUANTITY
1	VENT SCREW	1
2	VENT SEAL	1
3	ACCUMULATOR	1
4	.375" X 1.5" ALLEN CAP SCREW	4
5	ACCUMULATOR CLAMP	1
6	ACCUMULATOR SPRING	1
7	PISTON SEAL	1
8	ACCUMULATOR PISTON	1
9	MANIFOLD	1
10	.375" X .875" ALLEN CAP SCREW	24
11	1.5" X 1.5" BACKING PLATE	4
12	O-RING	4
13	ADJUSTMENT NUT	2
14	CHECK VALVE SPRING	2
15	CHECK VALVE INSERT	2
16	CHECK VALVE CARTRAGE	2
17	90 DEG. O-RING BOSS FITTING	2
18	O-RING BOSS FITTING SEAL	2
19	SHUTTLE VALVE THREADED INSERT	1
20	SHUTTLE VALVE CARTRAGE	1
21	SHUTTLE VALVE INSERT	1
22	LOCKING NUT	1
23	1.5" X 2.0" BACKING PLATE	2
24	SPOOL SPRING	2
25	SPOOL	2
26	3/8" GALLARY PLUG	4
27	#10 GALLARY PLUG	4

Figure A2: Control Valve's drawing with parts description.

(Courtesy of Amsted Rail).

CYLINDER			
	DESCRIPTION	QUANTITY	PART NO.
1	CYLINDER WALL ASSEMBLY	1	2901-22
2	RETAINING RING	1	
3	DOWEL PIN	1	
4	PISTON	1	2901-12
5	PACKING SEAL	1	2901-09
6	PACKING SEAL O-RING	1	
7	RETAINING RING	1	
8	CYLINDER ROD	1	2901-14
9	BREAK BLEED VALVE	2	
10	PISTON TO ROD SEAL	2	
11	HIMOD SLYDRING	1	
12	TURCON AQ-SEAL	1	
13	TURCON STEPSEAL 2K	1	
14	HIMOD SLYDRING	1	
15	TURCON VL SEAL	1	
16	ZURCON SCRAPER DA 24	1	
17	SPHERICAL BEARING	2	2901-16

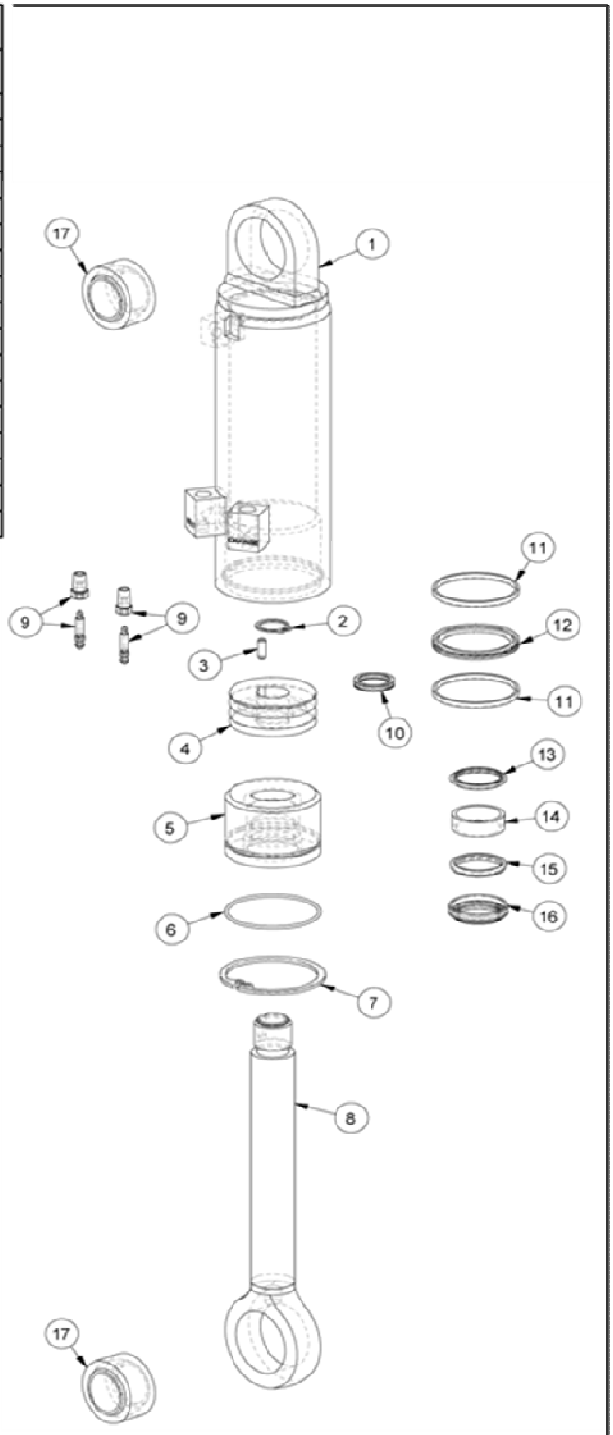

Figure A3: Cylinder's drawing with parts description (Courtesy of Amsted Rail).

APPENDIX B

APPENDIX B

FOSTER HYDRAULIC POWER UNIT

DRAWINGS WITH COMPONENTS DESCRIPTION

COMPONENT DESIGNATED NUMBER AND DESCRIPTION:

(1) RETURN LINE HOSE, IN CIRCUIT/HEAT EXCHANGER.

(2) ELECTRICAL STEP-DOWN TRANSFORMER, 120 V SUPPLY.

(3) ADJUSTABLE THERMOSTAT, HEAT EXCHANGER CONTROL.

(4) POP-UP INDICATOR/ PRESSURE FILTER.

(5) MAIN PRESSURE HOSE, SUPPLY CIRCUIT.

(6) RETURN LINE HOSE, OUT CIRCUIT TO RETURN FILTE.

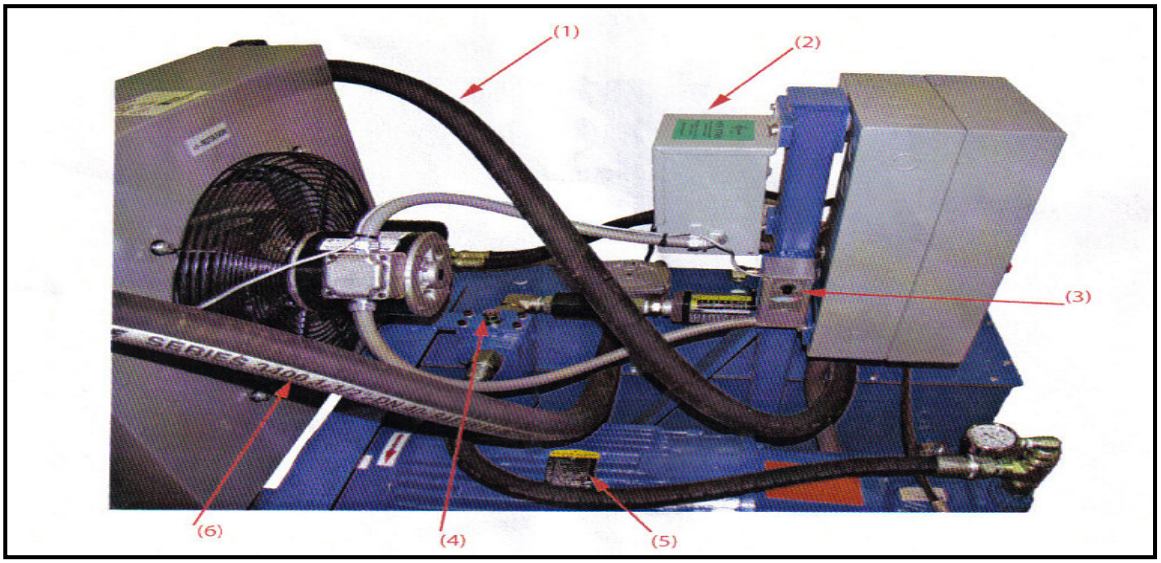

Figure B1: Hydraulic power unit Model 400-1P-18 EC system components.

COMPONENT DESIGNATED NUMBER AND DESCRIPTION:

(1) PRESSURE GAUGE, 0-4000PSI, LIQUID FILLED

(2) 40 H.P. ELECTRIC MOTOR, 3/60/240/480V. 1760 R.P.M., T.E.F.C.

(3) RESERVOIR DRAIN DOWN BALL VALVE

(4) FAN-COOLED HEAT EXCHANGER, 120 V. MOTOR

(5) HEAT SENSOR/ BULB WELL, THERMOSTAT PROBE

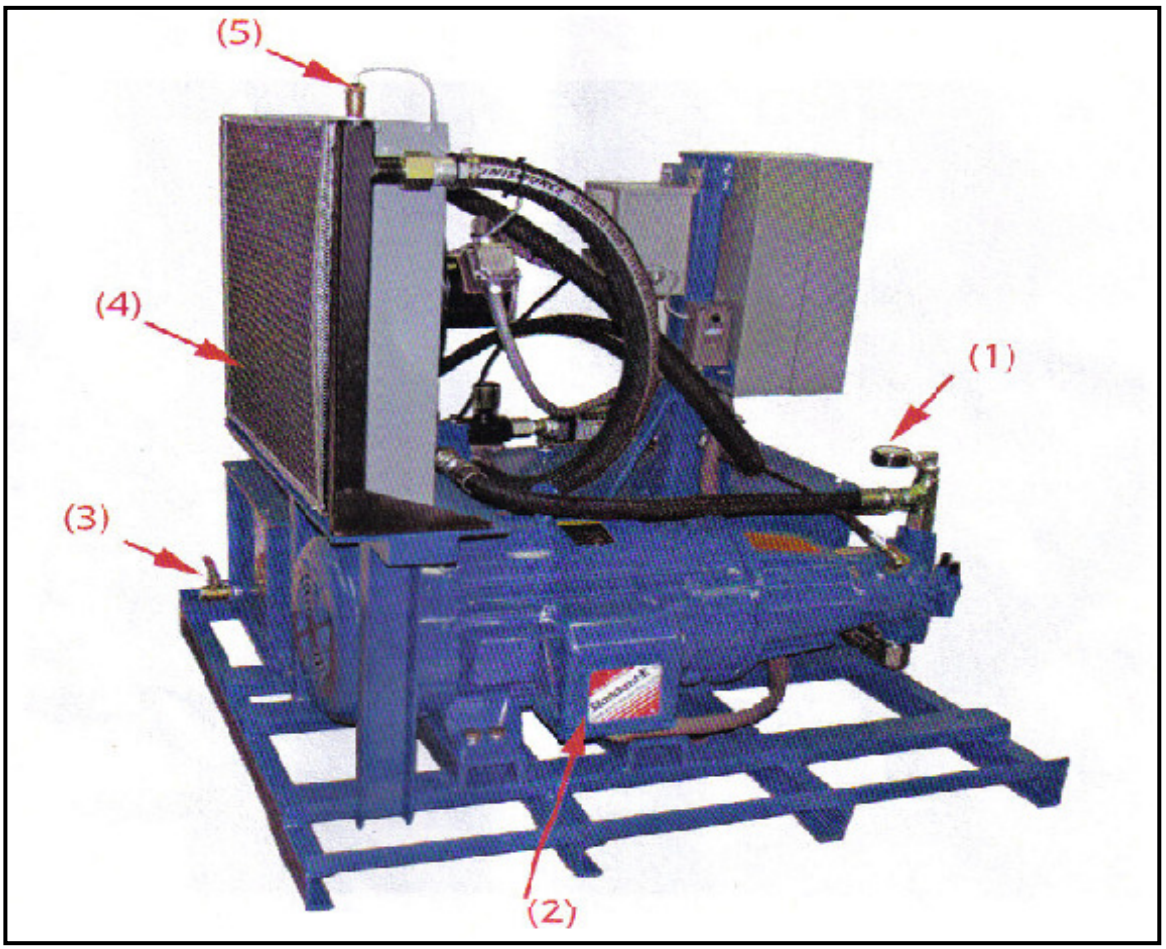

Figure B2: Hydraulic power unit Model 400-1P-18 EC system components.

COMPONENT DESIGNATED NUMBER AND DESCRIPTION:

(1) DUAL CROSS-OVER RELIEF VALVE.

(2) WORKING PORT, PLUMBED TO CYLINDER OR MOTOR.

(3) WORKING PORT, PLUMBED TO CYLINDER OR MOTOR.

(4) NORMALLY-OPEN, MAINTAINED CLOSED ACTIVATING SWITCH, CIRCUIT #1.

(5) NORMALLY-OPEN, MAINTAINED CLOSED ACTIVATING SWITCH, CIRCUIT #2.

(6) HAND-HELD PENDANT ASSEMBLY ON CORD SET.

(7) ADJUSTABLE RELIEF VALVE, CROSS-OVER RELIEF CIRCUIT #1.

(8) ADJUSTABLE RELIEF VALVE, CROSS-OVER RELIEF CIRCUIT #2.

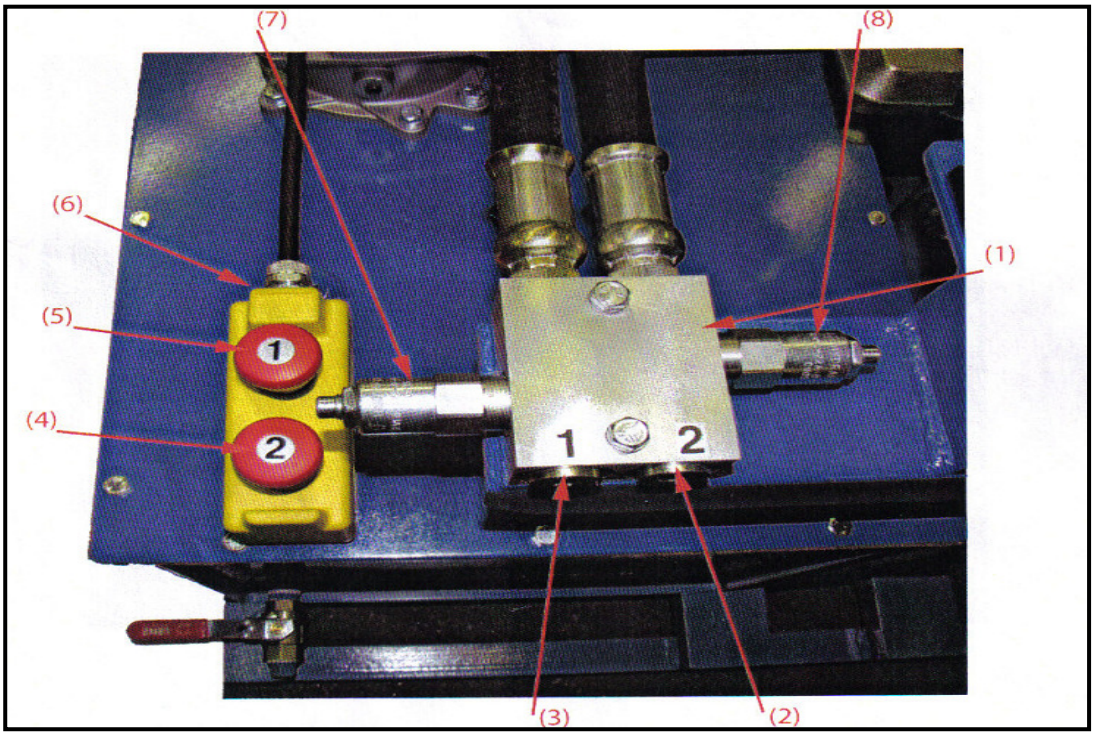

Figure B3: Hydraulic power unit Model 400-1P-18 EC system components.

COMPONENT DESIGNATED NUMBER AND DESCRIPTION:

(1) HYDRAULIC PRESURE FILTER, 5 MICRON ELEMENTS.

(2) PRESSURE SUPPLY HOSE, CIRCUIT #2.

(3) PRESSURE SUPPLY HOSE, CIRCUIT #1.

(4) ADJUSTABLE FLOW CONTROL VALVE.

(5) RETURN LINE FILTER, SUBMERGED STYLE, 10 MICRON ELEMENT.

(6) INLINE PRESSURE SIDE FLOW METER.

(7) FILLER/BREATHER CAP.

(8) DIRECTIONAL CONTROL VALVE, 120 V CLOSED CENTER “E” SPOOL.

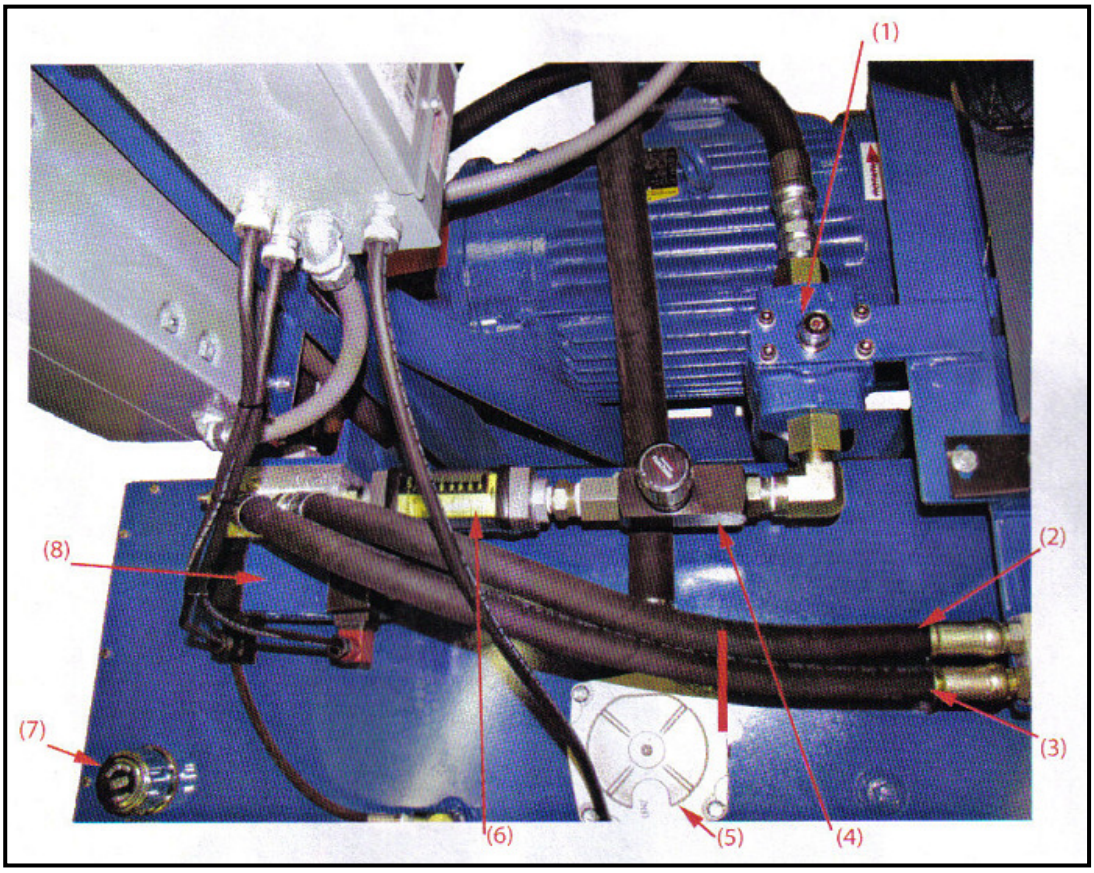

Figure B4: Hydraulic power unit Model 400-1P-18 EC system components.

COMPONENT DESIGNATED NUMBER AND DESCRIPTION:

(1) HYDRAULIC RESERVOIR, 40 GALLON CAPACITY.

(2) SKID/BASE.

(3) SIGHT/LEVEL/TEMPERATURE GAUGE.

(4) ON/OFF BALL VALVE, SUCTION SIDE, RESERVOIR SUPPLY.

(5) PRESSURE COMPENSATED VARIABLE DISPLACEMENT PUMP, AAV5045DFR, WESTREN.

(6) ALLEN-BRADLEY MAGNETIC MOTOR STARTER, 480 VOLT COIL AND HEATERS.

(7) MAIN SUPPLY CIRCUIT ADJUSTABLE RELIEF VALVE.

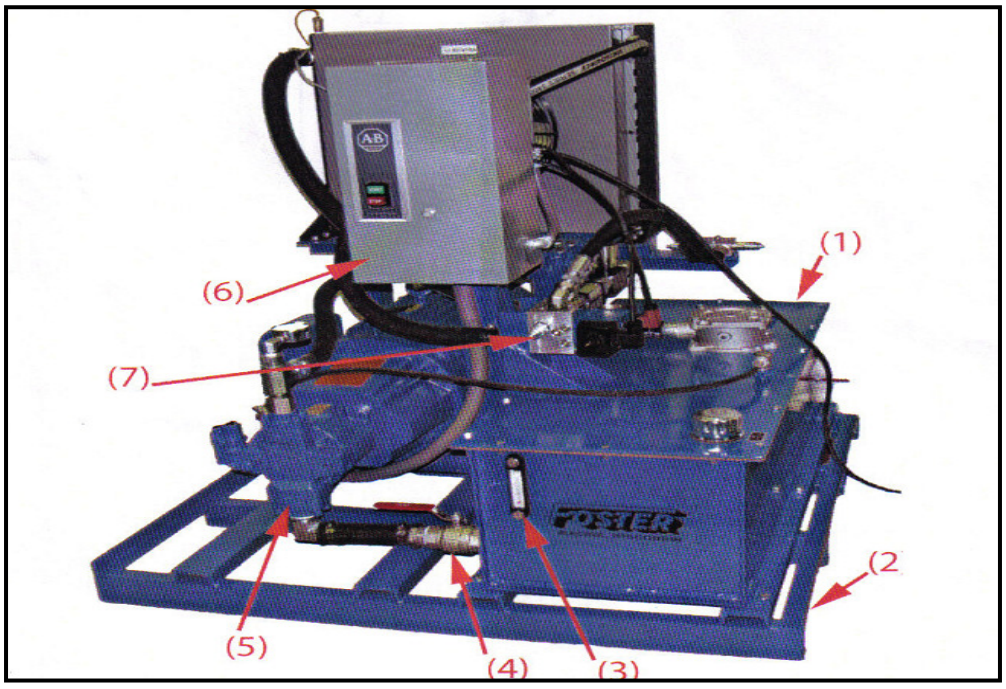

Figure B5: Hydraulic power unit Model 400-1P-18 EC system components.

COMPONENT DESIGNATED NUMBER AND DESCRIPTION (see Figure B6):

(1) RESERVOIR / TANK.

(2) ON/OFF BALL VALVE, RESERVOIR SUPPLY.

(3) PRESSURE COMPENSATED, VARIABLE DISPLACEMENT PUMP.

(4) MOTOR.

(5) PRESSURE INDICATOR.

(6) HYDRAULIC PRESSURE FILTER, 5 MICRON ELEMENT.

(7) VARIABLE VALVE TO ADJUST THE INLET FLOW.

(8) BUILT IN VARIABLE ORIFICE FLOW METER.

(9) MAIN RELIEF VALVE.

(10) DIRECTIONAL CONTROL VALVE, 120V CLOSED CENTER “E” SPOOL.

(11) ADJUSTABLE RELIEF VALVE, CROSS-OVER RELIEF CIRCUIT #1 AND #2.

(12) FAN-COOLED HEAT EXCHANGER, 120V MOTOR.

(13) RETURN LINE FILTER, SUBMERGED STYLE, 10 MICRON ELEMENT.

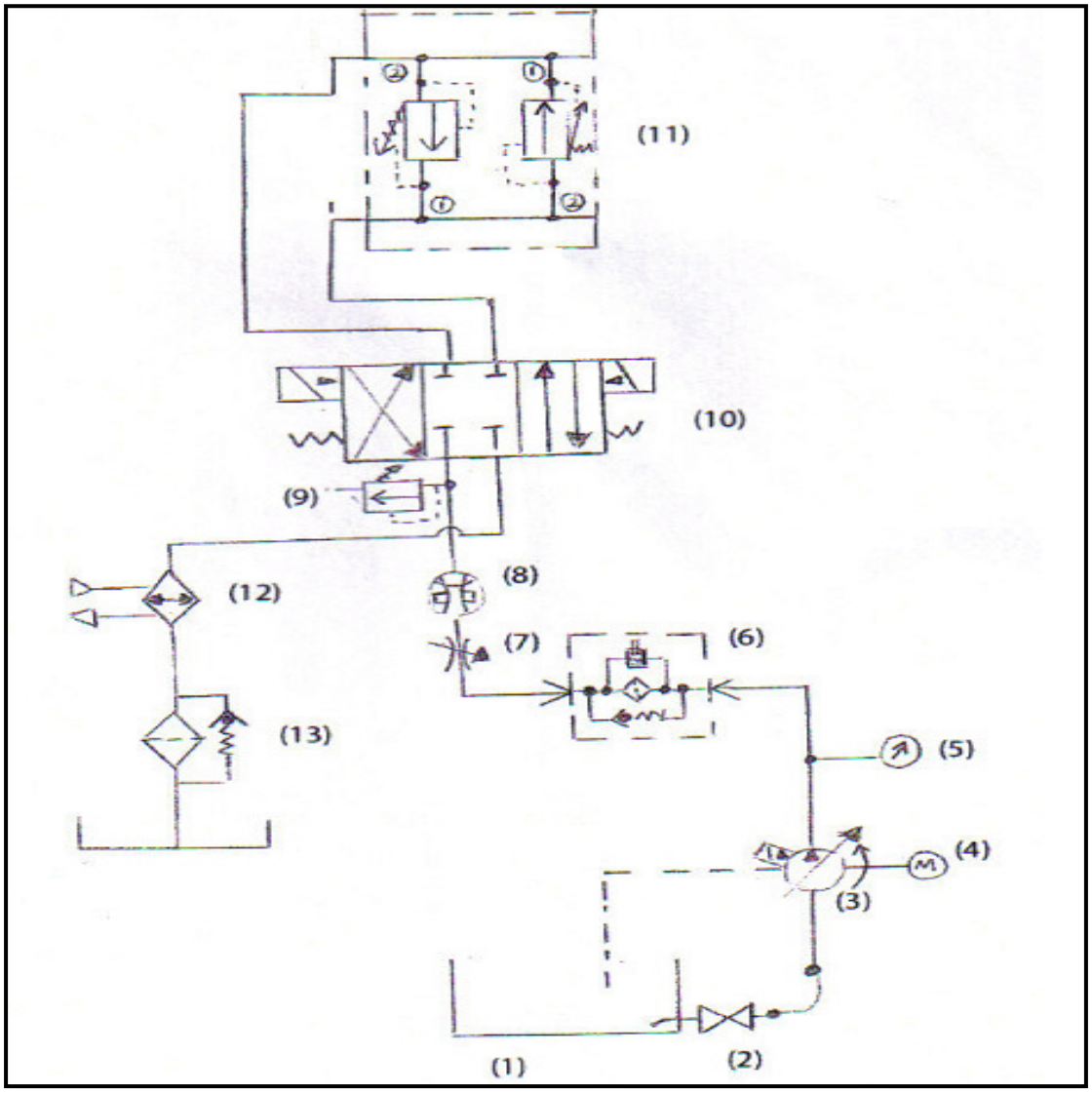

Figure B6: A schematic diagram of Hydraulic power unit Model 400-1P-18 EC system components.

APPENDIX C

APPENDIX C

DIMENSIONS OF THE TESTED SPOOLS

SPOOL #1

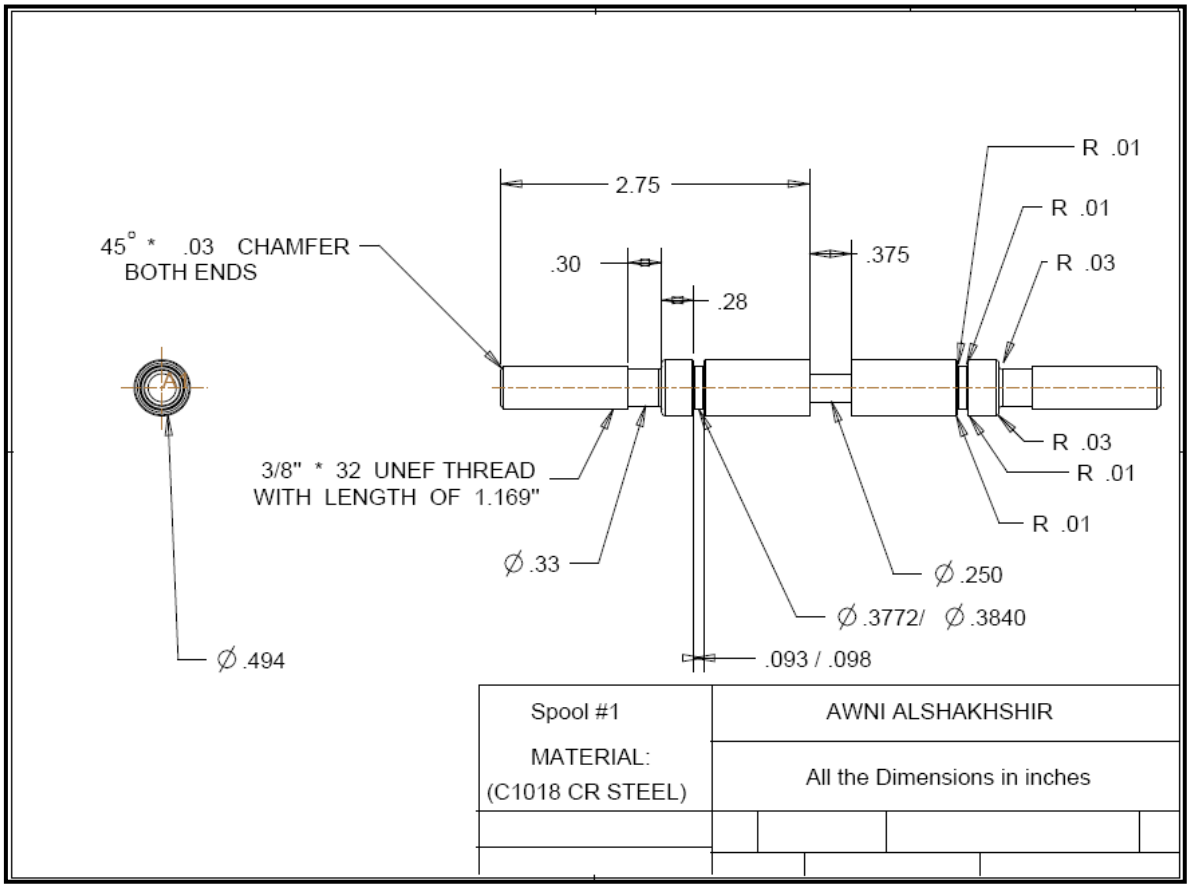

Figure C1: CAD drawing of spool #1.

All the other spools have the same dimensions as spool #1 except the land dimensions and shape as shown below:

SPOOL #2

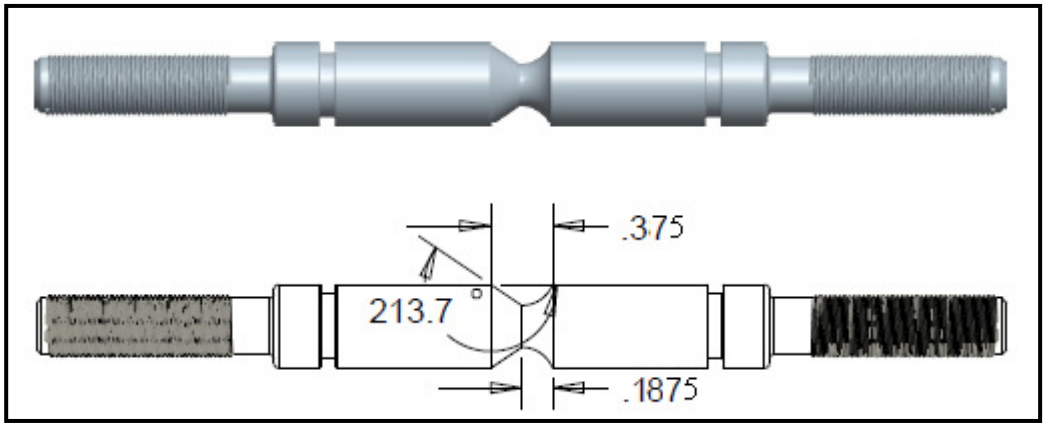

Figure C2: CAD drawing of spool #2.

SPOOL #3

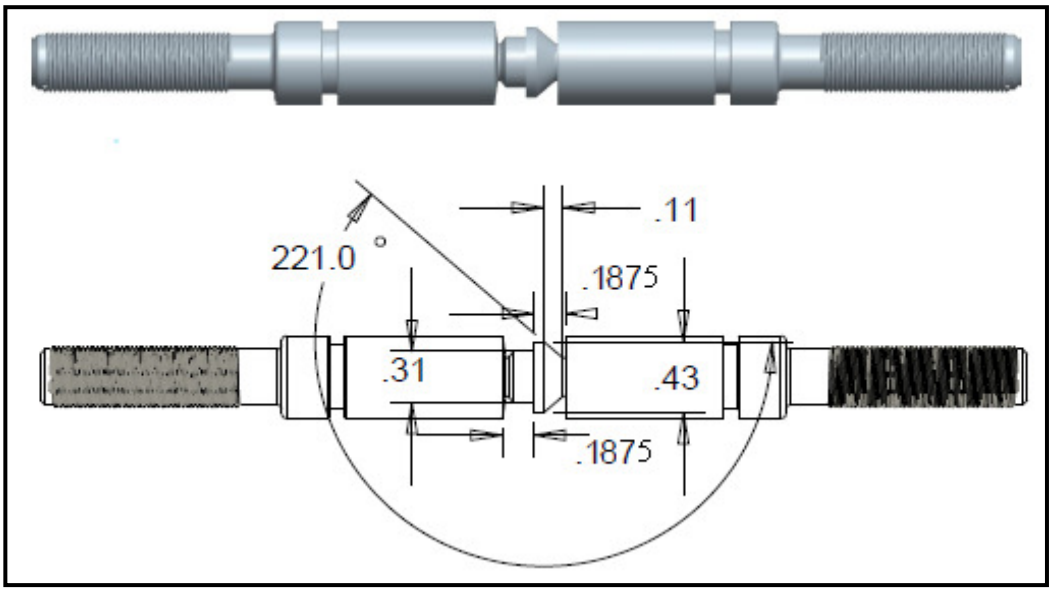

Figure C3: CAD drawing of spool #3.

SPOOL #4

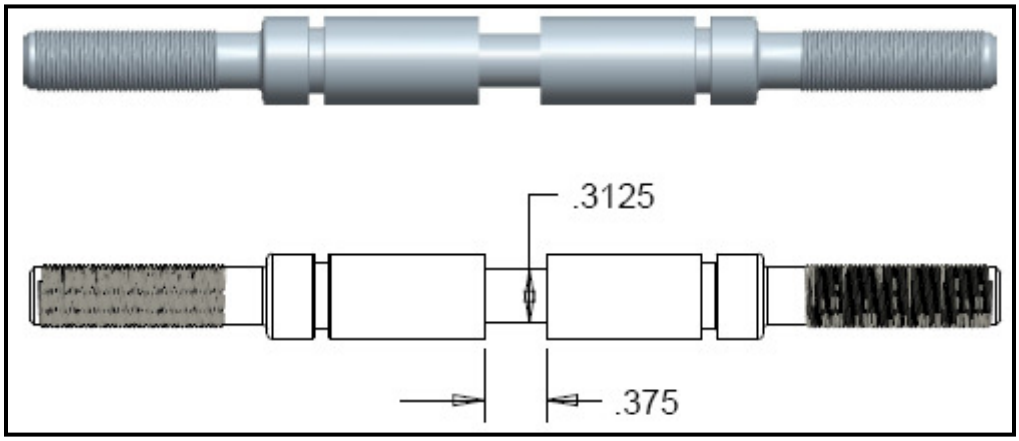

Figure C4: CAD drawing of spool #4.

SPOOL #5

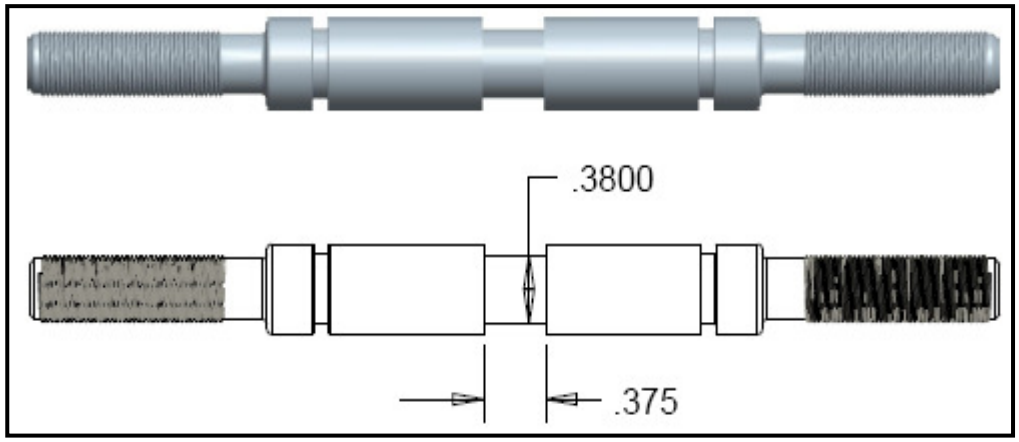

Figure C5: CAD drawing of spool #5.

SPOOL #6

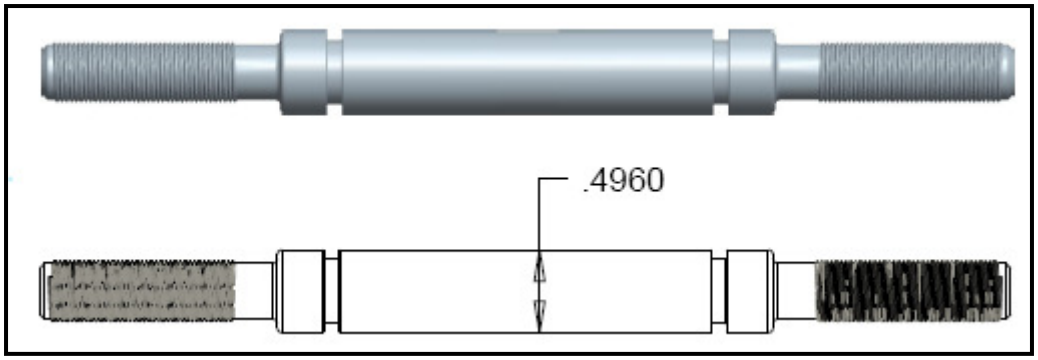

Figure C6: CAD drawing of spool #6.

SPOOL #7

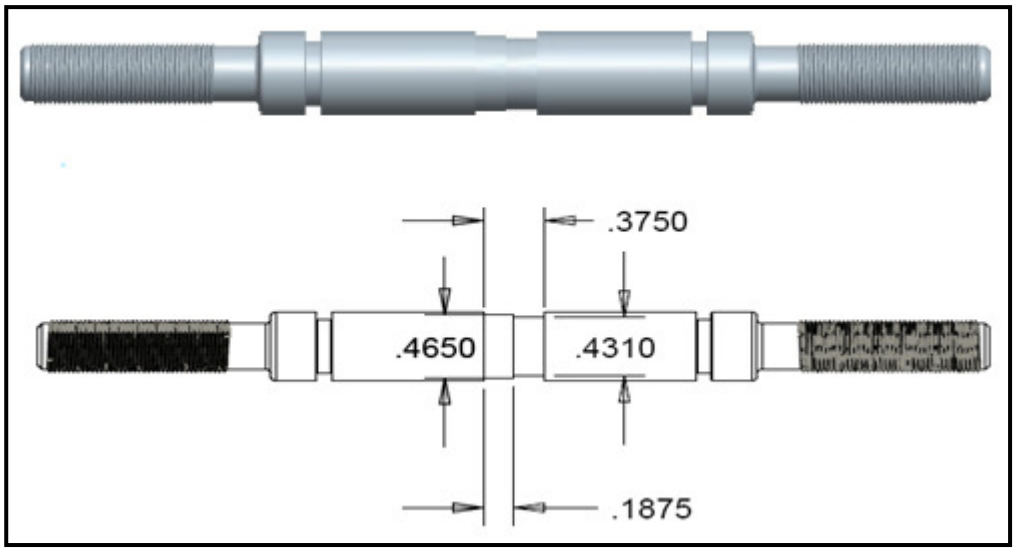

Figure C7: CAD drawing of spool #7.

SPOOL #8

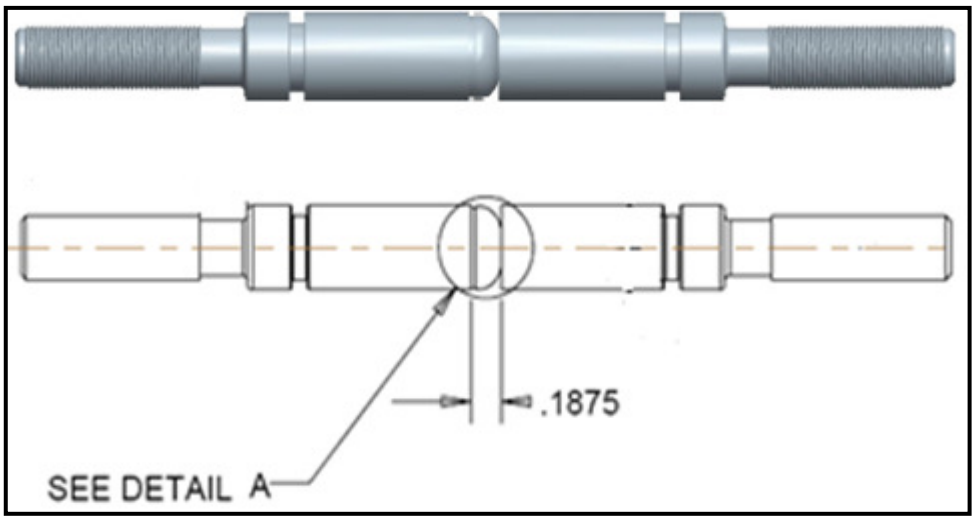

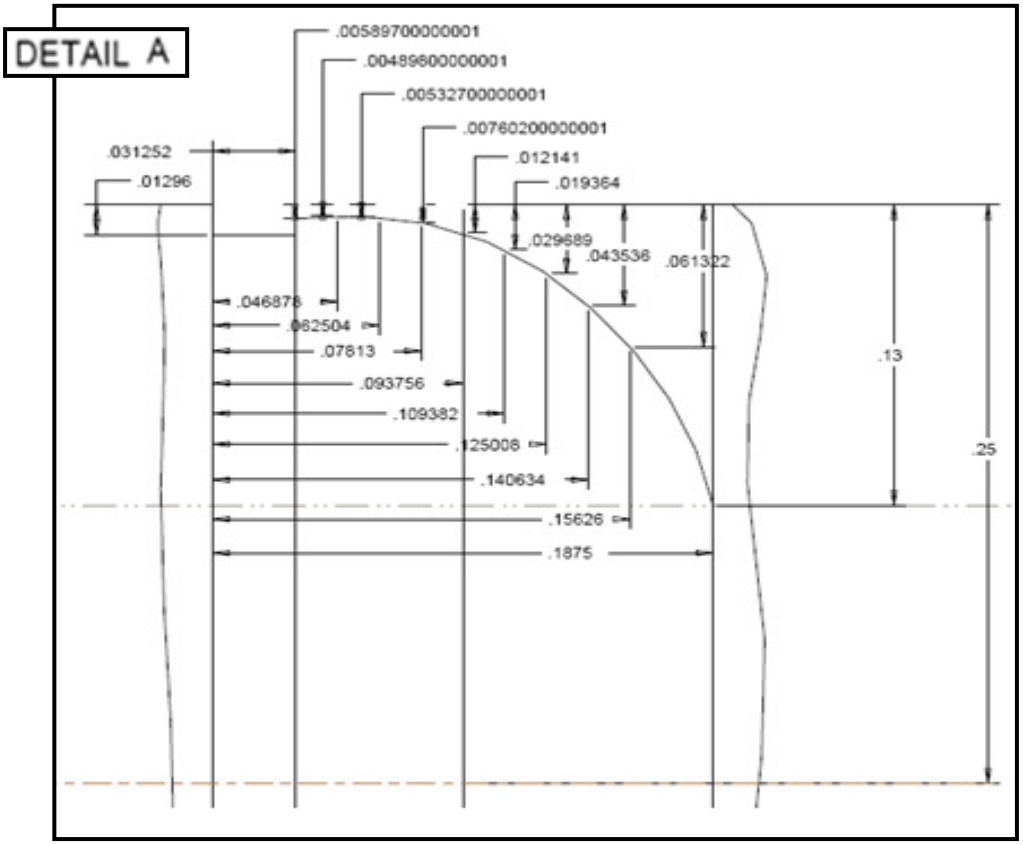

Figure C8: CAD drawing of spool #8.

SPOOL #8A

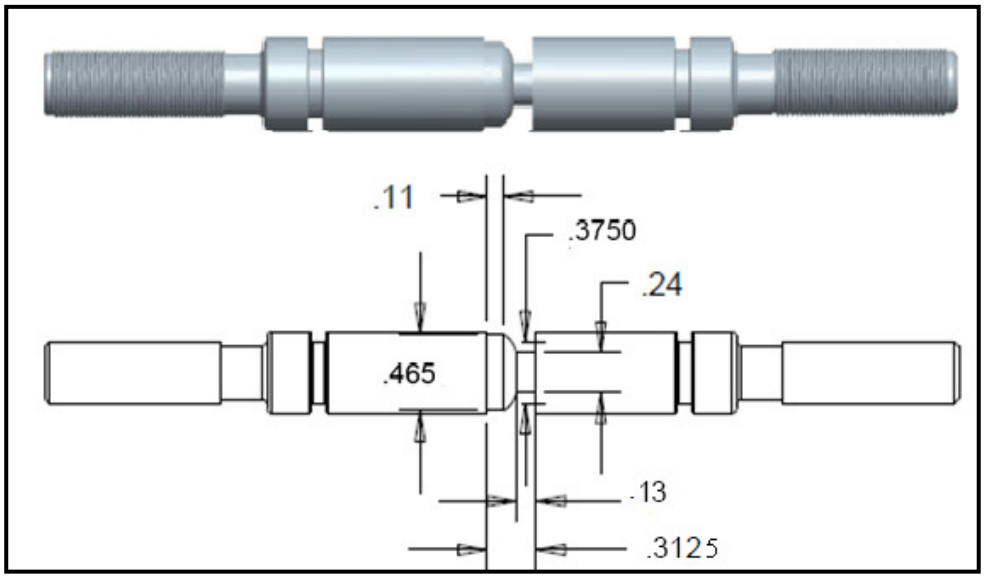

Figure C9: CAD drawing of spool #8A.

SPOOL #9

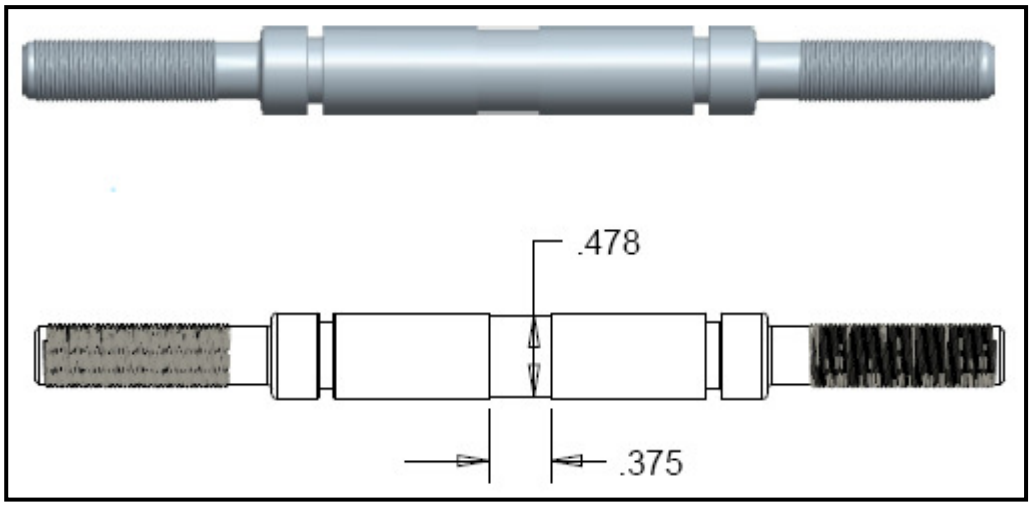

Figure C10: CAD drawing of spool #9.

SPOOL #10

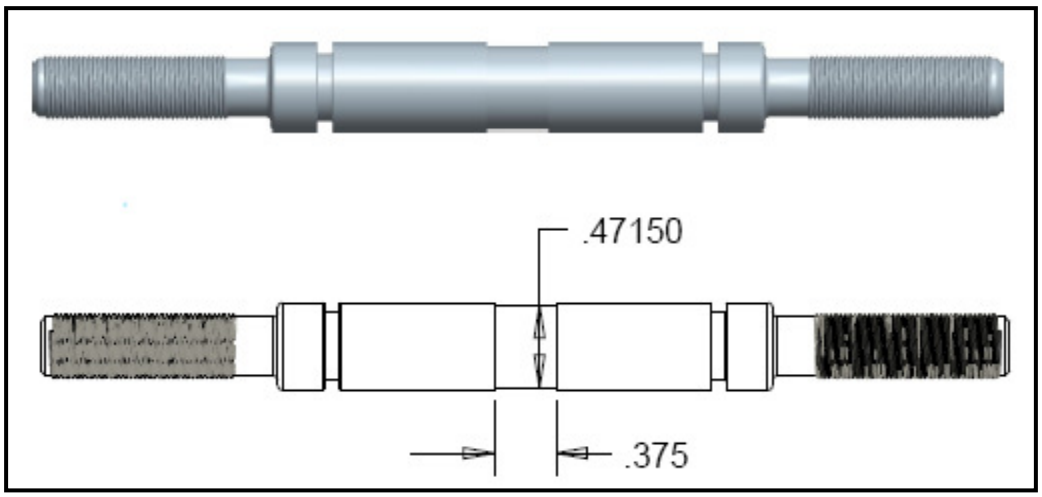

Figure C11: CAD drawing of spool #10.

SPOOL #11

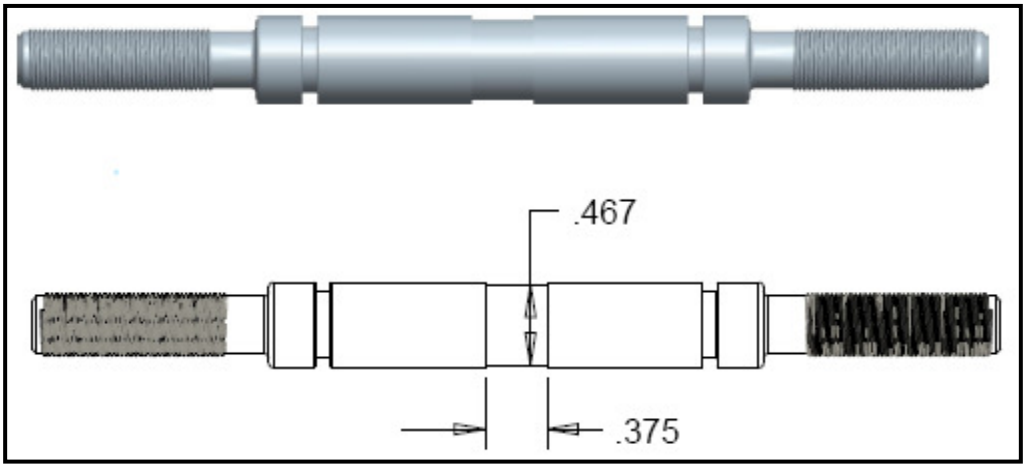

Figure C12: CAD drawing of spool #11.

SPOOL #12

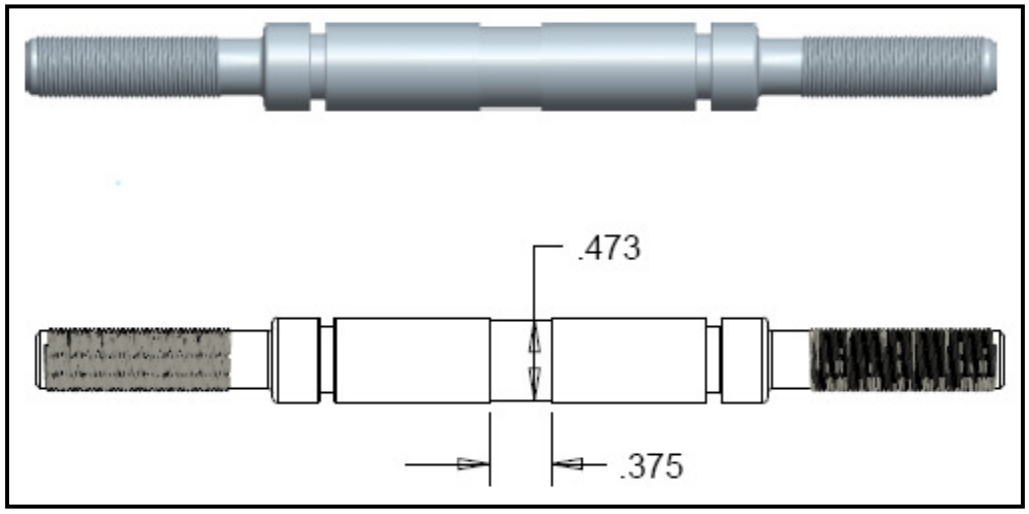

Figure C13: CAD drawing of spool #12.

APPENDIX D

APPENDIX D

ORIFICE WINDOW SIZING

Amsted Rail Engineering requested a sizing for a rectangular orifice passage (*i.e.* a rectangular duct) that will be used to straighten the flow before and after entering the spool valve chamber without causing significant pressure drop. In addition, it will be the test window upon which quantifying flow characteristics for different spool lands will be made.

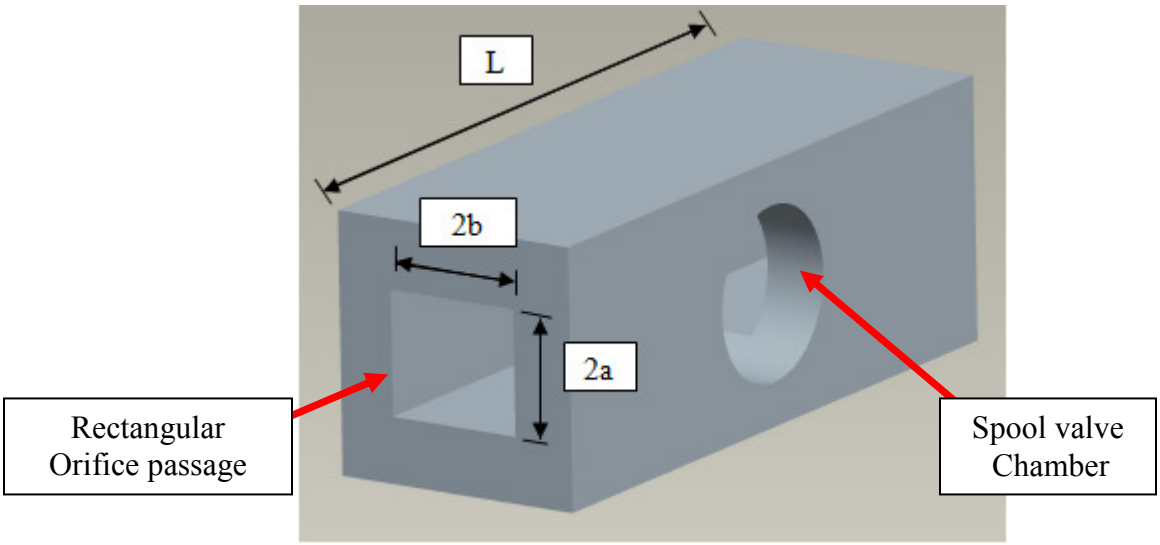

Figure D1: A schematic of the Orifice valve that need to be sized.

The width of the Orifice (*i.e. 2b*) was initially chosen by Amsted Rail to be 0.375 inch; since they were interested in test spools with this much of land length.

The objective was to find the ratio between the orifice height and its width (*i.e. a/b*) that would give the minimal pressure losses along its length (*i.e. L*). Thus; by assuming Newtonian, viscous and laminar fully developed flow through a rectangular orifice section, Equ. (D-1) and (D-2) were used to get the pressure drop at different $(a/b) \in [0.04, 1]$ as following[3]

$$\Delta P = \frac{-3\mu Q \times L}{4b^4 \left(a/b\right)^3 \times S} \tag{D-1}$$

and

$$S = 1 - \left[\frac{192(a/b)}{\pi^5} \times \sum_{i=1,3,5,....}^{\infty} \frac{\tanh\left(\frac{i\pi}{2(a/b)}\right)}{i^5} \right] \tag{D-2}$$

where the maximum value of Q was chosen (*i.e.*14.688 GPM, see Figure 10) and maximum value of μ was chosen (*i.e.* 412 cP for flow temperature of 0°C, see Table 30) in the pressure drop calculations; in order to create the worst case scenario of the flow that passing through the orifice at different (*a*/*b*) ratios.

[3] Frank M. White, Viscous Fluid Flow, 2nd edition, ISBN 0-07-069712-4.

As shown below, the pressure loss is minimal when (a/b) is equal to one (*i.e.* when the orifice section is square). Thus, the height of the orifice section (*i.e.* 2a) was chosen to be 0.375 inch.

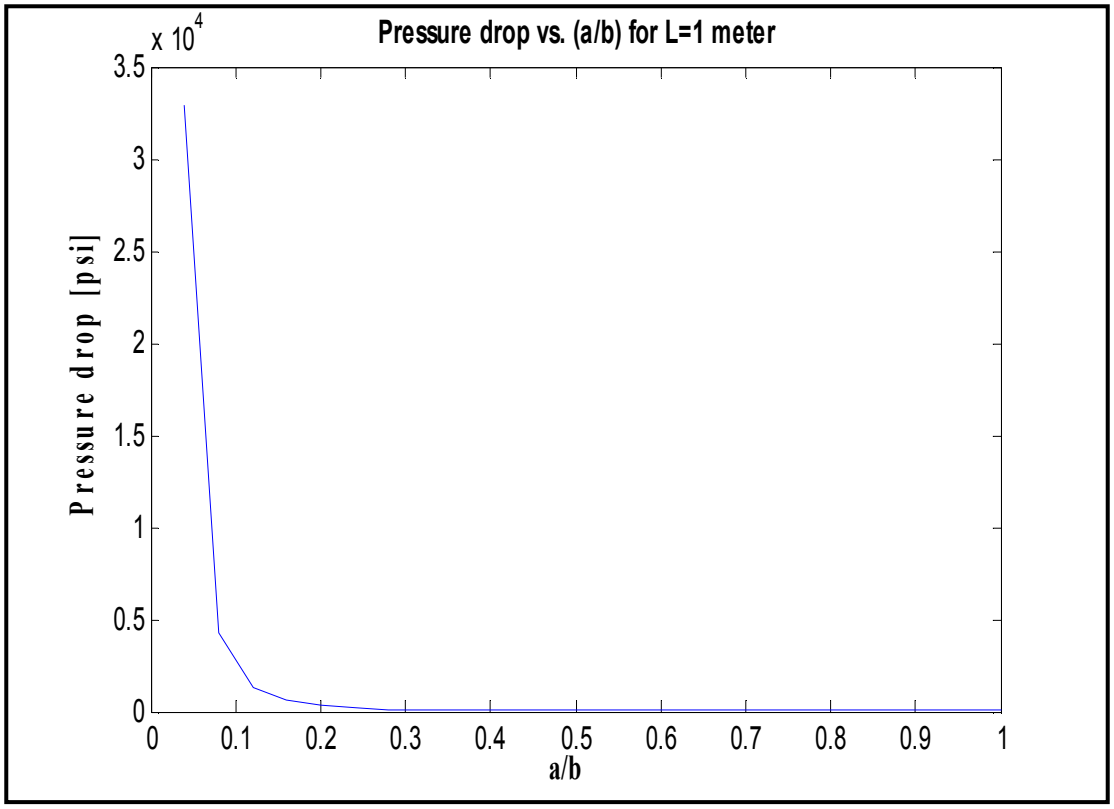

Figure D2: A plot of the pressure drop vs. different Orifice height-width ratios (a/b).

In addition, the corresponding Mean velocities and Reynolds Numbers for the aforementioned pressure loss calculations are shown below. It can be noticed that the flow stays laminar (Reynolds number is less than 2300) for all Orifice height to width ratios, which agree with the aforementioned assumption.

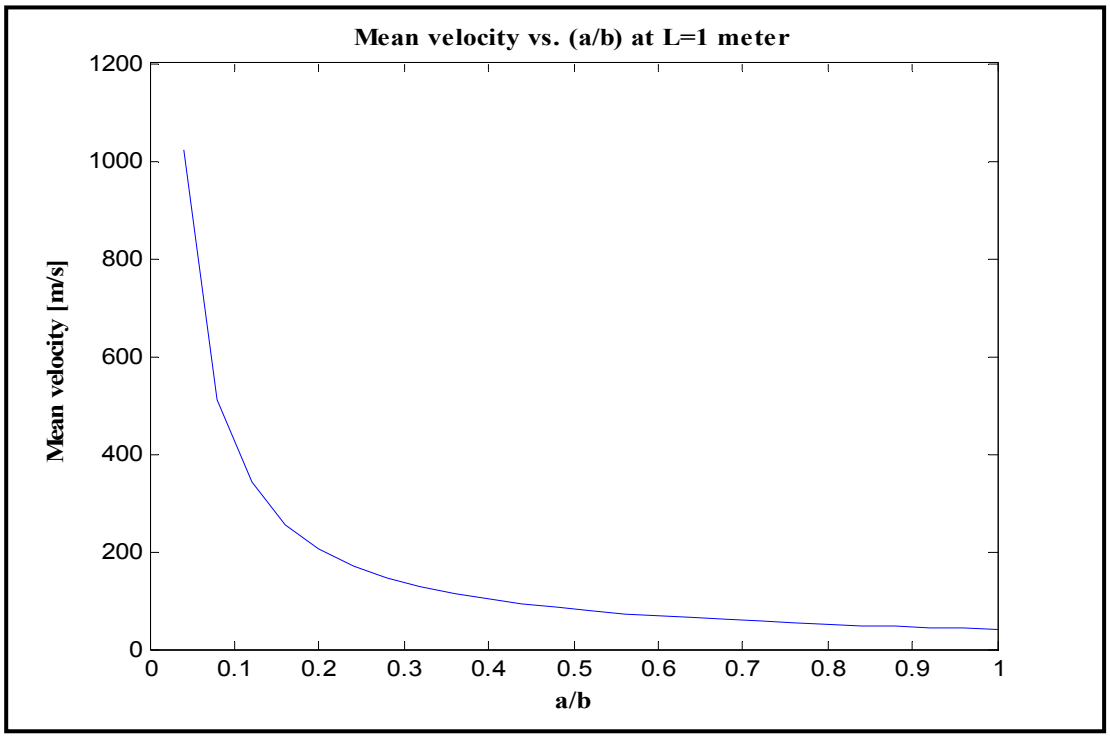

Figure D2: A plot of the Mean velocity vs. different Orifice height-width ratios (*i.e.* a/b).

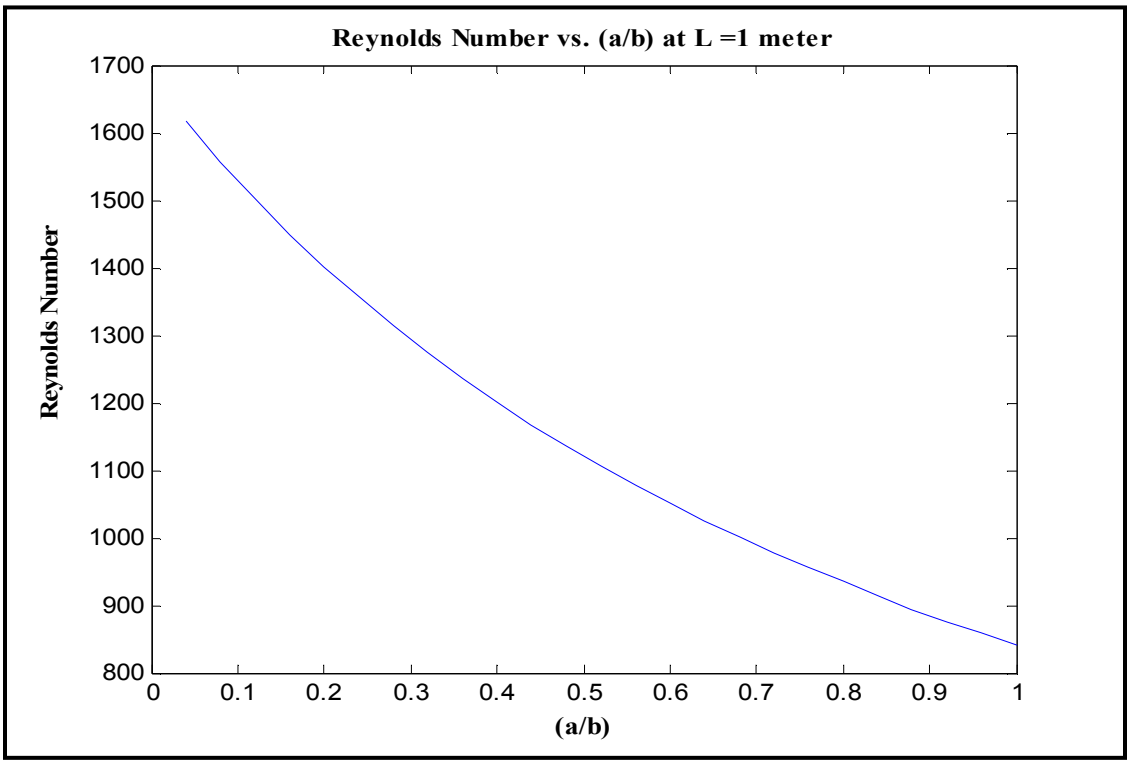

Figure D3: A plot of Reynolds Number vs. different Orifice height-width ratios (*i.e.* a/b).

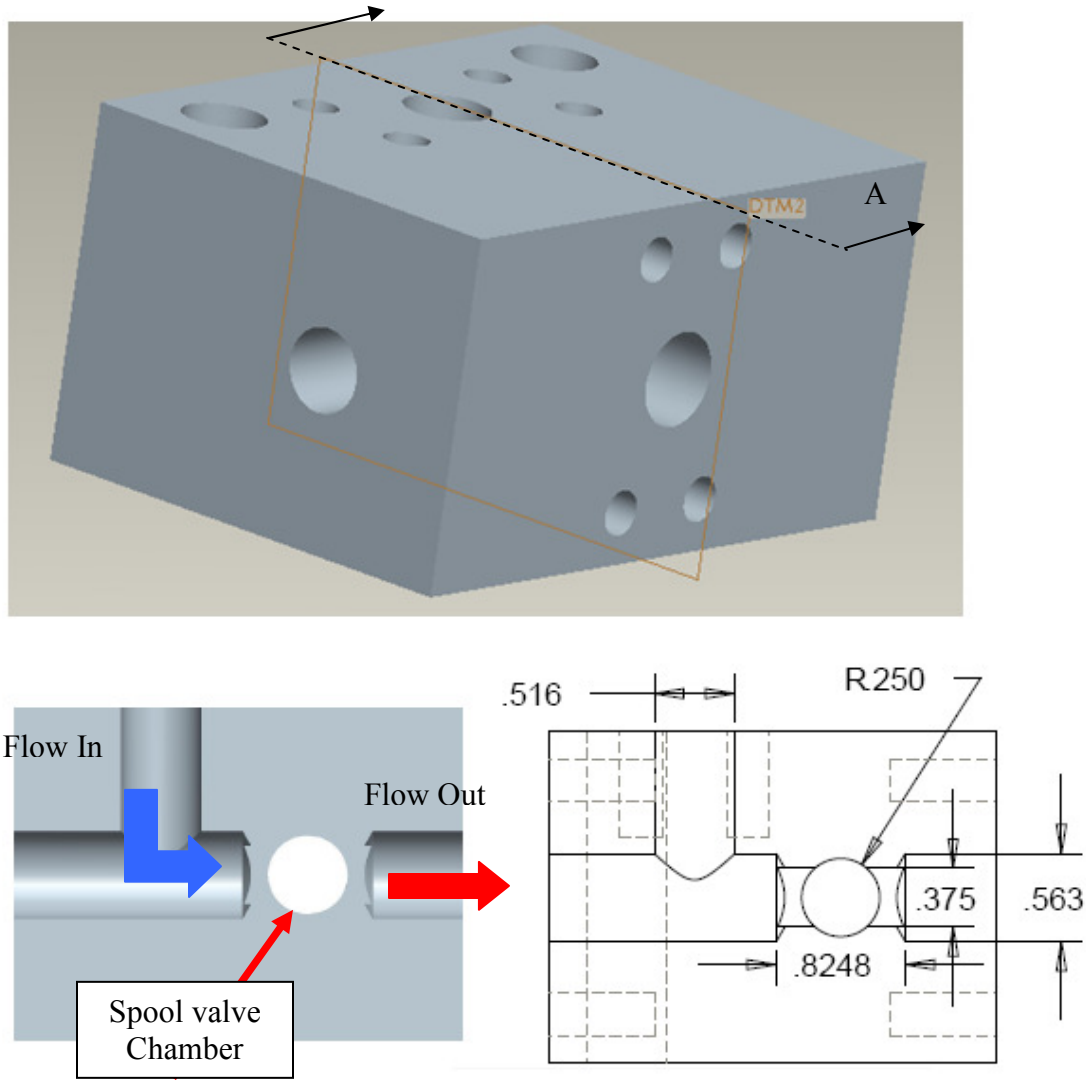

Figure D4: CAD drawing of the test valve provided from Amsted Rail and its internal features. (All the dimensions are in inches)

BIOGRAPHICAL SKETCH

Awni Kh. F. Alshakhshir was born in Al Salmiya, Kuwait on March 4th 1984. He chose to study mechanical engineering because of the variety of career paths it would give him after graduation. He realized that it would allow him to exercise his passion to study something that affects every aspect of our lives. He began studying engineering at Jordan University in Amman, Jordan in the Middle East. His love for mechanical engineering grew with every course he took. After graduation, he had the opportunity to pursue his master's degree at the University of Texas Pan American in Edinburg, Texas. Here he worked as a research assistant on a very interesting project funded by Amsted Rail. He was involved in assisting in the design and prototype testing for a new passive hydraulic suspension system for Amtrak's railcars. These opportunities provided by the graduate program gives him the confidence. It leads him to believe that hard work and dedication can make what seems impossible become attainable. He maintained a 3.88 GPA while becoming a member of associations including GOLDEN KEY, PHI KHAPPA PHI and SHPE along with participating twice in HESTEC science days. He had constant learning opportunities at UTPA. When the opportunity comes for him to continue his studies and pursue his PhD, he will likely study more in relation to dynamics and vibration, finite element methods, and thermal sciences. He looks forward to the future where he can further develop and learn. Currently, he lives at 406 E La Vista AVE, APT D, McAllen, TX, 78501.